学位論文

Probing High Energy Phenomena in the Vicinity of Super-massive Black Holes with Millimeter VLBI

（ミリ波VLBIによる超巨大ブラックホール近傍における高エネルギー現象の観測的研究）

平成26年12月博士(理学)申請

東京大学大学院理学系研究科
天文学専攻

秋山 和徳

Supervisors: Prof. Dr. Hideyuki Kobayashi

Dr. Mareki Honma

"Probing High Energy Phenomena in the Vicinity of
Super-massive Black Holes with Millimeter VLBI"

ABSTRACT

In this thesis, we present three millimeter-VLBI studies with the VLBI Exploration of Radio Astrometry (VERA) and the Event Horizon Telescope (EHT) on (1) the Galactic Center Sgr A* and (2) the nearby radio galaxy M87, which harbor supermassive black holes with the largest and second largest angular sizes, as well as (3) the γ-ray blazar NRAO 530 during its large GeV γ-ray outburst. Our studies provide the unprecedented information on the structure and activities of the regions very close to supermassive black holes (SMBHs), as summerized below.

In the work (1) on Sgr A*, we performed long-term monitoring observations of Sgr A* with the Japanese VLBI array VERA at 7mm (i.e. 43 GHz) for three years to investigate relation between variations in the radio flux and the structural size in the vicinity of its SMBH and to probe a possible mechanism of its variability, all of which have been not well understood. We found a new kind of the radio flare in Sgr A* with a long duration at least longer than 7 days without obvious changes in its size. The duration of flare is much longer than typical cooling timescales of electrons emitting the radio wave, indicating changes in the steady state of Sgr A*. We found the mas-scale properties of the flare cannot be explained by changes in the mass accretion rate of the thermal accretion disk models for Sgr A*, requiring other mechanism to explain this flare.

In the work (2) on M87, we performed 1.3 mm (i.e. 230 GHz) VLBI observations of M87 with EHT during the enhanced very-high-energy (VHE) γ-ray state in 2012. We obtained following three results. (2-i) For the first time, we have acquired 1.3 mm VLBI interferometric phase information on M87 through measurement of closure phase, that is consistent with physically-motivated models. We found that future EHT observations can effectively distinguish physical models and also confirm a signature of the gravitational lensing in M87. (2-ii) The brightness temperature of the event-horizon-scale structure is broadly consistent with the peak brightness of the radio cores at 1-86 GHz located within 100 R_s. A simple analysis predicts the magnetic field profile inversely proportional to the distance from the jet for the M87 jet, which is expected by the toroidal-field-dominant conical jet. (2-iii)

Our measurements, combined with results of multi-wavelength observations, favor a scenario in which the VHE region has an extended size of the VHE emission region of ~20-60 R_S. It seems incompatible with many VHE models expecting the compact emission region of a few R_S for this VHE activity.

In the work (3) on NRAO 530, we performed 1.3 mm (i.e. 230 GHz) VLBI observations of NRAO 530 with EHT, six months after a large γ-ray flare at GeV band. The observed 1.3 mm structure is resolved into two components consisting of the core and a relatively extended jet component that is the most probable counter part of the GeV γ-ray flare. The position angle of the inner jet is in South-West direction, being considerably different from the larger-scales jet directed to the north. 7 mm observations with the Very Long Baseline Array at 7 mm reveal that the 7-mm counter part of this jet component moved to the north as well, requiring the highly curved trajectory in the inner jet on sub-parsec scales. This is the first example that a jet component related with γ-ray activities actually moves along a curved trajectory, as suggested in previous studies on the γ-ray activities in other blazars. The flaring component has a size of $\sim 140\ \mu$as $=$ 1304 ld, much larger than the upper limit size of $\lesssim$ 49 ld at the GeV flare. This requires apparent super-luminal expansion of the flare component on the framework of the widely accepted scenarios assuming the co-spatiality of broadband emission, giving a strong limit with a jet speed of $\beta > 0.988$, Lorentz factor of $\Gamma > 6.41$, viewing angle of $\theta < 5.77^\circ$ and Doppler factor of $\delta > 9.85$.

In summary, we obtained several unprecedented findings about the physical nature of the accretion flow and relativistic jet in the vicinity of SMBHs with millimeter VLBIs. All of the three works in this thesis demonstrate importance of the future mm-VLBI observations particularly with EHT to understand fundamental nature of the high energy phenomena in the vicinity of the SMBHs.

ACKNOWLEDGEMENTS

First of all, I express my deepest gratitude to Dr. Mareki Honma in Mizusawa VLBI Observatory at National Astronomical Observatory of Japan (NAOJ). All of my works presented in this thesis were carried out under his direction. I have learned a lot of things related with astrophysics, astronomy, and more general issues of research activities under his mentorship. In addition, we have been working on many issues as a collaborator of each other beyond a simple relation between the mentor and a mentored student. He always stimulates and inspires me through many collaborative works. It is my pleasure and great honor to have spent very fruitful time with him in the last 5 years.

I express my sincere gratitude to Prof. Dr. Hideyuki Kobayshi, my supervisor, who approved my application to research at the Mizusawa VLBI Observatory. I express my deep gratitude to Dr. Motoki Kino, Dr. Hiroshi Nagai and Dr. Kazuhiro Hada. Motoki and Hiroshi organized a seminar dealing with many aspects of the active galactic nuclei (AGNs) for graduate and under graduate students in many Japanese universities. They invited me to this seminar when I was undergraduate student, and squeezed a trigger for me to study astrophysical phenomena in AGNs. After admission to the graduate school of the University of Tokyo (U. Tokyo), I have learned not only astrophysical issues on AGNs and the relativistic jets but also many practical issues on observations such as strategies for data calibration, proposing and planning observations particularly from Kazuhiro, Hiroshi and Motoki.

I also express my deep gratitude to friends and colleagues in Massachusetts Institute of Technology (MIT) Haystack Observatory, Harvard-Smithsonian Center for Astrophysics (CfA) and other institutions in the Event Horizon Telescope (EHT) collaboration. In particular, I express my sincere gratitude to Dr. Shepherd S. Doeleman, Dr. Vincent L. Fish and Dr. Ru-sen Lu. I spent every summer in the Haystack Observatory under mentership of Shep, Vicent and Ru-sen. It is quite sure that my stay in the Haystack observatory is the best experience in my Ph.D. program. It is really fruitful for me to experience the research activity at the foreign institutes in addition to learning many fundamental and/or practical things about millimeter VLBI and EHT. I note that with my room mate, Ru-sen, I have worked on many practical issues on data calibrations of EHT data jointly in the works on Chapter 3, 4 and other works (e.g. Lu et al., 2013). I also thank Dr. Michael D. Johnson and Dr. Leonid Benkevich for many fruitful discussions on imaging stuffs and polarimetry for EHT data.

I thank friends and colleagues in NAOJ, U. Tokyo and institutions participating in the Japanese VLBI Network (JVN). I have improved myself by learning from/with excellent graduate students and young professional researchers. In particular, I have been stimulated and inspired by Dr. Akihiro Doi, Dr. Kotaro Niinuma, Dr. Shoko Koyama, Dr. Takayuki Hayashi, Dr. Tazaki Fumie and Dr. Kataoka Akimasa. I give my acknowledge to Dr. Katsunori Shibata, Dr. Tomoya Hirota, Dr. Tomoaki Oyama, Mr. Ken Bushimata and Mr. Masahiro Kanaguchi for many helpful advises and supports on technical issues related with VERA observations. I thank secretaries at Mizusawa VLBI Observatory, Ms. Keiko Yoshihara and Ms. Akiyo Komori supporting my research activities.

I also thank other professional researchers in domestic institutions who had fruitful discussions and gave me many helpful comments. I thank Dr. Rohta Takahashi for many discussions on accretion disks through the works on Sgr A*. I thank Prof. Dr. Masato Okada, Dr. Shiro Ikeda, Dr. Makoto Uemura, Dr. Koji Hukushima and Dr. Kenji Nagata for many useful comments and discussions on the Exchange Monte Carlo method and the sparse modeling. I appreciate the referees of this thesis, Prof. Dr. Ken Ebisawa, Prof. Dr. Kotaro Kohno, Prof. Dr. Masato Tsuboi, Prof. Dr. Yuzuru Yoshii and Prof. Dr. Shin Mineshige. Finally, I deeply thank Dr. Kazuo Sorai in the Hokkaido University who created an opportunity to major in astronomy and recommend me to study in Mizusawa VLBI Observatory.

I thank my oversee friends and colleagues. I appreciate Prof. Dr. Gabriele Giovannini, Dr. Marcello Giroletti, Dr. Monica Orienti, Dr. Phillipo D'Ammando and Dr. Elisabetta Liuzzo. The Istituto Nazionale di Astrofisica (INAF) for many exciting collaborative works on blazars and γ-ray AGNs through "Radio Astronomy from the Space" which is a bilateral project to exchange researchers between Italy and Japan. I also thank my friend Mr. Rocco Lico in INAF for many supports during my stay in Bologna and also in Boston. I thank Dr. Avery Broderick, Dr. Jason Dexter for many fruitful discussions on M87 and Sgr A*. I thank Dr. Keiichi Asada, and Dr. Masanori Nakamura for many fruitful discussions on M87 and other important nearby AGNs. I thank Prof. Dr. A. Marscher, Dr. Svetlana G. Jorstad and Dr. Jose L. Gómez for discussions on M87 and NRAO 530. I thank Prof. Dr. Heino Falcke for inviting me to the Radboud University.

Finally, I thank my family and Ms. Yuka Tomimori continuously supporting me through my Ph.D. program.

All of studies in this Ph.D thesis are partially supported by a Grant-in-Aid for Research Fellows of the Japan Society for the Promotion of Science (JSPS). I utilized the data obtained with VERA, VLBA, SMA, and EHT consisting of SMA, JCMT, CSO, SMT/ARO and CARMA. Event Horizon Telescope work at the MIT Haystack Observatory and the Harvard Smithsonian Center for Astrophysics is supported by grants from the National Science Foundation (NSF) and through an award from the Gordon and Betty Moore Foundation (GMBF-3561). The Arizona Radio Observatory (ARO) is partially supported through the NSF University Radio Observatories (URO) program under grant No. AST 1140030. The Submillimeter Array is a joint project between the Smithsonian Astrophysical Observatory and the Academia Sinica Institute of Astronomy and Astrophysics and is funded by the Smithsonian Institution and the Academia Sinica. Funding for ongoing CARMA development and operations is supported by the NSF and the CARMA partner universities. Event Horizon Telescope work at the Mizusawa VLBI Observatory is financially supported by the MEXT/JSPS KAKENHI Grant Numbers 24540242, 25120007 and 25120008. EHT works have benefited from open source technology shared by the Collaboration for Astronomy Signal Processing and Electronics Research (CASPER). This study makes use of 43 GHz VLBA data from the Boston University gamma-ray blazar monitoring program (`http://www.bu.edu/blazars/VLBAproject.html`), funded by NASA through the Fermi Guest Investigator Program. The National Radio Astronomy Observatory is a facility of the National Science Foundation operated under cooperative agreement by Associated Universities, Inc.

CONTENTS

LIST OF FIGURES

LIST OF TABLES

1

BACKGROUND OF THE THESIS

1.1 REVIEW OF ACTIVE GALACTIC NUCLEI

Active galactic nuclei (AGNs) are very luminous galactic nuclei seen in some fraction of the extra-galaxies in the Universe. AGNs emanate a tremendous amount of energy from a quite compact region of $\lesssim$ 1 pc^3 comparable to the size of the Solar system. Their luminosities reach at $\sim 10^{39} - 10^{48}$ erg s^{-1}, often outshining the rest of their host galaxies. Such a huge luminosity of AGNs is attributed to the gravitational energy of a gas released in the process of its accretion into a central *super-massive black hole* (SMBH) with a mass of $\sim 10^{6} - 10^{10}$ M$_\odot$ at the galactic nucleus. The system of AGNs is an "engine" powered by accreting material as its "fuel", consisting of a SMBH, an accretion disk and a jet. The most luminous AGNs are the most powerful, continuously emitting sources in the Universe.

In the thesis, we present observational studies on high energy phenomena in the vicinity of SMBHs hosted by various kinds of AGNs. As the beginning of the thesis, we present an overview of AGNs focusing on the AGN zoology and its unification scheme.

1.1.1 *AGN Zoology*

The emission from AGNs is distributed in the whole electromagnetic spectrum from radio to γ-ray. AGNs have been categorized based on various criteria due to the diversity in their emission properties at various wavelengths. Here, we briefly review representative categorization of AGNs as an introduction to the "AGN zoology".

1.1.1.1 *Luminosity*

The simplest way to categorize AGNs would be classifying them with their luminosity. The luminous AGNs with $M_B < -23$ mag are categorized as *quasar*s (QSO; Greenstein & Schmidt, 1964), while faint AGNs with the Hα luminosity of

Table 1.1: AGN categorization with ratios of optical emission lines

Class	[OI]/Hα	[NII]/Hβ	[SII]/α	[OIII]/Hβ	Ref.
Seyfert galaxies	> 0.08	> 0.6	> 0.4	> 3	Veilleux & Osterbrock (1987)
LINERs	> 0.17	> 0.6	> 0.4	< 3	Veilleux & Osterbrock (1987)
transition objects	$0.08 - 0.17$	> 0.6	> 0.4	< 3	Ho et al. (1993)
BL Lac objects	—	—	—	—	Veilleux & Osterbrock (1987)
HII region galaxies	< 0.08	< 0.6	< 0.4	—	Veilleux & Osterbrock (1987)

Table 1.2: Classification of Seyfert galaxies

Type	Hβ/[OIII]λ5007	Broad Component
1	> 5.0	visible in Hα and Hβ
1.2	$2.0 - 5.0$	visible in Hα and Hβ
1.5	$0.333 - 2.0$	visible in Hα and Hβ
1.8	< 0.333	visible in Hα and Hβ
1.9	< 0.333	visible in Hα but not in Hβ
2	< 0.333	no broad component visible

$< 10^{40}$ ergs s^{-1} (corresponding to the bolometric luminosity of $\lesssim 10^{42}$ erg s^{-1}) are defined as *low luminosity AGN*s (LLAGNs; Ho et al., 1997a,b). The typical luminosity of quasars is $\sim L_{\rm Edd}$, where $L_{\rm Edd}$ is the Eddington luminosity defined as $L_{\rm Edd} \equiv 1.26 \times 10^{46}$ erg s^{-1} $(M/10^8\, M_\odot)$. On the other hand, the typical luminosity of LLAGNs is $\lesssim 10^{-4} L_{\rm Edd}$. The significant difference in the luminosity between quasars and LLAGNs is ascribable to difference in the mass accretion rate; more luminous AGNs have higher mass accretion rates (see §1.1.2.3).

1.1.1.2 *Optical Spectroscopy*

One of the most representative observational properties of AGNs is emission line features at optical bands. In terms of line ratio in optical spectroscopy, AGNs are categorized in four classes: *Seyfert galaxies* (Sy; Seyfert, 1943), *low-ionization nuclear emission-line region*s (LINERs; Heckman, 1980), *transition objects* (Ho et al., 1993) and *BL Lac objects* (Urry & Padovani, 1995). We show one of the classic criteria, for example, in Table 1.1 (see Ho, 2008, for a reviw on details and other criteria). BL Lac objects are classified as those without significant emission lines.

Seyfert galaxies are roughly categorized into two types in terms of line widths in optical spectroscopy: *type 1* Seyfert galaxies with broad line features with $\sim 1000 - 25000$ km s^{-1} and *type 2* Seyfert galaxies with only narrow line features less than $\sim$ 1000 km s^{-1}. More detailed classification has been considered for

Seyfert galaxies on the basis of appearance of the Balmer lines: the pure type 1, type 1.2, type 1.5, type 1.8 and type 1.9 (type 1.2-1.8: Osterbrock, 1977; type 1.9: Osterbrock, 1981). Pure type 1 Seyfert galaxies are typical members of the class, as described by Khachikian & Weedman (1971, 1974), while type 1.5 Seyfert galaxies are intermediate objects between pure type 1 and type 2, with an easily apparent narrow Hβ profile superimposed on broad wings. Type 1.2 and 1.8 are used to describe objects with relatively weaker and stronger narrow Hβ components, intermediate between pure type 1 and type 1.5 and between type 1.5 and type 2 respectively. In type 1.9, although the broad Hα emission is clearly evident, broad Hβ cannot be detected at least with mere visual inspection of the spectra. The more quantitative classification has been introduced after the first introduction in Osterbrock (1977, 1981). Here, for example, we show a classification of Winkler (1992) in Table 1.2. In addition to these subclasses, Seyfert galaxies which have moderately narrow broad-line features (< 2000 km s^{-1}) are named as *narrow-line Seyfert 1 galaxies* (NLSY1s; Osterbrock & Pogge, 1985).

Such type classification has been extended to other types of AGNs such as LINERs, transition objects and radio galaxies. For example, in the same manner, radio galaxies are categorized into *broad-line radio galaxies* (BLRG) and *narrow-line radio galaxies* (NLRG).

1.1.1.3 *Radio Luminosity*

Some fraction of the active galactic nuclei has a bright radio emission. In terms of radio luminosity, AGNs are divided into *radio-loud AGN*s and *radio-quiet AGN*s. As an indicator, *radio-loudness* $R_{\rm RL}$ is conventionally defined as the ratio of radio flux density at 5 GHz to B-band flux density. AGNs with $R_{\rm RL} > 10$ are classified as radio-loud AGNs, while AGNs with $R_{\rm RL} < 10$ are classified as radio-quiet AGNs (e.g. Kellermann et al., 1994). Radio-loud AGNs with intermediate luminosities are often called “*radio galaxies* (RG)”.

The most of optically selected quasars is radio-quiet, while $\sim 10 - 20$ % are radio-loud (e.g. Ho et al., 2001). As for NLSY1s, almost all objects are found to be radio-quiet AGNs (e.g. Zhou & Wang, 2002). For the case of quasars and radio galaxies, the radio emission is dominated by non-thermal synchrotron emission from the jet. The jets fainter and less powered than radio-loud AGNs have been detected also in radio-quiet AGNs in recent high sensitivity VLBI observations. The radio-loudness indicates the power of the jet emission for luminous parts of AGNs.

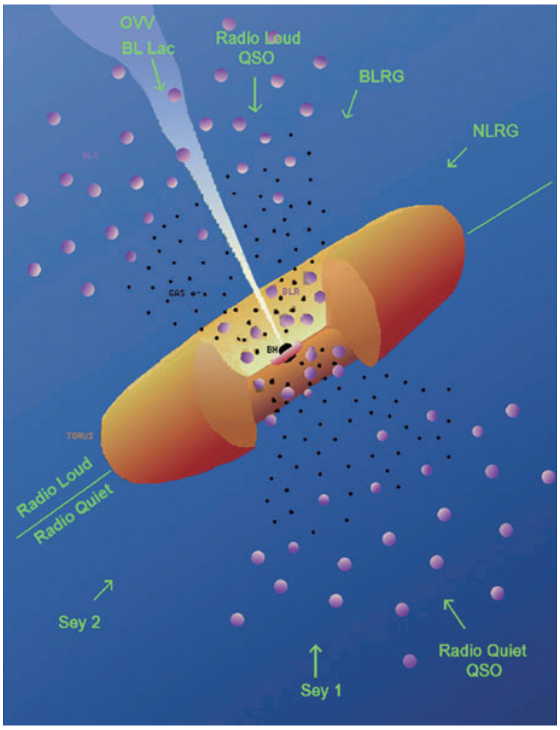

Figure 1.1: The basic structure of the active galactic nuclei as postulated by the unified scheme. (Perlman 2013, originally from Urry & Padovani 1995)

On the other hand, almost all compact LLAGNs smaller than several milliarcseconds are radio-loud (Terashima & Wilson, 2003). The origin of the radio emission in LLAGNs has been still under the debate; the radio emission could be originated in thermal and/or non-thermal synchrotron emission from the accretion disk and/or jet (see theoretical models for Sgr A*; §2.1.7).

1.1.2 *Unification of AGNs*

The most of diversity in AGNs is thought to be unified in the framework of the "unified scheme" (Antonucci, 1993; Urry & Padovani, 1995). In the unified scheme, the basic structure of AGNs consists of a supermassive black hole (SMBH) at the center, a material accreting through a disk as illustrated in Figure 1.1. Accretion is an elegant way to emanate a tremendous luminosity. Inside the accretion disk, the gas loses its angular momentum through viscous or turbulent processes and falls into the central SMBH. The gravitational energy of the accreting matter released in this process is efficiently (potentially up to $\sim$50%!) converted into other types of energies such as the thermal energy and the radiation energy, which are driving sources of the various AGN activities. Surrounding the accretion disk are various layers of warm and dense ionized gas, which would explain the broad and nar-

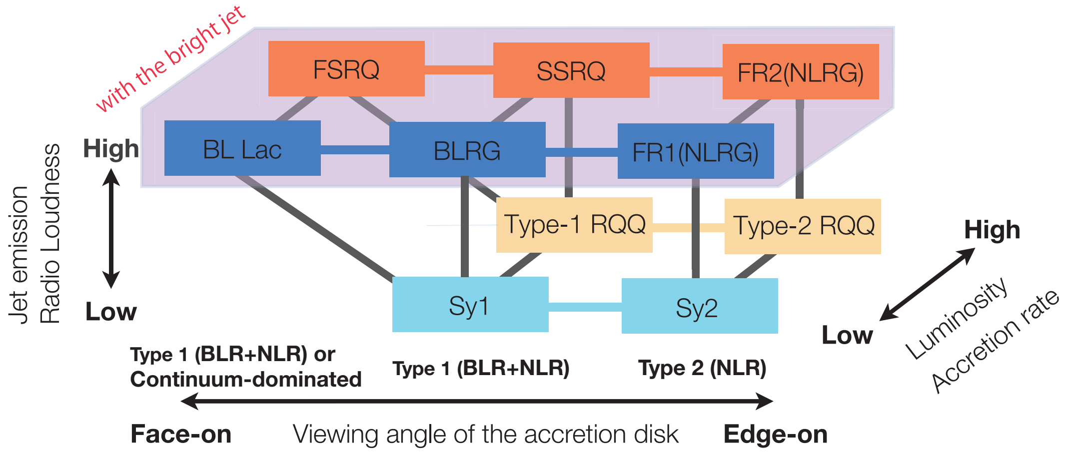

Figure 1.2: The relation between subclasses of the active galactic nuclei in the unified scheme

row emission line feature at the optical band. The inner ($\lesssim$1 pc), dense ($\sim 10^{7-11}$ cm^{-3}) and warm ($\sim 20,000$ K) ionized gas is called the *broad line region* (BLR), since it rapidly moves in a strong gravitational potential of the central SMBH generating the broad emission line feature. On the other hand, the larger (~ 100 pc), less dense ($\sim 10^{3-5}$ cm^{-3}) and slightly colder ($\sim 15,000$ K) ionized gas is called the *narrow line region* (NLR), since it more slowly moves in a weaker gravitational potential attributing the narrower emission line feature. The BLR and NLR are thought to be located at vastly different distance from the SMBH in quite different physical conditions.

In the unified scheme, AGNs are *intrinsically* different by (i) the luminosity reflecting the accretion rate of the SMBH and (ii) the radio-loudness reflecting the power of the jet, and show *apparently* different observational properties depending on (iii) the viewing angles (see Figure 1.2). We briefly summarize how the diversity of AGNs is interpreted in the unified scheme.

1.1.2.1 *Unification of Emission-line Properties at Optical Band*

A critical feature of the unified scheme is the presence of a large-scale ($1 - 100$ pc) dusty obscuring region surrounding the nucleus. The key idea of the unified scheme is that this region obscures the view of the BLR from some points of view. This idea can unify some subclasses of AGNs with different properties in optical spectroscopy (§1.1.1.2); objects that are viewed through the dusty obscuring region would be seen as type 2 AGNs like type 2 Seyfert galaxies and NLRGs, while objects viewed at a more direct angle would have broad emission line feature such as type 1 AGNs like type 1 Seyfert galaxies and BLRGs. Intermediate objects would have an intermediate amount of the obscuring material along the line of sight.

There is plenty of evidence supporting this scenario. First, spectropolarimetric observations of type 2 AGNs provide an evidence that *the broad line emissions are actually obscured* (e.g. Antonucci & Miller, 1985; Miller et al., 1991, for the type 2 Seyfert galaxy NGC 1068). Spectropolarimetry is a quite useful to investigate emission hidden by the obscuring region; it takes advantage of the fact that the obscuring region will scatter some fraction of the background light into polarized emission. The spectropolarimetric observations confirm that the broad line emission features appear in polarized emission from type 2 AGNs, strongly suggesting that the broad line emissions are obscured except polarized emission reflected in regions located outside of the dusty obscuring region. Second, observations of numerous type 2 AGNs with *Spitzer* provided a direct evidence that *there are obscuring materials* (e.g. Armus et al., 2006). The detections of silicates and molecular features as PAH and H_2 provide an evidence for presence of dusty, possibly molecular-rich materials obscuring the broad line emissions.

In the type 1 AGNs, the dusty obscuring region and accretion disk are thought to be viewed in nearly face-on orientation, while they are thought to be viewed in a direction closer to edge-on orientation in the type 2 AGNs. This type of scenarios connects the optical properties to the viewing angle of the accretion disk and possibly the obscuring material. This indication is consistent with indications from the relativistic effects on the jet in radio-loud AGNs. In addition, in some radio-loud AGNs, scattered broad-line emission has a polarization angle perpendicular to the axis of the jets (e.g. Antonucci, 1984, for the type 2 Seyfert galaxy 3C 234). This can be explained when the obscuring regions has an axis consistent with the jet axis. The obscuring region has been illustrated as having a uniform, optically and geometrically thick toroidal structure called “dusty obscuring torus” in the literature as depicted in Figure 1.1. Note that, however, this “simplest” geometry is by no means required to explain these observational properties; for instance, a obscuring region with a patchy geometry has been proposed as a more probable origin of obscuration in AGNs based on recent observations and theoretical works (e.g. see Wada, 2012, and references therein).

It is also noteworthy that some recent works on the huge samples of AGNs obtained with the Sloan Digital Sky Survey (SDSS) report some different statistical trends between type 1 and type 2 AGNs, that is difficult to be explained by difference of the viewing angles alone (e.g. Villarroel & Korn, 2014). This indicates some differences between type 1 and type 2 AGNs might be attributed to other origins (e.g. evolutional difference), while the majority of differences is ascribable to the difference of viewing angles.

1.1.2.2 *Radio-loud AGNs and their Unification*

In the radio-loud AGNs (possibly except some LLAGNs), one of the representative features is bipolar jets ejected from the nuclear regions at relativistic speeds as illustrated in Figure 1.1. The special relativistic effects on the relativistic flow in the jet play important roles to create diverse radio properties in radio-loud AGNs (Urry & Padovani, 1995).

Radio morphology of AGNs has a wide variety, but they have several common characters over various classes. The jets, i.e. highly collimated outflows are seen in one or both sides of the compact nucleus called "the radio core", depending on the degree of the Doppler (de-)beaming effect. The jet often extends to the outside of the galaxy in which the AGN resides and terminates in diffuse lobes. These lobes are often much larger than the host galaxy with a size of $1-10$ kpc and can extend for many hundreds of kilo-parsecs and sometimes reach at mega-parsecs. The largest radio lobes are one of the largest structure in the Universe, indicating that the jet is one of the most powerful phenomena in the Universe. On parsec scales, the jet is well-collimated and mostly appears as an one-sided structure that is approaching towards us, due to the Doppler beaming and de-beaming effects of the approaching jet and the receding counter jet, respectively.

The radio-loud AGNs have two subclasses, *blazars* and *radio galaxies*. The first one, blazars are the most extreme class of AGNs, where the jet is viewed from very close to our line of sight. The blazars have two subclasses. One is the *BL Lac objects*, which have featureless optical spectra. Another one is the *flat-spectrum radio quasars* (FSRQ), which are more luminous than BL Lac objects and also with broad-line emission features in optical spectra. They have differences in the luminosity and optical emission feature, but share many observational properties attributed to the strong special relativistic effects due to the small viewing angles.

The whole emission spectra of blazars is dominated by emission from the approaching side of the jet, which is highly amplified by the Doppler beaming effect (e.g. Urry & Padovani, 1995). This leads that the source is dominated by the jet properties and has a violent multi-waveband variability. The SEDs of blazars have an unusual shape dominated by two bumps of the non-thermal emission from the jet boosted by the Doppler beaming effect; the synchrotron emission dominates the lower energy side from radio to X-ray, while the inverse Compton emission dominates the higher energy side from X-ray to γ-ray up to MeV, GeV and sometimes TeV energies.

The jets in blazars generally show the apparent superluminal motion of the jet component (e.g. Whitney et al., 1971; Kellermann et al., 2004; Homan et al., 2001, 2009, 2014; Lister et al., 2009, 2013) as a consequence of the special relativistic effect (Rees, 1966). The continuum emission from blazars is generally polarized at the radio and optical bands (e.g. Angel & Stockman, 1980), indicating that most of emission at these bands is the non-thermal synchrotron radiation due to the interaction between the relativistic electrons and the magnetic fields in the jet.

Another subclass of radio-loud AGNs is radio galaxies, where the jet is misaligned with our line of sight. The jet in radio galaxies generally has a double-sided radio lobes on kilo-parsec scales. Majority of their host galaxies is the elliptical galaxy (e.g. Urry & Padovani, 1995). The radio galaxies are generally less affected by the relativistic effects due to their larger viewing angles.

The radio galaxies have been categorized in two subclasses with their morphology on kilo-parsec scales based on a criteria originally proposed in Fanaroff & Riley (1974). This categorization was applied to all radio-loud AGNs originally, but is mainly used for the radio galaxies at the present. The first one is the *Fanaroff-Riley type II* (FR II) sources with (i) a highly collimated jet, (ii) lobes with an edge-brightened morphology, (iii) the compact and bright hotspots where the jet terminates and (iv) a fairly straight large-scale morphology. The second one is the *Fanaroff-Riley type I* (FR I) sources, which are less powerful and do not have such an extreme morphology. FR I sources have (i) a less collimated jet with a larger opening angle, (ii) more plume-like lobes with an edge-darkened morphology, (iii) no hotspots and (iv) many bends in the jet. FR II sources are generally more luminous than FR I sources. The jet of both FR I and FR II radio sources is well collimated on parsec scales.

In the unified scheme, BL Lac objects represent a low-luminosity side of radio-loud AGNs, viewing FR I sources at small viewing angles. On the other hand, the more luminous FSRQs are located at a high-luminosity side, viewing FR II sources along close to our line of sight. The sources with intermediate inclination angles are BLRG at the low luminosity side and *steep-spectrum radio quasars* (SSRQ) at the high luminosity side.

1.1.2.3 *Interpretations for the Luminosity and Spectrum*

The luminosity is one of two intrinsic parameters causing the variety of the observational properties in AGNs in the unified scheme. The luminosity is thought to reflect the mass accretion rate the accretion disk, providing the difference in the spectrum between luminous AGNs and LLAGNs.

Figure 1.3 (a) shows typical spectrum energy distributions (SEDs) of radio-quiet AGNs, radio-loud AGNs and LLAGNs. Since the radio emission in the luminous AGNs is generally dominated by non-thermal synchrotron emission from the jet, the existence of the bright jet at radio band makes luminous AGNs radio-loud. The IR emission is mainly thermal emission re-emitted by the dusty obscuring region. The high energy emission such as X-ray and γ-ray is thought to be radiated by inverse-Compton scattering in which lower-energy photons are scatted by more energetic electrons in the relativistic jet and/or the hot corona surrounding the central engine. For LLAGNs, the high energy emission can be explained by inverse-Compton scattering and/or free-free emission.

In the luminous AGNs, the bolometric luminosity is mostly attributed to emission at the band between optical and ultra violet (UV), where the SED has a bump called the *big blue bump*. The big blue bump is thought to originate in emission from an optically-thick and geometrically-thin accretion flow called the *standard disk* (Shakura & Sunyaev, 1973). The standard disk is generated in the accretion flow with relatively high mass accretion rate of $10^{-3} \lesssim \dot{M}/\dot{M}_{\rm Edd} \lesssim 1$ (Abramowicz et al., 1995), where $\dot{M}_{\rm Edd}$ is the Eddington mass accretion rate. The standard disk has the accreting matter enough to be optically thick, leading that the accretion flow can efficiently release the gravitational energy into the radiational energy. The standard disk has a relatively lower temperature due to its efficient radiative cooling, leading to the lower gas pressure and geometrically-thin flow structure. The SED of the standard disk is a composite of the optically-thick thermal emission (i.e. the black body radiation) spectra over a range of temperatures of $\sim 10^4 - 10^6$ K, creating the big blue bump in optical and UV regimes.

Figure 1.3 (b) shows various SEDs of the radio-quiet AGNs at different bolometric luminosities. The big blue bump is seen in the luminous AGNs ($L/L_{\rm Edd} \gtrsim 10^{-3}$). The big blue bump has a lower luminosity and a lower peak frequency for

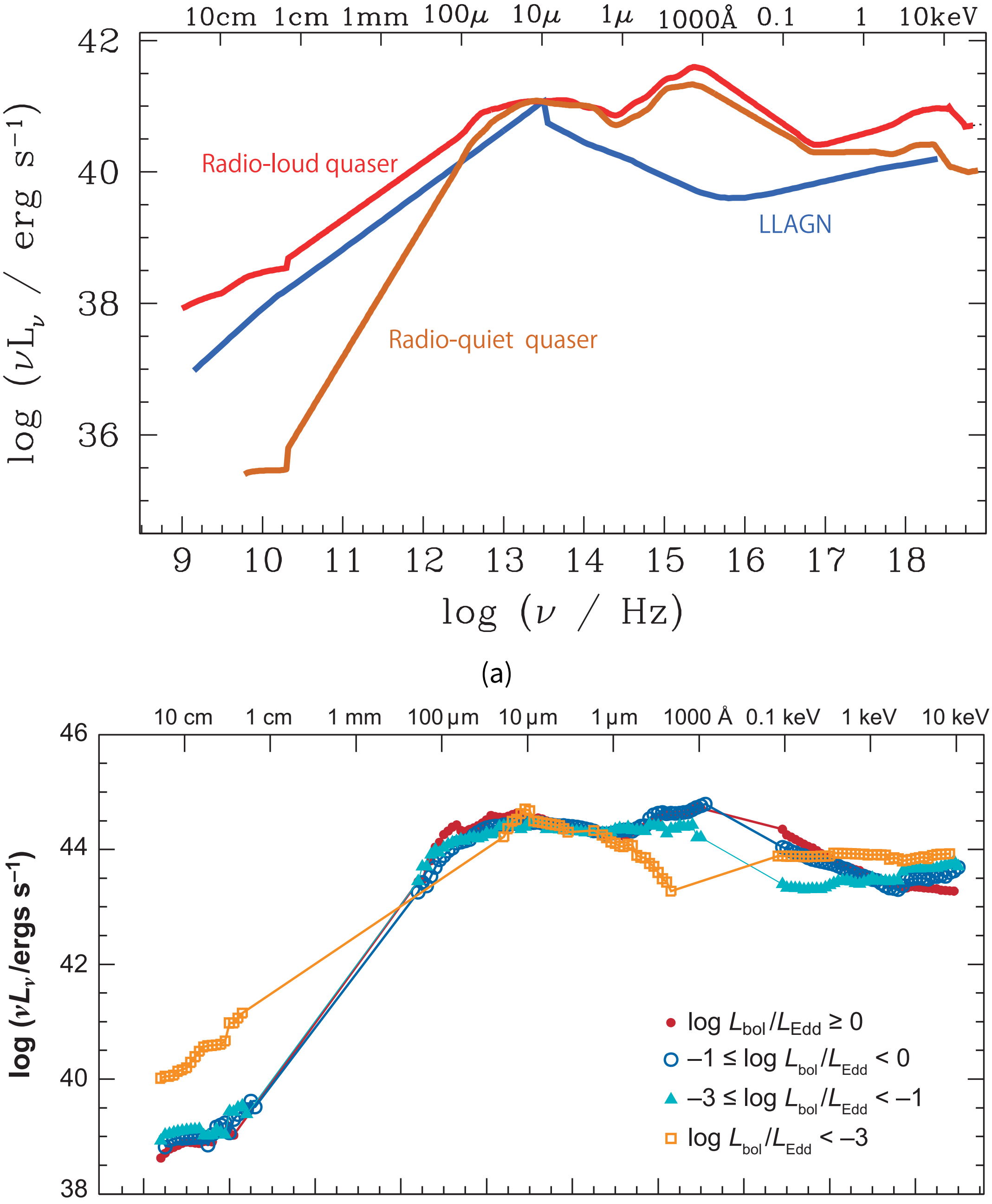

(a)

(b)

Figure 1.3: The composite SEDs of AGNs. (a) The average SEDs of low-luminosity AGNs (orange line), luminous radio-loud quasars (blue line) and radio-quiet quasars (red line) (edited a figure in Yuan, 2007). (b) The averaged SEDs of the radio-quiet AGNs with different bolometric luminosities (Ho, 2008).

sources with a lower bolometric luminosity, that is ascribable to lower mass accretion rate. However, the big blue bump suddenly disappears in the LLAGNs. The most prominent feature of LLAGNs is the lack of the big blue bump in their spectra. This leads to the hard spectrum from X-ray to optical regime and also large radio-loudness. Another important feature is the existence of a bump in sub-mm or far infra-red (FIR) regime. Interpretation of sub-mm/FIR bump depends on theoretical models, but the accretion flow in LLAGNs is thought to be vastly different from the standard disk. Due to a low accretion rate of $\dot{M}/\dot{M}_{\rm Edd} \ll 1$, the disk becomes optically thin and radiatively inefficient, so that the advection cooling becomes predominant instead of the radiative cooling. This leads to a quite different physical behavior of the accretion flow called the *radiatively inefficient accretion flow* (RIAF; see 2.1.7.1).

1.1.2.4 *Low Luminosity AGNs in the Unified scheme*

LLAGNs do not follow the standard unification scheme (see Ho, 2008, for a review); LLAGNs are not simply located in the low-luminosity end of Figure 1.2. First of all, their central engines undergo fundamental changes when the accretion rate drops to extremely sub-Eddington values. The accretion disk becomes the RIAF (see 2.1.7.1) with a lack of the big blue bump in optical and UV regimes, leading that the circum-nuclear gas is less ionized by UV photons from the accretion disk. The results of spectropolarimetric survey toward type 2 Seyfert galaxies seeking for reflected broad-line emission indicate that the “true type 2” (“naked type 2”) Seyfert galaxies, which intrinsically do not have any broad line region, are more common in LLAGNs (e.g. Tran, 2001, 2003). In addition, the Palomar survey of the nearby LLAGNs provides a statistical trend that the BLR vanishes at the lowest luminosities or Eddington ratios (Ho, 2008). Similarly, the obscuring region disappears at very low luminosities, indicated by observational evidences such as the low absorbing column densities and weak or undetected Fe Kα emission in a large fraction of LINERs (Ho, 2008). LLAGNs are not simply scaled-down versions of such powerful AGNs, since the BLR and the obscuring region disappear in LLAGNs in extremely sub-Eddington regime.

1.2 BRIEF OVERVIEW OF THE RELATIVISTIC JET IN AGNS

The relativistic jets, which are one of the representative features in radio-loud AGNs, have posed many intriguing questions in astrophysics. In this subsection, we briefly overview typical issues on the relativistic jet in AGNs. Since the debated issues on the relativistic jet are highly diversified and wide-ranging, here we take up specific issues related to the present thesis.

The relativistic jet launched in AGNs is one of the most powerful phenomena in the Universe as introduced in §1.1.2.2. The relativistic jet is ultimately powered by the SMBH and the accretion disk at the center of AGNs. The launched jet is gradually accelerated to a relativistic speed near the speed of light, collimated into a narrow flow with a very small opening angle of a few degrees. The jet penetrates the external environment such as the interstellar medium in its host galaxy and the intergalactic medium on more larger scales, and then ends at a huge radio lobe with a terminal shock called a hot spot. At some regions in the jet, some amount of the kinetic energy of the flow is converted into the internal energy of the particles through a shock or other processes, causing highly energized particles radiating the non-thermal emission at the whole energy band from radio to γ-ray.

1.2.1 *Formation of the Relativistic Jets*

One of the most fundamental question is how the relativistic jets are formed in the vicinity of SMBHs. Although numerous studies have been performed both observationally and theoretically in the last several decades, this issue is still open question and not fully understood. A primary challenge is still explaining the following *most basic* observational properties; (i) the collimation process causing the narrow streams with opening angles of only a few degree Jorstad et al. (e.g. 2005); (ii) the acceleration process resulting in the relativistic flows with bulk Lorentz factors of up to 10-30 or more (e.g. Kellermann et al., 2004; Homan et al., 2001, 2009, 2014; Lister et al., 2009, 2013); (iii) the mechanism sustaining such a structure over a wide range of distance from the central engine to kilo- or mega-parsecs.

One of possible scenarios is that the jets are hydrodynamical, kinetic energy-dominated flows accelerated by gas pressure gradients. If the gas is heated to a temperature high enough that the mean energy of particles exceeds its gravitational biding energy, a substantial mass loss will occur in the accretion disk. Such a condition can be achieved when the outer surface of an accretion disk is irradiated by the X-ray from the inner part of the disk (Begelman et al., 1983), or when the accretion disk is a hot accretion disk (Takahara et al., 1989) such as RIAFs (see §2.1.7.1). The jets can be collimated by a gas pressure from the external medium surrounding the jets as originally proposed by Blandford & Rees (1974). The external gas pressure can also form a de Laval nozzle where the flow of the hot gas gets supersonic.

Alternatively, the current theoretical paradigms are preferable based on magnetohydrodynamic (MHD) schemes, where the magnetic field plays important roles for collimating and accelerating the jets (e.g. Lovelace, 1976; Blandford, 1976). On the framework of MHD schemes, the differential rotation in the black holes's ergosphere or the inner accretion disk creates the tightly-twisted magnetic field. The flow is initially highly-magnetized so that the Poynting flux dominates the total jet energy. The jet can be launched and accelerated by the magnetic pressure gradient of the toroidal-field component and magneto-centrifugal force of the poloidal component, resulting that the Poynting energy of the jet is gradually converted into the kinetic energy. The jets are confined by the magnetic hoop stress of the toroidal-field component and/or the external pressure from the accretion disk or the ambient medium. The ultimate source of the jet energy is the rotational energy of the spinning black hole (Blandford & Znajek, 1977) and/or the gravitational energy of the accreting material released in the accretion disk (Blandford & Payne, 1982).

Recently, significant progresses have been achieved in the theoretical studies based on the general relativistic-MHD (GRMHD) simulations (e.g. McKinney, 2006; Komissarov et al., 2007). GRMHD simulations have shown that the jet is initially formed with a large opening angle, and collimated/accelerated gradually in the inner 10^3 R_s region. The jet has a paraboloidal shape confined by the external medium and the internal magnetic hoop stress in this region. The Poynting energy is gradually converted into the kinetic energy in the acceleration process, resulting in the bulk Lorentz factor of ~ 10 at the end of the collimation/acceleration region. Beyond this region, the flow shape gets conical due to the lack of forces confining the stream.

1.2.2 *High Energy Particles and Photons in the Relativistic Jets*

Another fundamental question is how high-energy particles and photons are generated in the relativistic jets. Radio observations have revealed that the relativistic jets are generally illuminated by synchrotron emission attributed to the relativistic leptons. High-energy photons with up to GeV or TeV energies would be attributed to the relativistic leptons and possibly hadrons. The particle acceleration processes in the relativistic jets are very important to understand their observational properties.

The origin, in particular, the location of such high-energy leptons in the jet has been unclear. A widely preferred scenario is the internal shock scenario in which the particle energization is expected to occur at about 10^{16-17} cm ($\sim 0.01 - 0.1$ pc $\sim 10 - 100\ R_s$ for $M_{\rm BH} \sim 10^8\ M_\odot$) from the central engine. On the other hand, it is recently proposed based on multi-wavelength observations towards blazars and the radio galaxy M87 that the particle (re-)acceleration occurs at larger distance, even more than 1-20 pc from the black hole possibly attributed to the stationary shock feature (e.g. Marscher et al., 2008, 2010) possibly attributed to over-collimation of the jet (e.g. Stawarz et al., 2006; Cheung et al., 2007; Asada & Nakamura, 2012).

Recent theoretical works have shown that the particle acceleration can occur more inner region of the jet or the accretion disk. (Riquelme et al., 2012) performs two-dimensional (axis-symmetric) Particle-in-cell (PIC) simulations and reveals that magnetic reconnection produces a distinctive power-law component in the energy distribution function of the particles, indicating the likelihood of non-thermal ion and electron acceleration in collisions accretion disks. On the other hand, very recently, (Broderick & Tchekhovskoy et al., 2014) have shown that the efficient acceleration of leptons can occur within the jet near the stagnation surface of the black hole where the separatrix between material that falls back into the black hole and material that is accelerated outward forming the jet. These processes might explain non-thermal emission from the inner $\sim 10\ R_s$ region, where both internal-shock and far-side stationary-shock scenarios can not explain the particle acceleration.

1.2.3 *Importance of Observational Studies at High Spatial Resolution*

At the present, observational studies of the jet formation or production of high energy particles/photons are extremely limited due to the insufficient spatial resolution. For probing the formation mechanism of the relativistic jet or the particle acceleration at the jet base and/or accretion disk, it is very important to spatially resolve the flow and emission structure of the accretion disk and/or the jet base in the vicinity of the SMBH on scales of $< 10^2\ R_s$.

On the other hand, for high-energy emission, in addition to the location, many fundamental properties such as the size of the emission region, kinds of emitting particles and the structure of underlying jet flow are not well confirmed also due to the lack of spatial resolution. The spatial resolution of ~ 0.1 pc is required for resolving the emission region and probing its detailed structure (see §4.1).

1.3 MILLIMETER VLBI: TECHNICAL BACKGROUND OF THE THESIS

High spatial resolution of the telescope is one of the most important factors to probe the physical nature of the central engine in AGNs. For instance, the spatial resolution of $\sim$ 1 mas is required for probing a region with a size of $R < 10^2\,R_s \sim 0.1\,\mathrm{pc}$ in the nearby AGNs with a $M_{\mathrm{BH}} \sim 10^8\,M_{\odot}$ at a distance of 100 Mpc, which corresponds to extent of the accretion disk, the production region of the relativistic jet and the size of the high-energy-emission region.

If a telescope has a diameter of D at an observing wavelength of λ, the spatial resolution of the telescope is given by $\theta \sim \lambda/D$. For achieving higher spatial resolution, we need to perform an observations at a shorter wavelength (a higher frequency) with a larger diameter. In Figure 1.4, we show the spatial resolution of existing astronomical instruments.

Very Long Baseline Interferometers (VLBI) are a unique instruments achieving very high spatial resolution of $\lesssim$ 1 mas thanks to their extremely large effective diameters comparable to or larger than the size of earth. In particular, the spatial resolution of VLBI can reach at few tens of micro-arcseconds at short-millimeter wavelengths, comparable to the Schwarzschild or gravitational radii of the nearest super-massive black holes. Such a extremely high-spatial resolution will be achieved with the *Event Horizon Telescope (EHT)* in the next decades, providing a great deal of progresses in studies of astrophysical phenomena in the vicinity of the SMBHs, such as mass accretion processes, formation of the relativistic jet and production of high-energy particles and photons.

In the thesis, we present studies on the main targets of the EHT with millimeter VLBI facilities including EHT itself as pre-studies for the next EHT era. In this section, we briefly introduce VLBI and EHT as the technical background of the thesis.

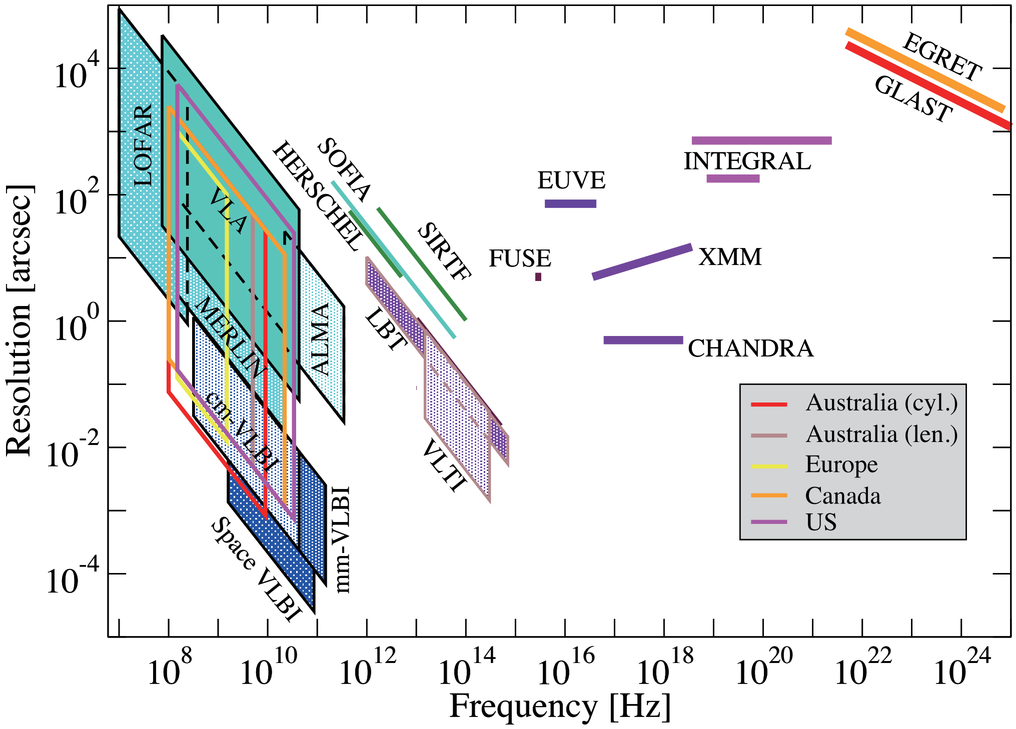

Figure 1.4: Spatial resolution of the existing instruments as a function of the observing frequency (edited in a figure in Lobanov (2007).

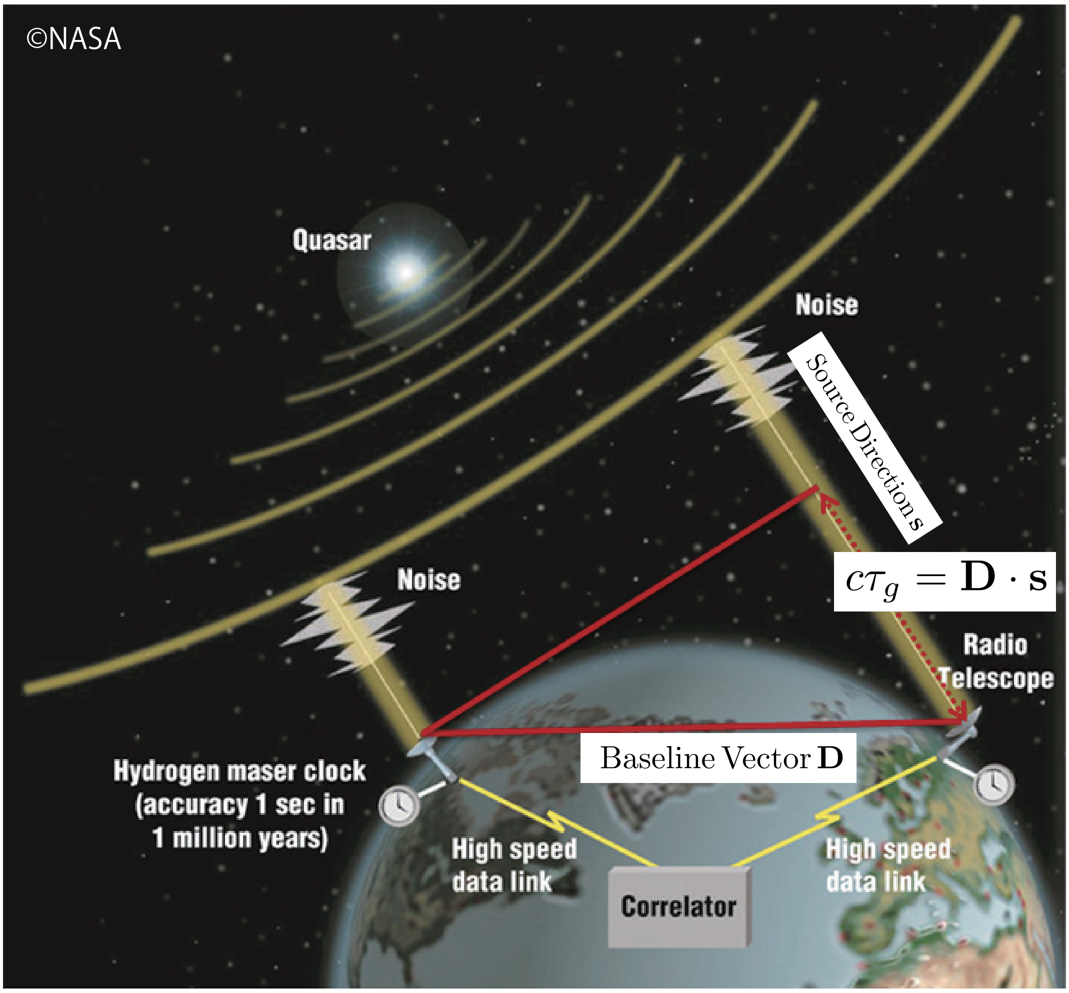

Figure 1.5: A schematic view of Very Long Baseline Interferometers. Image is taken from the website[1] of the space-geodesy group in NASA/JPL.

1.3.1 *The Basic Concepts of VLBI*

VLBIs and more generally radio interferometers consist of arrays of widely separated single-dish telescopes. The key idea of the radio interferometry is based on the fact that the signals from cosmic sources arrive at different telescopes on different times. For the case of an interferometer with two stations shown in Figure 1.5, the signal from the point source is received at two stations with a *geometric delay* of $\tau_g = \mathbf{D} \cdot \mathbf{s}/c$, where $\mathbf{D}$ is a baseline vector and $\mathbf{s}$ is a unit vector directed into the source from the Earth. We can measure the brightness and direction of the source from the magnitude of the signals and the geometric delay, respectively. In the VLBI observations, the signals are separately recorded at each station with very accurate measurements of their arrival time using the hydrogen maser clock synchronized by the GPS clock. Data are generally transferred to a central facility of the VLBI observatory and processed in the correlator at there.

The goal of the interferometric observations is of course to obtain the intensity distribution $I(x, y)$ of a target source at a frequency ν. (x, y) is a sky coordinate (usually in the equatorial coordinate) relative to a reference position so called *the phase-tracking center*. The observed quantity is a complex function called *visibility* $V(u, v)$, which is related to $I(x, y)$ by two-dimensional Fourier transform given by

$$I(x, y) = \int_{-\infty}^{\infty} \int_{-\infty}^{\infty} du\, dv\, V(u, v) \exp\left(i2\pi(ux + vy)\right) \tag{1.1}$$

Here, u and v are the projections of the baseline vector (i.e. projected baseline lengths) normalized by the observing wavelength $\mathbf{D}/\lambda$ into x-axis and y-axis, respectively. Since the intensity $I(x, y)$ is a real function, the visibility $V(u, v)$ is a complex function with the Hermit symmetry of $V(-u, -v) = V^*(u, v)$. $V(u, v)$ is obtained from the Fourier transformation of the cross correlation of the input signals at two stations, which is performed in the *correlator*.

The visibility can be expressed with the amplitude term V_{amp} and the phase term ϕ as

$$V(u, v) = V_{\mathrm{amp}} \exp(i\phi). \tag{1.2}$$

u and v are also called as the spatial frequency, because the visibility $V(u, v)$ is the Fourier transformation of the intensity distribution. The visibility amplitude

---

[1] `http://space-geodesy.nasa.gov/techniques/VLBI.html`

indicates a strength of the sinusoidal pattern with the spatial frequencies of u and v inside the image, while the visibility phase indicates a position of that pattern. The visibility at larger u and v reflects smaller fluctuations in the image. It means that observing at the larger baseline length and shorter wavelength is equivalent to correcting information of the intensity distribution on finer spatial scales, leading to high spatial resolution of $\sim \lambda/D$.

Here, we consider physical meaning of the amplitude term and phase term using a circular Gaussian component in the sky. The intensity distribution of the component can be written by

$$I(x,y) \quad = \quad \frac{F}{2\pi\sigma} \exp\left(-\frac{(x-x_0)^2+(y-y_0)^2}{2\sigma^2}\right), \qquad (1.3)$$

where F, σ and $(x_{0,}y_0)$ is the total flux, the variance ($\propto$ the FWHM size) and the position of the component. The visibility for the intensity distribution is given by

$$V(u,v) \quad = \quad F \exp\left(-\pi^2\sigma^2\left(u^2+v^2\right)\right) \exp\left(i2\pi\left(ux_0+vy_0\right)\right). \qquad (1.4)$$

The amplitude and phase terms of the visibility are $V_{\mathrm{amp}} = F\exp\left(-\pi^2\sigma^2\left(u^2+v^2\right)\right)$ and $\phi = 2\pi\left(ux_0+vy_0\right)$. The flux density and the size is included in the amplitude term, while the position is included in the phase term. Although such a information is not simply separated into the amplitude and phase term for the case of more than two components, we can estimate characteristic flux density and size of the sources from the amplitude measurements. One can easily imagine that the measurements of phases is closely related to the geometric delay since both quantities reflect the position of the sources.

The most important thing in interferometric observations is the precise measurement of the visibility phase and amplitude. In VLBI observations, visibility measurements are severely affected by the Earth's atmosphere, in which water vapor is distributed non-uniformly and the signals from the source thus propagate through different optical paths. In particular, the atmospheric (in particular, tropospheric) fluctuations cause the time variation in the signal delay, leading to the phase fluctuations. In VLBI observations, generally, we need to detect signals within a time duration so-called the *coherence time* in which the phase is rotated by the atmospheric fluctuation. The typical coherence time is ~1 min at $\sim$ 1 cm and $\sim$ 10 sec at ~1 mm.

The phase fluctuations is very severe problem at short-millimeter wavelengths of ~ 1 mm, because it is generally very difficult to measure visibilities with a high SNR in such a short coherence time. This difficulty can be overcome by incoherent averaging techniques (Rogers et al., 1995) for the amplitude measurements, where the amplitude can be estimated by averaging shortly segmented data (within the coherence time) over an integration time much longer the coherence time. On the other hand, since the visibility phase information is destroyed in the process of the incoherent averaging, the visibility phase still needed to detect within a short coherence time. In general, the robust measurements of the visibility phase is considerably difficult particularly for not strong sources.

In millimeter VLBI observations at ~ 1 mm, *the closure phase* has been used instead of the visibility phase as an interferometric phase information. The closure phase is defined by the sum of the visibility phases on three closed baselines making a triangle as

$$\phi_{ijk} = \phi_{ij} + \phi_{jk} + \phi_{ki},$$

where ϕ_{ij} is the visibility phase on the baseline between stations i and j. The closure phase must be zero if the structure has a point symmetry. In other words, the structure should have asymmetric structure if the closure phase is not zero.

The biggest advantage of the closure phase is that it is not affected by systematic errors of the visibility phase attributed to the station-based origins such as the atmospheric fluctuation effects. If such phase error of $\Delta\phi_i$ is induced at each station, it is cancelled out in the closure phase as follows:

$$\begin{aligned}
\phi_{ijk}^{\mathrm{obs}} &= \phi_{ij}^{\mathrm{obs}} + \phi_{jk}^{\mathrm{obs}} + \phi_{ki}^{\mathrm{obs}} && (1.5)\\
&= \left(\phi_{ij}^{\mathrm{int}} + \Delta\phi_i - \Delta\phi_j\right) + \left(\phi_{jk}^{\mathrm{int}} + \Delta\phi_j - \Delta\phi_k\right) + \left(\phi_{ki}^{\mathrm{int}} + \Delta\phi_k - \Delta\phi_i\right) && (1.6)\\
&= \phi_{ij}^{\mathrm{int}} + \phi_{jk}^{\mathrm{int}} + \phi_{ki}^{\mathrm{int}} && (1.7)\\
&= \phi_{ijk}^{\mathrm{int}}. && (1.8)
\end{aligned}$$

This means that the closure phase only reflects the information of the source structure, and then it is the robust quantities not biased by station-based errors. The closure phase is a key quantity for modeling images in short-millimeter VLBI observations . For measuring the closure phases with good SNRs, the sensitivity must be enough high at all three stations, since the errors are dominated by the errors on the baseline with the lowest sensitivity.

1.3.2 *Long-millimeter VLBI Facilities Used in This Thesis*

Here, we briefly introduce millimeter VLBI facilities VERA and VLBA (Figure 1.6), with which we perform millimeter VLBI observations at 43 GHz (i.e. 7 mm) in this thesis.

VERA (the VLBI Exploration of Radio Astrometry) is the first VLBI array dedicated to phase-referencing VLBI for Galactic astrometry, consisting of 4 antennas with a diameter of 20 m across Japan (e.g. Honma et al., 2000). Observing frequencies of VERA are 6.7 GHz (S-Band), 8 GHz (X-Band), 22 GHz (K-Band) and 43 GHz (Q-Band). The maximum baseline length of VERA is 2,270 km between Mizusawa and Ishigaki stations, providing a maximum angular resolution of ~ 0.5 mas at 43 GHz. A noteworthy feature of VERA is the dual-beam receiving mode (e.g. Honma et al., 2003) with two movable receivers, in which two sources can be simultaneously observed. It provides a unique ability to perform simultaneous observations of two sources within $0.3^\circ - 2.2^\circ$ separation from each other on the sky. This provides a great advantage for the phase-referencing observations, in which the atmospheric effects on the visibility phases for a weak target source is solved by nearby strong source. In the traditional “fast-switching” method, the two sources (target and phase calibrator) are alternately scanned every few minutes, i.e., timescale shorter than that of the atmospheric change, reducing the integration time of the target source down to a half or a quarter of the observing duration and thus reducing the sensitivity. The dual-beam method does not need this “trade-off” and allows to allocate much longer integration time on the target source.

VLBA (the Very Long Baseline Array) is the largest ground-based VLBI array, dedicated in full time to astronomical studies. It consists of 10 antennas with a diameter of 25m across the United States. VLBA covers various observing frequencies of 0.3 GHz, 0.6 GHz, 5 GHz, 8 GHz, 15 GHz, 22GHz, 43 GHz and 86 GHz. The maximum baseline length of VLBA is 8,611 km between Mauna Kea and Saint Croix stations, yielding a spatial resolution of ~ 0.2 mas at 43 GHz.

1.3.3 *Importance of VLBI Observations at Short-millimeter Wavelengths*

The global VLBI array across the Earth can achieve an extremely high spatial resolution of few tens of microarcseconds at short-millimeter wavelength ($\lambda \leq 1.3$

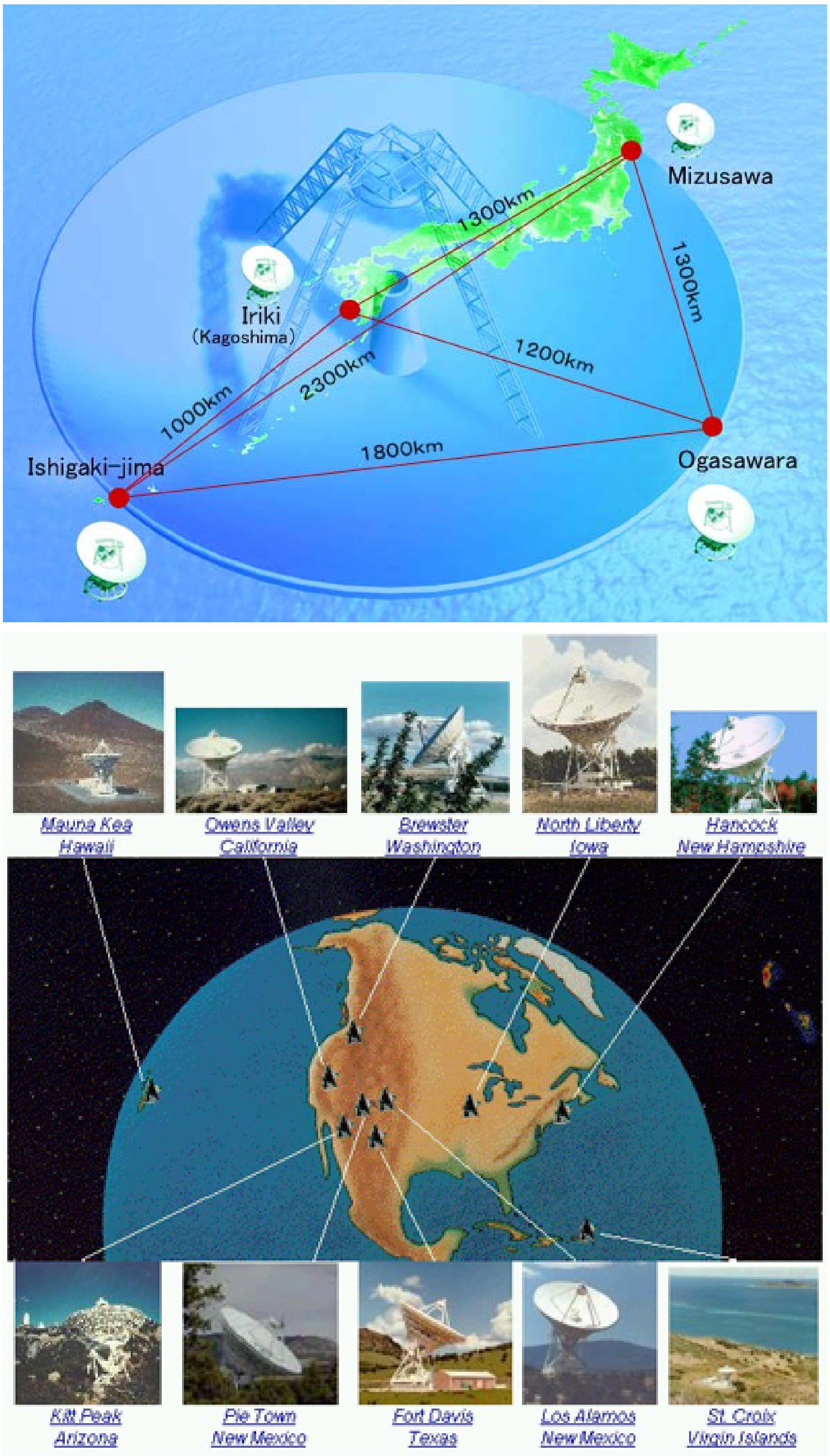

Figure 1.6: (Upper) Four antennas of VERA array across Japan. Image was adopted from `http://veraserver.mtk.nao.ac.jp/system/index-e.html`. (Lower) Ten antennas of the VLBA across the United States. Image was adopted from `http://www.vlba.nrao.edu/sites/`.

Table 1.3: The angular size of Schwarzschild radius of typical AGNs

Source	Mass (10^6 M$_\odot$)	Distance (Mpc)	Angular Size of R_s (μas)	Ref.
Sgr A*	4	8×10^{-3}	10	§2.1.3
M87 (NGC4486;Virgo A)	3-6 $\times$ 10^3	15	3-7	§3.1.2
M104 (NGC4594;Sombrero)	1 $\times$ 10^3	10	2	Ferrarese & Ford (2005)
Cen A (NGC5128)	5 $\times$ 10	4	0.25	Ferrarese & Ford (2005)

mm, $\nu \geq 230$ GHz). The microarcsecond-scale resolution is quite important to probe the high energy phenomena in the vicinity of the SMBHs at least following two reasons.

1) Resolving the R_s-scale structure of the nearby SMBHs

Table 1.3 shows the top 4 nearby AGNs with the largest angular sizes of R_s. Here, we limited to AGNs, because they are more luminous than normal galactic nuclei at radio band and then more suitable for investigating environment near central black holes with VLBI. Some nearby normal galaxies such as M31 ($\sim 10^8$ M$_\odot$; Bender et al., 2005) host SMBHs with larger angular sizes, but their nuclei are too faint to be studied with VLBI.

The spatial resolution of the global short-millimeter VLBI array can reach at the angular size of the SMBHs in the galactic center Sgr A* and the nearby radio galaxy M87. This means that the short-millimeter VLBI can (1) test the Einstein's general relativity in a strong gravity regime by obtaining an image of the black hole shadow around their event horizon (e.g. Falcke et al., 2000; Doeleman et al., 2009; Fish et al., 2014), (2) probe the accretion flow around a black hole and (3) probe the jet production region in these sources on scales of $\sim R_s$ through the direct imaging of the event-horizon-scale structure in the vicinity of the SMBHs. It is quite clear that observations on this scale will provide significant progresses in studies of physical processes in the vicinity of the black holes.

1.3.3.1 *Resolving the high-energy-emission region in the relativistic jet*

The extremely high-spatial resolution is also beneficial to investigate the high-energy-emission region in the relativistic jet. First, its spatial resolution can reach at a few tens of microarcsecond corresponding to $\lesssim 0.1$ pc at $z \lesssim 2$. Considering that most of *fermi*-detected γ-ray AGNs are located at $z \lesssim 2$ (Ackermann et al., 2011a), short-millimeter VLBI can resolve the γ-ray emission region in vast majority of γ-ray AGNs. This provides a potential to directly measure the size and detailed structure of high-energy emission region as well as the trajectory of the jet around it, which are key parameters of theoretical models (see §4.1 for details). Second, observations at shorter wavelength are less affected by synchrotron self-absorption (SSA) effects, providing a deeper view of the relativistic jet (see §3.1.3.2 for details). Previous studies revealed a delayed brightening of the radio flux density at lower frequencies that can be attributed to stronger SSA effect at the high γ-ray state (e.g. Orienti et al., 2013; Hada et al., 2014), suggesting that shorter-wavelength observations are desirable to investigate the jet structure in connection with γ-ray emission.

1.3.4 *Event Horizon Telescope*

VLBI observations at short-millimeter wavelengths have been technically challenging due to the limited sensitivity of the instruments, fast atmospheric phase fluctuations and small number of available stations. Recent technical developments (e.g. phased-array processors, digital backends and recording systems with broader bandwidths) and the addition of new (sub)millimeter telescopes have led to a breakthrough to (sub)millimeter VLBI observations. In particular, significant progress on 1.3 mm VLBI observations has been achieved in the last few years with the Event Horizon Telescope (Doeleman et al., 2008, 2009, 2012; Fish et al., 2011, 2013; Lu et al., 2012, 2013, 2014; Akiyama et al., 2014b).

The Event Horizon Telescope (EHT) is an international project to construct global short-millimeter VLBI array observing at 1.3 mm and 0.87 mm. The main goal of the EHT is (i) testing general relativity by imaging the shadow feature due to the event horizon of the super-massive black hole (SMBH), (ii) understanding accretion around a black hole and (iii) understanding jet genesis and collimation, through the direct imaging of the event-horizon-scale structure in the close vicinity of the SMBH in Sgr A*, M87 and other nearby AGNs. EHT is also expected to provide the most inner-view of the radio core ever in other radio AGNs, which is crucial to constrain on the physical nature of the high energy phenomena in the relativistic jet.

1.3.4.1 *History of EHT and Background of Chapter 3 and 4 in the Technical Context*

Early EHT observations (Chapter 3 and Chapter 4, Doeleman et al. 2008, 2012; Fish et al. 2011; Lu et al. 2012, 2013; Akiyama et al. 2014b) were performed with an array at three geographic site: the Arizona Radio Observatory's Submillimeter Telescope (ARO/SMT) on Mt. Graham in Arizona, both two single antennas and a phased array of Combined Array for Research in Millimeter-Wave Astronomy

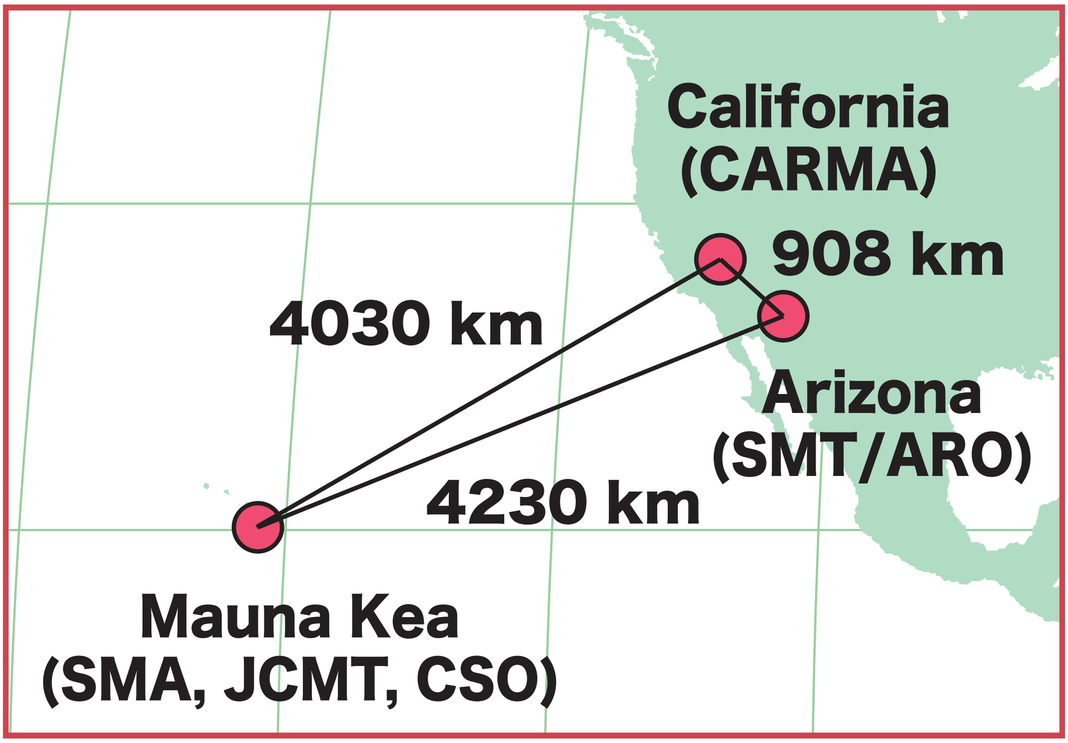

Figure 1.7: The array configuration of early EHT observations

(CARMA) on Cedar Flat in California, and Caltech Submillimeter Observatory(CSO) , James Clerk Maxwell Telescope (JCMT) and a phased array of Submillimeter Array (SMA; Ho et al. 2004) with CSO/JCMT on Mauna Kea in Hawaii (Figure 1.7).

EHT works are the nostalgia trip to 1970s[2], which is the era of the dawn of Very Long Baseline Interferometry (Moran, 1998). In 2007, EHT made the first footprint by acquiring information of the micro-arcsecond-scales structure in the Universe through measurements of only amplitude of the correlated complex visibility. 2007 Observations were performed with an array of three single-dish telescopes consisting of SMT, a single antenna in CARMA and JCMT, successfully resolving the event-horizon-scale structure of Sgr A* (§2.1.5.2; Doeleman et al. 2008). The second EHT observations were held in 2009 with a slightly updated array of SMT, two single antennas in CARMA and JCMT. 2009 observations detected daily variations in event-horizons-scale structure of Sgr A* (§2.1.5.2; Fish et al. 2011) and the ISCO-scale structure of M87 (§3.1.3.3; Doeleman et al. 2012). These results are based on the measurements of the characteristic size derived from the visibility amplitude distribution, as the first VLBI observations in 1967 (Broten et al. e.g. 1967a,b; Bare et al. e.g. 1967; and see Moran (1998))

---

[2] This was actually what a referee commented on Lu et al. (2012) in the peer-reviewing process.

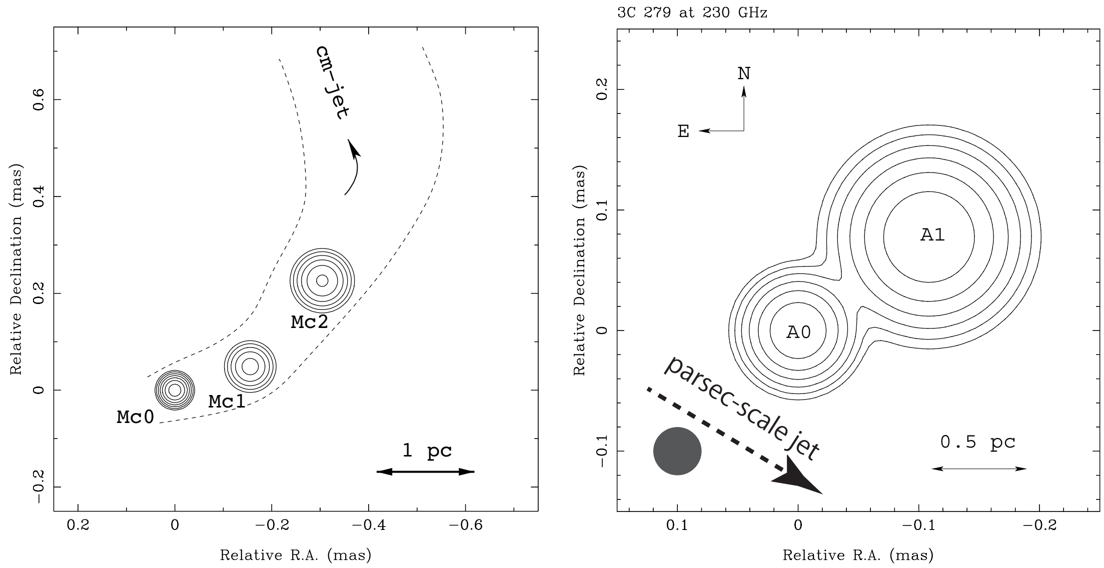

Figure 1.8: The 1.3 mm VLBI image of FSRQs 1921-293 (left; Lu et al., 2012) and 3C 279 (right; Lu et al., 2013) modeled by observed visibility amplitudes and closure phases.

Another important update in 2009 observations is the first detection of the closure phase on the blazar 1921-293, providing the first 1.3 mm VLBI interferometric phase information of the Universe. This gives more detailed structural information such as relative positions of resolved components, enabling to model the image using the visibility amplitude and closure phase (Figure 1.8; Lu et al. 2012). This is what Rogers et al. (1974) did on FSRQ 3C 273 and FR I radio galaxy 3C 84 using the closure phase detected for the first time.

In 2011 the phased-array processor was introduced in SMA and CARMA, enabling to use the whole interferometer as a single very sensitive telescope after test observations with SMT, a phased array of SMA and Atacama Submillimeter Telescope Experiment (ASTE) in 2010. 2011 observations were performed with SMT, phased array of CARMA and phased stations in Hawaii. Atacama Pathfinder EXperiment (APEX) and IRAM 30 m also joined in 2011 observations, but failed to detect fringes probably due to system failures. Although there was also a system trouble in CARMA (Lu et al., 2013), observations revealed the fine-scale structure of the blazar 3C 279 (Figure 1.8; Lu et al. 2013). In chapter 4, we report on EHT observations of the blazar NRAO 530 in this year. Observations provide the fine-scale structure of NRAO 530. Although imaging blazars with EHT is not a new step in the technical context, it is the first following-up observations with EHT after the large γ-ray flare in AGNs.

In 2012 observations, observations were performed with SMT, CARMA, phased SMA and JCMT using new digital backend systems and recording systems. In chapter 3, we report on M87 observations in this year. We acquired the 1.3 mm VLBI interferometric phase information of the event-horizon-scale structure in the close vicinity of SMBH for the first time for the sources whose black holes will be expected to be imaged. This is very important foot print in the technical context for imaging the black holes in Sgr A* and M87 in the next decades. We also got a preliminary result detecting apparent super-luminal motion and expansion of the 1.3 mm structure in the blazar for the first time for 3C 279 in 2012 observations (see Chapter 5; Akiyama et al. in prep.).

The number of geographic sites will significantly increase after 2015, which will enable to image the 1.3 m emission structure using newly developed imaging techniques. Future prospect of EHT observations after 2013 are introduced in Chapter 5.

Finally, we note about 1.3 mm emission structure of blazars detected in Lu et al. (2012) and Lu et al. (2013). EHT observations have revealed that the innermost structure at 1.3 mm is suggested to have a curved geometry (Figure 1.8) for all of EHT-observed blazars including NRAO 530 presented in Chapter 4. We discuss its physical implications in Chapter 4.

2

LONG-TERM VARIATION OF THE MILLIARCSECOND-SCALE STRUCTURE IN SGR A*

2.1 REVIEW: THE GALACTIC CENTER SAGITTARIUS A*

There is plenty of evidence that the center of our galaxy hosts a SMBH with a mass of $\sim$4 × 10^6 $M_\odot$ at a distance of $\sim$8 kpc. The compact radio source Sagittarius A* (Sgr A*), located in the galactic center, is associated with this SMBH. In this section, we introduce various properties of Sgr A*.

2.1.1 *Sgr A* as an AGN : Extremely Low Luminosity AGN*

In a word, Sgr A* is an extremely faint object as an AGN with extremely sub-Eddington luminosity. The bolometric luminosity of Sgr A*, which is $\sim 10^{36}$ erg s^{-1}, is $\sim$ 8.5 orders of magnitude smaller than the Eddington limit for its black hole mass of $\sim$ 4 × 10^6 $M_\odot$ in spite of the existence of the large gas reservoir from stellar winds in its vicinity (Melia et al., 2001). Even when compared with LLAGNs, its luminosity is $\sim$ 3-4 orders of magnitude smaller than typical LLAGNs. However, studies of *the fundamental plane of black hole activity* indicate that Sgr A* and AGNs share a common system powered by releasing gravitational energy of accreting gas through an accretion disk onto a SMBH. In Figure 2.1, we show the fundamental plane, which indicates a relation between radio and X-ray luminosities and mass, independently found by Merloni et al. (2003) and Falcke et al. (2004). As clearly seen in Figure 2.1, Sgr A* is located almost on the fundamental plane and linking between stellar mass black holes and other AGNs with SMBHs. Although it is difficult to know the detail emission mechanism from the fundamental plane, theoretical studies of Sgr A* reveal that the mechanism of the central engine of Sgr A* is ap-

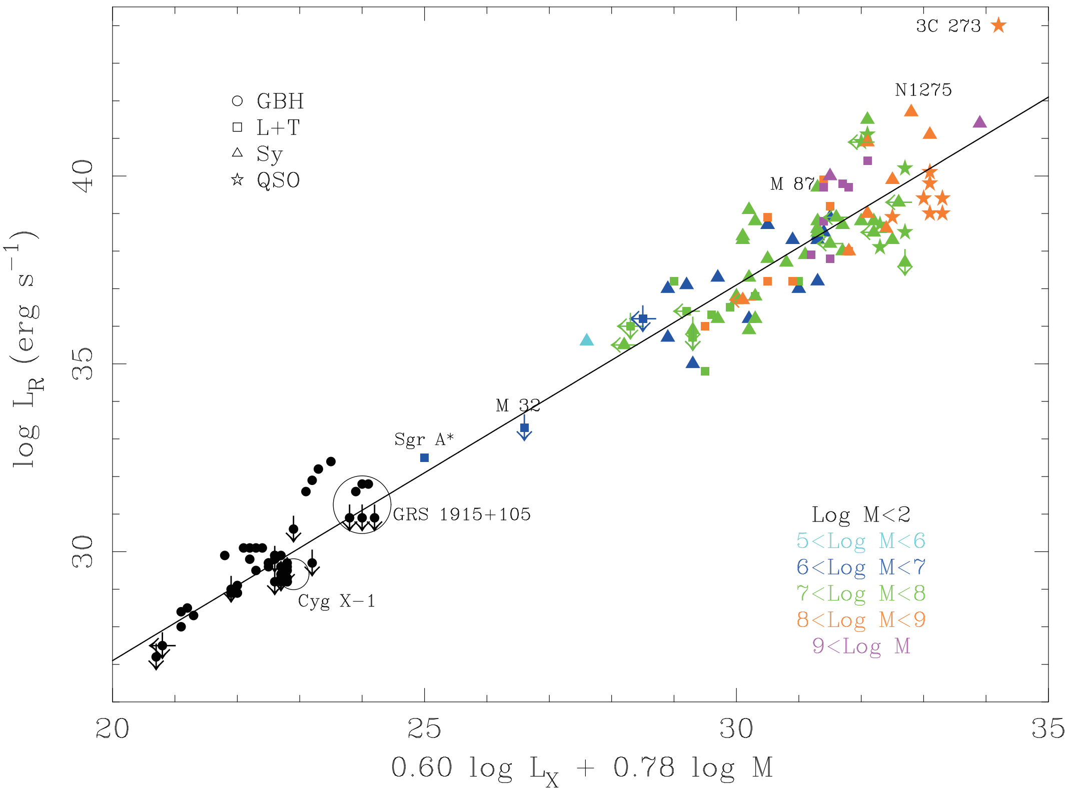

Figure 2.1: The fundamental plane of black hole activity, relating radio luminosity, X-ray luminosity and mass over more than eight orders of magnitude in black hole mass (Fender et al., 2007).

plicable to LLAGNs (see §1.1.2.3, §1.1.2.4 and §2.1.7), which are the majority of the nearby AGNs and also hosted by $\sim 40\%$ of nearby galaxies (e.g. Ho, 2008).

2.1.2 *Uniqueness of Sgr A* : the Nearest Black Hole Laboratory*

The proximity of Sgr A* is the most unique point of Sgr A*, which makes it the nearest laboratory of the SMBHs. The distance of ~ 8 kpc is $\sim$ 100 times smaller than that of the next closest galactic nucleus in M31 (NGC224; Andromeda Galaxy). Thanks to its proximity, the SMBH in Sgr A* has the largest angular size of the Schwarzschild radius ($R_{\rm s}$) among known black hole candidates in the Universe (see Table 1.3). Sgr A* is one of two main targets of the Event Horizon Telescope (EHT; §1.3). EHT is expected to achieve a direct imaging of the event-horizon of the SMBH at 1.3 mm in the next several years, which is crucial to test the Einstein's general relativity in a strong gravity regime.

Another uniqueness of Sgr A* is its short dynamical time-scales owing to its relatively low black hole mass. Typical dynamical time-scales are orders of minutes to hours relating with the orbital period near the *inner most stable circular orbit* (ISCO). For example, the Keplerian orbital period at the inner most stable circular orbit is $\sim$ 30 minutes for assuming a non-rotating black hole. In the case of a maximally rotating Kerr black hole, it becomes $\sim$ 4 minutes (prograde case) to $\sim$ 54 minutes (retrograde case) depending on the relation of orbital motion of the matter and the black hole spin (Melia et al., 2001, recalculated for 4×10^6 M$_\odot$). Therefore, variability of Sgr A* is expected to have short time-scales comparable to the orbital periods. Compared to time scale associated with stellar mass black holes and other AGNs, in particular M87, variabilities on such short time-scales are practical for coordinating multi-wavelength observations.

2.1.3 *The Black Hole Mass and Distance*

There are many robust evidences that Sgr A* is associated with the SMBH of $\sim 4 \times 10^6$ M$_\odot$ at the Galactic center, provided by NIR observations of the gas and stellar dynamics in the vicinity of Sgr A* and the VLBI astrometry of Sgr A* .

First, we introduce the excellent works achieved with NIR observations of the stars and gas in the nuclear clusters (Figure 2.2) around Sgr A*. The patient monitoring observations over three decades revealed the detailed dynamics of the stars and gas, providing the direct evidence for presence of the SMBH at the position of Sgr A*.

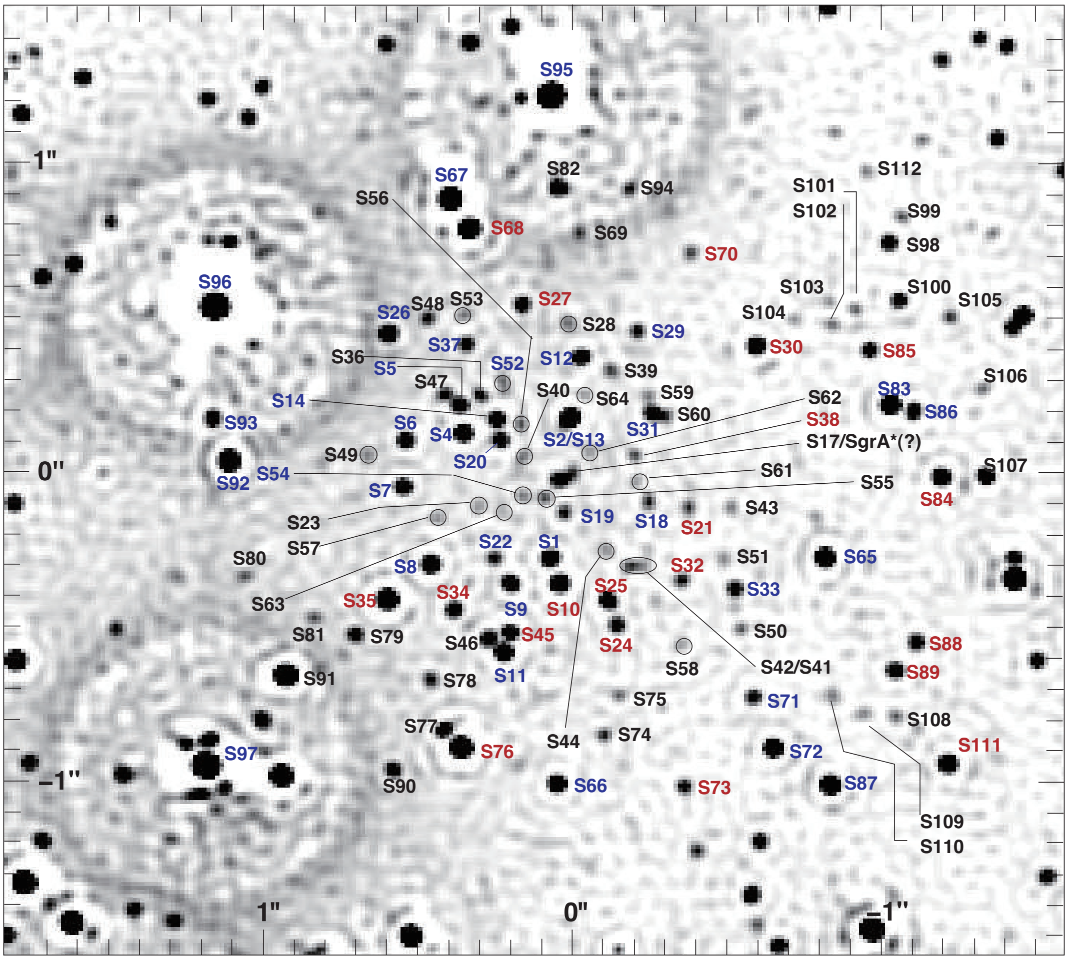

Figure 2.2: The image of the S-star cluster (Gillessen et al., 2009). In this image, some light is seen at the position of Sgr A*, which could be either due to Sgr A* itself or due to a faint, so far unrecognized star being confused with Sgr A*.

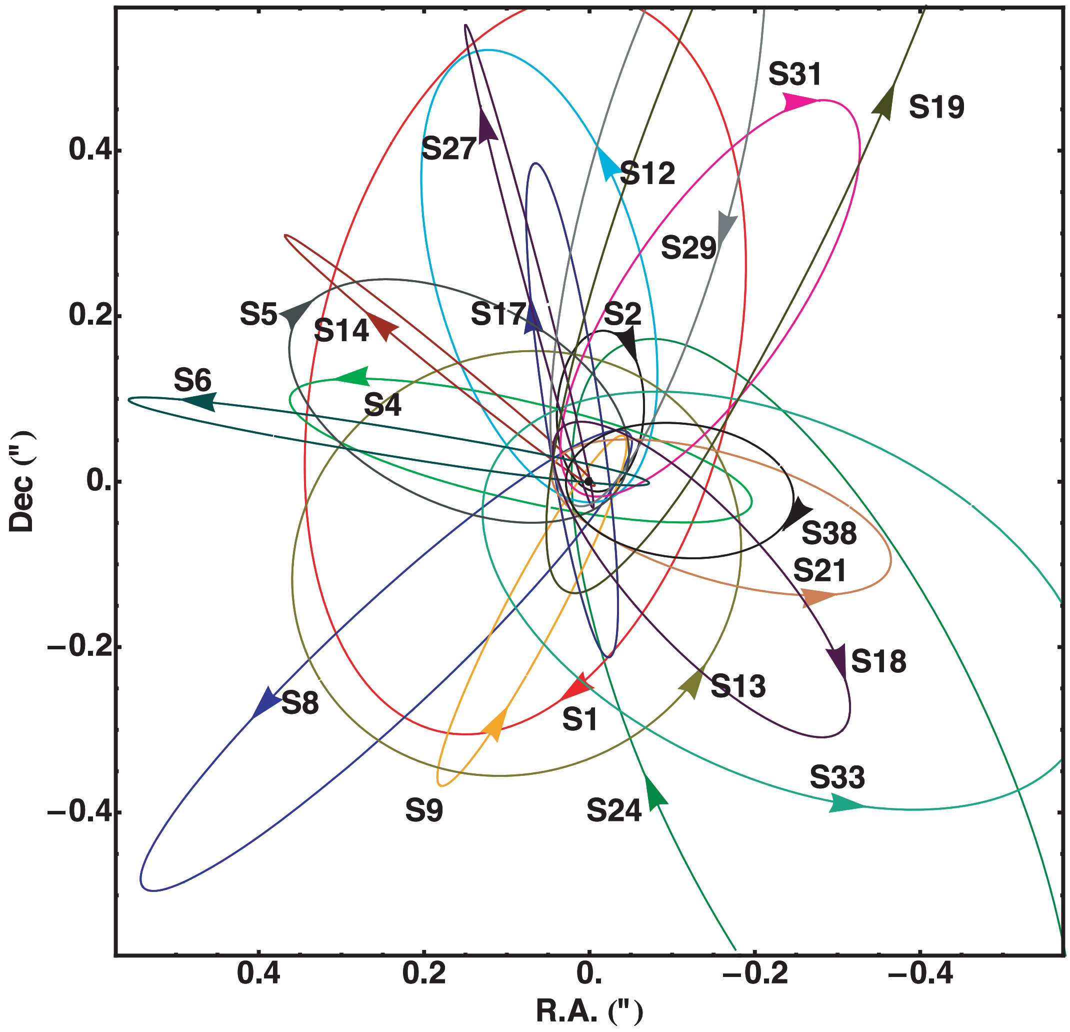

Figure 2.3: Stellar orbits of the stars in the central arcsecond. In this illustrative figure, the coordinate system was chosen such that Sgr A* is at rest (Gillessen et al., 2009).

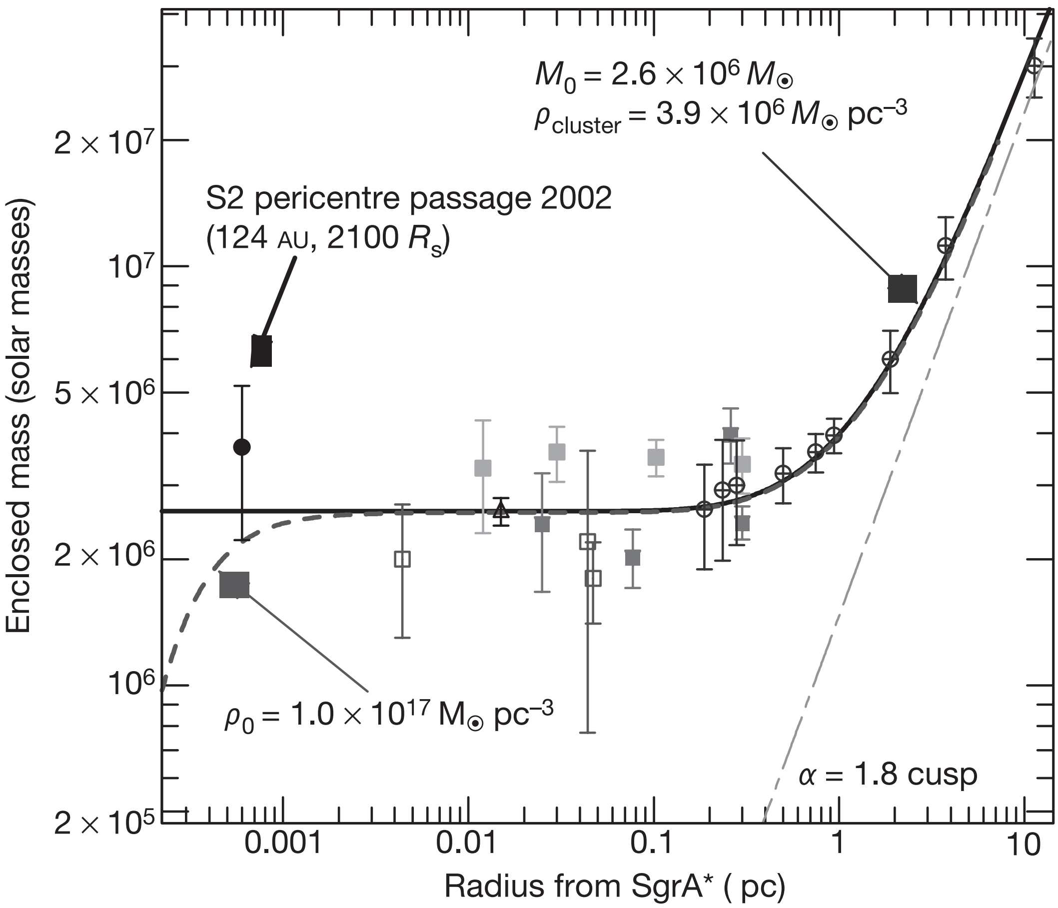

Figure 2.4: Mass distribution in the Galactic Center (for a distance of 8 kpc Schödel et al., 2002). The filled circle denotes the mass derived from the orbit of S2. Grey filled rectangles are mass estimates from a parametrized Jeans-equation model including anisotropy and differentiating between late and early type stars. Open circles are mass estimates from a parameterized Jeans-equation model of the radial velocities of late type stars, assuming isotropy. Open rectangles denote mass estimates from a non-parametric, maximum likelihood model, assuming isotropy and combining late and early type stars.

In early observations, the dynamics of stars around Sgr A* was discussed using only radial velocities assuming circular stellar obits and an isotropic distributions of stars (see Genzel & Townes, 1987, and reference therein). The early results of the proper motion measurements confirmed that the dependence of velocity dispersion of stars in the distance from Sgr A* was consistent with that obtained from radial velocities (Eckart & Genzel, 1996; Ghez et al., 1998). This results strengthened the evidence for the existence of a massive point source.

The accumulation of the proper motion measurements enabled to measure accelerations of stars, providing some constraints on the location of the dark mass (Ghez et al., 2000; Eckart et al., 2002). The fully orbital motions of the nearest star was obtained in early 2000s, providing the position and mass of Sgr A* (Schödel et al., 2002; Ghez et al., 2005). As of 2009, 26 stellar orbits (see Figure 2.3) have been measured (e.g. Eckart & Genzel, 1996, 1997; Eckart et al., 2002; Schödel et al., 2002; Eisenhauer et al., 2003; Ghez et al., 2000, 2005, 2008; Gillessen et al., 2009). The measurement of the radial velocity of the young stars also allows the geometric determination of the distance to the Galactic Center (R_0) from stellar orbits (e.g. Eisenhauer et al., 2003, 2005; Ghez et al., 2003).

We summarize important results of NIR studies as below:

1. The mass density distribution (Figure 2.4) determined by the orbital motions and velocity dispersion in the nuclear cluster excludes any possibilities that Sgr A* is other than a SMBH.
2. The position of Sgr A* and the position of the central point mass coincide within $\sim$ 20 AU (i.e. $\sim$ 2 mas). This comparison were enabled by registration of the radio and NIR reference frame (see Reid et al., 2007).
3. The measured mass is $\sim 4 \times 10^6$ $\mathrm{M}_\odot$, while the distance is $\sim$ 8.4 kpc.

Another constraint on the mass of Sgr A* is provided from the direct measurement of the proper motion of Sgr A* with VLBI astrometry. Reid & Brunthaler (2004) measured the position of Sgr A* with VLBA with respect to two extragalactic radio sources over a period of 8 yr (see Figure 2.5). The apparent proper motion of Sgr A* was 6.379 ± 0.024 mas yr^{-1} along a position angle of $209^\circ.60 \pm 0^\circ.18$, almost entirely in the plane of the Galaxy. The effects of the orbit of the Sun around the Galactic center accounts for this motion, and the residual proper motion of Sgr A* perpendicular to the plane of the Galaxy was -0.4 ± 0.9 km s^{-1}. A maximum likelihood analysis of the motion expected for a massive object within the nuclear cluster indicates that Sgr A* contains more than about $\sim$ 4 $\times$ 10^5 $\mathrm{M}_\odot$ which corresponds to $\sim$ 10 % of the mass deduced from stellar orbits.

Another constraint on the distance to Sgr A* has been provided by the measurements of the trigonometric parallaxes and proper motions of masers located in massive star-forming regions with VLBI Exploration of Radio Astrometry (VERA) and Very Long Baseline Array (VLBA) (Reid et al., 2009, 2014; Honma et al., 2012). The distance to the Sgr A* is of great importance, since it is the fundamental parameter of the galactic structure. The distance to the galactic structure can be estimated using three dimensional positions and kinematics of the massive star-forming regions based on measurements of parallaxes and proper motions com-

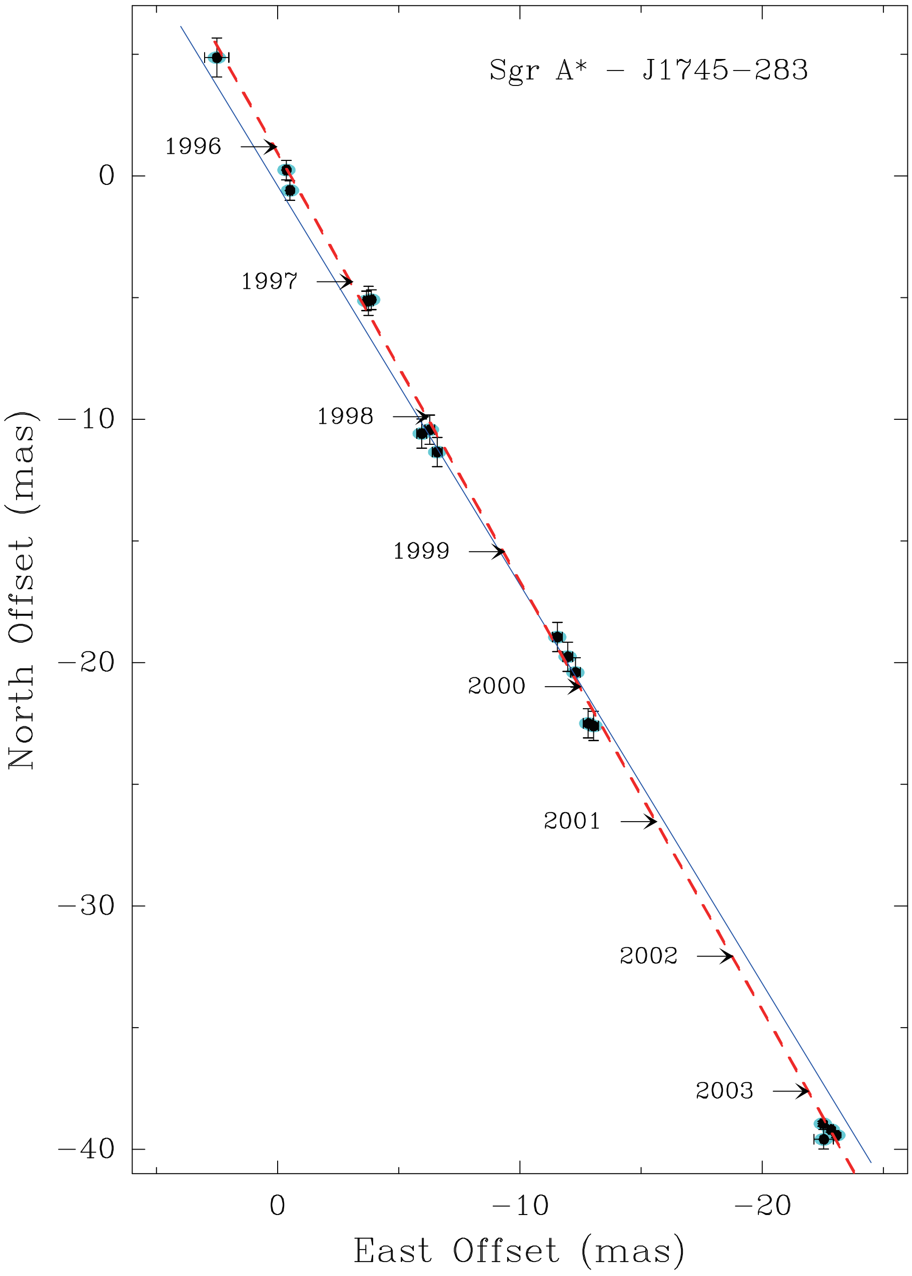

Figure 2.5: Position residuals of Sgr A* relative to J1745-283 on the plane of the sky (Reid & Brunthaler, 2004). The dashed line is the variance-weighted best-fit proper motion, and the solid line gives the orientation of the Galactic plane, which is tilted by 31.40° in east of north in J2000 coordinates.

Table 2.1: The recent revisions of the central black hole's mass and distances

Method	Mass (10^6 M$_\odot$)	Distance (kpc)	Reference
NIR	4.5 ± 0.4	8.4 ± 0.3	Ghez et al. (2008)
NIR	$4.31 \pm 0.06 \mid_{\rm stat} \pm 0.36 \mid_{R_0}$	8.33 ± 0.35	Gillessen et al. (2009)
VLBI	—	8.35 ± 0.44	Honma et al. (2012)
VLBI	—	8.34 ± 0.16	Reid et al. (2014)

bined with the model of the rotation curve of the our galaxy. The measured distance is ~ 8.4 kpc, being consistent with NIR observations.

Finally, we summarize the recent revisions of the central black hole's mass and distances in Table 2.1.

2.1.4 *Spectrum of Sgr A**

As of 2014, emission from Sgr A* has been detected at radio, NIR and X-ray bands. In addition, the galactic center is also well-known to be a luminous γ-ray source at MeV, GeV and TeV energies, but it is not clear that Sgr A* is the dominant source of the detected γ-ray emission.

Figures 2.6 show SEDs of Sgr A* from radio to X-ray at both the quiescent state and flaring state. One can clearly see a similarity of its SED to LLAGNs (see Figure 1.3), although its luminosity is $\sim$ 3-4 orders of magnitude smaller than LLAGNs. The fact that there is no big blue bump in SED indicates the accretion disk is a radiatively inefficient accretion flow (§1.1.2.3 and §2.1.7.1) rather than the standard disk (see §1.1.2.3). Moreover, the existence of the sub-mm bump in radio regime and the strong radio-loudness even at flaring states indicate Sgr A* has common nuclear properties to LLAGNs (§1.1.2.3). Here, we introduce properties of the spectra at each band separately.

2.1.4.1 *Radio*

Historically, Sgr A* was discovered at radio band (Balick & Brown, 1974). The properties of radio emission have been studied for four decades since its discovery. Figure 2.7 shows the radio spectrum of Sgr A* from 1 GHz to 670 GHz. One can clearly see existence of two breaks in the radio spectrum (Melia et al., 2001).

The first break is located around $\sim$10 GHz. Below this break frequency, the spectrum index α (i.e. $S_\nu \propto \nu^\alpha$) is $\sim$0.3 (Zhao et al., 2001), while the spectrum becomes

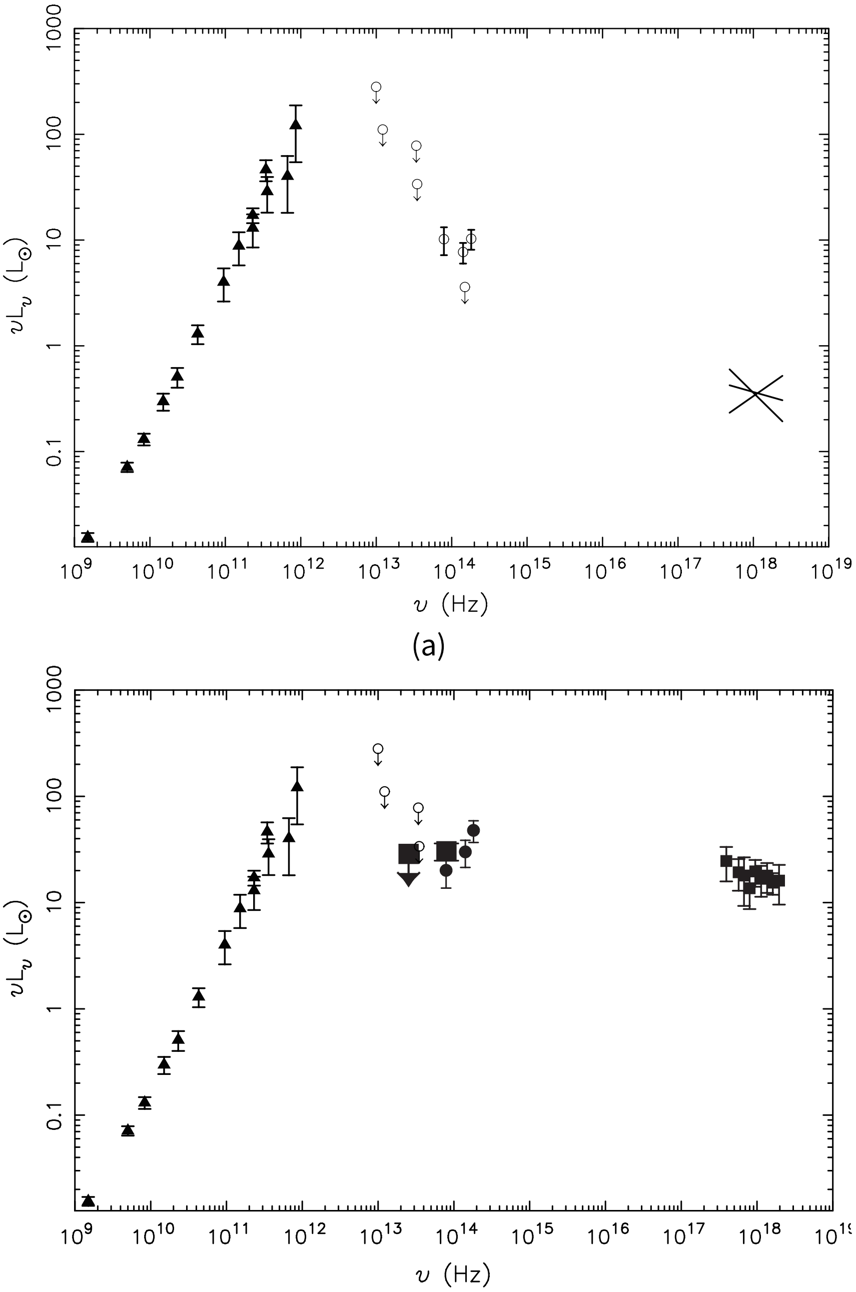

(a)

(b)

Figure 2.6: The SEDs of Sgr A* (edited figures in Dodds-Eden et al., 2009): filled triangles are radio to submillimeter measurements of the quiescent state (Markoff et al., 2001; Zhao et al., 2003). Note that these measurements are time-averaged measurements and the error bars include variable emission of up to 50 %. As open black circles with arrows are shown 30 μm, 24.5 μm, and 8.6 μm upper limits taken from Melia et al. (2001), the upper limit at 8.6 μm from (Schödel et al., 2007) and the limit on the quiescent state at 2 μm from (Hornstein et al., 2002). (a) : The SED of the quiescent state. IR values from (Genzel et al., 2003) are shown as the open black circles with error bars. The X-ray values are shown as the black bow-tie (Baganoff et al., 2003). (b) : The example of SEDs at the flaring state. IR and X-ray values are taken from Dodds-Eden et al. (2009).

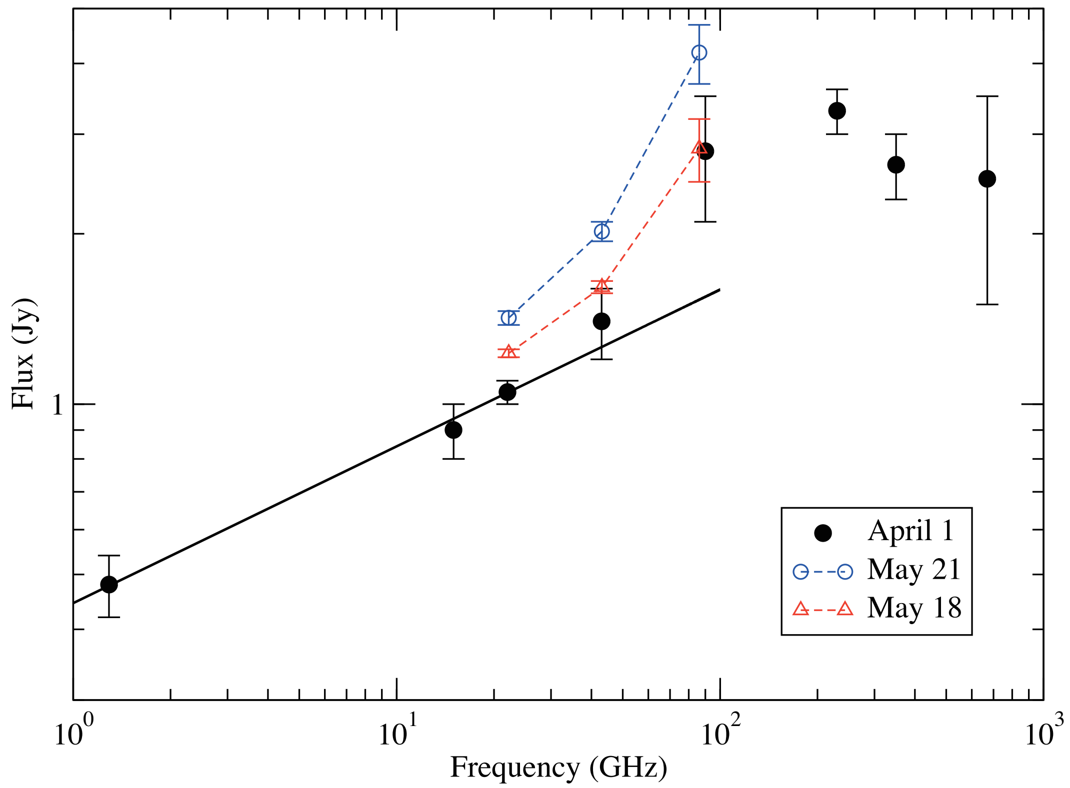

Figure 2.7: The radio spectrum of Sgr A* (Lu et al., 2011). Filled circles denote a quasi-simultaneous spectrum obtained around April 1, 2007 during a multi-wavelength campaign (Yusef-Zadeh et al., 2009). The error bars on the data points indicate the variability of Sgr A*. The solid black line indicates a power law fitted to the radio data up to 43 GHz ($\alpha \sim 0.3$). Above 43 GHz, a flux density excess over this line is apparent. Open symbols connected by dashed lines indicate the new and quasi-simultaneous flux density measurements of May 18 and 21, 2007, from which high frequency spectral indices were derived, respectively (Lu et al., 2011). Note a spectral turnover is between 100-230 GHz.

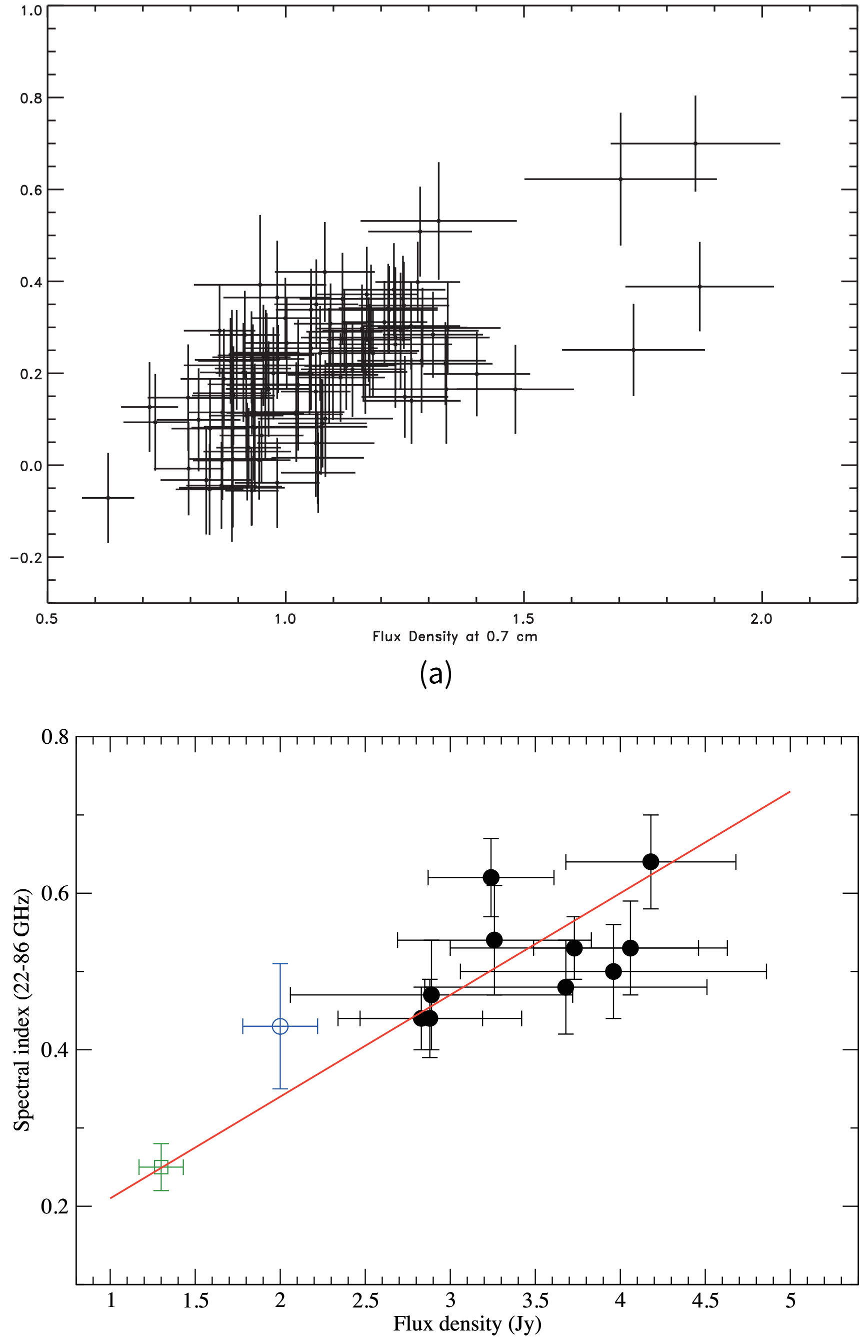

(a)

(b)

Figure 2.8: (a) Spectral index α as a function of flux density at 43 GHz. (Herrnstein et al., 2004) (b) Spectral index α as a function of flux density at 86 GHz. Filled black circles are data from Lu et al. (2011). Two additional data points at lower flux density levels observed in earlier experiments are added: Falcke et al., 1998, open circle and Serabyn et al., 1997, open square.

steeper above this break frequency. The excess of flux densities at above ~ 10 GHz is called as "sub-mm excess". The exact frequency of the first break is unclear (Falcke et al., 1998; Zhao et al., 2003). The VLBI fluxes measured in Lu et al. (2011) (blue and red line in Figure 2.7) clearly show that the sub-mm excess is attributed to the milliarcsecond-scale structure of Sgr A*. This fact excludes any possibilities of extrinsic causes such as diffuse free-free emission, a transient source, and dust emission surrounding Sgr A*. At the sub-mm excess region, the variation of spectral index was reported in several studies; Herrnstein et al. (2004) and Lu et al. (2011) reported a correlation between the spectral index and the flux at mm-wavelength (see Figures 2.8).

The second break is the sub-mm bump, which we have already introduced at the beginning of this subsection. Although the sub-mm bump is one of the most prominent feature of Sgr A*'s SED, the sub-mm bump is still poorly understood. Similarly to the first break frequency, the peak frequency of the bump has been unclear (e.g. Falcke et al., 1998; Zhao et al., 2003). (Marrone, 2006) concluded that the average spectrum peak existed between 230 GHz and 690 GHz from the observations with SMA. Yusef-Zadeh et al. (2006a) found that the quiescent spectrum had a peak at 350 GHz using the data of multi-frequency campaign, while Yusef-Zadeh et al. (2009) found a peak at 230 GHz (see Figure 2.7). The future ALMA observations are expected to reveal the detail spectral shape of the sub-mm bump.

There are two common understandings for radio emission from Sgr A*; (1) the radio emission in radio regime is synchrotron emission, although the energetics of emitting electrons is poorly understood; (2) the sub-mm bump is produced by synchrotron self-absorption (SSA), reflecting the transition between optically thin emission at higher frequencies and optically thick emission at lower frequencies. However, the plasma emitting radio emission is depending on theoretical models (see §2.1.7). The radio emission and structure are of great importance to understand a plasma physics around the SMBH in Sgr A*.

2.1.4.2 *NIR and X-ray*

In optical regime, it is difficult to detect emission from Sgr A* owning to the strong dust absorption in the galactic center region. However, interstellar medium becomes transparent for IR and high energy photons. The first detections of NIR and X-ray emission were achieved with a discovery of dramatic NIR (Genzel et al., 2003) and X-ray (Baganoff et al., 2001) flares. In both NIR and X-ray bands, Sgr A* has

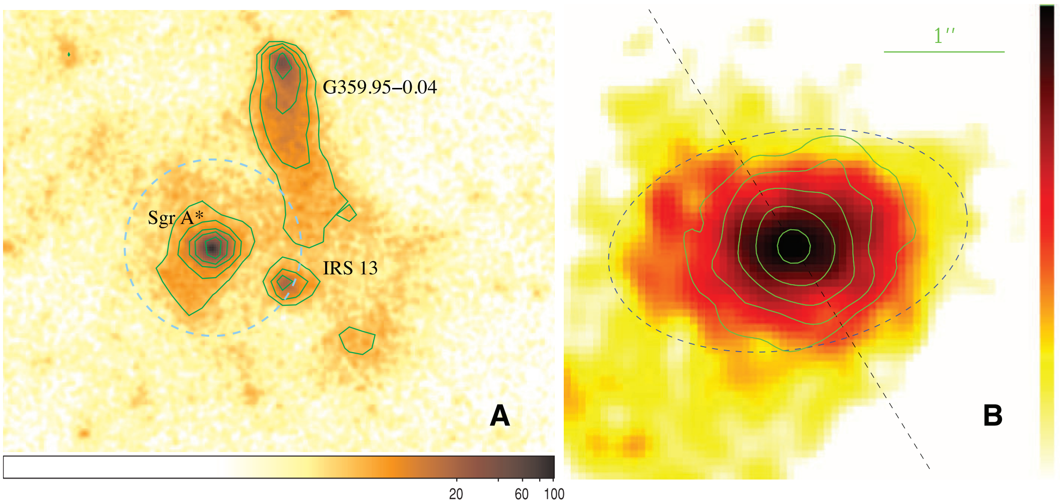

Figure 2.9: Deep X-ray images of Sgr A* in quiescence observed with Chandra (Wang et al., 2013). (a) An image at the 1- to 9-keV band. The dashed circle around Sgr A* indicates its Bondi capture radius (assumed to be 4). (b) A magnified image of Sgr A*. The emission is decomposed into extended (color image) and point-like (contour) components. The latter component is modeled with the net flare emission. The straight dashed line marks the orientation of the Galactic plane, whereas the dashed ellipse of a 1.5 semi-major axis illustrates the elongation of the primary massive stellar disk, which has an inclination of $\sim 127^\circ$, a line-of-nodes position angle of $\sim 100^\circ$, and a radial density distribution $\propto r^{-2}$ with a sharp inner cutoff at $r \sim 1''$.

strong flaring activities (see §2.1.6.2). Here, we introduce the quiescent state (for flaring activities, see §2.1.6.2).

Sgr A* in quiescent state was never unambiguously been detected in the NIR in early 2000s (e.g. Hornstein et al., 2002; Schödel et al., 2007) after a discovery of a NIR flare (Genzel et al., 2003). At the present, the quiescent NIR flux can be regularly detected with high sensitivity observations using an adaptive optics system (e.g. NIRC2 in the Keck 10-m Telescope and NaCo in the Very Large Telescope). The de-reddened mean flux densities at NIR band are 3.8 $\pm$ 1.3 mJy at 4.8 μm and 5.0 $\pm$ 0.6 mJy at 3.8 μm (Schödel et al., 2011). No counterpart of Sgr A* has been detected at 8.6 μm or longer wavelength in MIR regime on the high-frequency side of the sub-mm bump. The available data indicates that Sgr A* cannot be detected with currently available instruments at MIR band even during flares (Schödel et al., 2011).

On the other hand, Chandra X-ray observations revealed a steadily emitting source at X-ray wavelengths (Baganoff et al., 2003), with a spatial extent of $\sim$ 1”. However, because of the spatial extent, this steady source must be produced in the outer regions of the accretion flow. In other word, it cannot be directly related to the compact source, which must be produced at small radius from the central black hole. The quiescent X-ray source most likely originates from Bremsstrahlung emission. The outer regions of the accretion flow close to the Bondi radius are expected to contribute the most emission. The properties of this steady X-ray emitting plasma set the outer boundary conditions of Sgr A*'s accretion flow (see §2.1.7.1).

Recently, Wang et al. (2013) provides an excellent X-ray image of the steady structure with unprecedented deep observations with Chandra at an exposure time of a 3 Ms (Chandra X-ray Visionary Project[1]; Figure 2.9). The X-ray emission is elongated and aligns well with a surrounding disk of massive stars, excluding a concentration of low-mass coronally active stars as the origin of the emission on the basis of the lack of Fe Kα emission. The extremely weak hydrogen (H)–like Fe Kα line feature suggests that a large fraction of the accreting gas should be lost from the accretion flow probably via a strong outflow. Such a strong outflow is expected to occur in some subclasses of RIAF (e.g. ADIOS; see §2.1.7.1 andBlandford & Begelman 1999). Indeed, the hydrogen (H)–like Fe Kα line exclude semi-analytic RIAF solutions with no outflow solution (e.g. ADAF; see §2.1.7.1; Manmoto et al. 1997; Narayan et al. 1998).

2.1.4.3 γ-ray

The galactic center is also known as a γ-ray source. However, owing to the poor spatial resolution of γ-ray telescopes, it has been unclear whether Sgr A* is the origin of γ-ray emission. Thus, γ-ray emission from the galactic center sets upper limit on the γ-ray emission from Sgr A*. INTEGRAL observations (20-600 keV) detected a faint and persistent emission from the region which coincides the Sgr A* within 1' (Goldwurm, 2007). In MeV regime, ≥ 100 MeV emission were reported from EGRET. Fermi Gamma-ray Space Telescope has also detected MeV and GeV γ-ray from the Galactic center (1FGL J1745.6-2900; see Chernyakova et al., 2011, and references in). In the very-high-energy regime over 100 GeV, the emission is also detected by several ground-Cherenkov-telescopes (HESS J1745-29; see Aharonian et al., 2006a,b, and references therein). Recent VHE observations excluded Sgr A East with high probability as the dominant source of the VHE emission (Abramowski et al., 2010) .

In addition to the lack of spatial resolution, the lack of variability also makes the association of γ-ray emission with Sgr A* not definitive. If the γ-ray radiation

---

[1] `http://www.sgra-star.com/`

is produced in the vicinity of the central black hole, intensity variation would be expected as at other wavelengths. However, no variability on any available time-scales was found so far in γ-ray regime (e.g. Aharonian et al., 2008, 2009). If γ-ray emission is associated with Sgr A*, emission mechanism or emission region are not likely to be same to variable X-ray and NIR emissions from Sgr A*.

2.1.5 *VLBI Structure*

Sgr A* has the largest angular size of R_s among known black hole candidates as shown in Table 1.3. The angular size of R_s is $\sim$ 10 μas, meaning that current cm/mm VLBI can approach to the structure on scales of $\lesssim$ 100 R_s. However, imaging of the detailed structure has been prevented from the effects of the interstellar scattering.

2.1.5.1 *Angular-broadened Structure*

Figures 2.10 show multi-frequency VLBI images of Sgr A*. Sgr A* has two specific features of its structure on milliarcsecond scales (e.g. Lo et al., 1998; Bower et al., 2004; Shen et al., 2005; Bower et al., 2006; Falcke et al., 2009; Lu et al., 2011).

1. The observed size follow a λ^2-dependence at wavelength longer than $\sim$1 cm, where λ is wavelength.
2. The apparent structure can be described by an elliptical Gaussian distribution.

These features are not thought to be intrinsic, but highly affected by an interstellar scattering. Here, we summarize the effect of the interstellar scattering on the interferometric data along with a nice overview in §2.1 of Fish et al. (2014). Detailed observational and theoretical properties are extensively described in Rickett (1990). Essential and very readable explanations are presented in Narayan (1992) and a subsection “*Phase Fluctuations*” in §13.1, §13.4 and §13.6 of Thompson et al. (2001).

In general, the density fluctuations of the interstellar plasma scatter radio waves, causing temporal and angular broadening of sources as well as scintillation in frequency and time . These variations induce stochastic phase fluctuations. The fluctuations along an initially plane wavefront can be characterized by a so-called structure function of the phase, defined as

$$D_\phi(\mathbf{r}) \quad = \quad \left\langle \left[\phi\left(\mathbf{r}\right) - \phi\left(\mathbf{r} - \mathbf{r}'\right)\right]^2 \right\rangle, \tag{2.1}$$

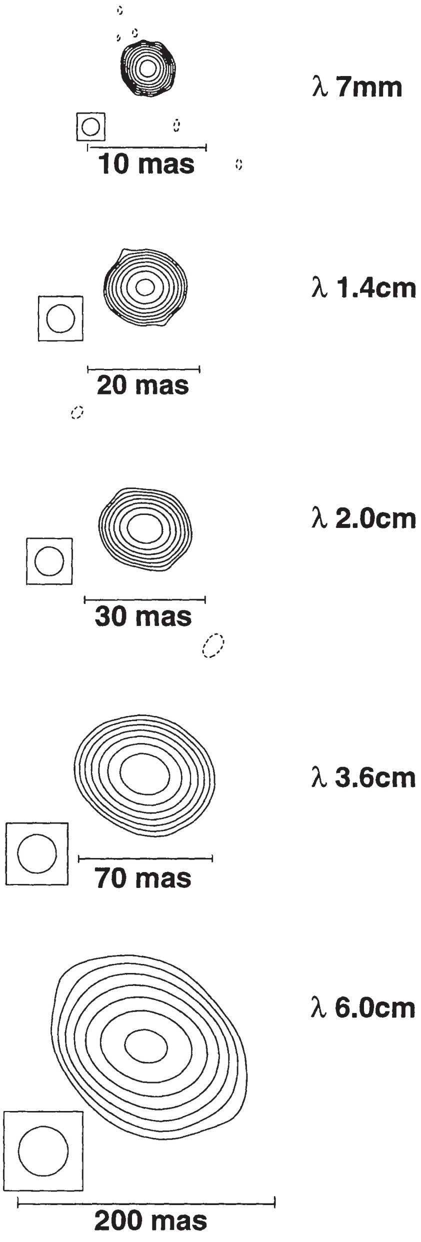

Figure 2.10: VLBA images of Sgr A* at wavelength 6.0, 3.6, 2.0, 1.35 and 0.7 cm. (Lo et al., 1998)

where $\mathbf{r}, \mathbf{r}'$ are transverse coordinates at the scattering screen, $\phi(\mathbf{r})$ is the phase at point $\mathbf{r}$, and the angle brackets indicate an ensemble average. The structure function is well modeled with a power low distribution of $D_\phi(\mathbf{r}) \propto \lambda^2 |\mathbf{r}|^a$ for ionized astrophysical turbulent plasma (e.g. Armstrong et al., 1995). Strongly scattered sources often have a power-law index a close to 2, which is similar to the value of $5/3$ for Kolmogorov turbulence, over scales from $r_{\rm in} \sim 10^7$ cm $= 10^3$ km to $r_{\rm out} \sim 10^{16}$ cm $\sim 10^3$ AU (Rickett, 1990). This could arise from scattering by a medium consisting of discrete scatterers with abrupt boundaries; This also could arise from scattering at wavelength such that the phase coherence length r_0 on the scattering screen is shorter than the inner length scale $r_{\rm in}$ of the fluctuations, where $r_0 \propto \lambda^{-2/a}$ is defined such that $D_\phi(\mathbf{r}) = 1$ for $|\mathbf{r}| = r_0$ (Tatarskii, 1971; Narayan, 1988; Lambert & Rickett, 1999). r_0 is also called as the diffractive scale size, representing the maximum extent on the screen from which radiation can reach the observer.

The dominant effects of scattering depend on the size of source as well as the time and frequency resolution with which the source is observed (e.g. Goodman & Narayan, 1989; Narayan & Goodman, 1989; Narayan, 1992). For the case of strong scattering, three distinct data averaging regimes are important for constructing images from interferometric data obtained on a timescale $t_{\rm obs}$. These three regimes are characterized with two timescales associated with strong scattering in the interstellar medium; the one is the diffractive time scale $t_{\rm dif} = r_0/v_s$, where v_s is a velocity of the scattering medium; another one is the refractive time scale $t_{\rm ref} = D\theta_s/v_s = D\lambda/r_0 v_s$, where D is a distance to the scattering medium and the angular size θ_s of the scattering disk given by λ/r_0.

SNAPSHOT-IMAGE REGIME $(t_{\rm obs} < t_{\rm dif})$

Observations of a very compact source with very high time and frequency resolution will detect stochastic variations in both time and frequency due to diffractive scintillation.

AVERAGE-IMAGE REGIME $(t_{\rm dif} < t_{\rm obs} < t_{\rm ref})$

The interferometer effectively averages over multiple snapshot images, suppressing fast diffractive scintillation. However, visibilities will fluctuate on significantly broader scales in frequency and time due to refractive scintillation.

ENSEMBLE-AVERAGE REGIME $(t_{\rm obs} > t_{\rm ref})$

The interferometer averages over many realizations of the scattering screen. The response of the interferometer to a point source is

$$V(\mathbf{u}) = \exp\left[-\frac{1}{2}D_\phi\left(\frac{\lambda\mathbf{u}}{1+M}\right)\right] \tag{2.2}$$

where $V(\mathbf{u})$ is a visibility at a spatial frequency of $\mathbf{u} = (u, v)$ and λ is the observation wavelength. M is the magnification factor of the scattering medium defined by $M = R/R'$, where R and R' are the observer-scatterer distance and the source-scatterer distance, respectively. The exponent of the scattering kernel (Eq. 2.2) is proportional to $\lambda^{2+a}\,|\mathbf{u}|^a$, since $D_\phi(\mathbf{r}) \propto \lambda^2\,|\mathbf{r}|^a$. For $a = 2$, the exponent is proportional to $(\lambda^2)^2\,|\mathbf{u}|^2$, resulting that the scattering kernel becomes a Gaussian of which size is proportional to λ^2.

Interstellar scattering is significant throughout the galactic center region (e.g. van Langevelde et al., 1992). The wavelength-dependence of the scattering kernel is measured to be $\propto \lambda^{\sim 2}$ from angular broadening measurements, indicating $a \sim 2$. This implies that ensemble-average scatter broadening is well approximated by a Gaussian, indeed as observed in many compact masers and radio-loud AGNs. The observed structure and wavelength-dependence of the scattering kernel are accurately Gaussian and $\propto \lambda^2$, respectively, for Sgr A* (Bower et al., 2004, 2006). The scattering disk is anisotropic, in many regions including Sgr A*, suggested by anisotropic size of the scattering kernel (Goldreich & Sridhar, 1995).

The effective size of the intrinsic structure $\phi_{\rm int}$ (hereafter the intrinsic size) of Sgr A* can be estimated by

$$\phi_{\rm int} = \sqrt{\phi^2_{\rm obs} - \phi^2_{\rm scatt}}, \tag{2.3}$$

where $\phi_{\rm int}$ is intrinsic size, $\phi_{\rm obs}$ is observed size and $\phi_{\rm scatt}$ is the scatter size, on an assumption that intrinsic structure follows elliptical Gaussian distribution. Thus, the intrinsic size is possible to be estimated, if one measures scattering law at wavelengths longer than $\sim$ 17 cm where the intrinsic size is negligibly-small compared with scattering size. Figure 2.11 shows λ-dependency of Sgr A* size. As shown in Figure 2.11, measurements of the apparent size of Sgr A* showed that the size is proportional to a square of wavelength at a wavelength longer than $\sim$ 1.3 cm. In other word, the scattering size dominates the intrinsic size at a wavelength longer than $\sim$ 1.3 cm. However, at a wavelength shorter than $\sim$ 1.3 cm, one can clearly see deviations from the λ^2-dependence (see, Bower et al., 2004; Shen et al., 2005, and supplements of them). This is commonly interpreted as an effect of intrinsic

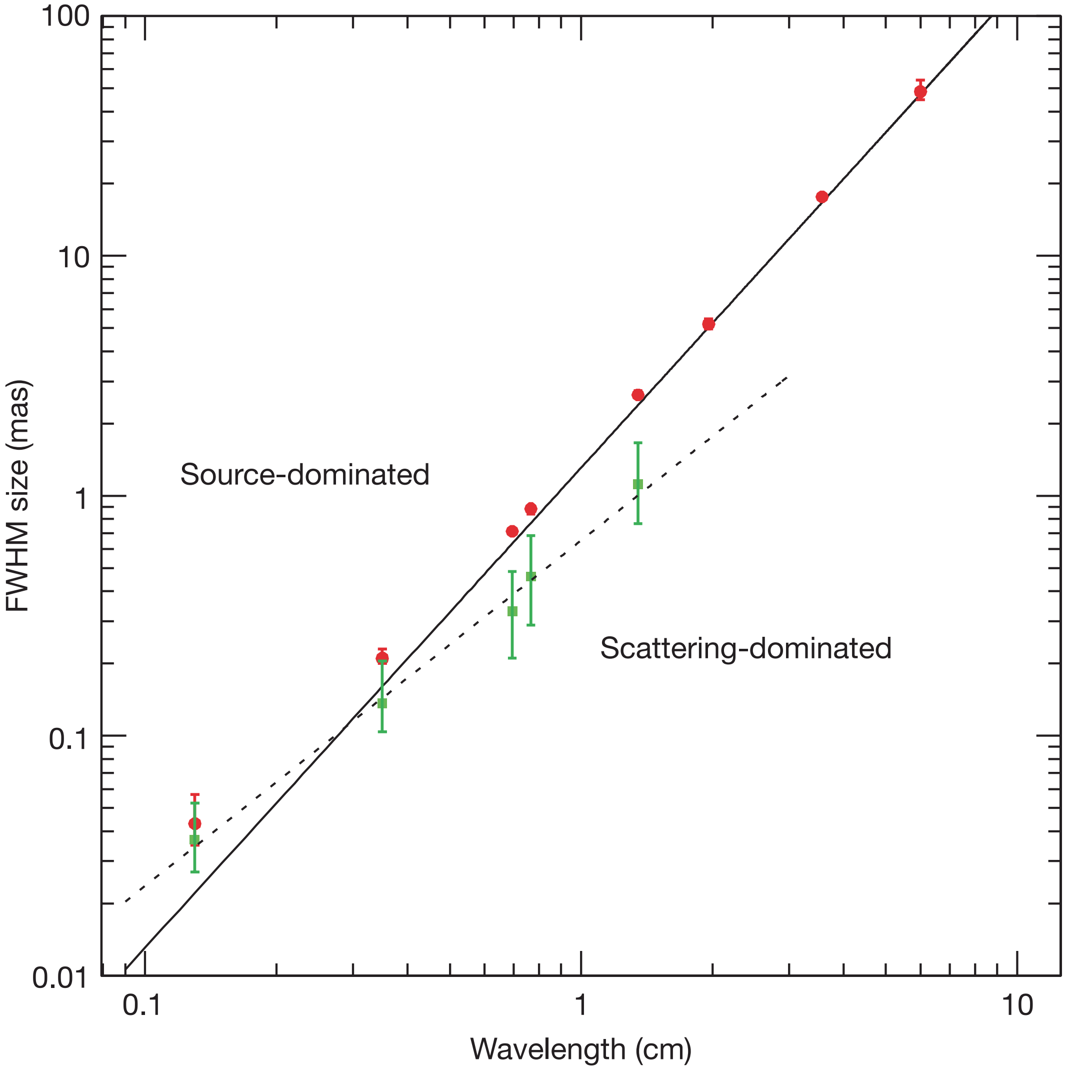

Figure 2.11: Apparent angular size of Sgr A* along the major axis as a function of wavelength (Doeleman et al., 2008). Red circles show major-axis observed sizes of Sgr A* from VLBI observations (all errors 3 sigma). Data from wavelengths of 6 cm to 7 mm are from Bower et al. (2004), data at 3.5 mm are from Shen et al. (2005), and data at 1.3 mm are from the observations reported here. The solid line is the best-fit scattering law from Bower et al. (2006). Below this line, measurements of the intrinsic size of Sgr A* are dominated by scattering effects, while measurements that fall above the line indicate intrinsic structures that are larger than the scattering size (a 'source dominated' regime). Green points show derived major-axis intrinsic sizes from 2 cm $\geq \lambda \geq$ 1.3 mm, and are fitted with λ^{α} power law ($\alpha = 1.44 \pm 0.07$) shown as a dotted line.

structure becoming dominant. Moreover, one can also see the λ-dependency of the intrinsic size. This suggests that the intrinsic size of Sgr A* at radio band is determined by the photosphere of optically thick plasma (e.g. Loeb & Waxman, 2007; Falcke et al., 2009). Taking the existence of the sub-mm bump into consideration, the transition between optically thin and optically thick regime is expected to occur in the sub-mm band.

2.1.5.2 *Intrinsic Structure*

The presence of strong scattering has pushed observations to toward shorter wavelengths, where scattering effects decrease and intrinsic source structure may dominate. The robust size measurement at 43 GHz and 86 GHz using closure amplitude method (Bower et al., 2004; Shen et al., 2005) found a break in the λ^2-dependence.

In addition to the discovery of a break, recently, dramatic results of the Event Horizon Telescope (Global short-millimeter VLBI array; §1.3) have been reported on detections of the event-horizon-scale structure in recent years. Here we summarize their recent results.

The first milestone of EHT works was achieved by Doeleman et al. (2008). Reliable detections of fringes at 230 GHz on a long Hawaii(JCMT) - Arizona (SMTO) baseline and a short California (CALMA) - Arizona (SMTO) baseline enable to measure the effective size of Sgr A*. By fitting to observed visibilities with circular Gaussian distribution (see, Figure 2.12), they obtained full-width-half-maximum (FWHM) size of 43^{+14}_{-8} μas, where errors are 3 sigma. Using scattering low of Bower et al. (2006), they estimated an intrinsic size of 37^{+16}_{-10} μas corresponding to ~ 4 $R_{\rm s}$.

The derived intrinsic size indicates that the structure of Sgr A* is not a spherically symmetric photosphere which centered a black hole. If the radiation of Sgr A* is originated from a spherical surface, a larger apparent size is observed. If such a surface of radius R centered on a non-rotating black hole will have an apparent radius, $R_{\rm app}$, given by

$$R_{\rm app} = \begin{cases} 3\sqrt{3}R_s/2 \ (\text{if } R \leq 1.5R_s) \\ R/\sqrt{1-R_s/R} \ (\text{if } R \geq 1.5R_s). \end{cases} \tag{2.4}$$

When R equals to 1.5 R_s (the ISCO), an apparent diameter has a minimum value corresponding to 5.2 R_s. In the case of Sgr A*, this corresponds to a minimum apparent diameter of 52 μas. This size is only marginally consistent with the 3

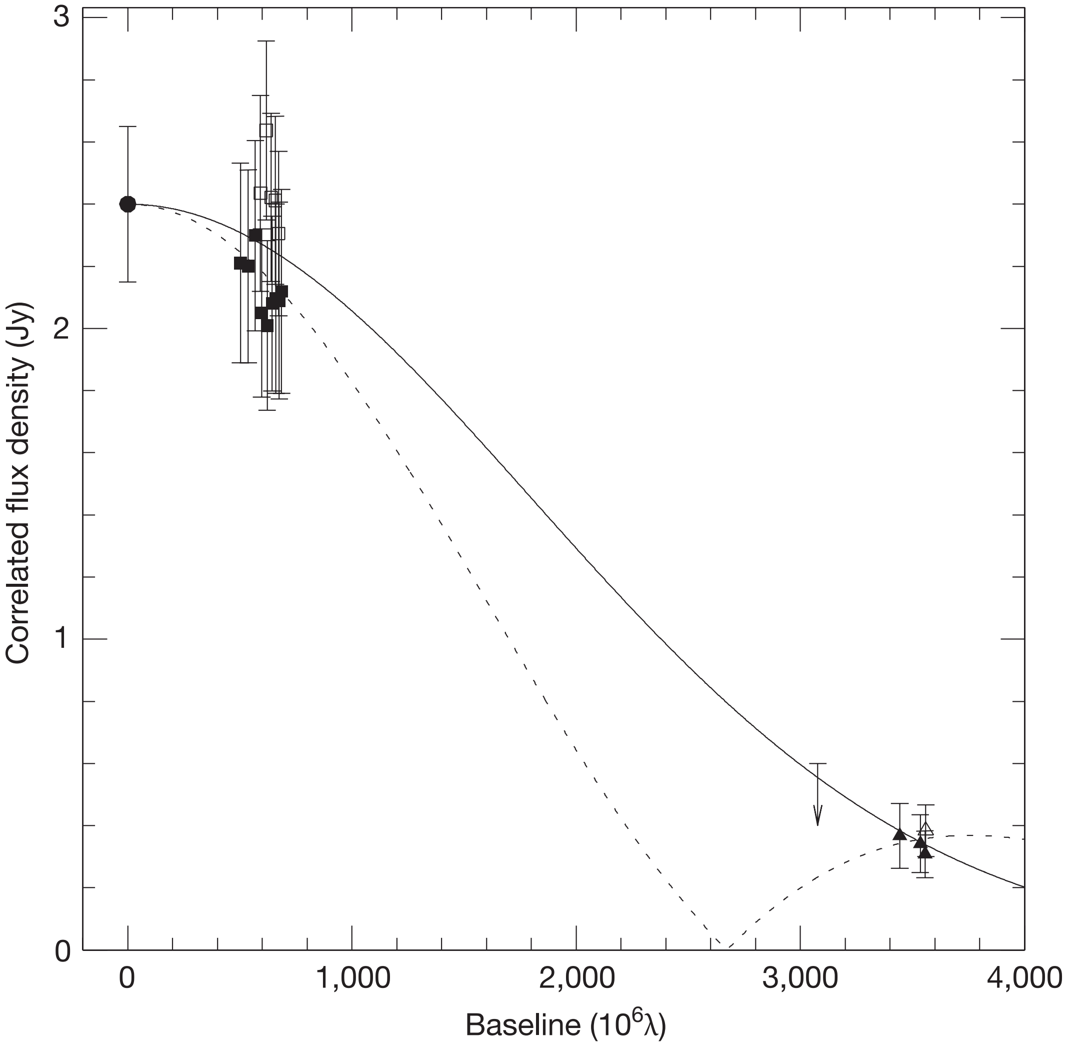

Figure 2.12: The UV distance plot of SgrA* at 1.3mm in Doeleman et al. (2008). It shows the correlated flux density data on the SMTO(Arizona)-CARMA(California) and SMTO(Arizona) -JCMT(Hawaii) baselines plotted against projected baseline length (errors are 1 sigma). Squares show SMTO(Arizona)-CARMA(California) baseline data and triangles show SMTO(Arizona)-JCMT(Hawaii) data, with open symbols for 10 April and filled symbols for 11 April. The solid line shows the weighted least-squares best fit to a circular Gaussian brightness distribution, with FWHM size of 43.0 μas. The dotted line shows a uniform thick-ring model with an inner diameter of 35 μas and an outer diameter of 80 μas convolved with scattering effects due to the interstellar medium. The total flux density measurement made with the CARMA array over both days of observing (2.46±0.25 Jy : 1 sigma error) is shown as a filled circle. An upper limit for flux density of 0.6 Jy, derived from non detections on the JCMT(Hawaii)-CARMA(California) baseline, is represented with an arrow.

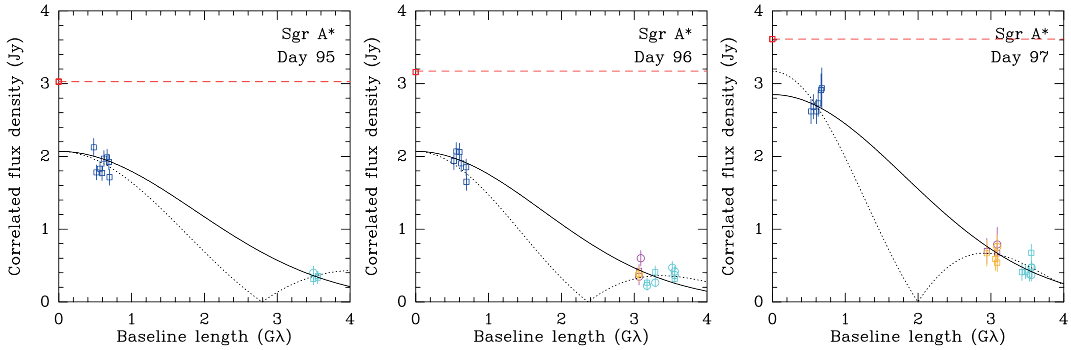

Figure 2.13: The UV distance plots of SgrA* at 1.3mm in Fish et al. (2011). Solid lines show best-fit circular Gaussian models of the compact emission in Sgr A* and are consistent with a source size of approximately 43 μas on all days. The dotted lines show the best ring model fits to Sgr A* data. Each baseline data is colored as follows: SMTO-CALMA(1) and SMTO-CALMA(2) baselines in blue, CALMA(1)-CALMA(2) baseline in red, JCMT-CALMA(1) baseline in orange, JCMT-CALMA(2) baseline in pink, JCMT-SMTO baseline in light-blue.

sigma upper limit for the derived intrinsic size. Thus, this fact suggests that Sgr A* arises in a region offset from the black hole, in other words, in a compact Doppler-enhanced portion of an accretion disk or jet. Based on accretion disk model, this fact suggests the inclination of accretion disk is closer to edge-on rather than face-on. This argument also holds in the case of a maximally rotating black hole of the same mass: the minimum apparent size in the equatorial plane would be 45 μas, which is also larger than the intrinsic size derived here. The intrinsic sizes of Sgr A* measured with VLBI at 3.5mm and 7mm exceed the minimum apparent size. Thus, presence of Doppler-boosted emission can not be revealed without Event Horizon Telescope.

Fish et al. (2011) reported the detection of daily flux variation on scales of several tens of μas. Figures 2.13 show the results of 2009 observation in Fish et al. (2011). The arc-second-scale flux densities of Sgr A* on days 95 and 96 coincided within uncertainties, but on day 97 the flux density of Sgr A* was ~17 % higher. This brightening was accompanied by changes on VLBI scales as well.

The flux density increase appears as an event that establishes a new steady state in Sgr A*. In general, an increase in source size is expected for models assuming that the flux variation is attributed to one-shot heating of plasma such as a jet knot (e.g. Falcke et al., 2009; Maitra et al., 2009) or partially heated plasma blob in the accretion disk (e.g. Yusef-Zadeh et al., 2006b, 2008, 2009). However, as seen in Figures 2.13, Fish et al. (2011) did not find any evidence of an increase in source size.

In summary, EHT is still under development, but EHT has already reveal a small scale structure and its intrinsic variation as follows:

1. First results of EHT (Doeleman et al., 2008) ruled out a spherically symmetric photosphere centered on the central dark mass, and they indicated that Sgr A* arose in a compact Doppler-enhanced portion of an accretion disk or jet.
2. Based on RIAF models, a low-inclination disk is ruled out.
3. Fish et al. (2011) found a new steady state in Sgr A* which seems not able to be explained by the models of the intra-day variability.

Future observations of more developed EHT and simultaneous multi-wavelength observations with EHT would reveal further new and detail phenomena of intrinsic structure of Sgr A*.

2.1.6 *Variability*

Sgr A* is known to vary at all wavelengths. The variability of Sgr A* was already reported in the first discovery of Sgr A* (Balick & Brown, 1974).

2.1.6.1 *Daily variation*

The variability on time scale longer than a day in radio regime has been discussed mainly based on observations with connected interferometers (see Macquart & Bower, 2006, and references therein). As an origin of the variation, both intrinsic and extrinsic models are proposed, but the mechanism of the time variation is still under discussion. As a candidate of long-term intrinsic variation, 106-day quasi-periodic variation was reported at wavelengths shorter than $\sim$ 3 cm (Zhao et al., 2001) and 57-day quasi-periodic variation was also reported at 2.3 GHz (Falcke et al., 1999). However, Macquart & Bower (2006) carried out the analysis of uniformly sampled data with proper accounting of the sampling errors, and rejected existences of these quasi-periodic variations. On the other hand, interstellar scintillation is the primary mechanism that may cause extrinsic variability. However, it is difficult to judge whether the interstellar scattering can totally explain the flux variation, since the detailed structure of scattering medium is still unknown. Previous studies suggested that if the scattering medium of Sgr A* lies on a thin screen, all the observed flux variability must be intrinsic to the source itself (Macquart & Bower, 2006). Meanwhile, an extended scattering region may explain broad characteristics of the variability longer than 4 days (Macquart & Bower, 2006), although the physical structures associated with this extended scattering medium is unknown.

Recently studies at short cm- and mm-wavelengths reported the existence of long time-scale flux variations at short-cm/mm wavelengths, where interstellar effects are negligible. A massive monitoring of Sgr A* with VLA and the detections of high fluxes of Sgr A* at mm wavelengths indicate the existence a possible bimodal distribution of flux density, such as low/high-flux density states at these frequencies (see Figures 2.8 and following references: Herrnstein et al., 2004; Li et al., 2009; Lu et al., 2011). As written in §2.1.4.1, at high state, the spectrum index becomes harder. In simple models of interstellar scattering, the modulation index of the flux density decreases with frequency in the strong scattering regime (e.g. Rickett, 1990). This leads to an anti-correlation between spectral index and mm-flux. Thus, this correlation would favor some intringic variations in Sgr A* for the origin of the flux variation rather than interstellar scintillation effects.

2.1.6.2 *Intra-day variability*

Sgr A* is also known as intra-day variable (IDV) source. The first detection of IDV was achieved in radio regime (Miyazaki et al., 2004). After that, IDV has been reported at various frequencies (e.g. Yusef-Zadeh et al., 2006b, 2008, 2009; Miyazaki et al., 2004; Li et al., 2009). IDV at the radio band has a variability time-scales of a few or several hours with following properties;

1. Time-delays detected between peaks of flare emission at cm/mm/sub-mm wavelengths (e.g. Yusef-Zadeh et al., 2006b, 2008, 2009).
2. A flare activity in radio regime is lower (at a level of 4.5 and 7 %) than NIR and X-ray regime.

In addition to these feature, the flare in radio regime may have been occurred after the NIR/X-ray flare with the duration of $\sim$ 2-3 hours (Yusef-Zadeh et al., 2006b, 2008, 2009). However, the relation between NIR/X-ray flare and radio flare is still not clear due to poor time-coverage of multi-wavelength campaigns compared with possible duration of the flares.

Three types of models have been proposed as of 2014: expanding plasma blob models, jet models, and thermal outflow model. The expanding plasma blob model (or expanding plasmon model; e.g. van der Laan, 1966; Yusef-Zadeh et al., 2006b, 2008, 2009; Li et al., 2009) explains observed light-curve and time-delays in radio regime well. Arising part of light-curve in radio regime is interpreted as the opacity of emitting blob becomes thinner at observed frequency due to the expansion. On the other hand, decaying part of light-curve is interpreted as adiabatic cooling associated with the expansion of the emitting plasma. Time-delays are interpreted to be owing to the difference of opacity of emitting blob. The expansion speed of emitting blob is sub-relativistic (e.g. Yusef-Zadeh et al., 2006b, 2008, 2009; Li et al., 2009).

The jet model (Falcke et al., 2009; Maitra et al., 2009) also explains observed light-curve and time-delays in radio regime well. In this model, decaying part of light curve is interpreted similarly to the expanding plasma blob model, but arising part of light curve is caused by a passage of emitting blob over photosphere of Sgr A*. Thus, observed time-delays are mainly determined by the size of photosphere of Sgr A* (i.e. intrinsic size of Sgr A*) and the bulk velocity of the emitting blob. The bulk velocity becomes relativistic, while expansion velocity is similarly to the expanding plasma blob model.

Another models is an orbiting hot spot model (e.g. Broderick & Loeb, 2006; Meyer et al., 2006a; Trippe et al., 2007; Eckart et al., 2006, 2008; Li et al., 2009). This model has been frequently used to mainly explain observations of short-term NIR and X-ray variability. The hot spot is modeled by an over-density of non-thermal electrons centered in its Keplerian orbit around SMBH. This situation may arise in the case of a magnetic reconnection event similar to the solar flare. Due to the Doppler shift and relativistic beaming, the approaching portion of the hot spot orbit appears considerably brighter than the receding portion. This model is successful in explaining the NIR 17 minute quasi-periodic oscillation (Genzel et al., 2003). The hot spot model is applied to the radio band by including the effects of disk opacity for a typical RIAF model (Broderick & Loeb, 2006). Li et al. (2009) tried to fitting this model and the expanding plasma blob model to the light-curve with multi-flares at 100 GHz, and then found both the models could reasonably fit observed flares.

The general properties of the IR and X-ray flares are reviewed in detail in the introduction of Dodds-Eden et al. (2009). Here, we introduce some of them for comparison to flares in radio regime. First, NIR flares occur on average $\sim$4 times per day or between 30% and 40% of the observing time. On the other hand, strong X-ray flares occur on average $\sim$1 per day. Thus, the flare activity in NIR and X-ray regime is more active than radio regime. However, an enhanced rate of X-ray flaring can be observed within a time interval of roughly half a day. Second, every

X-ray flare appears to be associated with an NIR flare, but not every NIR flare is associated with an X-ray flare. When both flares occur, they occur simultaneously, with no significant delay. Polarimetric investigations of the flares in the NIR have shown that the source is significantly polarized and that the polarization angle can swing in the tail end of the flare. It indicates the NIR emission is originated in synchrotron emission. However, the origin of X-ray emission is uncertain. Inverse Compton scattering and synchrotron emission are proposed, but dominant emission is highly depends on models and individual flare.

2.1.6.3 *Another exploration of IDV with VLBI : Position Wander*

Reid et al. (2008) carried out exploration of the variability in the centroid position of Sgr A* in intra-day scale by phase-referencing observations with VLBA at 43 GHz. They found an average centroid wander of 71 $\pm$ 45 μas for timescales between 50 and 100 minutes and 113 $\pm$ 50 μas for timescales between 100 and 200 minutes, with no secular trend. From these observational facts, they constrained the variability of the accretion hot spot model proposed in Broderick & Loeb (2006). It is possible to rule out hot spots with orbital radius above $15GM/c^2$ that contribute more than 30 % of the total 43 GHz flux. However, closer or less luminous hot spots remain unconstrained. Since the fractional variability of Sgr A* during our observations was 20 % on time-scales of hours, the hot spot model for Sgr A*'s radio variability remains consistent with these limits.

2.1.7 *Theoretical Models*

2.1.7.1 *Radiative Inefficient Accretion Flow*

The most representative model for emission of Sgr A* is a radiatively inefficient accretion flow (RIAF; see Kato et al., 2008; Yuan & Narayan, 2014, for a review). We summarize representative RIAF models for Sgr A* in Table 2.2. Note that the model is applicable to LLAGNs (including M87). Here, we briefly review interpretations of the accretion process around Sgr A* and also RIAF models.

First of all, we note outer boundary conditions before introducing inner flow of an accretion disk. The accretion flow starts at the Bondi radius, where the gravitational potential energy of the gas is balanced with its thermal energy. Chandra observations (Baganoff et al., 2003) resolved the Bondi radius and inferred gas density and temperature as $\sim$ 100 cm^{-3} and $\sim$ 2 keV on scales of $1''$, respectively. This results correspond to the Bondi radius of $\sim 10^5\ R_s$ and the Bondi accretion

Table 2.2: Overview of typical RIAF models for Sgr A*

Model	Method	Dimensions	GR Effect inflow	Non-thermal electron	Mass Loss	Radiation Transfer[a]	Low frequency spectrum	Polarization
Manmoto et al. (1997)	Semi-Analytic	1D	Yes	No	No	plane-parallel	No	No
Narayan et al. (1998)			Yes	No	No	plane-parallel	No	
Yuan et al. (2002)			PW potential	No	Yes	plane-parallel	No	
Yuan et al. (2003)			PW potential	Yes	Yes	plane-parallel	Yes	
Yuan et al. (2006)			PW potential	Yes	Yes	plane-parallel	Yes	
Yuan et al. (2009)			Yes	No	Yes	plane-parallel	No	
Broderick et al. (2009, 2011)	Self-Similar	1D	PW potential	Yes	Yes	GR Ray-tracing	Yes	No
Kato et al. (2009)	GRMHD	2D	Yes	No	—	Monte-Calro[a]	Yes	No
Mościbrodzka et al. (2009)							No	
Mościbrodzka et al. (2012)							No	
(Dexter et al., 2009)						—	—	
Dexter et al. (2010)	GRMHD	3D	Yes	No	—	GR Ray-tracing	No	No
Dexter & Fragile (2011)								No
Shcherbakov et al. (2010)								Yes

[a] The method for calculating the radio emission. The GR ray-tracing method is used to calculate radio images in Mościbrodzka et al. (2009) and Mościbrodzka et al. (2012).

rate of $10^{-5}\ M_\odot$ yr^{-1}. The gas density, temperature, the Bondi radius and Bondi accretion rate constitute the outer boundary conditions that any accretion models must satisfy.

The Bondi accretion rate of $10^{-5}\ M_\odot$ yr^{-1} rules out the standard disk model. If the gas was accreted at this rate onto the central black hole via the standard disk, the expected luminosity would be L $\sim$ 0.1 $\dot{M}_{\rm bondi}c^2$ $\sim$ 10^{41} erg s^{-1}, five orders of magnitude higher than the observed luminosity. Moreover, the lack of big blue bump in its SED, which is thought to be produced by multi-temperature black body emission from the standard disk, is also against the standard disk model. Moreover, its hard spectrum needs hot accretion flow rather than relatively cold accretion flow predicted by standard disk.

The luminosity of Sgr A* far less than “optically-thick” standard disk implies that a low mass accretion rate can not supply an enough amount of the matter to obtain an optical depth of unity. The accretion flow is expected to be optically thin and radiatively inefficient.

The most classic type of RIAF is the advection-dominated accretion flow (ADAF). The ADAF solution for the black hole accretion disk was originally found in Ichimaru (1977) and independently re-discovered in Narayan & Yi (1994). "Advection-dominated" means that the radiative cooling is dominated by the advective cooling. Here, we introduce the physical meaning of "advective cooling" and "advection-dominated" from two different views: the co-moving frame and the rest frame. In the co-moving frame, we will see that the matter does not cool at all due to inefficient radiative cooling attributed to a low optical depth. This leads that the matter rather heats up due to viscous heat dissipation. In other words, the radiative time-scale is much longer than the accretion time-scale highly affected by the advection-term in the equation of motion. The most of the viscously dissipated energy is not released by radiative cooling but stored in the accretion flow, leading that the ion heats up to a high temperature near Virial temperature. On the other hand, in the rest frame, when we keep our eyes on a fixed region at some radius, we will see that low-entropy material enters this region from an adjacent outer zone. That inflow material will eventually go out (or fall into) adjacent inner zone, after acquiring entropy as a result of viscous heat dissipation. Hence, low-entropy material comes in and high-entropy material goes out. It is equivalent with net cooling at some fixed radius, which is called as "advective cooling".

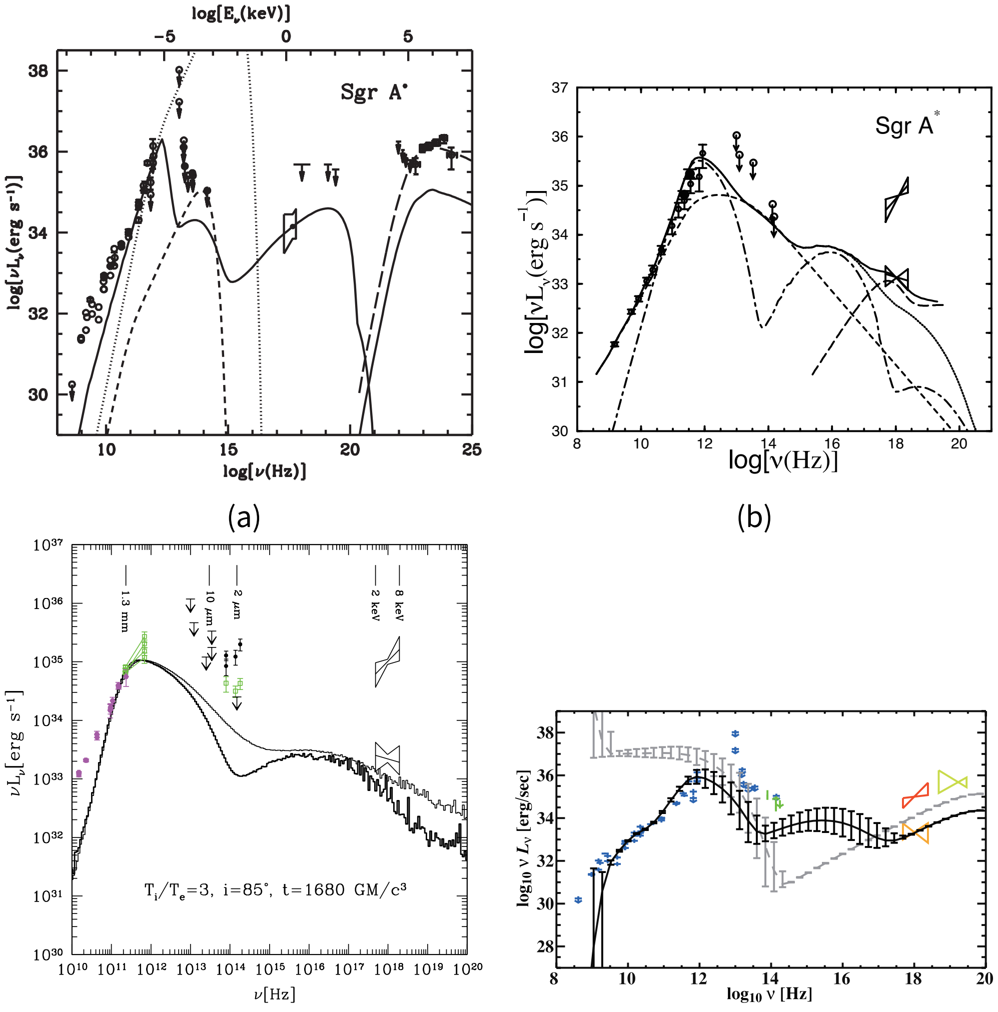

(a) (b)

(c) (d)

Figure 2.14: The SEDs of typical RIAF models for Sgr A*. (a) The classic ADAF (Narayan et al., 1998). (b) ADIOS with non-thermal electrons (Yuan et al., 2003). (c) A 2D axis symmetric GRMHD model (Mościbrodzka et al., 2009). (d) Another 2D axis symmetric GRMHD model (Kato et al., 2009).

Thus, in an ADAF, the ion temperature becomes high nearly Virial temperature. On the other hand, the electron temperature is expected to be lower owing to the radiative cooling and weak coulomb coupling between electrons and ions, although it is still as high as $T_e \sim 10^9 - 10^{11} K$ (e.g. Manmoto, 2000; Yuan et al., 2009). The high ion temperature leads to a geometrically thick flow.

The most famous ADAF models for Sgr A* are models in Manmoto et al. (1997) and Narayan et al. (1998). They apply the ADAF model to Sgr A* and successfully explained the most important features of Sgr A* such as its low radiative efficiency and the sub-mm bump (see Figure 2.14 (a)). However, the ADAF models have mainly two problems; (1) the spectrum in the radio regime at low frequencies can not be explained; (2) the mass accretion rate is assumed to be constant with radius. As a results, the rotation measure predicted in this model is much larger than that required from the polarization observation (e.g. Bower et al., 2003; Marrone et al., 2006; Macquart & Bower, 2006).

2D/3D hydrodynamical simulations revealed distinct forms of accretion flows in the radiatively inefficient regimes. A nearly one-dimensional ADAF appears only when the viscosity parameter α is moderate, 0.01$\leq \alpha \leq$0.1. If α is very small, convection occurs and largely modifies the flow structure. Such a flow is called convection-dominated accretion flow (CDAF; e.g. Narayan et al., 2000; Quataert & Gruzinov, 2000). However, the spectrum of CDAF can not explain the SED of Sgr A* (see Kato et al., 2008). On the other hand, if α is large, the strong outflows occur. Blandford & Begelman (1999) constructed a model of ADIOS (adiabatic inflow-outflow solutions) based on this idea. For implementing this mass loss effect, they assumed that the mass-accretion rate varies as $\dot{M} \propto r^s$ with $0 \leq s < 1$. ADIOS can explain not only the SED of Sgr A* similarly to ADAF (e.g. Yuan et al., 2002, 2009), but also the observed rotation measures (e.g. Yuan et al., 2003).

The rest of problems is the radio spectrum at low frequencies. Yuan et al. (2003) and Yuan et al. (2006) succeed to reconstruct the low-frequency spectra by involving non-thermal electrons to the ADIOS model (see Figure 2.14 (b)). In this model, the low frequency radio emission is dominated by non-thermal emission produced by power-low distributed electrons, although the production mechanism of such electrons has been unclear. The emission in original models is calculated by the plane-parallel method, but recent studies show that the radio spectrum can be well explained by more realistic general relativistic (GR) ray-tracing calculation (Broderick et al., 2009, 2011).

Recent progress in the computational science enables to carry out a general relativistic magnetic hydro-dynamic (GRMHD) simulation of RIAF (e.g. Kato et al., 2009; Mościbrodzka et al., 2009, 2012; Dexter et al., 2009, 2010; Dexter & Fragile, 2011; Shcherbakov et al., 2010). However, as of 2014, the GRMHD models have failed to explain the low-frequency radio spectrum only with thermal electrons except the model of Kato et al. (2009) which introduces spatial variation in electron temperature distribution (see Figure 2.14 (c) and (d)).

Nowadays, it has been a hot topic to check consistency between the emission structure observed with millimeter VLBI and theoretically predicted ones. Yuan et al. (2006) and Yuan et al. (2009) calculated the intensity profile with the plane-

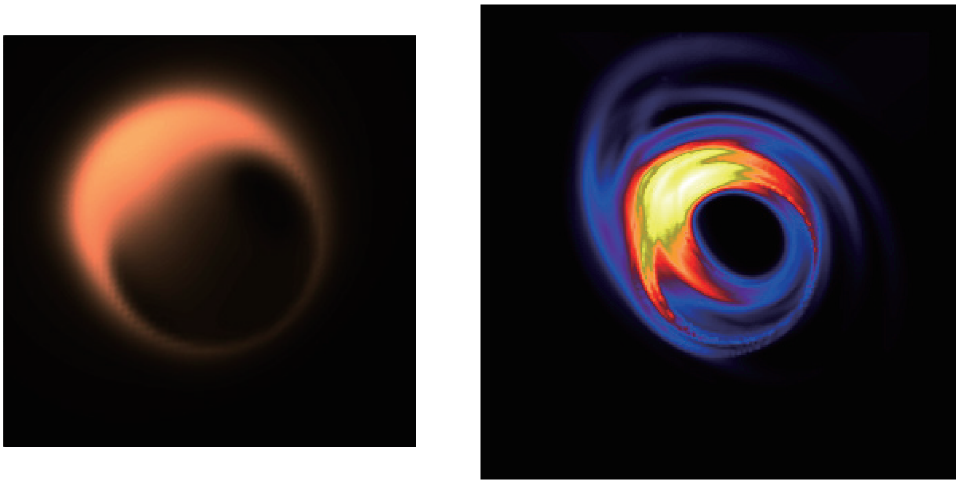

(a)

(b)

Figure 2.15: 1.3-mm emission structure predicted by semi-analytic and GRMHD RIAF models. (a) The latest best-fit semi-analytic RIAF model in Broderick et al. (2011). (b) One of the best-fit 3D GRMHD models in Dexter et al. (2010).

Table 2.3: Overview of Jet models for Sgr A*

Model	Method	With RIAF	Data sets to fit	Radiation Transfer	GR effect in flow
Falcke & Markoff (2000)	Semi-analytic	No	Radio & X-ray	Plane-parallel	No
Markoff et al. (2007)		No	Radio & IR	Plane-parallel	No
Yuan et al. (2002)		w/ ADAF	Radio & X-ray	Plane-parallel	PW potential for ADAF
Mościbrodzka & Falcke (2013)	GRMHD	w/ RIAF	Radio, IR & X-ray (at flare)	GR Ray-Tracing	Yes
Mościbrodzka et al. (2014)					

parallel technique, and found that it could not be well represented by a Gaussian distribution because most of emission is generated in the inner most region of the accretion disk, $\sim$ a few R_s. However, they found that by including the effect of interstellar scattering, predicted size is consistent with VLBI observations at short cm- and long mm-wavelengths. For the structure detected with EHT observations at 1.3 mm (Doeleman et al., 2008; Fish et al., 2011), both semi-analytic solutions of RIAF (Broderick et al., 2009, 2011) and GRMHD simulations (Mościbrodzka et al., 2009, 2012; Dexter et al., 2009, 2010; Dexter & Fragile, 2011; Shcherbakov et al., 2010) ruled out a low-inclination disk, being consistent with implications from the observed size of emission (Doeleman et al., 2008) (see Figure 2.15 for the predicted 1.3 mm emission structure).

2.1.7.2 *Jet*

The other representative model is a jet model originally proposed in (Falcke & Markoff, 2000) based on models for LLAGNs (Falcke, 1996). We summarize an overview and spectra of representative jet models for Sgr A* in Table 2.3.

In the classic semi-analytic models, the models assume that the jet is thermally driven by a pressure gradient (Falcke & Markoff, 2000; Yuan et al., 2002; Markoff et al., 2007). The radiation in these models are basically calculated with the plane-parallel method for the plasma in the jet only (Falcke & Markoff, 2000; Markoff et al., 2007) and the jet and ADAF (Yuan et al., 2002). Very recently, Mościbrodzka & Falcke (2013) and Mościbrodzka et al. (2014) developed more realistic coupled disk-jet models based on the GRMHD simulation for Sgr A* (Figure 2.16).

The spectra of the models are shown in 2.17. In radio regime, the flat radio spectrum at low frequency is a consequence of superposition of self-absorbed synchrotron emission (see Figure 2.17 (a)). In the classic semi-analytic jet-dominated models (Falcke & Markoff, 2000; Markoff et al., 2007), the sub-mm bump is mainly from the compact "nozzle" component, which is the acceleration zone of the jet where most energetic electrons exist. In the case of coupled jet-disk models (Yuan et al., 2002; Mościbrodzka et al., 2014), emission from jet dominates at low frequency, but emission from RIAF becomes comparable or dominant in sub-mm excess regime. In particular, Mościbrodzka et al. (2014) pointed out that the short-millimeter emission is favored to be dominated by the emission from RIAF to reproduce 1.3 mm visibilities and broad-band SED consistent with observations. Markoff et al. (2007) pointed out that the radio spectrum can be well explained by electrons with both of thermal relativistic Maxwellian and non-thermal power-law distributions.

In the semi-analytic models, X-ray emission is synchrotron self-Compton (SSC) emission, while IR emission is mainly synchrotron emission determined by the highest-energetic electrons in the jet nozzle. In the case of the GRMHD models, emission in X-ray and IR regime is dominated by emission from RIAF. Note that Falcke & Markoff (2000) and Yuan et al. (2002) used steady X-ray emission for fitting free parameters. As described in §2.1.4.2, this steady emission is diffuse and produced in the outer regions of the accretion flow and cannot be directly related to the compact source, which must be produced at small radius. Thus, their treatments of X-ray data would not be appropriate. The recent models (Markoff et al., 2007; Mościbrodzka et al., 2014) used only radio and IR data for preceding reasons.

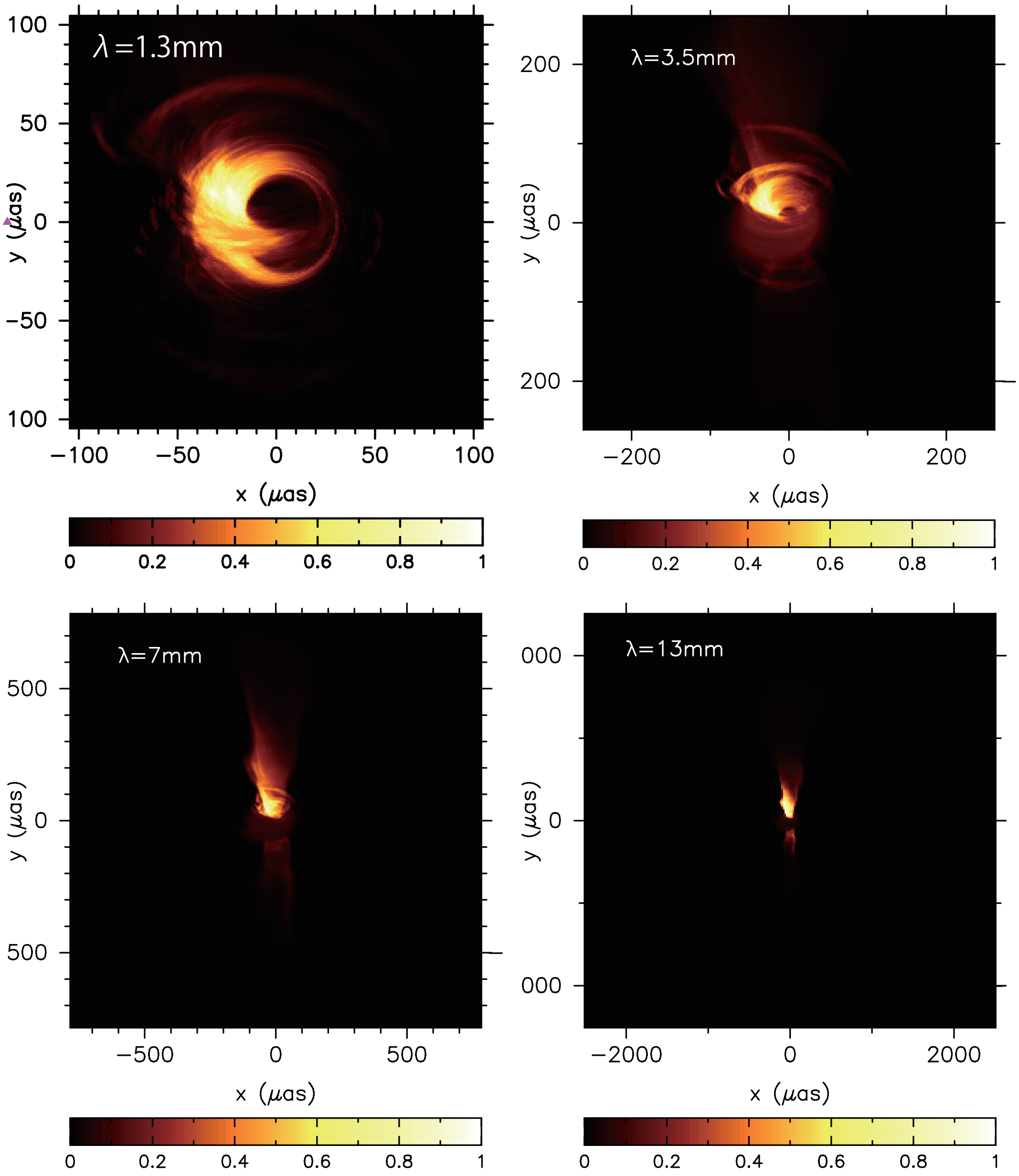

Figure 2.16: The radio images of the latest GRMHD jet model for Sgr A* (Mościbrodzka et al., 2014). The optically-thick thermal synchrotron emission from the jet dominates emission near the central SMBH at lower frequencies, but emission becomes optically thin and is dominated by the thermal synchrotron emission from the accretion disk at 1.3 mm.

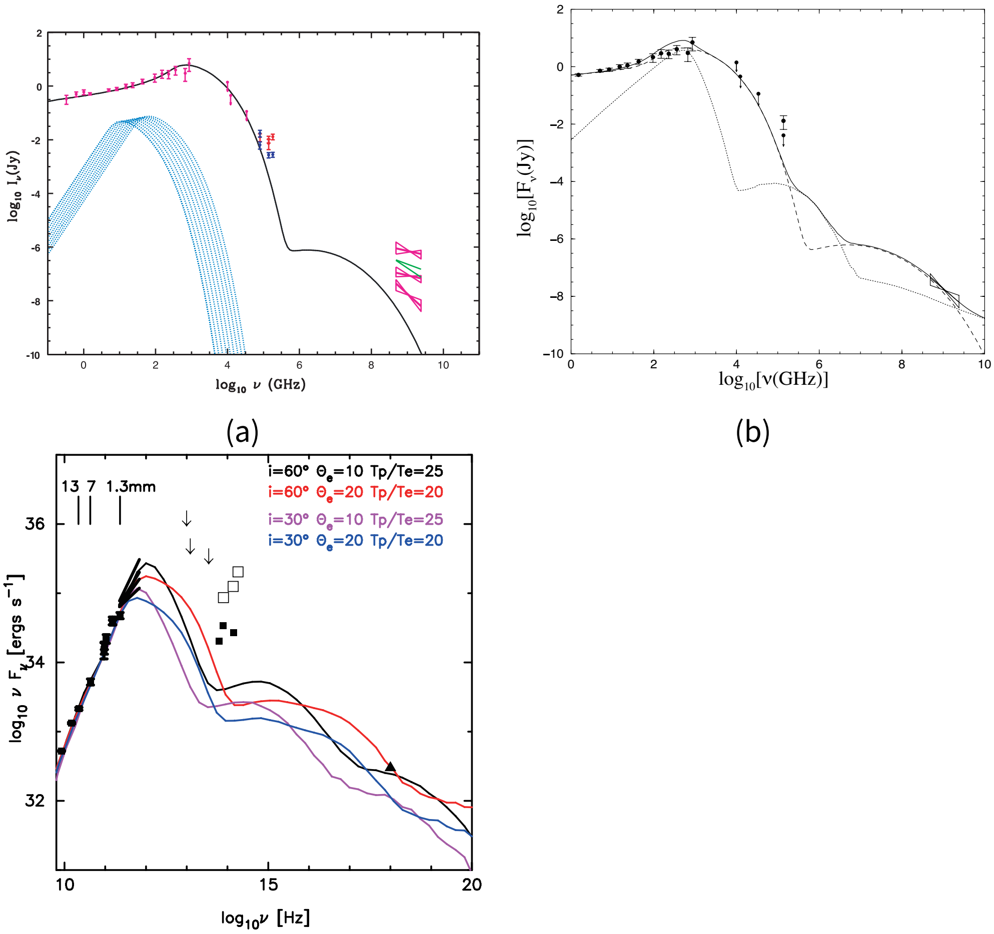

(a)

(b)

(c)

Figure 2.17: The spectra or SEDs of representative jet models for Sgr A*. (a) The spectrum of the latest semi-analytic model (Markoff et al., 2007). The solid curve shows a representative quiescent model with synchrotron and synchrotron self-Compton peaks. The dotted lines illustrate the contribution of the quasi-thermal particles from each increment along the jet, which superimpose to give the characteristic flat/inverted synchrotron spectrum. (b) The spectrum of the jet-ADAF model (Yuan et al., 2002). The dotted line is for the ADAF contribution, the dashed line is for the jet emission, and the solid line shows their sum. (c) The SED of the latest GRMHD jet-disk model (Mościbrodzka et al., 2014).

2.2 SCOPE OF STUDIES IN THIS CHAPTER

In this section, we reviewed on observational and theoretical studies of Sgr A*. There is plenty of evidence that the center of our galaxy hosts a massive black hole with a mass of approximately 4×10^6 $M_\odot$ at a distance of about 8 kpc (§2.1.3). The compact radio source Sagittarius A* (Sgr A*), located in the galactic center is believed to be associated with this black hole. The measurements of the proper motion of Sgr A* showed that Sgr A* must contain > 4×10^5 $M_\odot$ (Reid & Brunthaler, 2004) and provided support for the existence of a massive black hole in the vicinity of Sgr A* (§2.1.3).

High spatial resolution of VLBI enables monitoring of the flux and structure in the vicinity of a black hole. Hence, a monitoring observation with VLBI is of great importance to investigate a mechanism of time-variation of Sgr A* in the innermost region of the accretion disk and/or the jet base. However, there have been no VLBI studies aiming to monitor the time variation of both the flux and structure of Sgr A* in time scales longer than a month. Previous VLBI studies on the size of Sgr A* found that the intrinsic structure can be estimated from VLBI observations at a frequency higher than $\sim$ 22 GHz. Moreover, simultaneous observations of Very Long Baseline Array (VLBA) and Very Large Array (VLA) indicated that the total flux of Sgr A* obtained by a connected array tend to be over-estimated by sampling the diffuse emission from the vicinity of the Sgr A* (Yusef-Zadeh et al., 2009). Thus, VLBI observations are most suitable for a detailed study of the long-term variation of the Sgr A*. Hence, in order to investigate the relation between the flux and intrinsic size of Sgr A*, we have carried out the observations of Sgr A* from 2004 to 2008 with VLBI Exploration of Radio Astrometry (VERA) at 43 GHz, and here we report the results. Throughout this chapter, the mass of Sgr A* M is assumed to be 4×10^6 $M_\odot$, and the distance to Sgr A* D is assumed to be 8 kpc.

2.3 OBSERVATIONS AND REDUCTIONS

2.3.1 *Observations*

VERA observations of Sgr A* at 43 GHz were regularly performed between November, 2004 and April, 2009. The observations were done in the dual-beam mode observing Sgr A* and J1745-2820 simultaneously for aiming at astrometry of Sgr A*. NRAO 530 is also observed in several scans for checking the consistency of the amplitude calibration. In this thesis, we focus only on the data of Sgr A*. Results of the astrometry of Sgr A* will be discussed elsewhere.

In some epochs, one or more stations were partly or fully missed due to system trouble or/and bad weather. Since the VERA array consists of only four stations, a lack of stations causes severe degrading of synthesized images, and would introduce a large error in quantities derived from images or model-fitting toward visibilities. Hence, in this thesis, we use the data of 10 epochs for which full stations are available under relatively good conditions. The epochs presented here are: day of year (DOY) 294 in 2005, 079, 109 and 308 in 2006, 073, 093 and 264 of 2007, 076, 085 and 310 of 2008 (October 21 of 2005, March 20, April 19 and November 4 of 2006, March 14, April 3 and September 21 of 2007, March 16, March 25, November 8 of 2008). The system noise temperatures at the zenith were typically 400-600 K through all the epochs.

Left-hand circular polarization (LHCP) signals were received and sampled with 2-bit quantization, and filtered using the VERA digital filter unit (Iguchi et al., 2005). The data were recorded at a rate of 1024 Mbps, providing a bandwidth of 256 MHz. One of two IF-channels of 128 MHz bandwidth was assigned to Sgr A* (and also NRAO 530). Correlation processes were performed with the Mitaka FX correlation (Chikada et al., 1991).

2.3.2 *Data Reductions*

Data reductions were carried out with the NRAO Astronomical Imaging Processing System (AIPS) first, using the standard algorithms including phase and delay calibrations and fringe-fitting. A standard *a priori* amplitude calibration was performed using the AIPS task APCAL based on the measurements of system temperature ($T_{sys}*$), which were obtained based on the chopper-wheel method during observations. Delays and rates were determined with fringe-fitting directly to the Sgr A* visibilities using the AIPS task FRING. We set a solution interval of $\sim$ 1 min and minimum S/N ratio of = 3. To avoid false detections, we set a practical search window of 20 nsec $\times$ 50 mHz. In this search window, the false detection probability is $\sim$ 5 %. Since Sgr A* has still scattered broad structure at 43 GHz and its FWHM size is $\sim$ 0.7 mas at 43 GHz, fringes were not detected for most visibilities observed in baselines longer than 200 Mλ. Figure 2.18 shows a typical uv-coverage of Sgr A*. In fact, all the detected fringes are located within 200 Mλ. Visibilities related to the closure of Mizusawa, Iriki and Ogasawara stations are mostly valid, while

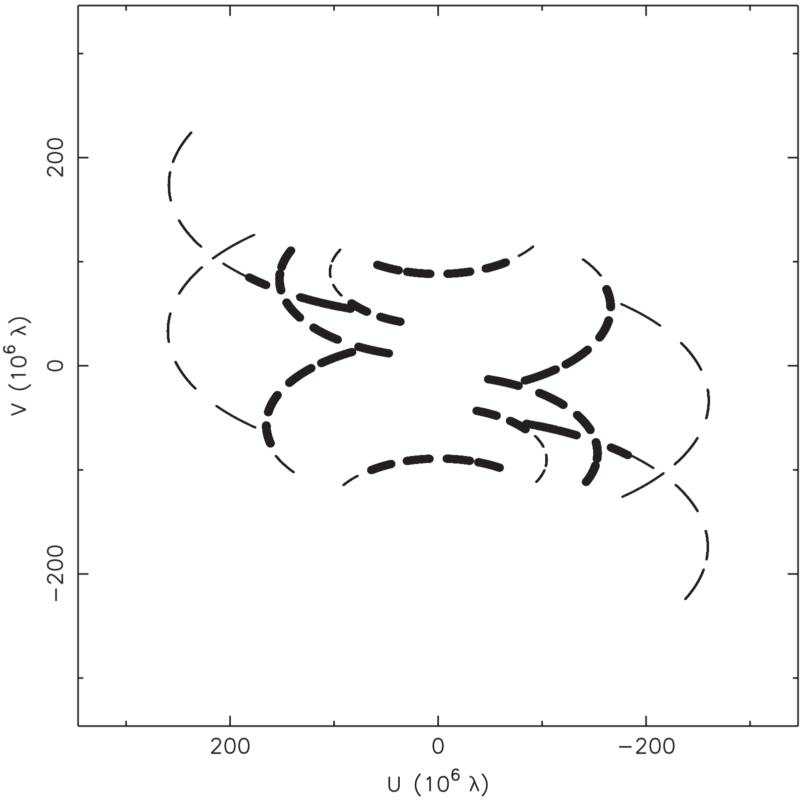

Figure 2.18: The distribution of visibilities on the $uv-$plane of epoch (j). Thin lines indicate all visibilities sampled during observation, while bold lines indicate UV for which fringes are detected. All detections are concentrated in baselines shorter than 200 Mλ.

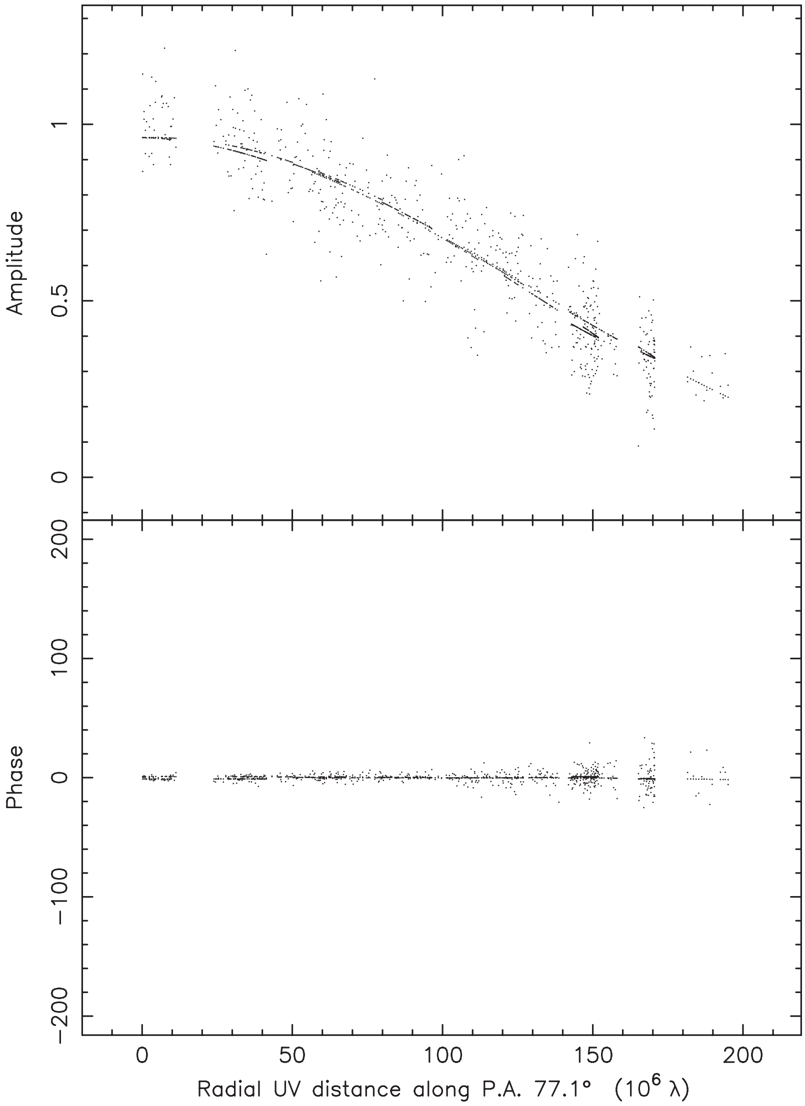

Figure 2.19: The visibility amplitude and phase of epoch (j) as a function of projected uv-distance for Sgr A*. All visibilities are plotted along a PA of 77.1 degrees East of North, corresponding to the major axis of the Gaussian model of epoch (j). The solid lines indicate the model obtained by elliptical Gaussian fitting. Parameters of the Gaussian model are shown in Table 2.6.

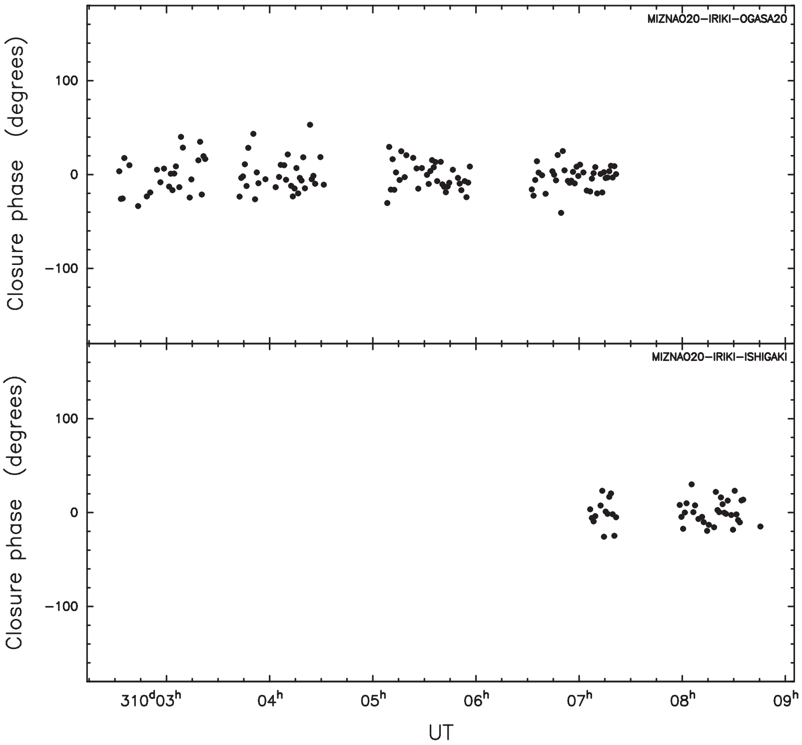

Figure 2.20: The closure phase of epoch (j) as a function of Universal Time.

more than 70 % of visibilities sampled with Ishigaki-jima station are invalid, since Ishigaki-jima station mainly provides baselines exceeding 200 Mλ. As an example of the visibilities after applying all calibrations, we show the uv-distance plot of the data obtained in November 8 of 2008 (in later sections, named as epoch (j)) in Figure 2.19. The horizontal axis of Figure 2.19 is the uv-distance projected along the major axis of the elliptical Gaussian models of visibilities (see, Section 3.2). The top panel of Figure 2.19 shows that the visibility amplitude decreases with uv-distance down to $\sim$ 200 mJy at 200 Mλ. Moreover, from the distribution of the visibility phases (the bottom panel), one can see that the scatter of phases becomes larger for longer baselines, which is due to lower S/N ratio for longer baselines. The minimum detected flux in Figure 2.19, $\sim$ 200 mJy, is comparable to the fringe detection limit of VERA under typical conditions. In fact, the minimum detectable flux is $\sim$ 200 mJy for S/N = 3 and $T_{\rm sys}* = 500$ K). This fact is consistent with the non-detection of fringe-fitting solutions for baselines longer than 200 Mλ.

After the fringe fitting, calibrated data were output to DIFMAP. We averaged visibilities to $\sim$ 60 s in DIFMAP. We checked the closure phase of Sgr A* and confirmed that the closure phase of Sgr A* is obtained throughout almost all the time in each epoch, and that their S/N ratios are high enough to apply self-calibration to the visibility phases. As an example, we show the closure phases of epoch (j) in Figure 2.20. As seen in Figure 2.20, closure phases of the combination of Mizusawa, Iriki and Ogaswara stations are mostly determined, while more than 60 % of the closure phases of the combination of Mizusawa, Ogasawara and Ishigaki stations are missed because the sources are mostly resolved out with long baselines. Two other closures including Ishigaki-jima station were totally invalid. Finally, we carried out imaging of Sgr A* by iterating the self-calibration of visibility phase and CLEAN using DIFMAP.

2.3.3 *Model Fitting*

After imaging, we also conducted Gaussian fitting to the calibrated visibilities, since most previous VLBI studies of Sgr A* also adopted this technique. We output visibilities to text files using AIPS task PRTUV, and fitted Gaussian models to visibilities directly by using the least-square method. We confirmed that the results of Gaussian fitting, which is obtained with our own code of least-square fit, coincides with the results obtained with the Gaussian fitting program in DIFMAP.

For estimating the fitting errors of Gaussian parameters, we used the non-parametric Percentile Bootstrap method (Wall & Jenkins, 2003). This method is straightforward in deriving estimates of confidence intervals of fitted parameters. We briefly summarize a process of estimating confidence intervals: at first, we created a dataset which has the same number of data by re-sampling the observed visibilities allowing repetition of the data. Re-sampling was simply done using a uniform random-number generator. Then, we fitted the Gaussian model to the new dataset and obtained a bootstrap estimate. We repeated this process 30,000 times and obtained 30,000 sets of the bootstrap estimates. The Percentile bootstrap confidence limits of each parameter are obtained as the edges of the middle 99.7 % fractions of the Bootstrap estimates. We confirmed that the averages of bootstrap parameters coincides to the results of the least-square method within 1 %. Finally, the errors of each parameter are obtained as one-third of displacements between the averages of bootstrap parameters and the confidence limits, so that the obtained error corresponds to 1-σ uncertainty. The obtained errors are slightly greater than the standard errors estimated from the co-variance matrix of the least-square method. This means that the bootstrap method provides more conservative error estimates than the standard errors of the least-square method.

The systematic errors of the total flux are estimated as below. In our observations, it is difficult to estimates systematic errors using calibrators, since our obser-

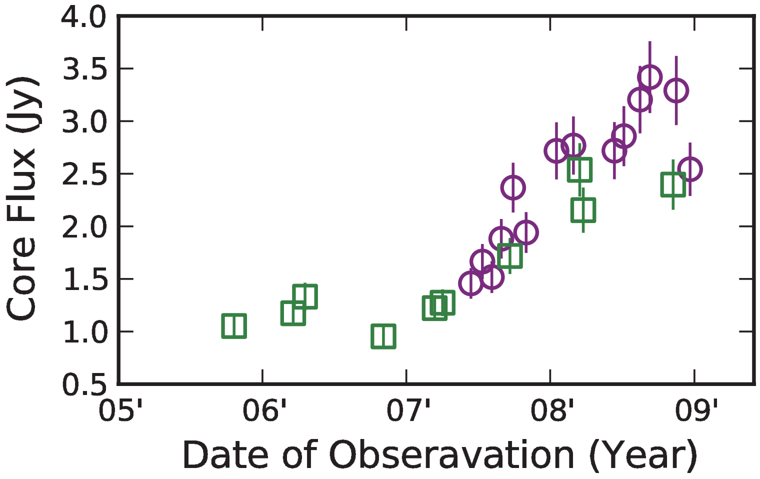

Figure 2.21: The time variations of the core-flux of NRAO 530. The squares indicate our results, while the circles indicate VLBA results.

vations were carried out over an interval longer than one month and calibrators are also variable in such time scales.

Instead, we estimated 10 % of the total flux as a systematic error, and added them in quadrature to the fitting error. This is a reasonable estimate, since the amplitude calibration was done by a-priori calibration using the system temperature $T_{sys}*$ measured by the chopper-wheel method.

For checking the fairness of amplitude calibration, we also analyzed NRAO 530 which was observed simultaneously as an amplitude calibrator. We confirmed that the r.m.s. of gain solutions obtained from the amplitude self-calibration of NRAO 530 were around or less than 10 % for most epochs. Figure 2.21 shows the core-flux variations of NRAO 530. These core-fluxes were obtained by the elliptical Gaussian-fitting to the visibilities and their errors were estimated in the same way as Sgr A*. In addition to VERA data, Figure 2.21 shows the core-fluxes obtained from data of the Boston University blazar monitoring program with the VLBA[2]. These data were obtained by model-fitting to calibrated visibilities. Figure 2.21 suggests the trend of core-flux variation obtained from VERA and VLBI is presumably consistent, though both observations were not carried out simultaneously.

2.3.4 *Calculation of Intrinsic Size*

After model fitting, we calculated the intrinsic size of Sgr A* using the total flux and the major and minor axes sizes obtained from Gaussian-fitting. We estimated

---

[2] `http://www.bu.edu/blazars/VLBAproject.html`

the major axis intrinsic size based on a traditional method used in previous VLBA observations (Lo et al., 1998; Bower et al., 2004, 2006; Falcke et al., 2009). We adopted the scattering law of Falcke et al. (2009), in which the scattering size ϕ_{scatt} was given by

$$\phi_{\mathrm{scatt}} = 1.36\,\mathrm{mas} \times \left(\frac{\lambda}{1\,\mathrm{cm}}\right)^2, \tag{2.5}$$

yielding ϕ_{scatt} of $\sim$ 661 μas at 43.0 GHz. Assuming that the intrinsic brightness distribution of Sgr A* is elliptical Gaussian, the intrinsic size ϕ_{int} is given by

$$\phi_{\mathrm{int}} = \sqrt{\phi_{\mathrm{maj}}^2 - \phi_{\mathrm{scatt}}^2}. \tag{2.6}$$

We note that here the scattering effect is assumed to be the same throughout all the epochs. To convert units of intrinsic size ϕ_{int}, one can refer to following relation between angular scale in μas and Schwarzchild radius $\mathrm{R_s}$ given by

$$1\,\mathrm{R_s} = 9.87\,\mu\mathrm{as} \times \left(\frac{D}{8\,\mathrm{kpc}}\right)^{-1} \left(\frac{M}{4 \times 10^6\,M_\odot}\right). \tag{2.7}$$

2.3.5 *VLBA data of Sgr A**

To trace the variation of Sgr A* better, we combined the results of previous VLBA observations with our results. We calculated the major axis intrinsic size from data in the same way as §2.4. We show the data in Table 2.4. These data are taken from the following references: Bower & Backer (1998a); Lo et al. (1998); Bower et al. (2004); Shen et al. (2005); Lu et al. (2011). Bower et al. (2004) and Shen et al. (2005) used the closure-amplitude method for fitting Gaussian-models to visibilities. The use of closure amplitude discards the information of total flux. Hence, the only available parameters are the sizes of major and minor axis. Bower & Backer (1998a), Lo et al. (1998) and Lu et al. (2011) used visibility fitting. Thus, parameters of both the sizes and total flux are available. To consider the systematic error of *a priori* amplitude calibration, we add 10 % of the total flux to the error originally reported. In Table 3, we also present intrinsic sizes that are calculated in the same manner as those in §3.2. We note that observed on September 9 of 1994 and February 14 are obtained by the same observation, but analyzed by different methods (Bower & Backer, 1998a; Bower et al., 2004; Shen et al., 2005). We adopt all the data here.

Table 2.4: The source structure derived from previous VLBA observations.

Epoch (yyyy-mm-dd)	Freq. (GHz)	$S_{\rm total}$ (Jy)	$\phi_{\rm maj}$ (μas)	$\phi_{\rm int}$ (μas)	$R_{\rm int}$ ($\rm R_g$)	Reference and comment
1994-04-26	43.151		720^{+10}_{-10}	296^{+24}_{-24}	$30.0^{+2.5}_{-2.5}$	Shen et al. (2005)
1994-09-29	43.151	$1.28^{+0.16}_{-0.16}$	762^{+38}_{-38}	387^{+75}_{-75}	$39.2^{+7.6}_{-7.6}$	Bower & Backer (1998a)
1994-09-29	43.151		720^{+10}_{-10}	296^{+24}_{-24}	$30.0^{+2.5}_{-2.5}$	Shen et al. (2005)
1997-02-01	43.2	$1.03^{+0.10}_{-0.10}$	700^{+10}_{-10}	247^{+28}_{-28}	$25.0^{+2.9}_{-2.9}$	Lo et al. (1998)
1997-02-14	43.213		728^{+16}_{-11}	319^{+12}_{-8}	$32.3^{+1.2}_{-0.8}$	Bower et al. (2004)
1997-02-14	43.213		710^{+10}_{-10}	275^{+26}_{-26}	$27.9^{+2.6}_{-2.6}$	Shen et al. (2005)
1999-03-23	43.135		710^{+10}_{-10}	269^{+26}_{-26}	$27.3^{+2.7}_{-2.7}$	Shen et al. (2005)
1999-04-24	43.135		690^{+10}_{-10}	211^{+33}_{-33}	$21.4^{+3.3}_{-3.3}$	Shen et al. (2005)
1999-05-23	43.1		713^{+12}_{-9}	275^{+11}_{-8}	$27.8^{+1.1}_{-0.8}$	Bower et al. (2004)
2001-07-12	43.2		725^{+22}_{-12}	311^{+17}_{-9}	$31.5^{+1.7}_{-0.9}$	Bower et al. (2004)
2001-07-29	43.2		770^{+30}_{-18}	405^{+19}_{-12}	$41.0^{+1.9}_{-1.2}$	Bower et al. (2004)
2001-08-05	43.2		704^{+64}_{-43}	258^{+58}_{-39}	$26.2^{+5.9}_{-4.0}$	Bower et al. (2004)
2002-04-15	43.2		708^{+17}_{-13}	269^{+15}_{-11}	$27.2^{+1.5}_{-1.1}$	Bower et al. (2004)
2002-05-03	43.2		708^{+6}_{-4}	269^{+5}_{-4}	$27.2^{+0.5}_{-0.4}$	Bower et al. (2004)
2002-05-13	43.2		709^{+9}_{-6}	272^{+8}_{-6}	$27.5^{+0.8}_{-0.6}$	Bower et al. (2004)
2004-03-08	43.175		722^{+2}_{-2}	302^{+5}_{-5}	$30.6^{+0.5}_{-0.5}$	Shen et al. (2005)
2004-03-20	43.175		725^{+2}_{-2}	309^{+5}_{-5}	$31.3^{+0.5}_{-0.5}$	Shen et al. (2005)
2007-05-15	43.1	$2.02^{+0.22}_{-0.22}$	710^{+10}_{-10}	267^{+27}_{-27}	$27.0^{+2.7}_{-2.7}$	Lu et al. (2011)
2007-05-16	43.1	$1.59^{+0.17}_{-0.17}$	720^{+10}_{-10}	292^{+25}_{-25}	$29.6^{+2.5}_{-2.5}$	Lu et al. (2011)
2007-05-17	43.1	$1.99^{+0.21}_{-0.21}$	720^{+10}_{-10}	292^{+25}_{-25}	$29.6^{+2.5}_{-2.5}$	Lu et al. (2011)
2007-05-18	43.1	$1.61^{+0.17}_{-0.17}$	710^{+10}_{-10}	267^{+27}_{-27}	$27.0^{+2.7}_{-2.7}$	Lu et al. (2011)
2007-05-19	43.1	$1.86^{+0.20}_{-0.20}$	710^{+10}_{-10}	267^{+27}_{-27}	$27.0^{+2.7}_{-2.7}$	Lu et al. (2011)
2007-05-20	43.1	$1.66^{+0.18}_{-0.18}$	720^{+10}_{-10}	292^{+25}_{-25}	$29.6^{+2.5}_{-2.5}$	Lu et al. (2011)
2007-05-21	43.1	$2.02^{+0.22}_{-0.22}$	720^{+10}_{-10}	292^{+25}_{-25}	$29.6^{+2.5}_{-2.5}$	Lu et al. (2011)
2007-05-22	43.1	$1.90^{+0.20}_{-0.20}$	720^{+10}_{-10}	292^{+25}_{-25}	$29.6^{+2.5}_{-2.5}$	Lu et al. (2011)
2007-05-23	43.1	$1.92^{+0.21}_{-0.21}$	720^{+10}_{-10}	292^{+25}_{-25}	$29.6^{+2.5}_{-2.5}$	Lu et al. (2011)
2007-05-24	43.1	$1.78^{+0.19}_{-0.19}$	680^{+10}_{-10}	172^{+40}_{-40}	$17.4^{+4.0}_{-4.0}$	Lu et al. (2011)
2007-05-15∼24	43.1	$1.79^{+0.19}_{-0.19}$	710^{+10}_{-10}	267^{+27}_{-27}	$27.0^{+2.7}_{-2.7}$	average of Lu et al. (2011)

Table 2.5: The basic properties of CLEAN images.

Epoch (Name)	Epoch (DOY)	Epoch (yyyy-mm-dd)	Freq. (GHz)	θ_{maj} (μas)	θ_{min} (μas)	PA (°)	S_{clean} (Jy)	I_{peak} (Jy beam^{-1})	σ_I (Jy beam^{-1})
(a)	2005-294	2005-10-21	43.061	1098	642	6.51	0.85	0.64	0.02
(b)	2006-079	2006-03-20	43.061	1013	619	4.82	0.63	0.46	0.01
(c)	2006-109	2006-04-19	43.061	1078	609	-5.18	0.63	0.44	0.01
(d)	2006-308	2006-11-04	43.061	1126	581	-11.13	0.90	0.62	0.01
(e)	2007-073	2007-03-14	43.061	1079	683	1.69	0.78	0.59	0.02
(f)	2007-093	2007-04-03	43.061	1277	568	-15.91	0.93	0.64	0.02
(g)	2007-264	2007-09-21	43.061	1168	591	-12.39	0.75	0.52	0.01
(h)	2008-076	2008-03-16	43.061	1327	540	-21.67	0.60	0.42	0.01
(i)	2008-085	2008-03-25	43.061	1087	580	-14.46	0.62	0.42	0.01
(j)	2008-310	2008-11-08	43.061	1122	608	-14.15	0.95	0.66	0.01

2.4 RESULTS

2.4.1 *Clean Images*

Figure 2.22 shows the clean images for all the 10 epochs. The dynamic ranges of the images are more than 30 and the averaged value is about 50. As shown in Figure 2.22, Sgr A* has only one component which has nearly symmetric structure. One can also see the symmetry of Sgr A* structure from nearly zero closure phase in Figure 2.20. One of the most remarkable results in Figure 2.22 is that this feature has not changed for about 3 years. In other words, we did not detect ejection of knot-like components through all epochs (although Sgr A* certainly exhibits flux variation during the observed period).

We show in Table 2.5 the basic properties of these images, such as the size and position angle of the synthesized beam, the cleaned flux S_{clean}, the peak brightness I_{peak} and the image r.m.s σ_{I}. One can obviously see the existence of time variations of flux S_{clean}. On the other hand, non-detection of any knot-like structure suggests that the flux variation is associated with the flux change of the single component.

In previous studies, super-resolution images with restored circular beam are frequently used for examining the resolved structure. We also show the super-resolution images in the lower panels of Figure 2.22. One can see that the observed structure of Sgr A* is Gaussian-like rather than point-like. The Gaussian-like structure of Sgr A* is well-explained by the effect of the interstellar scattering (Goodman & Narayan, 1989; Narayan & Goodman, 1989). Sgr A* is well resolved along the east-west direction, since the size of scattering disk along the east-west direction is larger than the north-south direction (Bower et al., 2004). The size of

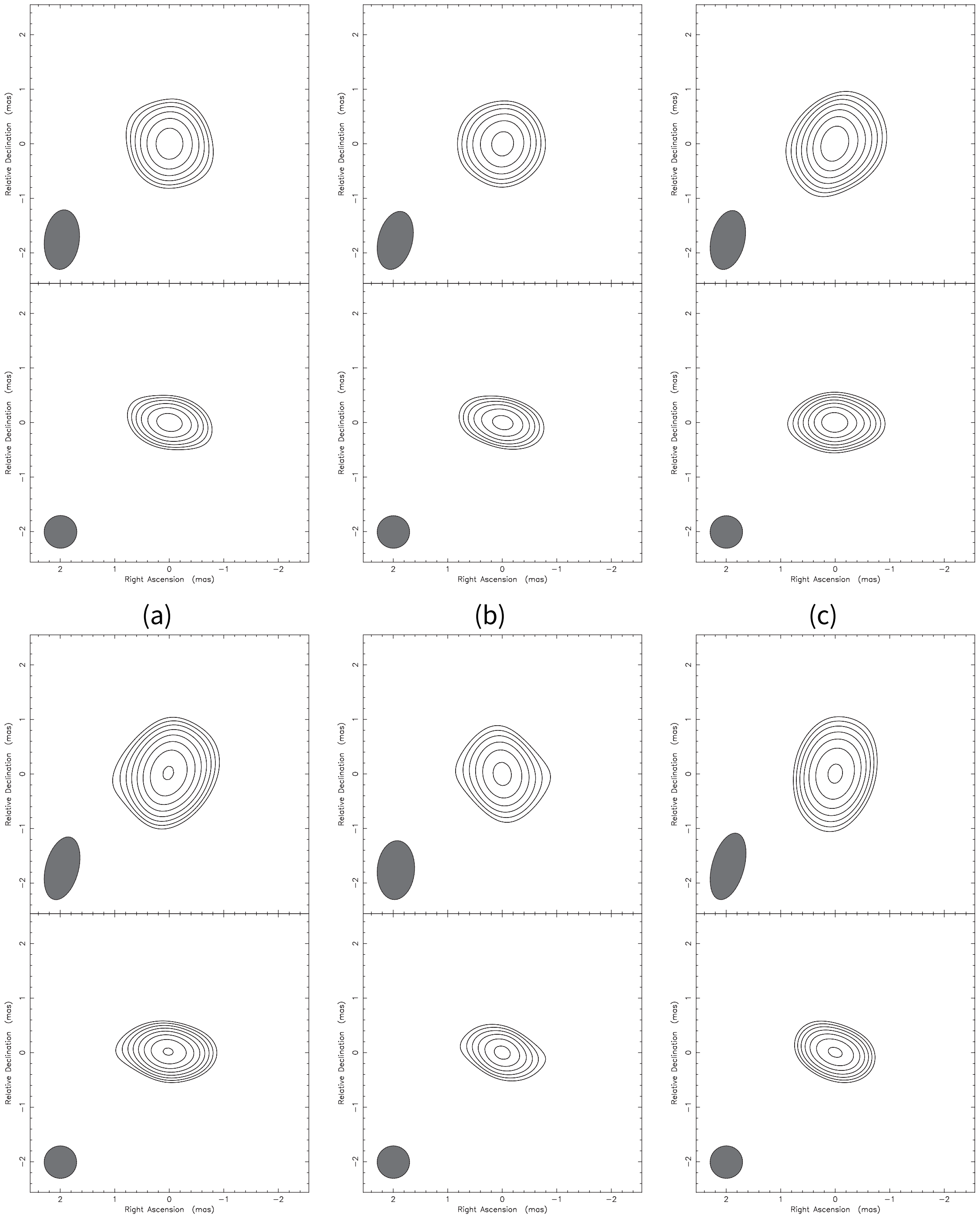

(a) (b) (c)

(d) (e) (f)

Figure 2.22: The uniform weighted clean images of Sgr A* (top panels). (a)-(j) are names of epochs shown in Table 2.5.Bottom panels are super-resolution images a restored circular beam with size of 0.6 mas. The contours are plotted at the level of $5S_{\rm rms} \times \sqrt{2}^{n}$ $(n = 1, 2, 3, \ldots)$.

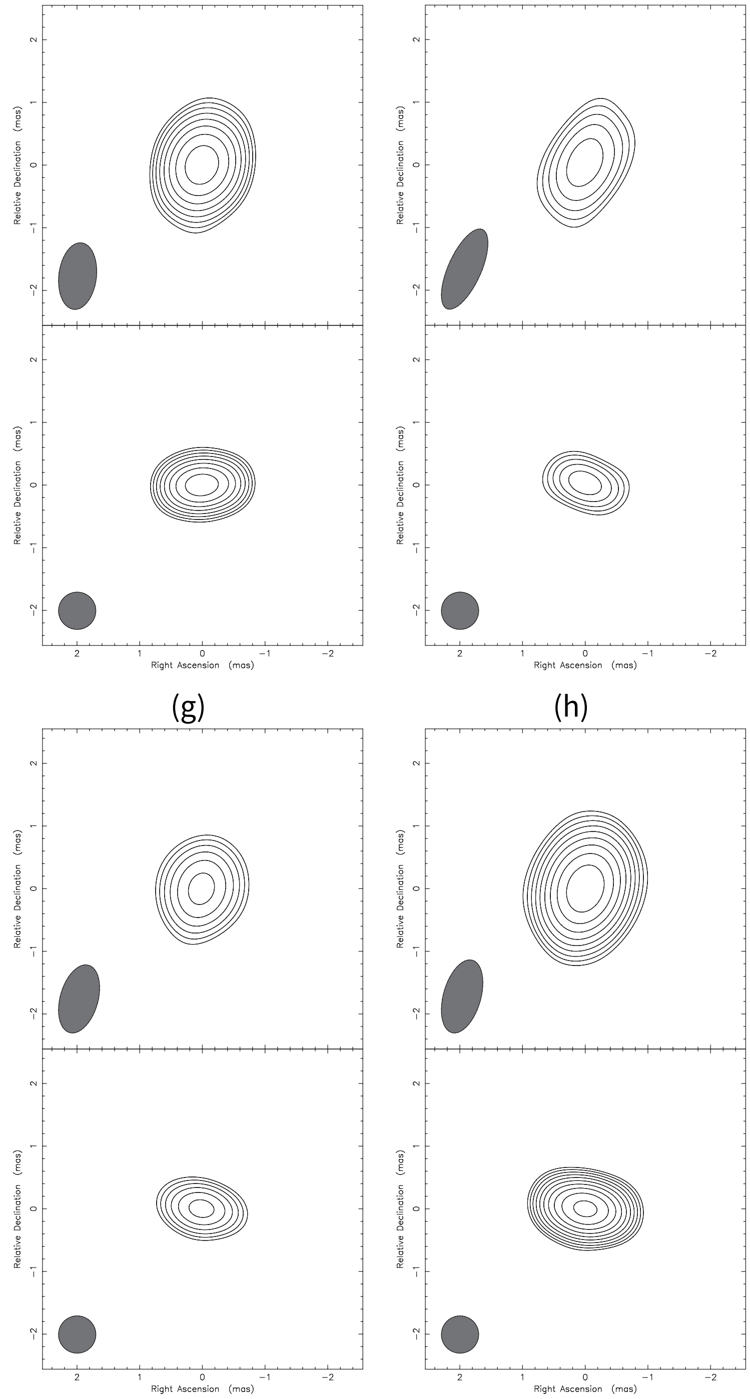

(g) (h)

(i) (j)

Figure 2.22: —Continued.

Table 2.6: The source structure obtained from Gaussian-fitting.

Epoch (Name)	$S_{\rm total}$ (Jy)	$\phi_{\rm maj}$[a] (μas)	$\phi_{\rm min}$[a] (μas)	PA[a] (°)	$\phi_{\rm int}$[b] (μas)	$R_{\rm int}$[b] (R_g)
(a)	1.0 ± 0.1	740 ± 10	<549	78^{+1}_{-1}	340 ± 20	34 ± 2
(b)	0.8 ± 0.1	760 ± 10	<507	77^{+1}_{-1}	380 ± 20	38 ± 2
(c)	0.7 ± 0.1	710 ± 20	<539	86^{+2}_{-2}	260 ± 50	26 ± 5
(d)	0.9 ± 0.1	710 ± 10	<563	82^{+1}_{-1}	260 ± 30	26 ± 3
(e)	0.8 ± 0.1	730 ± 20	<540	69^{+1}_{-1}	310 ± 50	31 ± 5
(f)	1.1 ± 0.1	700 ± 10	<639	71^{+1}_{-2}	240 ± 30	24 ± 3
(g)	0.9 ± 0.1	700 ± 10	430^{+50}_{-70}	94^{+4}_{-3}	240 ± 30	24 ± 3
(h)	0.8 ± 0.1	710 ± 10	350^{+40}_{-70}	67^{+2}_{-2}	260 ± 30	26 ± 3
(i)	0.7 ± 0.1	690 ± 10	<544	79^{+1}_{-1}	200 ± 30	20 ± 3
(j)	1.1 ± 0.1	700 ± 10	340^{+30}_{-40}	77^{+1}_{-1}	240 ± 30	24 ± 3
$\bar{X}$[c]	0.9	720	370	78	270	27
σ_X[d]	0.1	20	40	8	50	5

[a] Sizes and position angles obtained by elliptical-Gaussian-fitting to calibrated visibilities
[b] Intrinsic sizes of Sgr A*
[c] time-averages of each parameter
[d] Standard deviations of each parameter

the lowest contour in super-resolution map is about 1.8 mas in the direction of Right Ascension and about 0.6 mas in the direction of Declination.

These features are consistent with results of previous VLBA observations (Bower & Backer, 1998a; Lo et al., 1998; Lu et al., 2011). We note that the number of baselines of VERA is less than VLBA, but the size of the synthesized beam is almost the same as that of previous VLBA observations since long baseline data of VLBA observations are also flagged out because of low S/N ratio.

2.4.2 *Model-fitting Results*

In previous studies of Sgr A*, VLBI-scale source structure has been quantified by using Gaussian fitting to visibilities, since the observed Sgr A* structure is well explained by an elliptical Gaussian distribution (Bower et al., 2004; Shen et al., 2005; Lu et al., 2011). In fact, our results also show a symmetric and Gaussian-like structure consisting of a single component, as described in the previous subsection. Hence, we fitted Gaussian models directly to the calibrated visibility data with the least-square method as described in Section 2. Figure 2.23 shows their time variations. The parameters obtained from the fitting, such as total flux S_{total}, size of the major/minor axes $\phi_{\mathrm{maj}}/\phi_{\mathrm{min}}$, position angle PA and intrinsic size $\phi_{\mathrm{int}}\,/\,R_{\mathrm{int}}$ are summarized in Table 2.6. In addition to the fitting results of individual parameters, we show time-averages and standard deviations of each parameter throughout all the epochs at the bottom line of Table 2.6. As an example of Gaussian fitting, we have already shown the results for epoch (g) in Figure 2.19.

We note about the upper limits of the minor axis size of Sgr A* set in several epochs and the errors on PAs in Table 2.6. In some epochs, upper limits of the minor axis size are obtained. In these epochs, we could not detect structure elongated in the direction of the minor axis of Sgr A*. The most probable reason is the lack of spatial resolution; the major axis of the synthesized beam is oriented in the N-S direction closer to the direction of the minor axis of Sgr A* and major size of the beam is typically $\sim$ 1.2 mas, which is $\sim$ 3 times greater than typical minor axis size of Sgr A*. In addition to the lack of spatial resolution, the poor $uv-$coverage in the N-S direction probably makes the measurement of minor axis size of Sgr A* more difficult. Therefore, in these epochs, we set a half of the major axis size of the synthesized beam ($\sim$ 0.6 mas) as an upper limit of the minor axis size of Sgr A*. This upper limit (typically 0.5-0.6 mas) is reasonable, because the Gaussian distribution with the minor axis size of 0.5-0.6 mas should be resolved-out in our observations. We confirmed that if the minor axis size was 0.6 mas, fringes would have been detected only in Mizusawa-Ogasawara and Iriki-Ishigaki baselines considering the sensitivity of our observations, which is clearly inconsistent with our results. This fact strongly indicates that the minor axis size was smaller than 0.6 mas.

We successfully measured the major-axis size ϕ_{maj} through all the epochs. The time-average of ϕ_{maj} is 720 μas, which is consistent with previous VLBA observations (Bower et al., 2004; Lu et al., 2011). On the other hand, we could not determine the minor-axis size ϕ_{min} in several epochs. The time-average of ϕ_{min} and PA are about 370 μas and 78° (without using upper limit data), and also similar to previous results of VLBA. However, the minor axis size and also position angle of Sgr A* are possibly affected by synthesized beam (i.e. uv coverage and spatial resolution). Thus, it is difficult to discuss the time variation of the minor axis size and position angle. Hence, in this thesis, we concentrate on the variation of the flux and major axis size.

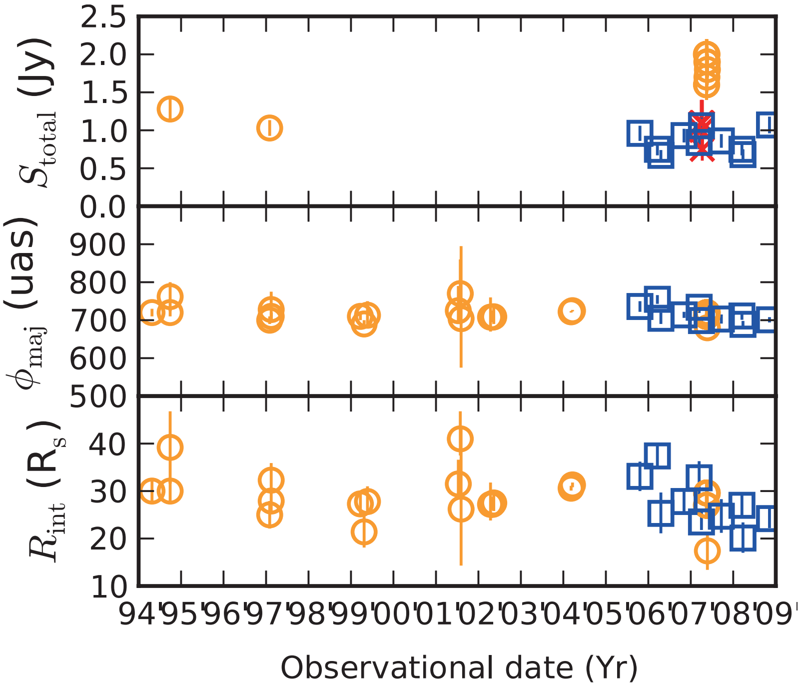

(a)

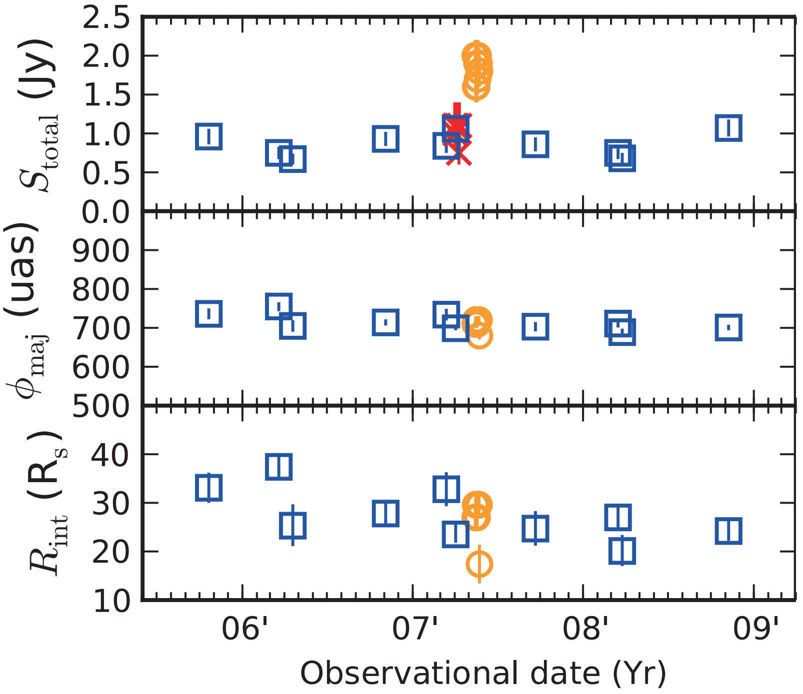

(b)

Figure 2.23: The time variations of the flux and structure of Sgr A*. From the top of figure, vertical axes are correspond to the flux, the size of Major axis and the intrinsic size. The squares are our results, while the circles and the crosses are VLBA results. The circled mark are the result of Yusef-Zadeh et al. (2009) and the error bar indicates the range of the intra-day variability. (a) shows all data shown in Table 2.6 and 2.4, while (b) shows VERA data and VLBA data observed around VERA epochs (2005-2008).

Remarkably, in addition to the flux variation, one can see the variation of the intrinsic size. The standard deviation of S_ν, 0.1 Jy corresponds to $\sim$ 11 % of the time-averaged flux $\bar{S}_\nu$, while that of $\phi_{\rm int}$, 50 μas corresponds to $\sim$ 19 % of the time-averaged intrinsic size $\bar{\phi}_{\rm int}$. We confirmed the significance of time variations in $S_{\rm total}$, $\phi_{\rm maj}$ and $\phi_{\rm int}$ from χ^2 tests of hypotheses of no time variation in those quantities. The error weighted averages of $S_{\rm total}$, $\phi_{\rm maj}$ and $\phi_{\rm int}$ are 0.9 Jy, 710 μas and 290 μas, resulting χ^2s based on the hypotheses are 20, 41 and 46 respectively. The χ^2 tests based on those χ^2s indicate that the hypotheses are rejected at the significance level of 5 %.

A noteworthy feature in Figure 2.23 is that the total flux of Sgr A* was flared up to about 2 Jy in May 2007 (Lu et al., 2011). They also reported that the fluxes at 22 GHz and 86 GHz are high in these epochs as well. Compared with the results of a dense monitor in Herrnstein et al. (2004), observed fluxes of Sgr A* are relatively high. In the present paper, we refer to this flaring of Sgr A* as ”the flaring event”.

Combination of our and VLBA results suggests that the duration of the flaring event was longer than 10 days and shorter than 151 days. The time-averaged flux during the flaring event is 1.79 $\pm$ 0.05 Jy. This is about 1.7 times higher than epoch (f) ($\sim$ 1 month prior to the flaring event), and also 2.1 times higher than epoch (g) ($\sim$ 6 months posterior to the flaring event). Meanwhile, the time-averaged intrinsic size during the flaring event is 267 $\pm$ 27 μas, which is consistent with those of epochs (f), (g) and the time-averaged value of our results within 1 σ level. This result indicates that the brightness temperature of Sgr A* increased during the flaring event (see §4.1).

2.5 DISCUSSION

2.5.1 *Variability of the Brightness Temperature*

The total flux and the major axis size of Sgr A* were successfully measured. They can be used for discussing the possibility of the variation in the brightness temperature T_b, which is calculated by

$$T_b = \frac{2c^2}{k_B\nu^2}\frac{S_{\rm total}}{\pi\phi_{\rm int\_maj}\phi_{\rm int\_min}} \tag{2.8}$$

$$= 9.54\times10^8\,{\rm K}\times\left(\frac{\nu}{43\,{\rm GHz}}\right)^{-2} \left(\frac{S_{\rm total}}{1\,{\rm Jy}}\right)\left(\frac{\phi_{\rm maj\_int}}{1\,{\rm mas}}\right)^{-1}\left(\frac{\phi_{\rm min\_int}}{1\,{\rm mas}}\right)^{-1}. \tag{2.9}$$

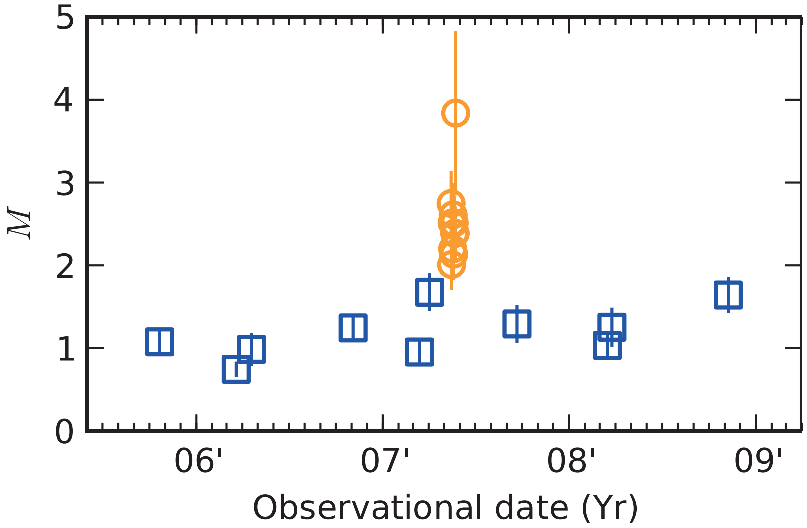

Figure 2.24: The time variations of the multiply of the intrinsic-minor-axis size and the brightness temperature.

$\phi_{\mathrm{int\_maj}}$ and $\phi_{\mathrm{int\_min}}$ are intrinsic sizes of the major and minor axes. Here, the brightness distribution is set to be an uniform elliptical disk. Its diameter is set to be FWHM sizes of the elliptical Gaussian model, ant its total flux equals to that of the elliptical Gaussian model.

Since the minor-axis size was not determined in many epochs, we define the multiple of the brightness temperature and the minor axis intrinsic size given by

$$M \equiv \left(\frac{T_b}{10^9\mathrm{K}}\right)\left(\frac{\phi_{\mathrm{min\_int}}}{260\,\mu\mathrm{as}}\right) \tag{2.10}$$

$$= 3.67\left(\frac{\nu}{43\,\mathrm{GHz}}\right)^{-2}\left(\frac{S_{\mathrm{total}}}{1\,\mathrm{Jy}}\right)\left(\frac{\phi_{\mathrm{maj\_int}}}{1\,\mathrm{mas}}\right)^{-1}, \tag{2.11}$$

where the normalization factor of 260 μas for the intrinsic-minor-axis size is referred to from averaged value of VLBA measurements in Bower et al. (2004). We show the time variation in M in Figure 7. If the brightness temperature does not varies with time, the variation in M should originate from that in the intrinsic minor size. Here, we assume the time-averaged value of the intrinsic-minor-axis size for our VERA data to be 260 μas.

In our VERA results (without VLBA data), the constant brightness temperature requires variation in observed-minor-axis size ranged from $\sim$ 190 μas to $\sim$ 415 μas. It would be difficult to detect such a variation with VERA considering the beam size along the N-S direction. Thus, the variation in M could be explained only by the variation in the intrinsic-minor-axis size.

On the other hand, the combination of VERA data and VLBA data requires the increase in the brightness temperature at the flaring event. The error-weighted averages of M are 1.0 for our VERA data and 2.3 for VLBA data at the flaring event. If there was no time variation in the brightness temperature through our VERA data and the flaring event, the observed-minor-axis size of $590\ \mu$as should have been required at the flaring event. However, Lu et al. (2011) reported the time-averaged minor axis size of $400 \pm 10\ \mu$as at the flaring event and inconsistent with predicted observed-minor-axis size of $590\ \mu$as. Thus, the increase in M at the flaring event cannot be explained only by variation of the intrinsic-minor-axis size, and requires the increase in the brightness temperature.

2.5.2 *The Origin of Variability in the Brightness Temperature*

2.5.2.1 *Possibilities of an Extrinsic Origin*

The variation of the total flux and intrinsic size of Sgr A* most likely requires the variation of the brightness temperature. Before discussing this, here, we comment on the possibility of interstellar scattering as an origin of the time variations of Sgr A*. Since the detailed structure of the scattering medium is still unknown, it is not possible to totally rule out the effect of interstellar scattering. The scattered image of Sgr A* is thought to be created by turbulent plasma along the line of sight. A typical time scale for the scattering is given by refractive time scale, which is determined by relative motions of the observer, turbulent plasma and background source. The refractive time scale for Sgr A* is estimated to be $\sim 0.5\ \lambda^2$ year cm^{-2} , given a relative velocity of 100 km s^{-1} (Goodman & Narayan, 1989; Bower et al., 2004). At 43 GHz, the refractive time scale becomes $\sim$ 3 months. Most of our observations are separated by periods longer than 3 months, implying that the time variations of the total flux may be partly caused by refractive changes. However, epochs (e), (f) and the flaring event reported by Lu et al. (2011) are separated by only a month (see Figure 2.23). Furthermore, Lu et al. (2011) reported that the spectral index became harder than previous results. In simple models of interstellar scattering, the modulation index of the flux density decreases with frequency in a strong scattering regime (Rickett, 1990). This would lead to an anti-correlation between spectral index and mm-flux. Therefore, the flaring event is inconsistent with the effects of simple models for interstellar scintillation. Thus, observed variation of brightness temperature is likely intrinsic. In the following subsections, assuming that the flaring event in Lu et al. (2011) is intrinsic, we discuss possible intrinsic origins of the flaring event in 2007.

2.5.2.2 *Models with Jets, Expanding Plasmon or Hot Spot*

Here, we discuss whether the brightness temperature variation associated with the flaring event can be explained by models suggested for intra-day variations. In previous studies, several models were proposed as the origin of intra-day variation, such as models with jet (Falcke et al., 2009; Maitra et al., 2009), expanding plasmon model (Yusef-Zadeh et al., 2008, 2009) and orbiting hot-spot model (Broderick & Loeb, 2006; Eckart et al., 2006, 2008).

Both VERA and VLBA have not detected any additional components in the Sgr A* images around the flaring event in 2007. From this fact, an ejection of a sub-relativistic or relativistic bright component (Falcke et al., 2009; Maitra et al., 2009) would be ruled out in this case. The size of Sgr A* at 43 GHz is about 0.7 mas along the major axis, corresponding to a light crossing time of $\sim$ 46 min. If the flaring event is owing to an ejection of an outflow or a jet, the velocity of the new component must be less than 0.003 c so that the new component cannot be resolved from the persistent component within 10 days. This velocity upper-limit is significantly smaller than the predicted value of 0.1c in Falcke et al. (2009).

The expanding plasmon model (van der Laan, 1966), in which creation of an expanding plasma blob causes flux variation, predicts an expansion velocity comparable to the upper limit of 0.003 c in case of the intra-day variation of Sgr A* (Yusef-Zadeh et al., 2008, 2009; Li et al., 2009). However, when the expansion velocity is comparable to 0.003 c, the adiabatic cooling time-scale is shorter than a day. If the expansion velocity is smaller than 0.003 c, the adiabatic cooling time-scale can be longer. However, in such a case, the synchrotron cooling dominates the adiabatic cooling. According to Marrone et al. (2008), the synchrotron cooling time-scale is given by

$$t_{\rm syn} = 39\,{\rm hrs}\,\left(\frac{\nu}{86\,{\rm GHz}}\right)^{-1/2}\left(\frac{B}{10\,{\rm G}}\right)^{-3/2}. \tag{2.12}$$

In previous studies, typical magnetic-field strength is estimated to be around or larger than 10 G (Yusef-Zadeh et al., 2008, 2009; Li et al., 2009). If the magnetic-field strength of 10 G is adopted, the flux decay time-scale at 86 GHz is much shorter than 10 days, which contradicts the results of Lu et al. (2011).

The observed VLBI structure presumably does not favor the expanding plasmon model. As described in Section 3, the total flux of 22 GHz also increased in the flaring event (Lu et al., 2011). If the expanding plasmon is the origin of the flaring event, this hot plasma should be generated outside of the 22-GHz photosphere. A typical intrinsic size of Sgr A* is 74 R_S or 0.73 mas at 22 GHz (Falcke et al., 2009). If there is a bright component outside of the radio-photosphere at 22 GHz, its should be resolved in VLBI maps at 43 GHz or 86 GHz, being inconsistent with the results in the present thesis. For the same reason, it is unlikely that the flux increase is caused by an orbiting hot spot (Broderick & Loeb, 2006; Meyer et al., 2006a; Trippe et al., 2007; Eckart et al., 2006, 2008; Li et al., 2009).

In summary, the models with new components emerged in optically-thin regions would not be able to explain the flaring event. Finally, we note that the persistent jet model (Falcke & Markoff, 2000; Yuan et al., 2002; Markoff et al., 2007) is not ruled out. Most likely, it is difficult to explain such a flux variation by newly emerged components, but it could be explained assuming that, for example, the flux variation is owing to the variation of the photosphere of the jet core.

2.5.2.3 *Models with RIAF disk*

The models with additional bright components would be not suitable for explaining the flaring event. Hence, the flaring event is likely to be associated with a brightness increase of the photosphere. Compared with the light crossing time and Keplerian orbital period, the flaring event had much longer duration. This fact suggests that the flaring event is likely owing to an event that establishes a new steady state in Sgr A*'s accretion disk. The existence of the high density state of Sgr A* is also suggested by Herrnstein et al. (2004) based on the preliminary bimodal distribution of flux density. Moreover, recent Event Horizon Telescope observations (Fish et al., 2011) found also such an establishment of new steady state with higher brightness temperature at 1.3 mm. Thus, the flaring event may be possibly caused by such a new steady state.

According to accretion disk models, an electron energy distribution and its spatial dependency are crucial for determining the radio emission of Sgr A*. However, the detailed properties of these have been unclear. For instance, some models succeeded in explaining the radio spectrum of Sgr A* by emission from thermal electrons (Kato et al., 2009), while other models fail to explain the radio spectrum of Sgr A* using only thermal electrons (Mościbrodzka et al., 2009) and need non-thermal electrons (Yuan et al., 2003; Broderick et al., 2009, 2011). In fact, recent theoretical studies imply that true electron distribution functions contain non-thermal components (Riquelme et al., 2012). Thus, at present we should consider both thermal and non-thermal electrons for the radio emission of Sgr A*.

Thermal electrons are probably not suitable for explaining the flaring event based on a self-similar RIAF model. If the flaring event is established by emission from thermal electrons, an increase in brightness temperature means increase in the electron temperature, since thermal synchrotron emission at 43 GHz is thought to be optically thick. According to studies of self-similar ADAF model (Mahadevan, 1997), an electron temperature T_e in ADAF has a dependency of $\propto \dot{m}^{-1/14}$, where $\dot{m}$ is a mass accretion rate. This dependency is not changed even in the self-similar ADIOS model (see Eq.(A.95) in Appendix A). Thus, an increase in the electron temperature needs a larger decrease in the mass accretion rate. On the other hand, because the luminosity of a RIAF disk is proportional to $\sim \dot{m}^2$ (Kato et al., 2008), the radio flux should decrease as the mass accretion rate decreases. This is inconsistent with our observational results that both the brightness temperature and the total flux increased at the flaring event. Thus, based on theoretical studies of self-similar RIAF, thermal electron origin is not favored. However, since the electron temperature profile, which seriously affects the radio emission, is poorly constrained, our results might be explained by a new steady electron temperature profile, for instance, owing to standing shock in accretion disk (Nagakura & Takahashi, 2010). Moreover, the recent numerical GRMHD simulations suggest that a scaling law between the radio flux and the mass accretion rate is slightly different from that of self-similar RIAF model (Mościbrodzka et al., 2012). Future numerical studies might explain this flaring event with only thermal electrons.

Non-thermal electrons could be the origin of that. Recent axis-symmetric particle-in-cell (PIC) simulation of the collision-less magnetic-rotational-instability (MRI) shows that MRI in RIAF causes magnetic re-connections and that non-thermal components can be produced by magnetic re-connections (Riquelme et al., 2012). However, the detailed production mechanism of stationary non-thermal components has been unclear. At least, a single event of electron acceleration is not favored (§4.2.1), but the mechanism of continuous injection of accelerated electrons should be required. A standing shock in the accretion disk (Nagakura & Takahashi, 2010) might explain continuous acceleration of electrons.

In summary, as the origin of the flared emission at the flaring event, thermal electrons are not favored based on a self-similar RIAF model. However, an establishment of a new steady electron temperature profile or future numerical GRMHD simulation might explain the flaring events. Non-thermal electrons could explain the flaring event assuming a continuous production mechanism of non-thermal electrons such as a standing shock in accretion disk. Simultaneous measurements of detailed radio spectra varied from cm to sub-mm wavelengths would be helpful to constrain the properties of electron distribution at the flaring event.

2.6 SUMMARY

We presented the results of multi-epoch VERA observations of Sgr A* at 43 GHz performed from 2005 to 2008. Observed images showed that Sgr A* has only one component for about 3 years and we did not detect any significant structural changes such as creation of new jet components through all epochs. Based on the analyses with Gaussian fitting to the observed visibilities, we detected time variations of the total flux and the intrinsic size. By combining the results of VLBA and VERA observations, we found the flaring events at least longer than 10 days. Furthermore, we have succeeded in determining the intrinsic size before/after the flaring event. Our measurements indicate that the intrinsic sizes remained unchanged within 1 σ level from the sizes before/after the flaring event, indicating that the brightness temperature of Sgr A* increased at the flaring event.

The flaring event of Sgr A* in 2007 occurred within one month, which is less than the typical reflective time-scale of interstellar scattering at 43 GHz. Moreover, the correlation between spectral index and flux densities reported in Lu et al. (2011) cannot be explained from simple models of interstellar scattering. Thus, the flaring event is likely to be intrinsic. Considering the features of the observed images and the cooling time-scale of electrons, it is unlikely that the flaring event is associated with an ejection of relativistic component or a temporal one-shot plasma heating such as an expanding plasma blob or a hotspot orbiting around the central black hole. Thus, the flaring event is likely to be associated with a brightness increase of the photosphere. Following self-similar ADAF (Mahadevan, 1997), our results do not favor the change of thermal electron temperature as the origin. To explain the flaring event, a new mechanism heating electrons continuously for much longer than orbital periods of accretion disk, such as a standing shock in an accretion flow. In future, simultaneous measurements of the detailed radio spectra varying from cm to sub-mm wavelengths would be helpful to constrain the property of electron distribution at the flaring event.

3

EVENT-HORIZON-SCALE STRUCTURE OF M87 AT THE ENHANCED VERY-HIGH-ENERGY γ-RAY STATE IN 2012

3.1 REVIEW: THE RADIO GALAXY M 87

M87 (Virgo A, 3C 274, NGC 4486) is the giant elliptical radio galaxy located at the center of the Virgo cluster. M87 hosts *the first extragalactic jet* discovered almost 100 years ago (Curtis, 1918), which is the most extensively studied AGN jet in the last century as the "*Prototype*" (e.g. Biretta & Meisenheimer, 1993) and "*Rosetta Stone*" (e.g. Nakamura & Asada, 2013b) of the relativistic jet. In this section, we review various properties of M87.

3.1.1 *Uniqueness of M87: the Rosetta Stone of the Relativistic Jet*

3.1.1.1 *The Prototype of the Relativistic Jet*

After the discovery of a curious "ray" on a photographic plate of M87 (Curtis, 1918), it took more than 30 years for the strong radio source Virgo A (3C 274) to be discovered (Bolton et al., 1949) and identified as a counter part of M87 (Baade & Minkowski, 1954). Baade (1956) confirmed the synchrotron emission process can provide a common origin for both radio and optical continuum radiation. In the sixties or later, it became more and more obvious that the jet is a predominant source of the radio emission from M87.

Fanaroff & Riley (1974) classified M87 as a FR I type radio source based on its edge-darkened morphology with plume-like lobes and luminosity of $P_{178\,\mathrm{MHz}} = 1.0 \times 10^{25}$ W Hz^{-1}. The jet is bright enough across the whole electromagnetic spectrum, leading that the jet in M87 has been a sort of the first detected source at many bands. Namely, M87 is the first extragalactic X-ray source to be identified (Bradt et al., 1967), and the first non-blazar AGN detected in very-high-energy (VHE) energies over 100 GeV (Aharonian et al., 2003). This makes M87 to be the most attractive sample to investigate the nature of the extragalactic jet and then intensively monitored at radio, optical and X-ray over the last several decades. In the last decade, M87 was discovered in γ-ray regime at MeV, GeV and TeV energies after the appearance of high sensitivity telescopes such as the Fermi γ-ray space telescope in GeV regime and the ground Cherenkov telescopes (VERITUS, MAGIC and HESS) in TeV regime. In particular, M87 is currently one of four radio galaxies detected at TeV energies with weak or moderate beaming compared to other VHE AGNs dominated by BL Lac objects. Since the radio galaxy has a relatively large viewing angle, it has a great advantage that finer structure in the jet can be observed with high resolution observations than blazars. This indicates that M87 is one of the most important sources to investigate the nature of the broadband emission from the relativistic jet in connection with its structure resolved at various wavelengths.

3.1.1.2 *Highly Massive Black Hole at the Center*

The proximity of M87 (16.7 Mpc; Jordán et al., 2005; Blakeslee et al., 2009) enables accurate mass measurements of the central SMBH using dynamics of stars and gasses at its center. Presence of the SMBH with a mass of $\sim (3-5) \times 10^9\ M_\odot$ was first suggested in Sargent et al. (1978) and Young et al. (1978) based on the surface brightness and stellar velocity dispersion profiles. At the present, much improved stellar-dynamical mass measurements were carried out in recent works of Gebhardt & Thomas (2009) and Gebhardt et al. (2011), reporting $M_{\mathrm{BH}} = (6.6 \pm 0.4) \times 10^9\ M_\odot$.

In addition to the stellar-dynamical M_{BH} measurements, there are also three gas-dynamical measurements for the SMBH in M87. Hubble Space Telescope (HST) observations revealed a presence of a rapidly rotating ionized gas disk at its center (Ford et al., 1994). The black hole mass was estimated to be $\sim (2-4) \times 10^9\ M_\odot$ based on the emission-line kinematics as a rotating disk (Ford et al., 1994; Harms et al., 1994; Macchetto et al. , 1997). The most recent HST observations measured the gas-dynamical mass of $M_{\rm BH} = (3.5^{+0.9}_{-0.7} \pm 0.4) \times 10^9\ M_\odot$ (Walsh et al., 2013) that differs from the stellar-dynamical mass by a factor of 2.

Origin of the difference in measured $M_{\rm BH}$ values between two independent methods has not been clear so far, but nevertheless the mass of the SMBH is an order of $\sim 10^9\ M_\odot$. This puts M87 at the extreme high-mass end of the $M_{\rm BH}$–host galaxy relations (e.g. Kormendy & Ho, 2013). Investigation of the central SMBH in M87 would be important also in the context of the evolutionary scheme of the SMBH in relation to that of the host galaxy.

In this thesis, we adopt a black hole mass of 6.2×10^9 M$_\odot$[1] following Gebhardt et al. (2011) and a distance of 16.7 Mpc following Blakeslee et al. (2009) along with Hada et al. (2011) and Doeleman et al. (2012).

3.1.1.3 *The Largest Angular Size of the SMBH among Known Relativistic Jets*

The proximity and the large $M_{\rm BH}$ of M87 provide an angular size of $R_{\rm s} \sim 3-7$ μas for the central SMBH, which is the secondary largest among known black hole candidates (see Table 1.3). In particular, this angular size of $R_{\rm s}$ is the greatest in the (obvious) relativistic jets in the Universe, since the largest SMBH in Sgr A* does not have any prominent jet features at least on scales of $\gtrsim 10^2\ R_{\rm s}$ (see §2.1.5). M87 provides an unique opportunity to study the relativistic jet on finest scales in the Universe.

In particular, M87 is one of two main targets of the Event Horizon Telescope (EHT; §1.3). EHT is expected to achieve a direct imaging of the event-horizon of the SMBH at 1.3 mm in the next several years, which is crucial to test the Einstein's general relativity in a strong gravity regime. In addition, M87 is particularly important for understanding the formation process of the relativistic jet and high energy particles in the EHT era in the next decade, since it would be tightly related with the event-horizon-scale structure in the vicinity of the SMBH. M87 will be physically and astrophysically the most important and attractive source in the next decades.

3.1.2 *M87 as an AGN: Low Luminosity AGN*

Despite its huge black hole mass, M87 is not a luminous source as an AGN. The total nuclear bolometric luminosity is estimated to be $L_{\rm bol} \lesssim 10^{42}$ erg s^{-1} (e.g. Biretta et al., 1991; Owen et al., 2000; Whysong & Antonucci, 2004), corresponding

---

[1] This black hole mass is recalculated for a distance of 16.7 Mpc.

to $L_{\rm bol} \lesssim 10^{-5} - 10^{-6} L_{\rm edd}$ in an extremely sub-Eddington regime. A strong mid-infrared emission was not detected from the center of M87 (e.g. Perlman et al., 2001b), suggesting that M87 does not have a dusty obscuring region as seen in LLAGNs with extremely sub-Eddington luminosities (see §1.1.2.4 and Ho (2008)). These facts indicate that M87 is located at less luminous end of LLAGNs.

Chandra X-ray observations measure the X-ray gas temperature and density profiles, giving the Bondi accretion rate of $\dot{M}_{\rm Bondi} \sim 0.1\ M_{\odot}$ yr^{-1} and the overall energetics of $P_{\rm bondi} = 5 \times 10^{45}$ at $r_B \sim 230$ pc for accretion at the Bondi rate (Di Matteo et al., 2003). However, the central core of M87 is highly under-luminous in the X-ray band; its X-ray luminosity of $L_{\rm X} \sim 7 \times 10^{40}$ erg s^{-1} is four orders of magnitude smaller than a luminosity of $L_{\rm bondi} \sim 5 \times 10^{44}$ erg s^{-1} inferred for the Bondi accretion flow with a canonical accretion radiative efficiency of 10% (Di Matteo et al., 2003). The low bolometric and X-ray luminosity imply the existence of radiatively inefficient accretion flow (see §2.1.7.1) possibly with a substantial decrease of the mass accretion rate $\dot{M} \ll \dot{M}_B$ at the inner region of $r \ll r_B$ in the nucleus of M87.

Very recently, Kuo et al. (2014) presented polarimetric observations of M87 at 1.3 mm with Submillimeter Array (SMA), providing the first constraint on the Faraday rotation measure (RM). Kuo et al. (2014) marginally detected a change in the polarization position angles between different frequencies, which can be interpreted as a result of external Faraday rotation of polarized jet emission due to surrounding plasma inside the accretion flow. Based on the self-similar solution (ADAF: Narayan & Yi 1994, 1995; Mahadevan 1997; RIAF: Appendix A) , the mass accretion rate can be described as a function of RM (see Quataert & Gruzinov, 2000; Marrone et al., 2006; Kuo et al., 2014). RM of the M87 core is measured to be between -7.5×10^5 and 3.4×10^5 rad m^{-2}, giving the upper limit in the mass accretion rate of $\dot{M} \lesssim 9.2 \times 10^{-4}\ M_{\odot}$ yr^{-1} at $r \sim 21\ R_{\rm s}$. This value is at least two orders of magnitude smaller than the Bondi accretion rate, suggesting significant suppression of the accretion rate in the inner region of the accretion flow. Similarly to Sgr A*, the RM measurements favor ADIOS- or CDAF-type disks with substantial mass loss effects rather than the classic ADAF-type disk (see §2.1.7.1).

We finally note that M87 is most likely powered by RIAF-type disk currently, but this poses an interesting question about the energetics of the overall structure in M87. The accretion power of $P_{\rm bondi} = 5 \times 10^{45}$ at $r_B \sim 230$ pc seems to match fairly well with the time-averaged bulk kinetic power as inferred from its large-

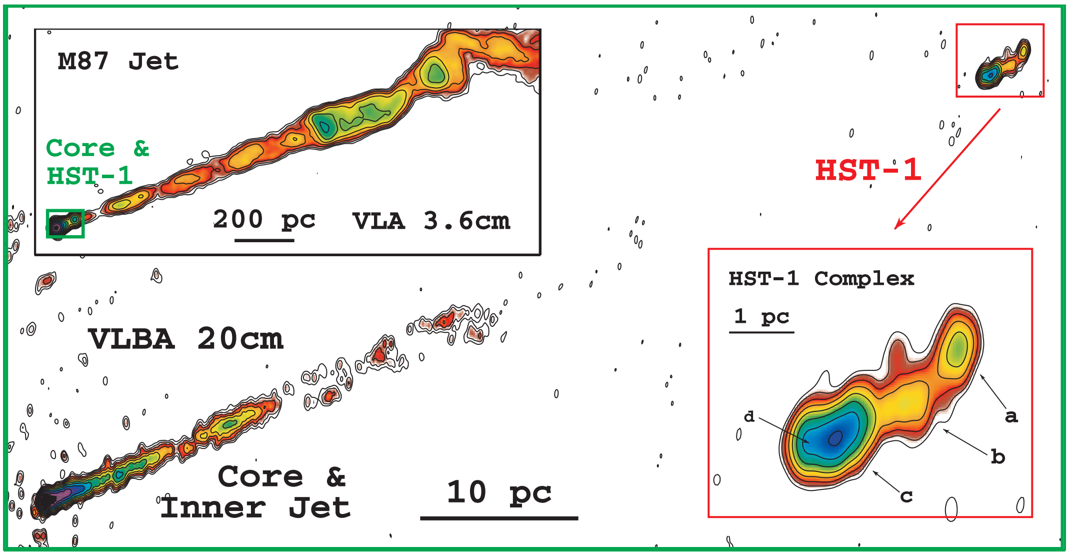

Figure 3.1: Multi-scale radio images of the relativistic jet in M87 (Cheung et al., 2007). The main panel shows the parsec-scale jet in inner ∼1”, as indicated by the corresponding green box in the left-top panel showing the large-scale jet on arcsecond scales. The bottom right panel is a zoom-in of the HST-1 complex located at ∼1” downstream of the radio core.

scale radio and X-ray morphology, ranging from $L_j \sim 3 \times 10^{42}$ erg s^{-1} (Young et al., 2002) to a few $\times 10^{44}$ erg s^{-1} (Biretta et al., 1991; Reynolds et al., 1996; Bicknell & Begelman, 1996; Owen et al., 2000). However, the current accretion rate is rather smaller than the Bondi accretion rate, indicating that the current accretion power is too small to account for the mean kinetic jet power on scales of $\sim 10^3$ pc (e.g. Rieger & Aharonian, 2012).

3.1.3 *Properties of the Relativistic Jet in Inner* 10^7 R_s

The proximity of M87 provides the finest view of the relativistic jet: 1 mas ∼ 0.081 pc ∼ 137 $R_{\rm s}$. This enables to explore the detail structure of the relativistic jet on quite broad scales ranging from a few $R_{\rm s}$ to $\gtrsim 10^8$ $R_{\rm s}$. In this subsection, we review on the typical properties of the relativistic jet in inner 10^7 $R_{\rm s}$ ∼ 5.8 × 10^3 pc ∼ 73” (Figure 3.1).

3.1.3.1 *Multi-scale View of the Jet*

On arcsecond scales, the radio emission is dominated by a well-collimated prominent jet extended for $\sim 20'' \sim 1.6$ kpc from the central nucleus (Figure 3.1). The high resolution observations with VLA on subarcsecond scales revealed that the arcsecond-scale structure is resolved into many knots (Biretta et al., 1983; Owen et al., 1989; Biretta et al., 1991). These resolved knots are referred to as D, E, F, I, A, B,

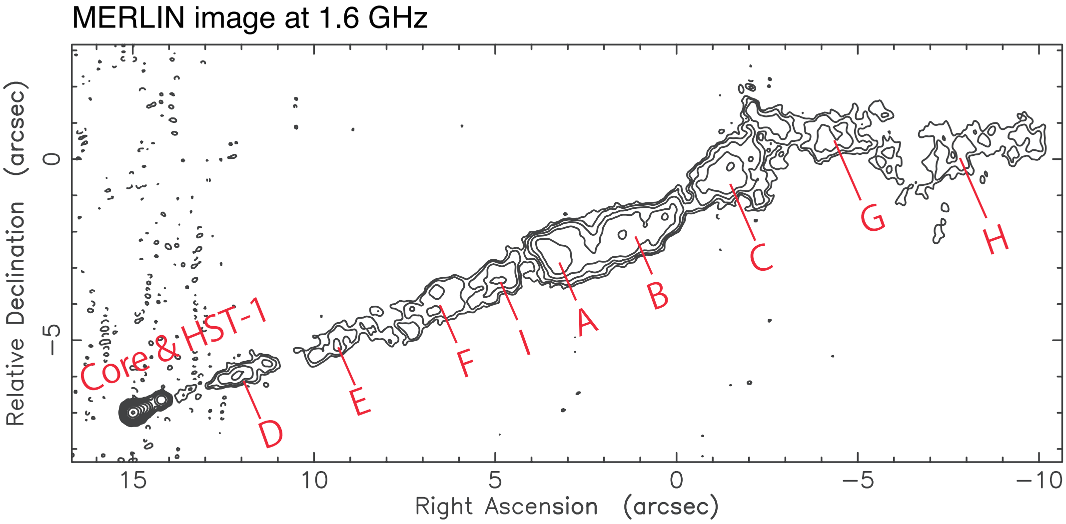

Figure 3.2: A fine view of the substructure in the arcsecond-scale jet at 1.6 GHz (edited a figure in Asada & Nakamura, 2012). The structure is well-characterized by the nuclear region with HST-1 and 8 knots named in Biretta et al. (1983) and Owen et al. (1989).

C, G that located at 3.5”, 6.0”, 8.5”, 11”, 12”, 14”, 17”, and 20” from the nucleus, respectively (Figure 3.2). HST and Chandra observations at optical and X-ray bands, respectively, found quite resemble morphology of the optical and X-ray jet with knots similar to radio ones (Perlman et al., 2001a; Marshall et al., 2002). This suggests that radio, optical and X-ray emission are synchrotron emission originating in common non-thermal electrons.

On subarcsecond scales, the jet has a peculiar knot located at the most vicinity of the radio core in the arcsecond-scale image (Figure 3.1 and Figure 3.2), which has been attracting many researchers in recent years. This knot *HST-1* was serendipitously discovered in monitoring observations with HST in 1999 on the way to the downward of the jet with a super-luminal speed of $\sim 6c$ at $\sim 1''$ (Biretta et al., 1999). It has revealed many peculiar properties in the last decade such as (i) a violent activity represented by a dramatic radio, optical, X-ray and VHE γ-ray flare with an ejection of super-luminal component in 2005 (see §3.1.4), (ii) the turning point of the jet collimation profile (see §3.1.3.4) and (iii) being located at $r \sim r_{\rm Bondi} \sim 10^5 R_{\rm s}$ from the central BH (e.g. Asada & Nakamura, 2012). The violent activity of HST-1 and the ejection of super-luminal components are quite resemble to properties of blazars (Harris et al., 2006; Cheung et al., 2007). The origin and detailed properties of HST-1 have been hot issues particularly on its physical links to the high energy emission and formation process of the relativistic jet.

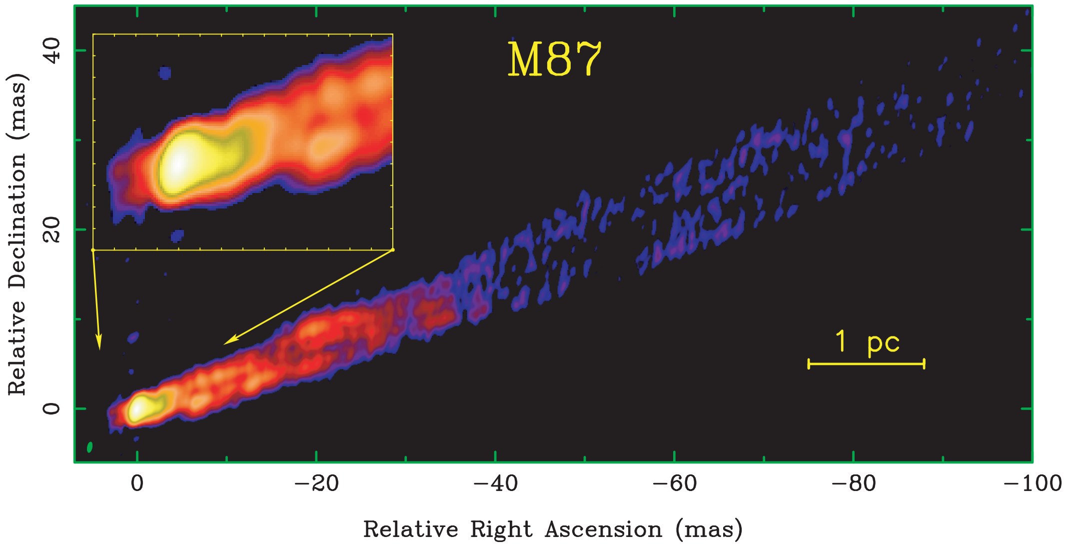

Figure 3.3: Deep image of the parsec-scale jet at 15 GHz (Kovalev et al., 2007). The weak “counter feature” is seen at the east side of the core.

On milliarcsecond scales, the jet is collimated tighter than the large-scale jet (Figure 3.3). One of remarkable feature is the transverse jet structure resolved in perpendicular to the jet axis. It shows the limb-brightened (edge-brightened) structure with transverse expansion (Figure 3.3; Reid et al. 1989; Dodson et al. 2006; Kovalev et al. 2007; Ly et al. 2007). Another noteworthy feature is a weak feature often seen in the high-dynamic-range image at the east side of the core called “the counter feature” suggested by several authors (Ly et al., 2004, 2007; Kovalev et al., 2007). It was not clear in 2000s whether this feature originates in emission from a receding counter jet or optically-thick part of the approaching jet. However, at the present, it is thought to be most likely emission from the counter jet since it is located at the east side of the location of SMBH (see §3.1.3.2).

The limb-brightened jet structure on parsec scales is smoothly connected to the inner jet on sub-parsec scales; it has been seen in the inner-jet structure on scales of $\lesssim 100\ R_\mathrm{s}$ (Figure 3.4). Junor et al. (1999) revealed the structure of the inner 10^2 R_s in the relativistic jet for the first time with global VLBI at 7 mm. The inner-jet structure has the strongly limb-brightened feature extending directly away from the radio core (see Figure 3.4 (a)). They also found that the opening angle of the limb-brightened feature seems to be broadened in the vicinity of the radio core (see white lines in Figure 3.4 (b)), implying that the region for collimation and formation of the relativistic jet might start to be resolved in the M87 jet.

Finally, we note about the viewing angle inferred for the M87 jet; the viewing angle of the jet is still under discussion. The fastest optical and radio proper motions

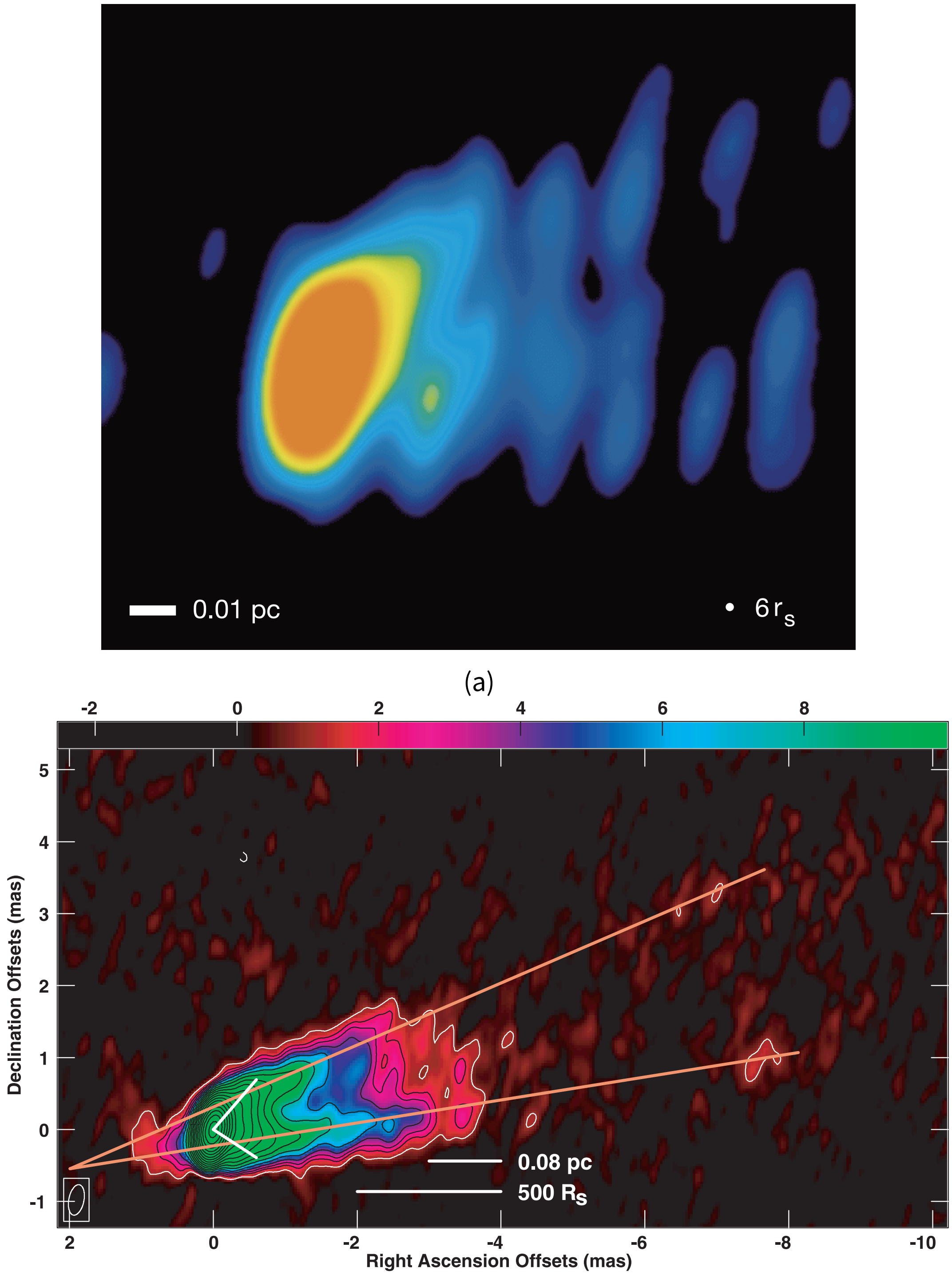

(a)

(b)

Figure 3.4: The jet structure on sub-milliarcsecond scales at 7mm. (a) The inner-jet structure on scales of $\lesssim 100\ R_\mathrm{s}$ (Junor et al., 1999). (b) Deeper view of the inner-jet structure. The orange lines follow the limb-brightened jet emission from 10 mas west of the core, with an opening angle of 15°, while the white lines represent the wide opening angle proposed by Junor et al. (1999). The counter feature is seen at the east side of the core in similar to Figure 3.3.

of $\sim 6c$ and $\sim 4c$ at the HST-1 region gives the inclination angle of $i \leq 19^\circ$ (Biretta et al., 1999) and $i \leq 28^\circ - 37^\circ$ (Cheung et al., 2007; Giroletti et al., 2012), respectively. On the other hand, $i = 30^\circ - 45^\circ$ is suggested on parsec scales based on the sub-luminal speed of the jet (see later paragraphs) and the brightness ratio between the approaching and counter jets (Ly et al., 2007). In this thesis, we assume $i = 15^\circ - 25^\circ$ as a likely range along with Acciari et al. (2009), Hada et al. (2011) and Doeleman et al. (2012).

3.1.3.2 *The Location of the Central Black Hole*

The discovery of the possible strong collimation on scales of $\lesssim 100\ R_\mathrm{s}$ (Junor et al., 1999) in the end of 1990s posed an interesting question "where is the location of the central SMBH and/or the jet base (i.e. launching region of the jet) ?". It was one of the hottest topic in the 2000s. Junor et al. (1999) proposed that the location of the SMBH is possibly located at the vicinity of the 7-mm radio core based on the possible wide-opening angle of the jet there. However, there was no reasons to verify this assumption. An alternative scenario was proposed by Biretta et al. (2002) and Ly et al. (2007) that the SMBH is located far from the 7-mm radio core and offset by a several mas eastward from the core: for example, the crossed point of the orange lines tracing the limb-brightened feature at the downstream in Figure 3.4 (b). The latter case assumes the rather smaller opening angle of the jet to $\sim 15^\circ$, suggesting completely different interpretation for the inner-jet structure.

Hada et al. (2011) achieved an epoch-making work to determine the location of the SMBH, using the nature of the radio core. First of all, here, we briefly review on the nature of the radio core in the relativistic jet. The radio core (or simply the core) is a compact and bright feature in the root of the jet imaged with VLBI. According to the standard conical jet model, the radio core seen in the VLBI images is not the true jet base that is the launching point of the jet and location of the SMBH, but the photosphere of the synchrotron self-absorption (SSA) where the optical depth of SSA (τ_SSA) is unity (Blandford & Königl, 1979; Begelman et al., 1984). In this case, the position of the radio core should be frequency dependent, since τ_SSA depends on (i) the magnetic-field strength B and (ii) the electron density n_e which are expected to be radially dependent, and also depends on (iii) the optically-thin spectral index α and (iv) the observing frequency ν (e.g. Rybicki & Lightman, 1986). This leads to the *core-shift* effect, which the position of the photosphere differs by the observing frequency (see Figure 3.5 (b)). If we assume

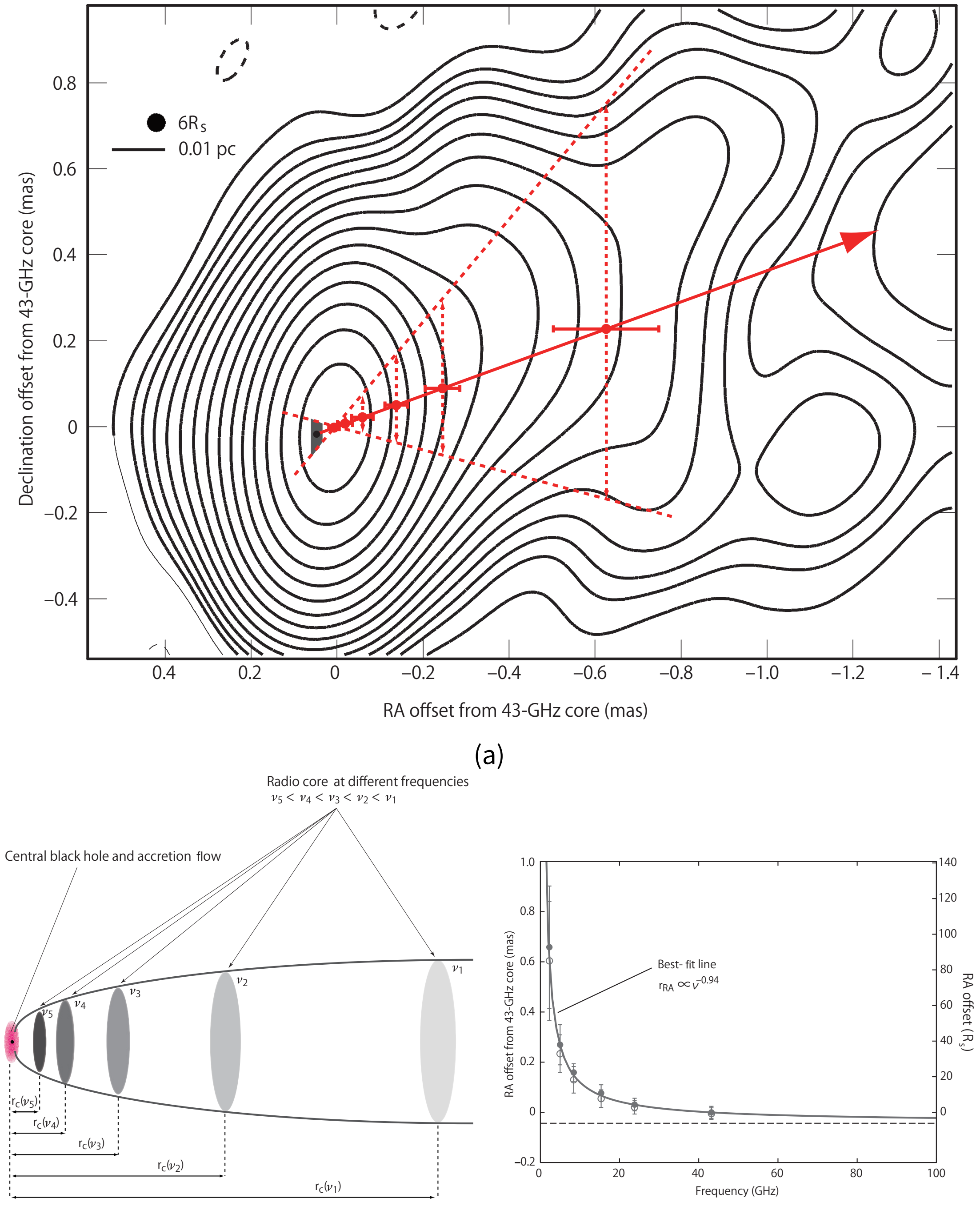

(a)

(b)

(c)

Figure 3.5: The black hole location of M87 relative to the inner-jet structure at 7 mm (Hada et al., 2011). (a) The inner-jet structure at 7 mm superimposed on the measured core-shift positions. Red circles indicate the core positions at 2.3, 5.0, 8.4, 15.2, 23.8 and 43.2 GHz relative to the 43.2-GHz core (the higher the frequency of the core, the closer it approaches the central engine). The shaded area at the east of the 43.2-GHz core represents the upstream end of the jet derived from the core-shift measurements. (b) Schematic diagram explaining the radio core-shift of a jet. (c) The core-shift in right ascension for M87 as a function of observing frequency.

$B(r) \propto r^{-m}$ and $N_e(r) \propto r^{-n}$ where r is the distance from the central SMBH, the frequency dependence of the core position is expressed as $r \propto \nu^{-1/k_r}$ (see Blandford & Königl, 1979; Begelman et al., 1984), where k_r is a function of m, n and α given by

$$k_r = \frac{(3-2\alpha)m + 2n - 2}{5 - 2\alpha}. \tag{3.1}$$

If k_r is determined by measurements of the core-shift between several frequencies, the location of the central engine can be derived by calculating the converging point of the core-shift relation. The core-shift is actually observed for several extragalactic sources (e.g. Bartel et al., 1986; Lobanov, 1998; O'Sullivan & Gabuzda, 2009).

Hada et al. (2011) performed multi-frequency phase-referencing VLBI observation to measure the position of the radio core at several frequencies relative to that in M84 which is a LLAGN near M87. Hada et al. (2011) revealed that (i) the location of the SMBH in only $\sim$20 R_s upstream of the 43-GHz core (Figure 3.5 (a)), (ii) the frequency dependence of the core position is well-explained by a power law of $r \propto \nu^{-0.94 \pm 0.09}$ as theoretically expected (Figure 3.5 (c)), (iii) the extrapolated position of the core-shift at 1.3 mm corresponds to the location of the black hole within uncertainty. The measured core-shift relation also allows to probe the radial profile of various physical quantities as a function of the distance from the SMBH (see §3.1.3.4). This strongly indicates that the jet becomes nearly optically-thin at 1.3 mm, resulting in that the event-horizon-scale structure at the close vicinity of the SMBH can be observed with 1.3 mm VLBI observations with the Event Horizon Telescope (§1.3). We note that this indication seems consistent with recent ALMA observations of M87. Doi et al. (2013) reports on preliminary results of the spectrum measurement of M87 with ALMA. The preliminary radio spectrum has a submillimeter bump with a break at $\sim$1 mm similarly to Sgr A* (§2.1.4.1) indicating the opacity transition at $\sim$ 1 mm.

Another important result of Hada et al. (2011) is that the orientation of the core-shift is exactly along the jet direction (Figure 3.5 (a)). This provides strong evidence that the jet emission dominates the emission from the radio core at frequencies at least lower than 43 GHz (=7 mm), disfavoring scenarios that the radio core is dominated by the emission from RIAF (Reynolds et al., 1996; Di Matteo et al., 2003; Nagakura & Takahashi, 2010; Takahashi & Mineshige, 2011). However, we emphasize that the origin of emission at shorter-millimeter wavelengths of ~ 1 mm is still an unsettled question. It could be dominated by synchrotron emission from either the jet (Zakamska et al., 2008; Gracia et al., 2009; Broderick & Loeb, 2009; Dexter et al., 2012) or RIAF (Dexter et al., 2012), since the extrapolated location of the radio core at ~ 1 mm coincides with the jet base and/or central black hole within its uncertainty, and thus emission from the accretion disk could dominate.

3.1.3.3 *Event-Horizon-Scale Structure of M87*

Recently, dramatic results of the Event Horizon Telescope (EHT; §1.3) have been reported on detections of the event-horizon-scale structure (Doeleman et al., 2012) as expected in the works of Hada et al. (2011) (§3.1.3.2).

Doeleman et al. (2012) successfully detected 1.3 mm interferometric fringes on long baselines between Hawaii (JCMT, SMA) – Arizona (ARO/SMT) and Hawaii – California (CARMA) and a short baseline between California – Arizona. The measured visibility clearly shows that 1.3 mm emission structure is resolved in VLBI baselines (Figure 3.6). The effective size derived by Gaussian-fitting is 40 ± 1.8 μas corresponding to 5.5 ± 0.4 $R_{\rm s}$, confirming that the 1.3-mm emission is compact comparable to the size of ISCO and the expected size of the black hole shadow.

This measured size matches with the width profile of the jet measured at the downstream of the jet, which is consistent with recent GRMHD simulations (McKinney, 2006; Gracia et al., 2009) (Figure 3.7 and §3.1.3.4). The width profile and the measured size is crossed at the apparent core distance of a few $R_{\rm s}$, which is absolutely consistent with the extrapolation of the core-shift relation measured in Hada et al. (2011). This strongly indicates that the detected structure is indeed located in the close vicinity of the SMBH and/or the jet base.

The derived size can be used to constrain the spin of the SMBH and favors a prograde ISCO orbit in the accretion flow. The ISCO is the critical size scale associated with the jet base, since the jet is thought to be launched from the accretion disk. Considering that the jet expands transversely after ejected from the central engine, the observed size of the jet base should not exceed the size of ISCO. The derived size is smaller than the apparent size of the ISCO for non-rotating black hole ($a = 0$), excluding the possibility of a retrograde ISCO orbit in the accretion flow. The measured 1.3-mm VLBI size corresponds to a prograde ISCO around a black hole with ($a > 0.2$).

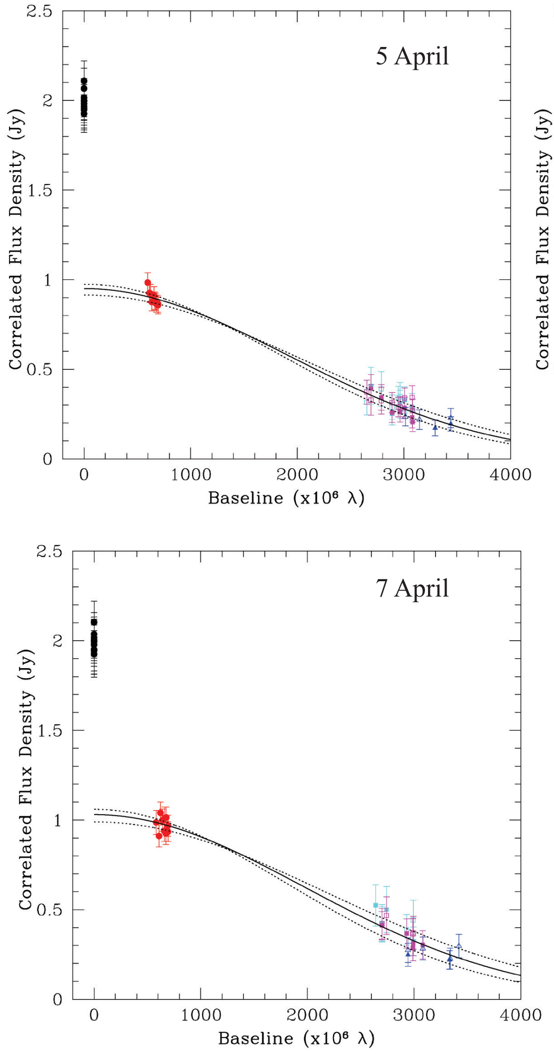

Figure 3.6: Correlated flux density data from 3 consecutive days of observing in 2009 observations are plotted as a function of uv-distance (Doeleman et al., 2012). The weighted least-squares best-fit circular Gaussian model is shown as a solid line and has a total flux density of 0.98 Jy and a FWHM size of 40.0 micro–arc sec.

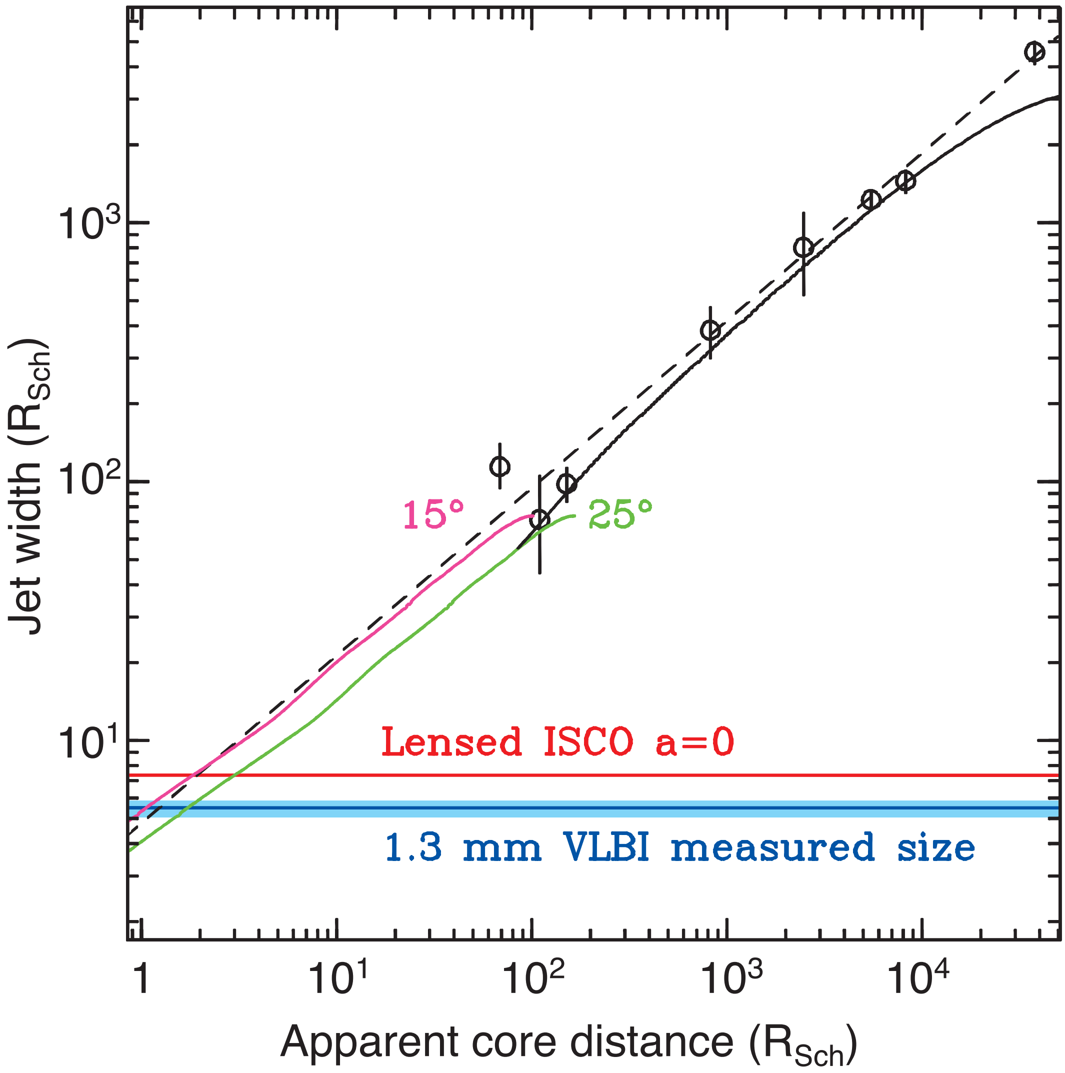

Figure 3.7: Width profile of the M87 jet as a function of distance from the core, based on measurements of the jet opening angle (Biretta et al., 2002) and the core-shift (Hada et al., 2011). Dashed black line indicates the best-fit power-law profile of $\theta \propto r^{0.69}$. The black line indicate the jet width derived from a GRMHD simulation of the larger-scale M87 jet (Gracia et al., 2009), while the green and magenta lines indicate the jet width derived from a GRMHD simulation on inner $10^2\ R_s$ (McKinney, 2006), assuming the inclination angle of $15° - 25°$.

Another noteworthy result is the stability of the emission structure (Figure 3.6). We might be able to expect a time variability on scales of a few days because of accretion disk inhomogeneity for a black hole spinning near the maximum rate (e.g. Dexter et al., 2012), considering the ISCO period ranging from 5 days ($a = 1$) to 1 month ($a = 0$) for the mass of the M87 black hole. The consistency of the 1.3-mm VLBI sizes through spanning 3 days of observation does not reflect dramatic structural changes in the jet. More sensitive searches for such periodic features in the jet launch region can be carried out with the full Event Horizon Telescope (Chapter 5).

3.1.3.4 *Collimation and Acceleration of the Relativistic Jet*

The other dramatic progress in the last few years is the measurements of collimation (Asada & Nakamura, 2012; Nakamura & Asada, 2013a; Hada et al., 2013) and acceleration (Asada et al., 2014) profiles of the jet in the inner $10^7\ R_\mathrm{S}$, based on the core-shift measurement (Hada et al., 2011) linking the physical quantities and the distance from the SMBH. Now is just in the exciting era when the theoretical models of the jet formation (e.g. Magnetohydrodynamic (MHD) model) start to be tested by the measurements of the profile of various physical quantities.

JET COLLIMATION

Asada & Nakamura (2012) extensively investigates the structure of the M87 jet on a broad range from milliarcsecond to arcsecond scales, revealing the jet collimation profile in the inner $10^7\ R_\mathrm{S}$ for the first time (Upper panel of Figure 3.8). Asada & Nakamura (2012) discovers the jet maintains a parabolic streamline ($\propto r^{0.56}$; Hada et al. 2013) in the inner $10^5\ R_\mathrm{S}$, with a transition to a conical streamline ($\propto r^{1.04}$; Asada & Nakamura 2012) at a peculiar knot HST-1 (see §3.1.3.1) located near the Bondi radius of $\sim 10^5\ R_\mathrm{S}$.

Hada et al. (2013) intensively investigates the collimation profile of the M87 jet in the inner $10^5\ R_\mathrm{S}$ (Upper panel of Figure 3.8). Hada et al. (2013) revealed a detailed collimation profile down from $10^5\ R_\mathrm{S}$ to $\sim 10\ R_\mathrm{S}$. Hada et al. (2013) found a possible tendency of a wider jet opening angle in the inner $\sim 10^2\ R_\mathrm{S}$ from the central engine. The possible wider profile has a profile of $\propto r^{0.76}$ more conical than outer $\sim 10^2\ R_\mathrm{S}$ region.

We summarize interpretations of the profile on the framework of magnetohydrodynamic (MHD) jets along with Hada et al. (2013). Historically, an idea that the relativistic jet is magnetically driven by the accretion disk was originally proposed

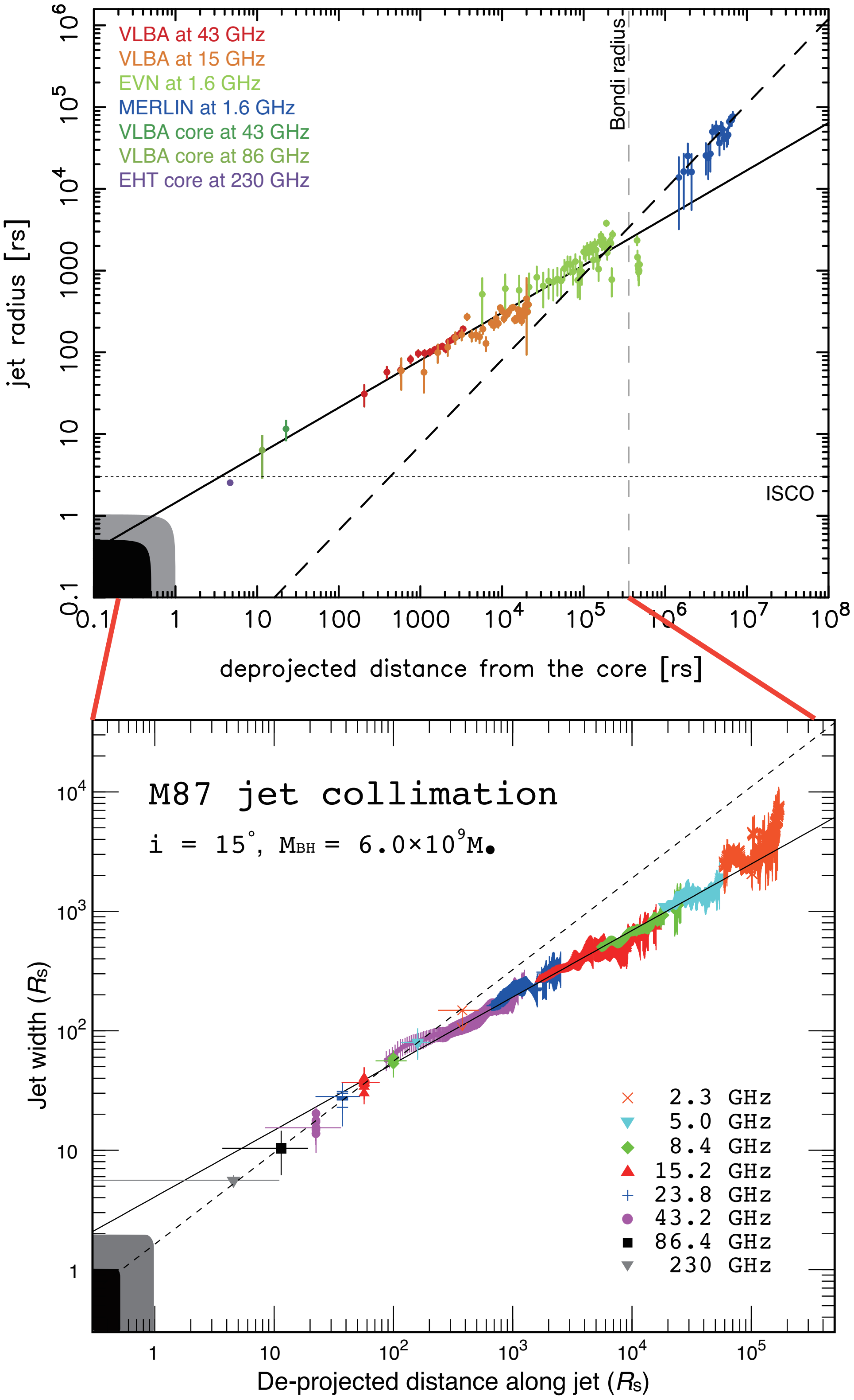

Figure 3.8: The width of the M87 of the jet as a function of the de-projected distance from the core. The black area shows the size of the minor axis of the event horizon of the spinning black hole with maximum spin. The gray area indicates the size of the major axis of the event horizon of the spinning black hole with maximum spin, and corresponds to the size of the event horizon of the Schwarzschild black hole. (a) The collimation profile at $\sim 10^2 - 10^7$ R_s (Nakamura & Asada, 2013a). (b) More intensively measured profile inside HST-1 at $10 - 10^5$ R_s (Hada et al., 2013).

by Lovelace (1976) and Blandford (1976) independently. The shape of a magnetized flow is determined by the detailed force balance across the poloidal magnetic-field lines. This is described as the transfield equation, which was originally derived by Okamoto (1975) for steady, axisymmetric, rotating magnetized flow in a gravitational field without external pressure. It is proposed that the jet is globally collimated by the magnetic hoop stresses associated with toroidal field lines (e.g. Blandford & Payne, 1982; Sakurai, 1985, 1987; Heyvaerts & Norman, 1989; Chiueh et al., 1991; Tomimatsu, 1994).

Recent theoretical studies indicate the importance of external pressure at the jet boundary to collimate the jet. Okamoto (1999) analytically showed that the magnetic hoop stresses alone would not account for the global collimation. Recent numerical studies actually come along this line (e.g. Nakamura et al., 2006; Komissarov et al., 2007; Toma & Takahara, 2013). Komissarov et al. (2009) shows that when the external gas pressure follows a power law of $p_{\rm ext} \propto r^{-a}$, the jet maintains parabolic ($\propto r^{a/4}$) for $a \lesssim 2$, while the jet eventually becomes conical due to insufficient external confinement for $a > 2$. If the edge of the radio emission traces the exterior edge of a magnetized jet, the measured width profile suggests $a \sim 2$ for inner $10^5\ R_{\rm s}$ region. As a source of such confinement medium, Asada & Nakamura (2012) propose an interstellar medium following the gravitational influence of the central black hole, such as a giant ADAF (Narayan & Fabian, 2011). HST-1 is located at almost the Bondi radius $10^5\ R_{\rm s}$ from the central engine, which the gravitational potential is expected to change its profile. This can lead to the change in the profile of the external pressure following the influence of gravity, causing the transition from parabolic shape to conical shape.

Interestingly, both Bromberg & Levinson (2009) and Asada & Nakamura (2012) suggest HST-1 as a stationary shocked feature resulting from over-collimation of the inner jet due to unbalance between the external and internal pressure, which is originally proposed by Stawarz et al. (2006) and Cheung et al. (2007) to explain the broadband flaring activity. This could explain super-luminal motions of overall structure of HST-1 (Biretta et al., 1999; Cheung et al., 2007; Giroletti et al., 2012), while a weak, slowly-moving feature at the upstream of the HST-1 (Giroletti et al., 2012) could be related to the re-collimation shock itself.

A transition of jet collimation profile in the inner $\sim 10^2\ R_{\rm s}$ is also suggested from some of theoretical aspects. First, this transition could correspond to the fast-magnetosonic point. On the frame work of relativistic MHD schemes, beyond this point, most of the conversion from the Poynting energy to the kinetic energy occurs (magnetic nozzle effect Li et al., 1992; Vlahakis & Königl, 2003), leading that the magnetized jet starts to be collimated asymptotically into a parabolic shape (Tomimatsu & Takahashi, 2003). The radius of the fast point is typically a few times the light cylinder radius (Li et al., 1992) that is of the order of $\sim 1-5\,R_{\rm s}$ (Komissarov et al., 2007). Thus, if the M87 jet is MHD-driven, the observed possible transition of the jet shape could be explained by this process. Second, this transition could be due to changes in the external pressure profile, because the jet in this scale is likely to have complicated interactions with surrounding medium such as accretion flow, corona and disk wind (McKinney, 2006). Third, this transition could happen as an apparent effect due to projection, if the jet inclination angle is not constant down to the black hole (McKinney et al., 2013).

We emphasize that a purely hydrodynamic (HD) jet is also possible to produce the gradual parabolic collimation of M87 (e.g. Bromberg & Levinson, 2009), suggesting that the collimation profile alone would not be able to prove whether the jet is MHD-driven or not.

JET ACCELERATION

Kinematics of the M87 jet has been intensively studied with VLBI on milliarcsecond scales, VLA and HST on arcsecond scales in the last two decades. VLBI observations at cm wavelengths revealed only sub-luminal motion of $< 0.3c$ of the jet in the inner 1" (Reid et al., 1989; Dodson et al., 2006; Kovalev et al., 2007; Hada et al., 2014). In particular, in the inner 1–20 mas, intensive monitoring with VLBA at 15 GHz revealed that the jet has only slow proper motions of $0.003c-0.05c$ (Kovalev et al., 2007). Only exception is a superluminal motion of $\gtrsim 1.1c$ detected with VLBA at 43 GHz on sub-milliarcsecond scales from the nucleus during the flaring event in 2008 (see also §3.1.4; (Acciari et al., 2009)).

Around a region 1" from the nucleus, there is a peculiar knot HST-1 (see §3.1.3.1). It shows super-luminal motions of $4c-6c$ (Biretta et al., 1999; Cheung et al., 2007; Giroletti et al., 2012). At the downstream of the HST-1, both super- and sub-luminal motions have been detected (Biretta et al., 1995; Meyer et al., 2013). On the other hand, very recently, Asada et al. (2014) detected several new components located at roughly middle of the core and HST-1 with EVN, showing a velocity fields with a systematic increase from sub- to superluminal speeds.

The present results reveal an intriguing picture of the jet acceleration in the M87 (Figure 3.9). The M87 jet seems gradually accelerated through a distance of $10^6\,R_{\rm s}$

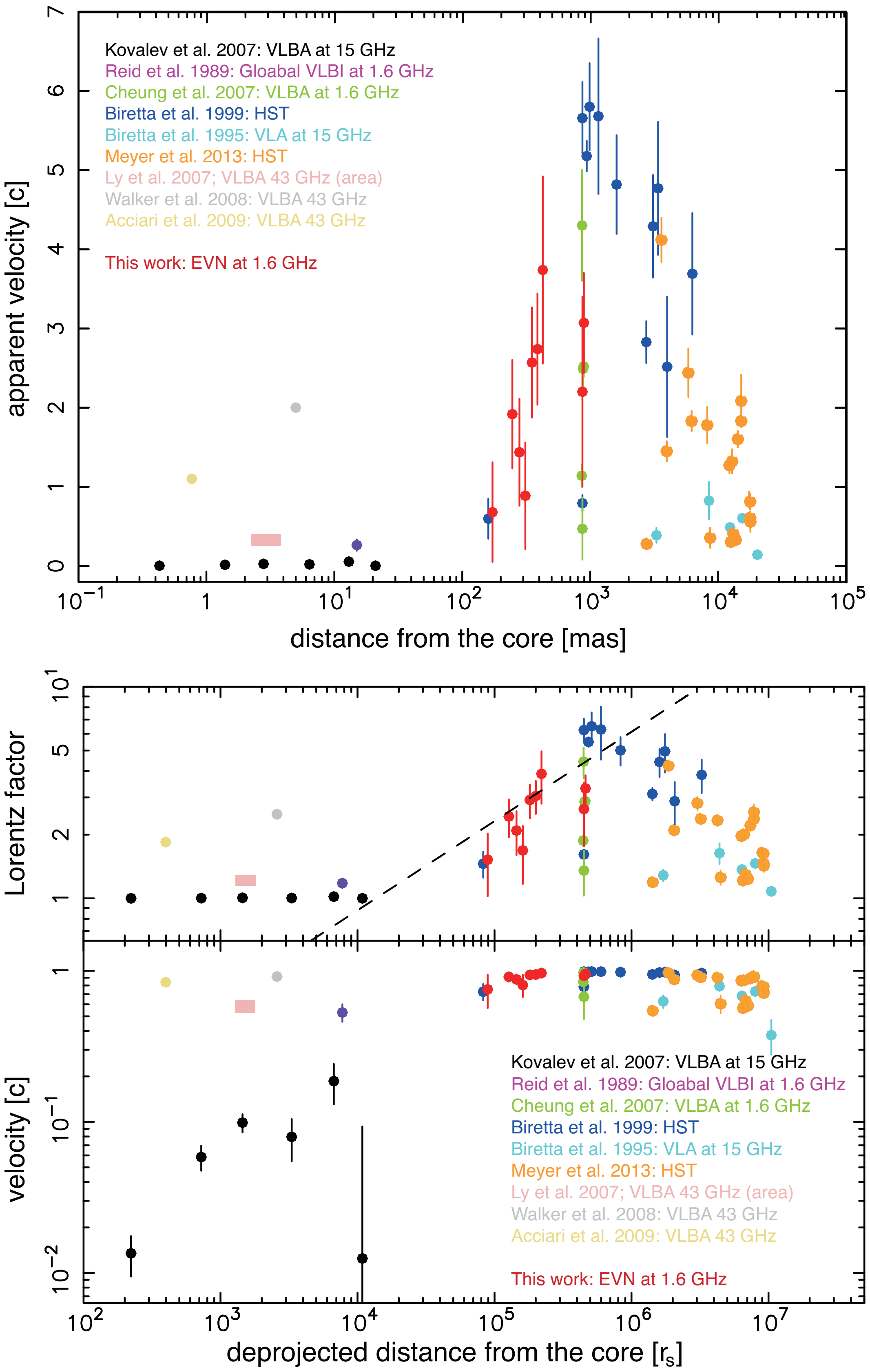

Figure 3.9: Acceleration profile of the M87 jet in the inner $10^7\ R_\mathrm{s}$ (Asada et al., 2014). (Upper panel) Distribution of the apparent velocity as a function of the projected distance from the core. (Lower panel) Distribution of the velocity and Lorentz factor as a function of the de-projected distance from the core. The dashed line represents the expected line for the MHD acceleration in parabolic streamline.

from the black hole, where the jet has a parabolic stream. This suggests that the acceleration and collimation occurs simultaneously in the M87 jet. The distribution of the velocity field has a peak at HST-1, which is considered as the site of being over-collimation, and shows a deceleration downstream of HST-1, where the jet has a conical shape.

On the framework of the MHD, the jet acceleration occurs by conversion of the Poynting energy to the kinetic energy (so-called “MHD acceleration”). Nakamura & Asada (2013a) derived an acceleration profile of $\beta \propto r^{2/b}$ for a non-relativistic flow, while Komissarov et al. (2007) and Komissarov et al. (2009) show an acceleration profile of $\Gamma \propto r^{(b-1)/b}$ in the relativistic regime, if the jet has a parabolic streamline of $\propto r^b$ ($b \sim 2$ for M87 in the inner $10^5\ R_{\rm s}$). The non-relativistic acceleration profile of $\beta \propto r^{2/b}$ seems broadly consistent with an acceleration profile in the inner $10^4\ R_{\rm s}$ where the jet is actually non-relativistic (Nakamura & Asada, 2013a), while the relativistic acceleration profile of $\Gamma \propto r^{(b-1)/b}$ is also consistent with an acceleration profile in $10^4 - 10^6\ R_{\rm s}$ (the dashed line in the bottom panel of Figure 3.9; Asada et al. 2014).

3.1.4 *Very High Energy γ-ray Emission in M87*

With the advent of the new-generation Cherenkov telescope arrays, M87 is now well known as one of the four radio galaxies to show γ-ray emission up to the very-high-energy (VHE; $E > 100$ GeV) regime. VHE γ-ray emission from M87 was first discovered with the High Energy Gamma-Ray Astronomy (HEGRA) Collaboration in 1998/1999 (Aharonian et al., 2003). The emission was confirmed by the High Energy Spectroscopic System (H.E.S.S) in 2003 to 2006 (Aharonian et al., 2006c), the Very Energetic Radiation Imaging Telescope Array System (VERITUS) in 2007 (Acciari et al., 2008), and Major Atmospheric Gamma-ray Imaging Cherenkov (MAGIC) telescope (Albert et al., 2008). In the high-energy (HE; 100 MeV $< E <$ 100 GeV) regime, the Fermi Large Area Telescope (LAT) detects a faint, point-like γ-ray emission within the central ~20 kpc of the galaxy in 10 months of all-sky survey (Abdo et al., 2009). The emission in the HE regime appears to be stable at least on a timescale of about 10-30 days, although faster variations are difficult to be observed due to faintness of the source currently (Abdo et al., 2009; Hada et al., 2014). The observed MeV/GeV spectrum seems to connect smoothly with the VHE spectrum at a quiescent state (Abdo et al., 2009).

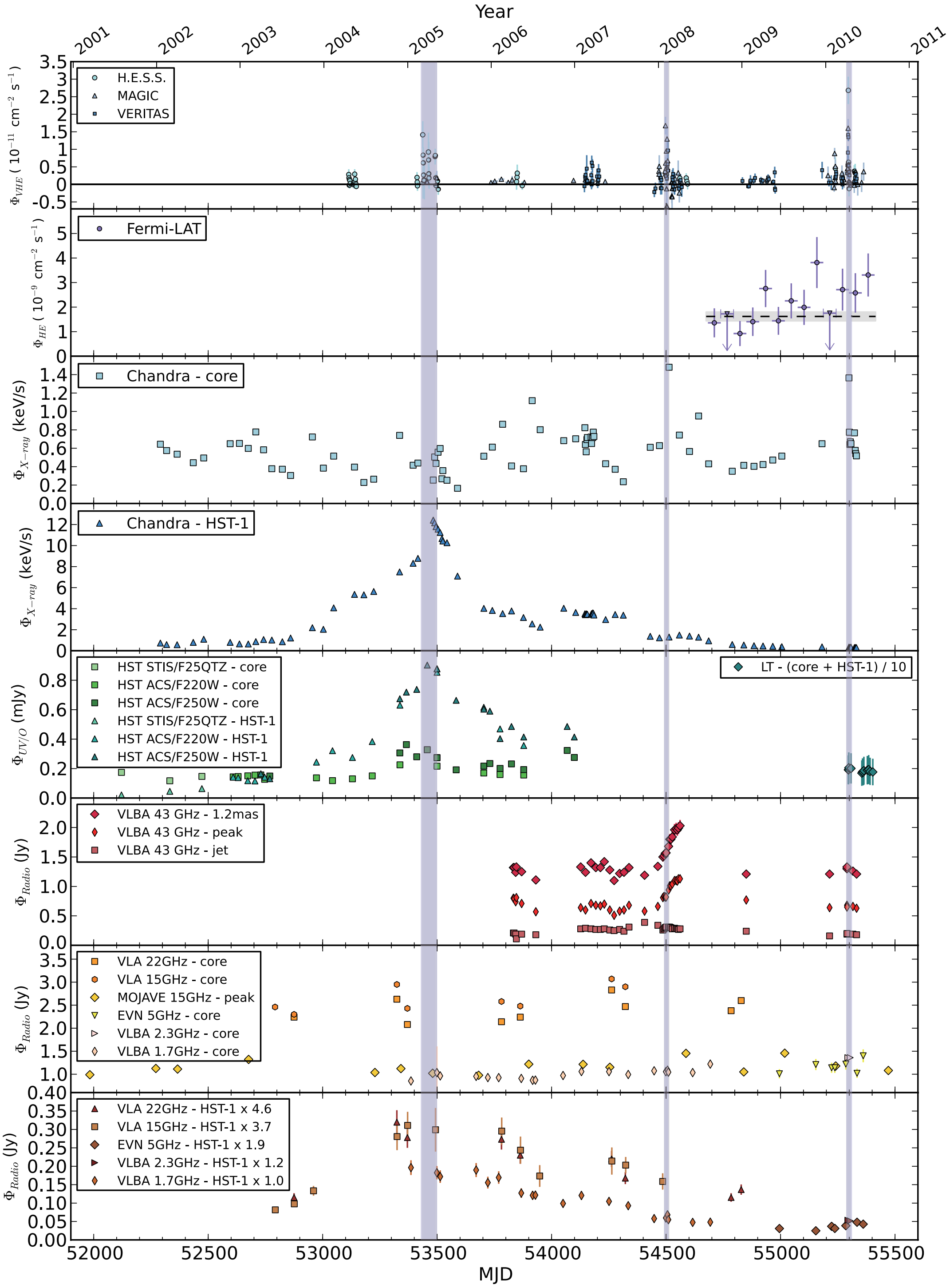

Figure 3.10: Multi-wavelength light curve of M87 from 2001 to 2011 (Abramowski et al., 2012). Gray vertical bands mark the duration of increased VHE activities in 2005, 2008 and 2010.

In the VHE regime, M 87 underwent three remarkable flares in 2005, 2008 and 2010 (Figure 3.10 and also see Abramowski et al. (2012) for a review). In 2005, a VHE flare (Aharonian et al., 2006c) was accompanied with the large radio-to-X-ray outbursts from a peculiar knot HST-1 (Harris et al., 2006), with an ejection of superluminal ($\sim 4c$) radio features (Cheung et al., 2007). These results suggest a quite impressive implication that HST-1 located more than $10^5\ R_{\rm S}$ far from the nucleus is most likely the location of the VHE γ-ray production for the 2005 event (e.g. Stawarz et al., 2006; Cheung et al., 2007; Harris et al., 2008, 2009). In the case of the 2008 event (Acciari et al., 2009), on the other hand, Chandra detected an enhanced X-ray flux from the nucleus, while HST-1 maintained a comparatively constant flux. The following up observations with VLBA at 43 GHz during the VHE activity detected a strong flux increase from the radio core at the jet base with an ejection of superluminal component. These facts provide a strong claim that the VHE flare originates in the core in the 2008 event (Acciari et al., 2009). The third event, i.e., the 2010 flare is rather elusive. Coincident with the VHE event, Chandra again detected an enhanced flux from the X-ray core (Harris et al., 2011; Abramowski et al., 2012), while HST-1 was quiescent at X-ray. VLBA observations around the 2008 event also suggested an weak enhancement of the radio core flux (Hada et al., 2012). These results favor the origin being in the nucleus for the 2010 flare. However, Giroletti et al. (2012) found the emergence of a superluminal component in the HST-1 complex near the epoch of this event similarly to the 2005 event.

Associated radio enhancements at the radio core at 7 mm in the 2008 and 2010 events indicate that VHE emission originates inside the radio core at 7 mm only a few tens of $R_{\rm S}$ downstream from the black hole and/or jet base, considering the results of the core-shift measurement (§3.1.3.2; Hada et al. 2011). In the past three flares, the compact sizes of VHE emission region ($< 5 \times 10^{15}\delta$ cm corresponding to a few $R_{\rm S}$, where δ is the Doppler factor of the emission region) are required by rapid variability timescales of $\sim$1 d based on causality arguments.

Recently, the VERITUS Collaboration has reported a new weak VHE γ-ray activity from M87 in early 2012 (Figure 3.11; Beilicke & VERITAS Collaboration 2012). The 2012 event has different properties compared to previous VHE flares. Its long duration ($\sim$2 months) and weak flux ($\sim$10 times weaker than the past three flares) may point to an origin in a different type of a VHE activity. VLBI observations with VERA at 7 and 13 mm on milliarcsecond scales revealed strong enhancement in the radio core after the 2012 event, suggesting an origin close to the black hole

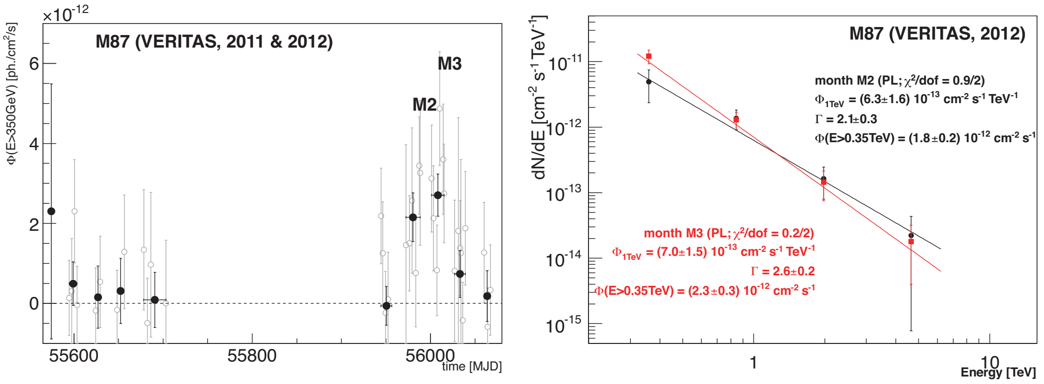

Figure 3.11: A new VHE γ-ray activity from M87 in early 2012 (Beilicke & VERITAS Collaboration, 2012).

and/or jet base, similar to the 2008 VHE flare (see 3.12; (Hada et al., 2014)). Eventually, the Event Horizon Telescope performed 1.3 mm VLBI observations of M87 in the middle of the radio brightening reported in Hada et al. (2014). We present studies based on these observations in this chapter.

3.2 SCOPE OF STUDIES IN THIS CHAPTER

The relativistic jet in the radio galaxy M87 is an excellent laboratory for investigating the astrophysics of the relativistic jet (§3.1.1). Because of its proximity ($D =$ 16.7$\pm$0.6 Mpc; Blakeslee et al. 2009) and the large estimated mass of its central black hole ($M_{\rm BH} \sim 3-6\times10^9 M_\odot$; §3.1.1.2; Macchetto et al. 1997; Gebhardt & Thomas 2009; Gebhardt et al. 2011; Walsh et al. 2013), the black hole in M87 subtends the second largest angular size of any known black hole (after Sgr A*; §2.1.2 and §2.1.3).

Millimeter/submillimeter-wavelength VLBI is ideally suited to observing M87 on these scales, since the event-horizon-scale structure around the black hole is expected to become optically thin at $\nu \gtrsim$ 230 GHz ($\lambda \lesssim$ 1.3 mm), based on the frequency-dependent position of the radio core (Hada et al., 2011) and the existence of the submillimeter bump in its radio spectrum at $\sim$ 230 GHz (Doi et al., 2013) (see §3.1.3.2).

The origin of 230 GHz emission is still an unsettled question (§3.1.3.2). The 230 GHz emission could be dominated by synchrotron emission from either the jet (Zakamska et al., 2008; Gracia et al., 2009; Broderick & Loeb, 2009; Dexter et al., 2012) or the accretion disk (Reynolds et al., 1996; Di Matteo et al., 2003; Nagakura & Takahashi, 2010; Takahashi & Mineshige, 2011; Dexter et al., 2012) in the regime of

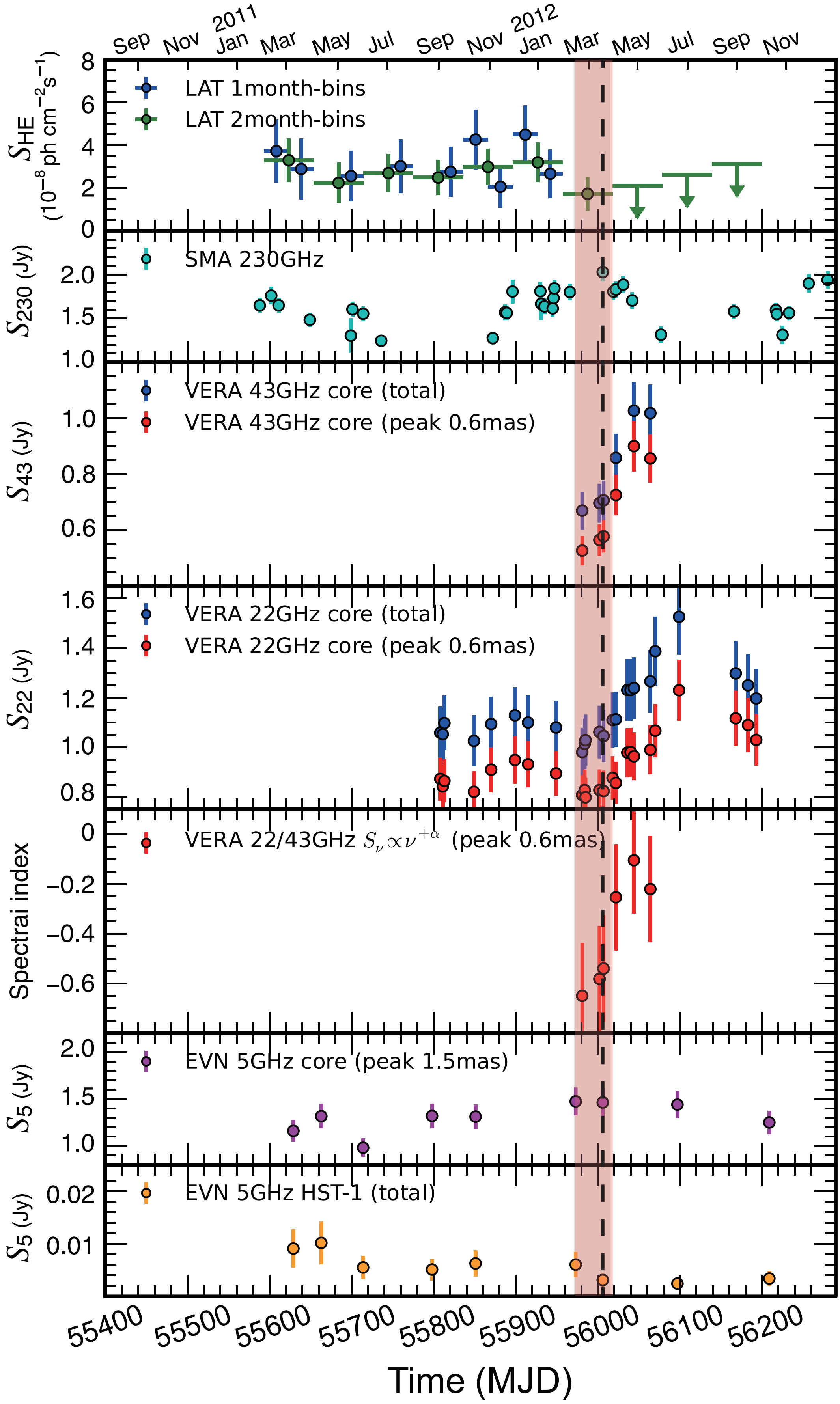

Figure 3.12: Multi-wavelength light curve of M87 around the 2012 event. The shaded area indicates the duration of the 2012 event in Figure 3.11. The dashed line indicates the day of EHT observations of M87 presented in Chapter 3.

radiatively inefficient accretion flow (e.g. Yuan & Narayan, 2014) with low mass accretion rate of $< 9.2 \times 10^{-4}$ M$_\odot$ y^{-1} (see §3.1.2 and Kuo et al. 2014). The discovery of the position shift of the radio core along the jet direction at different frequencies (Hada et al., 2011) provides strong evidence that the jet emission dominates the emission from the radio core at frequencies at least lower than 43 GHz (=7 mm). However, it is less clear for 230 GHz emission, since the extrapolated location of the 230 GHz radio core coincides with the jet base and/or central black hole within its uncertainty, and thus emission from the accretion disk could dominate.

Previous 230 GHz VLBI observations (Doeleman et al., 2012) with the EHT established the existence of compact structures on scales of few Schwarzschild radii (R_s) (§3.1.3.3), broadly consistent with a paraboloidal or possibly conical collimation profile of the jet width in the innermost region within $\sim$ 100 R_s of the central black hole (§3.1.3.4; Asada & Nakamura 2012; Nakamura & Asada 2013a; Hada et al. 2013). These are naturally explained by recent theoretical magnetohydrodynamic (MHD) schemes (e.g. McKinney, 2006; Komissarov et al., 2007; Nakamura & Asada, 2013a).

VLBI observations at 230 GHz can address at least two issues concerning the fundamental nature of M87. The first is the event-horizon-scale structure of the jet launching region, which is crucial for understanding formation process of the relativistic jets and also for testing presence of the signatures of strong-field gravitational lensing. Geometric models including a shadow feature at the last photon orbit, illuminated by a counter jet and/or accretion disk in the close vicinity of the black hole, can be fit to current 230 GHz observations. These models produce a relatively dim central region encircled by a brighter annulus (e.g. Broderick & Loeb, 2009; Dexter et al., 2012), which can be properly imaged as the number of (sub)millimeter VLBI sites increases (Lu et al., 2014; Honma et al., 2014; Inoue et al., 2014).

The second issue is the production mechanism of very-high-energy (VHE; $>$ $\sim$100 GeV) γ-ray photons in the vicinity of the black hole and/or the jet base (§3.1.4). M87 is one of the only four known AGNs with weak or moderate beaming compared to other VHE AGNs, which mostly consist of BL Lac objects. M87 has undergone three large VHE flares (see Abramowski et al., 2012, for an overview) and a weak VHE enhancement recently in March 2012 (Beilicke & VERITAS Collaboration, 2012). In the past three flares, the compact sizes of VHE emission region ($< 5 \times 10^{15}\delta$ cm corresponding to a few R_s, where δ is the Doppler factor of the emission region) are required by rapid variability timescales of $\sim$1 d based on causality arguments. VHE flares in 2008 and 2010 associated delayed strong and weak flux density enhancement, respectively, in the radio core at 43 GHz (Acciari et al., 2009; Hada et al., 2012), indicating that these flares originate inside the radio core at 43 GHz only a few tens of R_s downstream from the black hole and/or jet base (Hada et al., 2011).

On the other hand, a weak VHE enhancement in March 2012 (hereafter the 2012 event) has different properties compared to previous VHE flares. Its long duration ($\sim$2 months) and weak flux ($\sim$10 times weaker than the past three flares) may point to an origin in a different type of VHE activity. Multi-wavelength observations on milliarcsecond scales revealed strong enhancement in the radio core at both 22 and 43 GHz after the 2012 event, suggesting an origin close to the black hole and/or jet base, similar to the 2008 VHE flare (Hada et al., 2014). In summary, three of four previous VHE events are thought to originate in the vicinity of the black hole. 230 GHz VLBI is the ideal tool to constrain the location and structure of the VHE emission region.

In the following sections, we report on new 230 GHz VLBI observations of M87 with the EHT during the 2012 event using a four-telescope array, providing the interferometric visibility information on baselines shorter than $\sim$ 4 Gλ. These observations provide the first measurements of closure phase, imposing new constraints on accretion/jet models for M87, and the first constraints on the innermost structure of the relativistic jet on scales of a few R_s during VHE variability. In this chapter, we adopt a black hole mass of 6.2×10^9 $M_\odot$[2] following Gebhardt et al. (2011) and a distance of 16.7 Mpc following Blakeslee et al. (2009) along with Doeleman et al. (2012), resulting in $1R_s = 1.9 \times 10^{15}$ cm $= 5.9 \times 10^{-4}$ pc $= 7.3$ μas.

3.3 OBSERVATIONS

M87 and several calibrator sources were observed with four stations at three sites in 2012 on the nights of March 15, 20 and 21 (days 75, 80 and 81), as summarized in Table 3.1: a phased array of the Submillimeter Array (SMA; Ho et al. 2004; henceforth, P) antennas and the James Clerk Maxwell Telescope (JCMT; Newport 1986) on Mauna Kea in Hawaii, the Arizona Radio Observatory's Submillimeter Telescope (ARO/SMT; S) on Mt. Graham in Arizona, and both a single antenna and a phased

---

[2] This black hole mass is recalculated for a distance of 16.7 Mpc.

Table 3.1: Observatories in the 2012 Observations

Site	Observatory	Char.	Note
Hawaii	SMA	P	Phased sum of seven 6m dishes
Arizona	ARO/SMT	S	Single 10 m dish
California	CARMA (phased)	F	Phased sum of three 10.4 m and four 6.1 m dishes
California	CARMA (single)	D	Single 10.4 m dish

array of eight antennas of the Combined Array for Research in Millimeter-Wave Astronomy (CARMA; Mundy & Scott 2000; D and F, respectively) on Cedar Flat in California.

Observations were performed at two bands centered at 229.089 and 229.601 GHz (low and high band) with 480 MHz bandwidths with the exception of the single CARMA antenna, which observed only the low band. All telescopes observed left-hand circular polarization (LHCP). The SMT and phased CARMA, along with the JCMT on Mauna Kea, also observed right-hand circular polarization (RHCP). Hydrogen masers were used as timing and frequency references at all sites. Reconfigurable Open Architecture Computing Hardware (ROACH)[3] digital backends (RDBE) designed at MIT Haystack Observatory and National Radio Astronomy Observatory (NRAO) were used for all single-antenna stations. Data were recorded onto modules of hard drives using the Mark 5C for RDBE systems. The SMA and CARMA sites were equipped with 1 GHz bandwidth adaptive beamformers, built using an older generation of Collaboration for Astronomy Signal Processing and Electronics Research (CASPER)[4] technology. The beamformers compensate group delay and phase at each antenna in the array in real time, thereby recording a single data stream representing the coherent phased array sum of all antennas. The real time corrections are derived from simultaneous cross-correlations, and the data are formatted for Mark5B+ recorders at 4 Gb/s rate. Data were correlated with the Haystack Mark 4 VLBI correlator.

Hardware and disk failures occurred during observations on the first two days, with the result that many data products are missing or have low signal-to-noise ratio (S/N). The LHCP data of the first two days and RHCP data cannot be calibrated by the technique of amplitude self-calibration described below. In this paper, we focus on the results of LHCP data of M87 in day 81; other data will be presented elsewhere.

---

[3] `https://casper.berkeley.edu/wiki/ROACH`

[4] `https://casper.berkeley.edu`

3.4 DATA REDUCTION

Correlated data were analyzed using the Haystack Observatory Post-processing System[5] (HOPS). Initial coherent baseline fringe fitting was done using the HOPS task `fourfit`. Detections with high S/N were used to determine several important quantities for further processing. First, we derived the phase offsets between the 32 MHz channels within each band. Second, approximate atmospheric coherence times maximizing the S/N of detection were calculated to guide further incoherent fringe searching in the HOPS task `cofit`. Third, the residual single-band delay, multi-band delay, and delay rate were used to set up narrow search windows for each source to assist in fringe finding.

A form of phase self-calibration was used to find fringes on baselines with low S/N, including long baselines (e.g., SP) and baselines including the single CARMA antenna. The phased CARMA station is very sensitive and therefore can be used as a reference station to derive phase corrections to be applied to other antennas to remove rapid atmospheric phase fluctuations through baselines with the phased CARMA station. The fringe fitting was done on baselines to station F (i.e., FD, SF, and PF), and data were segmented at a $\sim$5 s cadence. These phases were then removed from each station prior to coherent fringe fitting on the low-S/N baselines using `fourfit`, leading to much better coherence and detections with higher S/N.

Detected fringes were segmented at a cadence of 1 s and incoherently averaged to produce noise-debiased estimates of the correlation coefficients not biased due to the noise and the coherent loss (Rogers et al., 1995). We confirmed that correlation coefficients derived with and without the phase-referencing technique were consistent (see Figure 3.13), indicating that this phase-referencing technique does not bias our amplitude estimates. We also confirmed that the closure phase derived with and without the phase-referencing technique were consistent as expected from its character. In addition, segmented bispectra were also formed at a 10 s cadence and averaged to construct scan-averaged estimates of the closure phase.

The visibilities were calibrated as in Lu et al. (2013) (see also Fish et al., 2011; Lu et al., 2012). Visibilities were a-priori calibrated by multiplying the VLBI correlation coefficient by the geometric mean of the System Equivalent Flux Density (SEFD) of the pair of antennas. Additional instrumental effects on the SMA were

---

[5] http://www.haystack.mit.edu/tech/vlbi/hops.html

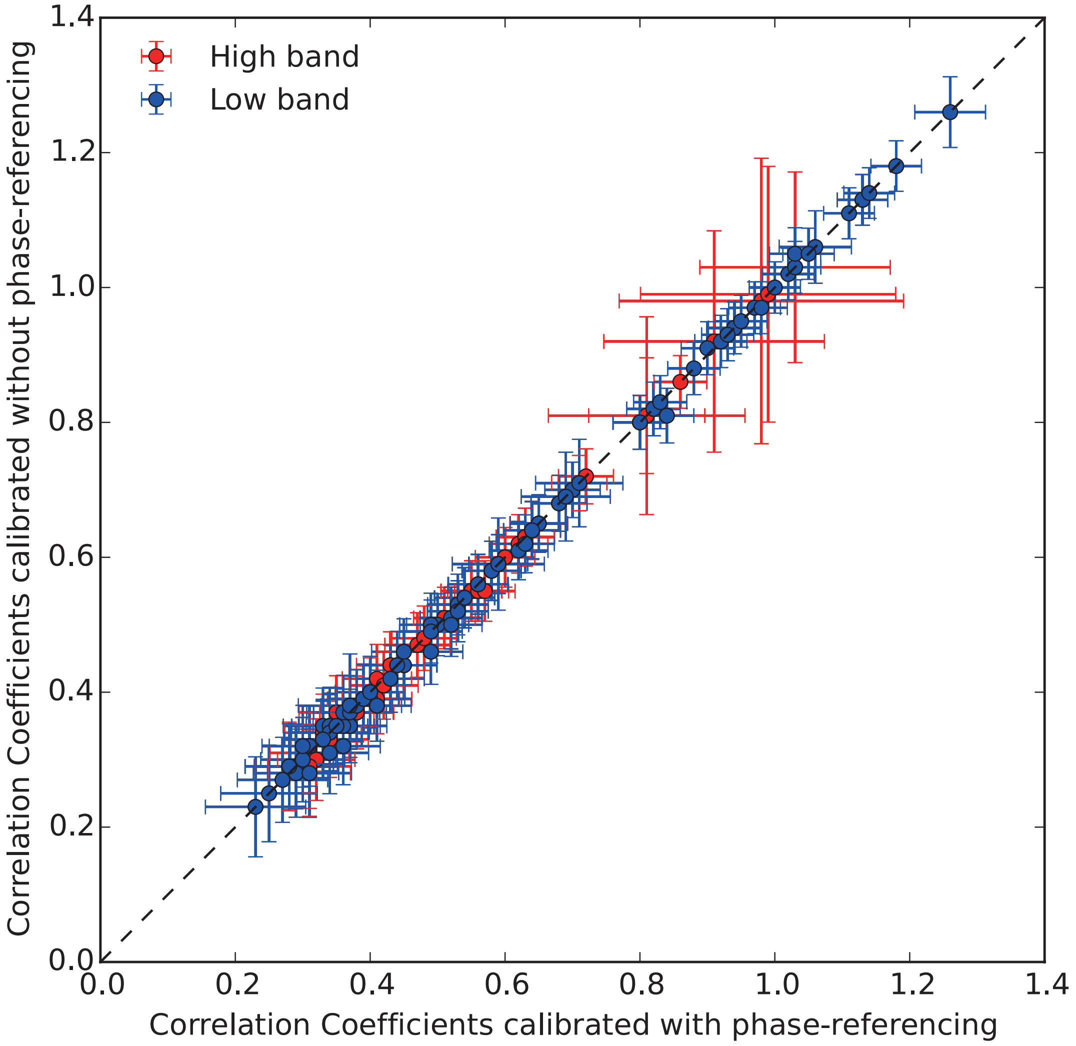

Figure 3.13: The correlation co-efficient of M87 derived with and without phase referencing.

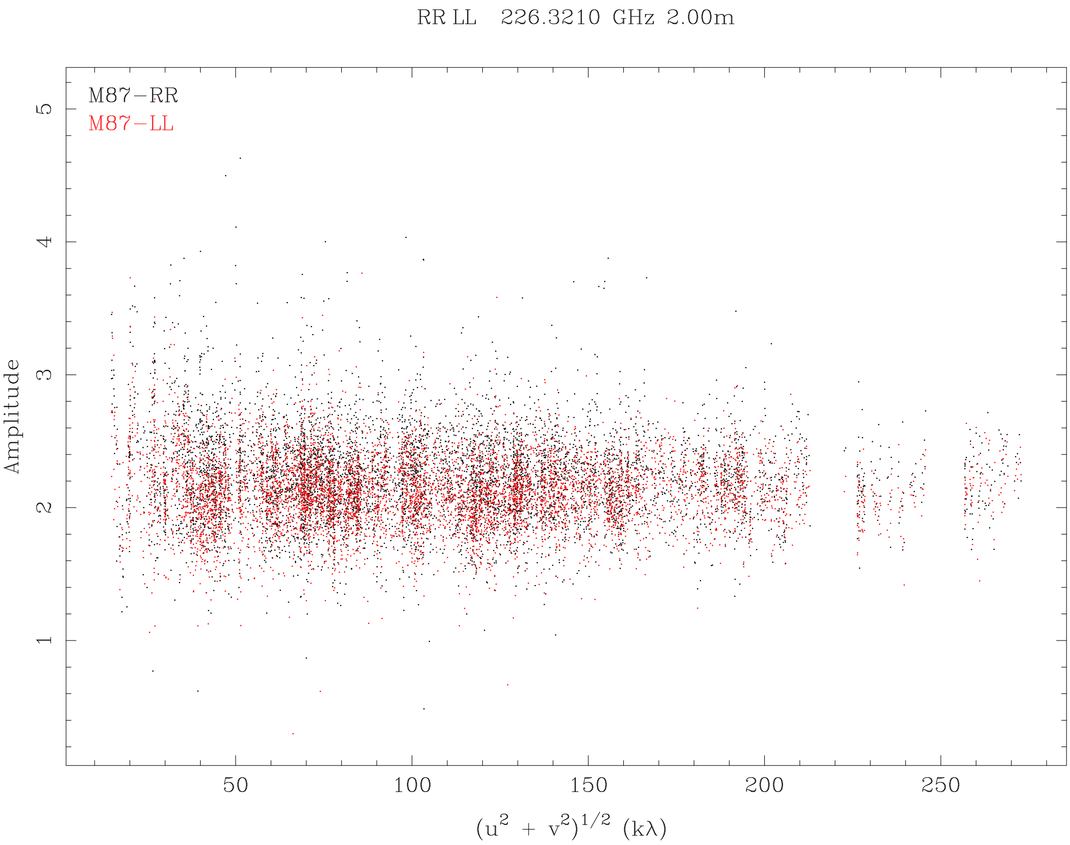

Figure 3.14: The visibility amplitude in CARMA as a function of baseline length.

corrected (see Lu et al., 2013, for details). Finally, visibilities were amplitude self-calibrated assuming that the intra-site VLBI baseline at CARMA (FD) measures the same total flux density as the CARMA interferometer. In principle this assumption could be incorrect due to arcsecond-scale structure in the jet, which could produce the appearance of different correlated flux densities on different baselines within CARMA. However, M87 in 2012 March satisfies our assumption, as the arcsecond-scale jet was dominated by its unresolved (i.e., point-like) radio core (see Figure 3.14), while the radio flux from extended components were < 1 % of the core flux. Thus, the VLBI amplitudes measured on the intra-site FD baseline should be consistent with the core flux density measured with CARMA as a connected array. For each scan, band and site, gains were calculated for each station to maximize self-consistency of the visibilities, including consistency of the calibrated FD flux density with the total flux density measured by CARMA. Calibration errors of 5% have been added in quadrature to the random errors associated with the fringe search and estimation of the correlation coefficient on each baseline. Note that we flagged data on scans when CARMA has a low phasing efficiency due

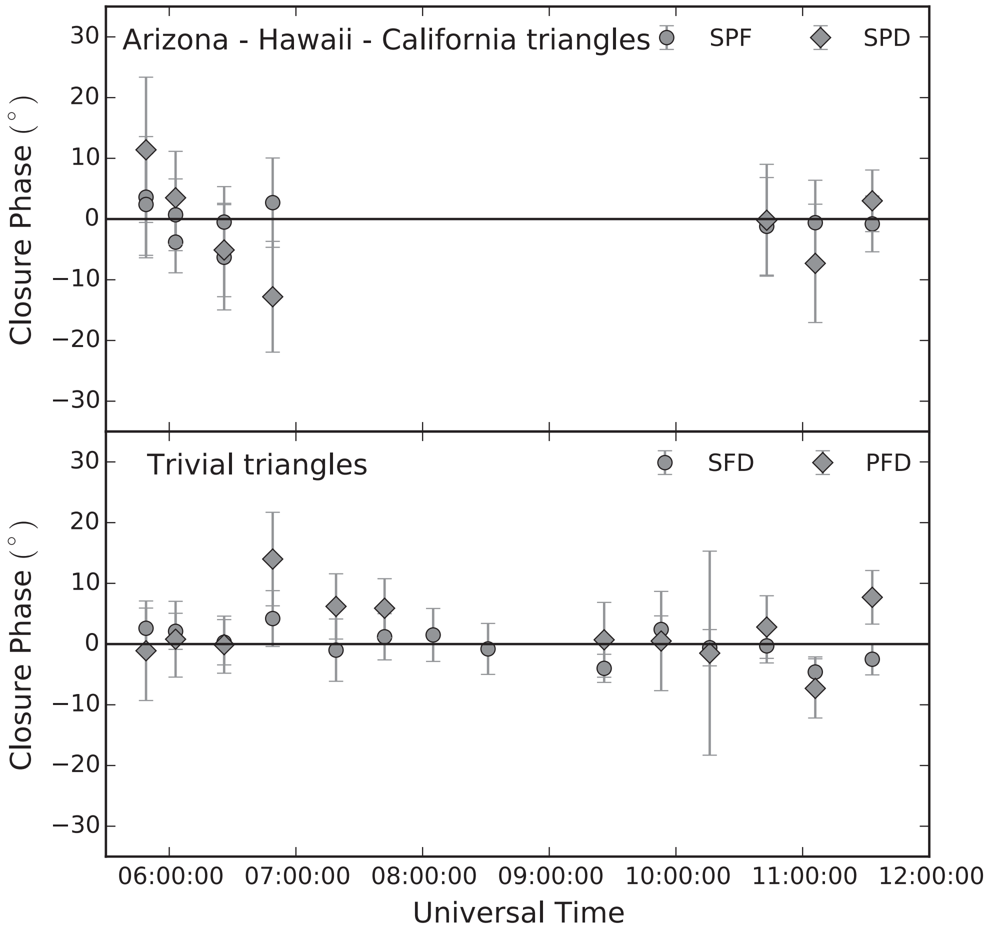

Figure 3.15: The measured closure phase of M87 as a function of time. Errors are 1σ. Upper panel: the closure phase on AZ-CA-HI triangles. Lower panel: the closure phase on trivial triangles, which include an intra-site baseline in CARMA. The closure phase on the trivial triangle is expected to be zero.

to bad weather conditions, showing systematic losses in gain-calibrated amplitudes.

3.5 RESULTS

3.5.1 *First Detections of Closure Phases of M87*

We detected fringes on baselines to all 3 sites, consistent with the results of Doeleman et al. (2012). Furthermore, we detected closure phases on the Arizona-Hawaii-California triangle. Figure 3.15 shows the measured closure phase on the SPF/SPD triangles (upper; hereafter VLBI triangles) and SFD/PFD triangles (lower; hereafter trivial triangles). The average error bar on closure phases is 10.3° for VLBI triangles and 5.0° for trivial triangles. The error-weighted average of the closure phases by the square of S/N is $-0.7^\circ \pm 2.9^\circ$ for VLBI triangles and $-0.1^\circ \pm 0.6^\circ$ for trivial triangles. The closure phase is consistent with zero on trivial triangles, as would be expected if the source is point-like on arcsecond scales. All closure phases on VLBI triangles coincide with zero within 1σ level except 1 data point, which is consistent with zero within 2σ levels. We note that non-detections in VLBI triangles during 7:00-10:00 UTC are attributable to non-detections on the SP baseline (Figure 3.16), possibly due to small visibility amplitudes on SP baselines inferred from geometrical models (see 3.5.2).

3.5.2 *The Geometrical Model of M87*

The correlated flux density of M87 is shown in Figure 3.16 and 3.17. The arcsecond-scale core flux density of 2.2 Jy is $\sim$17 % higher than the 1.9 Jy measured in 2009 (Doeleman et al., 2012). This brightening on arcsecond scales is not accompanied by changes on VLBI scales. The visibility amplitudes are broadly consistent with 2009 results of Doeleman et al. (2012), confirming presence of the event-horizon-scale structure. This indicates that the region responsible for the higher flux density must be resolved out in these observations and therefore located somewhere down the jet.

The most of the missing flux on VLBI scales most likely attributes to the extended jet inside the arcsecond-scale radio core including the bright and stable knots such as HST-1. In the last decade, no radio enhancement was detected in such bright knots except the 2005 VHE flare at HST-1. Even for the exceptionally variable HST-1, the radio flux has been decreasing from the 2005 VHE flare to at least the end of the 2012 event (see Abramowski et al., 2012; Hada et al., 2014). The observed increment in the missing flux seems incompatible with this trend in the bright knot features on arcsecond scales, favoring that the missing flux originates in the vicinity of the radio core on milliarcsecond scales. We discuss it in a physical context related with the 2012 event in §3.6.3.

The structure of M87 is yet not uniquely constrained, since millimeter VLBI detections of M87 remain limited in terms of baseline length and orientation, similar to previous observations in Doeleman et al. (2012). Even with our detections of closure phase, our small data set is consistent with a variety of geometrical models (see §3.6.1 for physically motivated models). It is still instructive to inves-

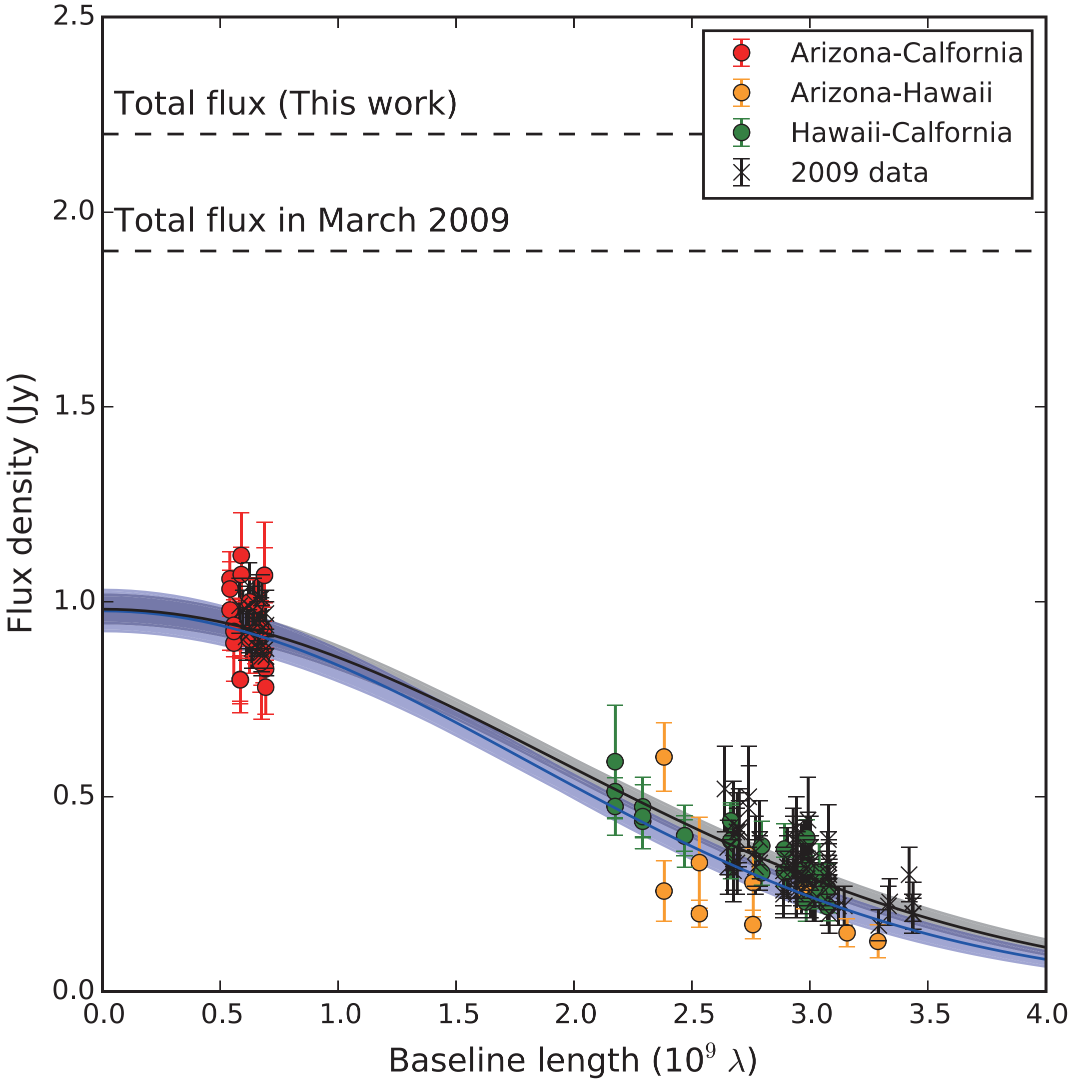

Figure 3.16: The measured correlated flux density of M87 as a function of baseline length. Circles and crosses indicate the correlated flux density observed in 2012 (This work) and 2009 (Doeleman et al., 2012), respectively. Errors are 1σ. The blue line and light-blue region are best-fit models for the 2012 data and 3σ uncertainties on it, respectively, while the black line and gray region are for the 2009 data.

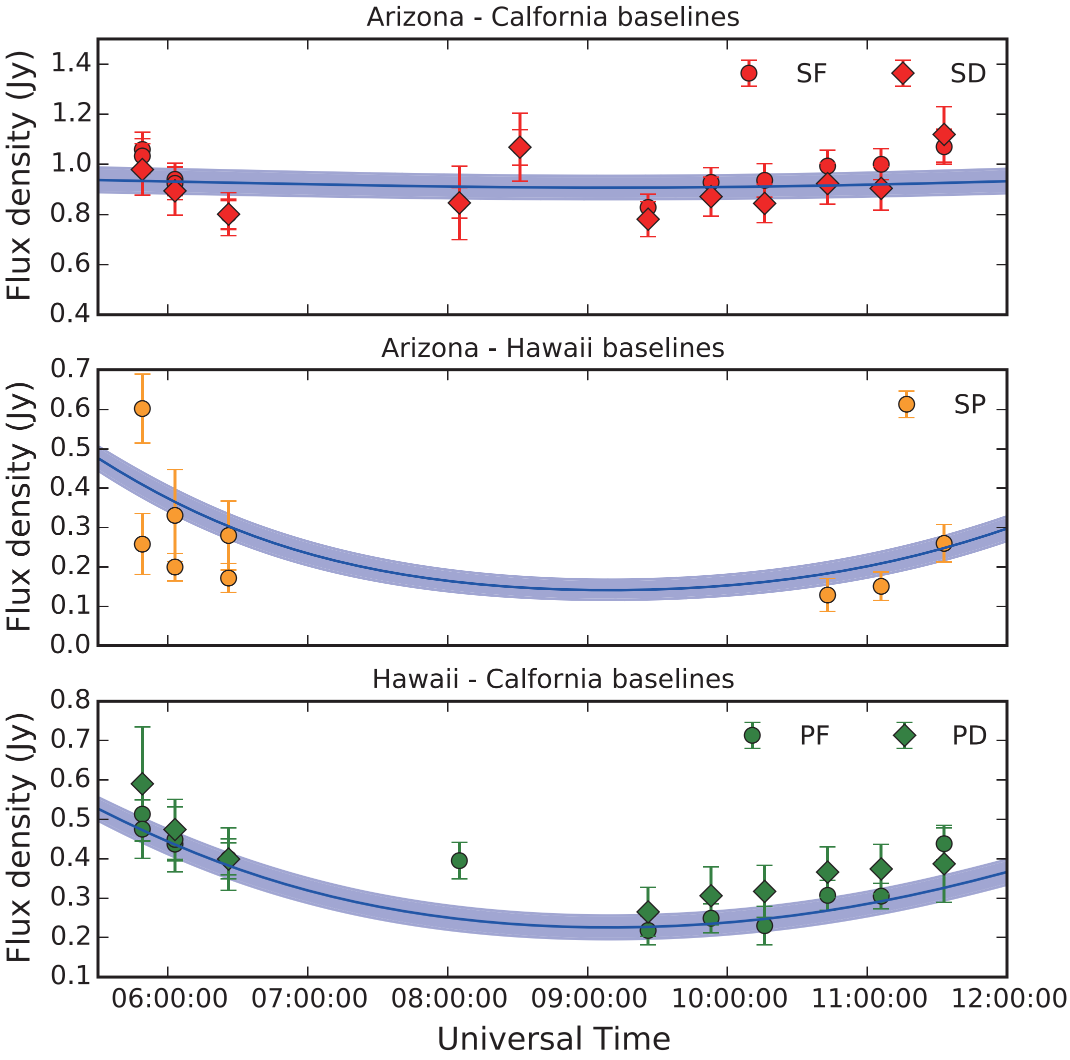

Figure 3.17: The measured correlated flux density of M87 as a function of universal time for each baseline. Circles indicate the correlated flux density observed in 2012 (this work). Errors are 1σ. The blue line and light-blue region are best-fit models for the 2012 data and 3σ uncertainties on it, respectively.

Table 3.2: Geometrical Models of M87. Errors are 3σ.

Model	Date (Year/DOY)	Compact Flux Density (Jy)	FWHM Size (¯as)	χ^2_ν (d.o.f)
2012	2012/81	0.98 ± 0.05	42.9 ± 2.2	2.2 (54)
2009[a]	2009/95-97	0.98 ± 0.04	40.0 ± 1.8	0.6 (102)

[a] Model obtained from all 3 days of data in the 2009 observations.

tigate single-Gaussian models, which inherently predict a zero closure phase, to estimate the flux and approximate size of VLBI-scale structure and compare with the results of the previous observations.

Circular Gaussian fits to the visibility amplitudes on VLBI baselines are shown in Table 3.2. The parameters of the best-fit circular Gaussian model agree with values obtained by Doeleman et al. (2012). The compact flux density of 0.98 ± 0.05 Jy is precisely consistent with the value of Doeleman et al. (2012), while the size of 42.9 ± 2.2 μas (corresponding to 5.9 ± 0.2 R_S) is slightly larger but still consistent within 3σ uncertainty. We find no evidence of significant changes in event-horizon-scale structure between the 2009 and 2012 observations.

3.6 DISCUSSION

3.6.1 *Physical Models for the Structure of 230 GHz Emission*

Physically motivated structural models have been proposed for the Schwarzschild-radius-scale structure at 230 GHz in M87 for both jet and disk models (Broderick & Loeb, 2009; Dexter et al., 2012; Lu et al., 2014). Although all proposed models predict the existence of a feature at the last photon orbit illuminated by a counter jet and/or accretion disk in the close vicinity of the black hole, there are significant differences between model images. The closure phase is an ideal tool to constrain physically motivated models, since relativistic effects such as gravitational lensing, light bending and Doppler beaming generally induce asymmetric emission structure at the vicinity of the central black hole, causing the closure phase to be nonzero.

Figure 3.18 shows images and visibilities of the approaching-jet-dominated models (Broderick & Loeb, 2009; Lu et al., 2014), counter-jet-dominated models (J2 in Dexter et al., 2012), and the accretion-disk-dominated models (DJ1 in Dexter et al., 2012). For jet models, 230 GHz emission structure can be categorized into

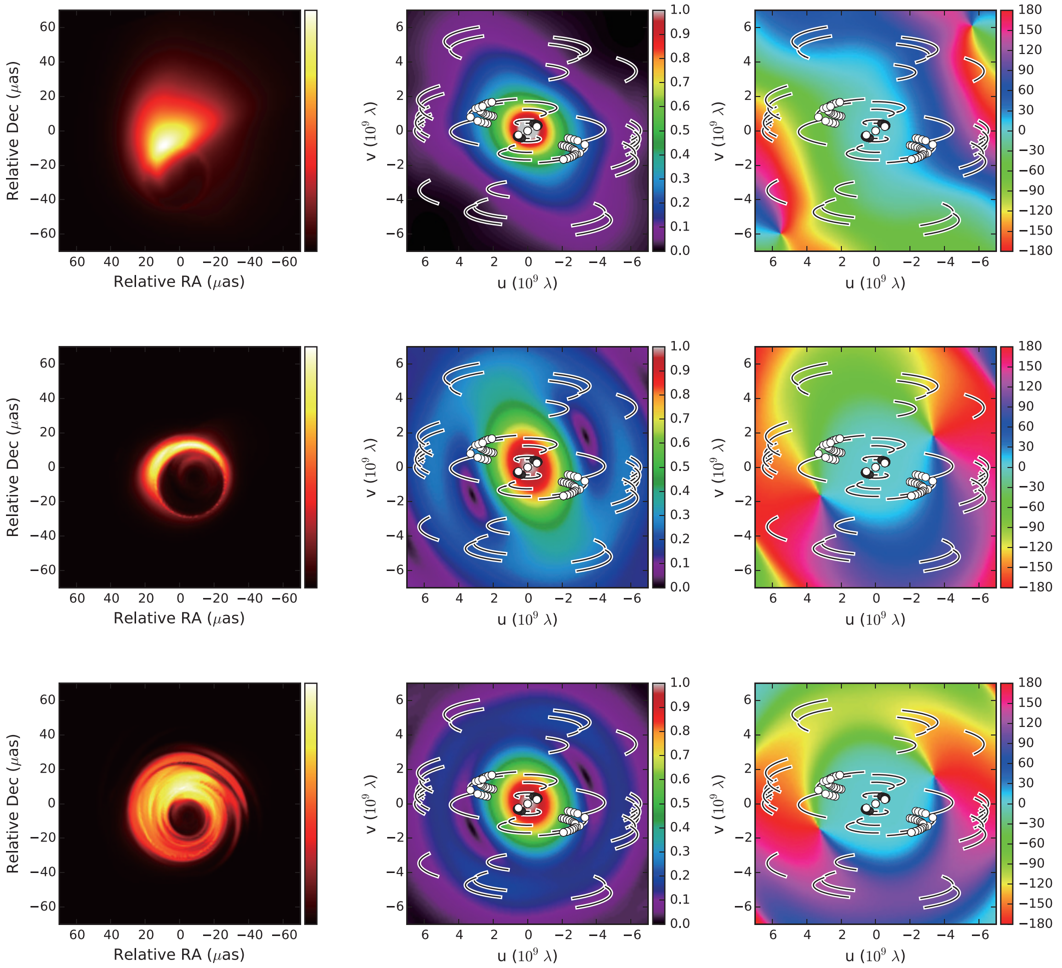

Figure 3.18: Images (left panels) and distributions of the visibility amplitude (middle panels) and visibility phase (right panels) of the physical models for the structure of 230 GHz emission. The white circle points shows the uv-coverage of our observations, while the black lines show the uv-coverage of future observations with current US stations, LMT in Mexico, IRAM 30m telescope in Spain, PdBI in France and ALMA/APEX in Chile. (Top panels) an approaching-jet-dominated model (Broderick & Loeb, 2009; Lu et al., 2014) fitted to 2009 data in Doeleman et al. (2009) (Broderick et al. in prep.). (Middle panels) a counter-jet-dominated model (J2) in Dexter et al. (2012) at a position angle of -70° inferred for the large-scale jet. (Bottom panels) an accretion-disk-dominated model (DJ1) in Dexter et al. (2012) at a position angle of -70° inferred for the large-scale jet.

two types. One is the approaching-jet-dominated models, where emission from the approaching jet is predominant at 230 GHz (Broderick & Loeb, 2009; Lu et al., 2014). The model images consist of bright blob-like emission from the approaching jet and a weaker crescent or ring-like feature around the last photon orbit illuminated by a counter jet. The emission from the approaching jet dominates the 230 GHz emission regardless of the loading radius of non-thermal particles where leptons are accelerated and the jet starts to be luminous, although the crescent-like feature appears more clearly at smaller particle loading radii (see Figure 3 in Lu et al., 2014). In counter-jet-dominated models, the counter-jet emission is predominant instead of the approaching jet. Such a situation could happen if the bright emission region in the jet is very close to the central black hole (within few $R_{\rm s}$) suppressing the approaching jet emission due to gravitational lensing. Photons from the counter jet illuminate the last photon orbit, forming a crescent-like feature. It is worth noting that Dexter et al. (2012) and Lu et al. (2014) have clear differences in their images even at the same particle loading radius of a few $R_{\rm s}$, most likely due to differences in the profiles of non-thermal particles and magnetic fields in their models. The accretion disk models are well characterized by a crescent-like or ring-like feature around the last photon orbit. The 230 GHz emission arises in the inner portion of the accretion flow ($r \sim 2.5\ R_{\rm s}$) near the mid-plane.

Measured closure phases are consistent with these models. In Figure 3.19, we show the model closure phases calculated in the MIT Array Performance Simulator[6] (MAPS) for an approaching-jet-dominated model, a counter-jet-dominated model and an accretion-disk-dominated model in Figure 3.18. The closure phase of the approaching-jet-dominated model is almost zero. On the other hand, the model closure phases of counter-jet-dominated and accretion-disk-dominated models are systematically smaller than observed closure phase in the later GST range, but the models and observed closure phases are consistent within 3-sigma level. We note that the results for counter-jet-dominated and accretion-disk-dominated models shown in Figure 3.18 disagree with Figure 9 of Dexter et al. (2012), due to a mistake in Dexter et al. (2012) in constructing the closure phase triangles.

All three models commonly predict small closure phases on the Hawaii-Arizona-California triangle. Visibility phases on the Arizona-California baseline, which barely resolves the source, are nearly zero. The closure phase on current VLBI triangles

---

[6] `http://www.haystack.mit.edu/ast/arrays/maps/`

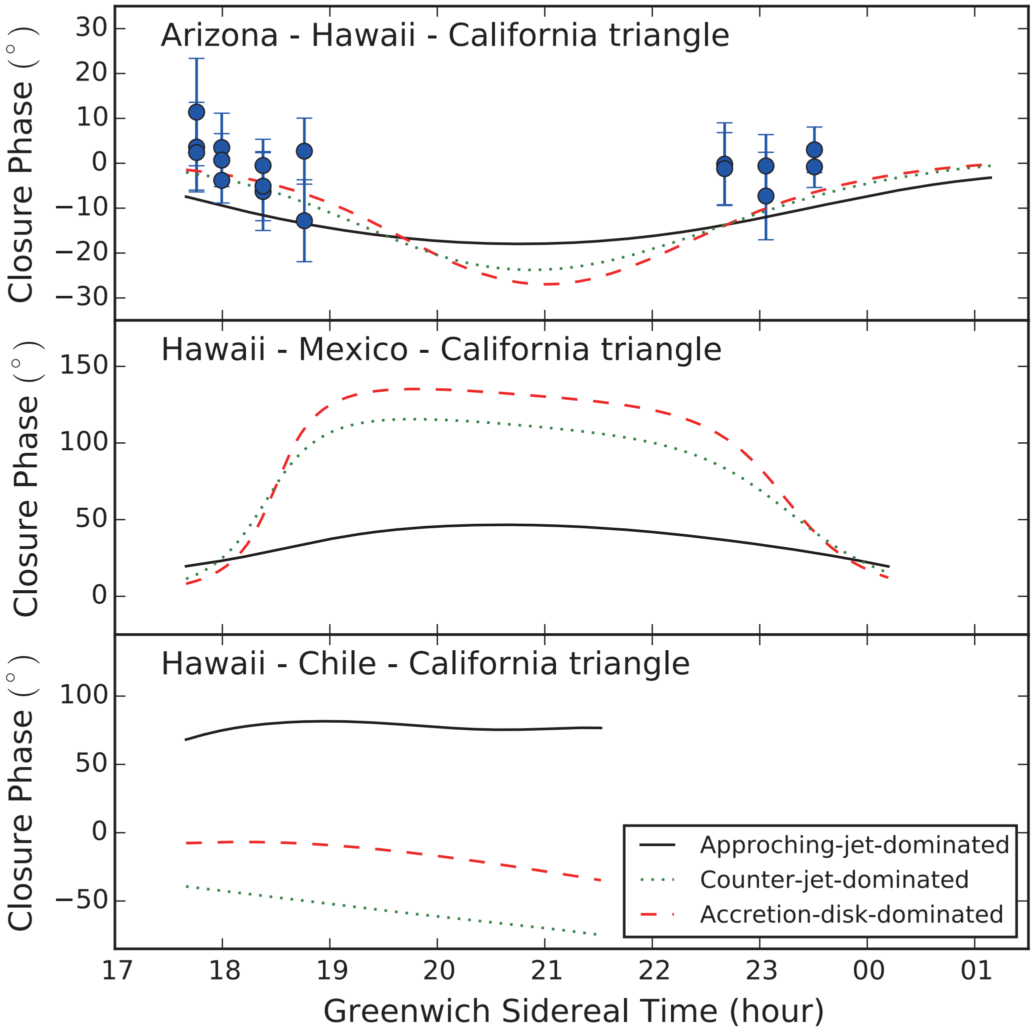

Figure 3.19: The closure phase of models in Figure 3.18 as a function of Greenwich Sidereal Time. The black solid-line shows an approaching-jet-dominated model (Doeleman et al., 2008; Lu et al., 2014) fitted to 2009 data in Doeleman et al. (2012) (Broderick et al. in prep.). The red dashed- and green dotted-lines indicate accretion-disk-dominated and counter-jet-dominated models (DJ1 and J2) in Dexter et al. (2012), respectively, at a position angle of -70° inferred for the large-scale jet. Upper panel: model closure phases on the current VLBI triangle. The circular points are our results shown in Figure 3.15. Middle panel: model closure phases on a triangle including SMA in Hawaii, CARMA in California and LMT in Mexico. Lower panel: model closure phases on a triangle including SMA in Hawaii, CARMA in California and ALMA in Chile.

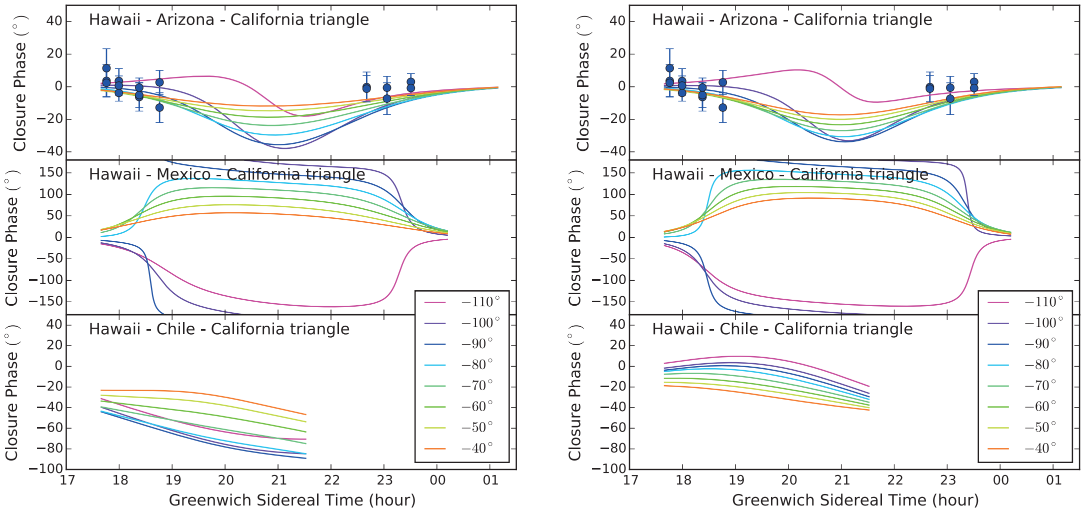

Figure 3.20: The closure phase of counter-jet-dominated (left panel) and approaching-jet-dominated (right panel) models for M87 at broader ranges of the position angles. The closure phases of each model are calculated at position angles ranging from -40° to -110°, considering the opening angle of $\sim 60^\circ$ in the inner jet of M87.

are almost same to differences in the visibility phase between other two baselines. For the case of the approaching-jet-dominated models, the phase gradient between other two baselines is expected to be moderate particularly at large particle loading radii, since emission is blob-like and fairly symmetric on spatial scales corresponding to the current long baselines. Models with a clear crescent-like or ring-like feature generally predict a steep phase gradient around the null amplitude region (see Figure 3.19), which would be detectable not with the current baselines but more longer baselines such as the Hawaii-Mexico baseline.

The position angle of the approaching-jet-dominated model is well-constrained by model-fitting to the visibility amplitudes, while that of the counter-jet- and accretion-disk- dominated models are not well constrained. Considering that the broad opening angle of the jet in the inner $10^2\ R_s$ region ($\sim 60^\circ$ Junor et al., 1999; Ly et al., 2004; Hada et al., 2011, 2013), it is instructive to check consistency with broader ranges of position angles for these models. Figure 3.20 shows closure phases at position angles ranging from -40° to -110° considering its uncertainty attributed to the large opening angle of the inner jet. The closure phases are systematically different by position angles, but still consistent with observed closure phases.

The observed closure phases cannot distinguish between models with different dominant origin of 230 GHz emission on the current VLBI triangle due to the large errors on the data points. However, future observations with a higher recording rate of 16 Gbps can measure the closure phase with an accuracy within a few degrees at 1 minute integration, which can constrain physical models more precisely. In addition, models can be effectively distinguished by near future observations with additional telescopes such as the Large Millimeter Telescope (LMT) in Mexico or the Atacama Large Millimeter/submillimeter Array (ALMA) in Chile. Differences in closure phases between models become more significant on larger triangles, as shown in the middle and bottom panels of Figure 3.19. In addition, the position angle of the jet and/or the disk can be well constrained as shown in Figure 3.20.

While all of the physically motivated models are broadly consistent with the currently measured closure phases and amplitudes, they make dramatically different predictions for forthcoming measurements. Models in which the image is dominated by contributions close to the horizon (counter-jet-dominated and accretion-disk-dominated models) exhibit large closure phases on triangles that include the LMT in stark contrast to those dominated by emission further away (approaching-jet-dominated). This extends to the visibility amplitudes: the compact emission models predict nulls on baselines probed by ALMA and the LMT (see Figure 3.18).

3.6.2 *The Brightness Temperature of the Event-horizon-scale Structure*

New VLBI observations of M87 at 230 GHz in 2012 confirm presence of the event-horizon-scale structure reported in Doeleman et al. (2012). The compact flux density and effective size derived from the circular Gaussian models allow us to estimate the effective brightness temperature of this structure, which is given by (e.g. Akiyama et al., 2013)

$$
\begin{aligned}
T_b &= \frac{c^2}{2k_B\nu^2}\frac{F}{\pi(\phi/2)^2} && (3.2)\\
&= 2.1\times10^{10}\,\mathrm{K}\times\left(\frac{\nu}{230\,\mathrm{GHz}}\right)^{-2}\left(\frac{F}{1\,\mathrm{Jy}}\right)\left(\frac{\phi}{40\,\mu\mathrm{as}}\right)^{-2}, && (3.3)
\end{aligned}
$$

where F, ν and ϕ are the total flux density, observation frequency, and the FWHM size of the circular Gaussian. The effective brightness temperature is $2.04\pm0.15\times10^{10}$ K for the 2009 model and $1.78^{+0.16}_{-0.15}\times10^{10}$ K for the 2012 model, where errors are 3 σ. These brightness temperatures of $\sim 2\times10^{10}$ K are below the upper cut-off in the intrinsic brightness temperature of $\sim 10^{11}$ K on the "inverse Compton catastrophe" argument (e.g. Kellermann & Pauliny-Toth 1969; Blandford & Königl 1979; Readhead 1994). Here, we briefly discuss physical implications for both the jet and accretion disk scenario.

In the case of the jet scenarios, the brightness temperature would not be highly affected by the Doppler beaming, and then not significantly differ from the intrinsic (i.e. not Doppler-boosted) brightness temperature. The brightness temperature is amplified by a factor of δ for an isotropic blob-like source (e.g. Urry & Padovani, 1995). The Doppler factor is $1-3$ at a moderate viewing angle of $15-25^{\circ}$ (e.g. Hada et al., 2011) and the Lorentz factor of $1-2$ in the inner 10^2 $R_{\rm s}$ region (e.g. Asada et al., 2014) inferred for the M87 jet.

Interestingly, the 230 GHz brightness temperature is broadly consistent with the peak brightness temperature of $\sim 10^{9-10}$ K at the radio cores at lower frequencies from 1.6 GHz to 86 GHz (e.g. Dodson et al., 2006; Kovalev et al., 2007; Ly et al., 2007; Asada & Nakamura, 2012; Hada et al., 2012; Nakamura & Asada, 2013a) located within $\sim 10^2$ $R_{\rm s}$ from the jet base (Hada et al., 2011) (see Figure 3.21). This would provide some implications also for the magnetic field structure of the jet. If we assume the radio core surface corresponds to the spherical photosphere of the synchrotron self-absorption at each frequency, the magnetic field strength at the radio core can be estimated by (e.g. Marscher, 1983; Hirotani, 2005; Kino et al., 2014a)

$$B = b(p)\nu^5\phi^4F^{-2}\frac{\delta}{1+z} \propto \nu T_b^{-2}\frac{\delta}{1+z}. \tag{3.4}$$

The constant Doppler factor and brightness temperature give the magnetic field strength roughly proportional to the observation frequency at the radio core (i.e. $B_{\rm core} \propto \nu_{\rm obs}$). Using the frequency-dependence of the radio core position ($r_{\rm core} \propto \nu_{\rm obs}^{-0.59\pm0.09}$; Hada et al., 2011), the magnetic field strength at the radio core is inversely proportional to the distance from the jet base approximately (i.e. $B_{\rm core} \propto r_{\rm core}^{-1}$) in the inner $\sim 10^2$ $R_{\rm s}$. This magnetic field profile can be obtained if the transverse (i.e. nearly toroidal) magnetic field dominates on this scale rather than the longitudinal (i.e. nearly poloidal) field along the conical stream with no velocity gradient under the flux frozen-in condition (Blandford & Königl 1979, and also see §5 in Baum et al. 1997). This profile also can be obtained if the longitudinal field dominates the transverse magnetic field along the paraboloidal stream under the flux frozen-in condition, although recent observations favor the conical stream in the inner $\sim 10^2$ $R_{\rm s}$ (Hada et al., 2013). This suggests that the dominance of

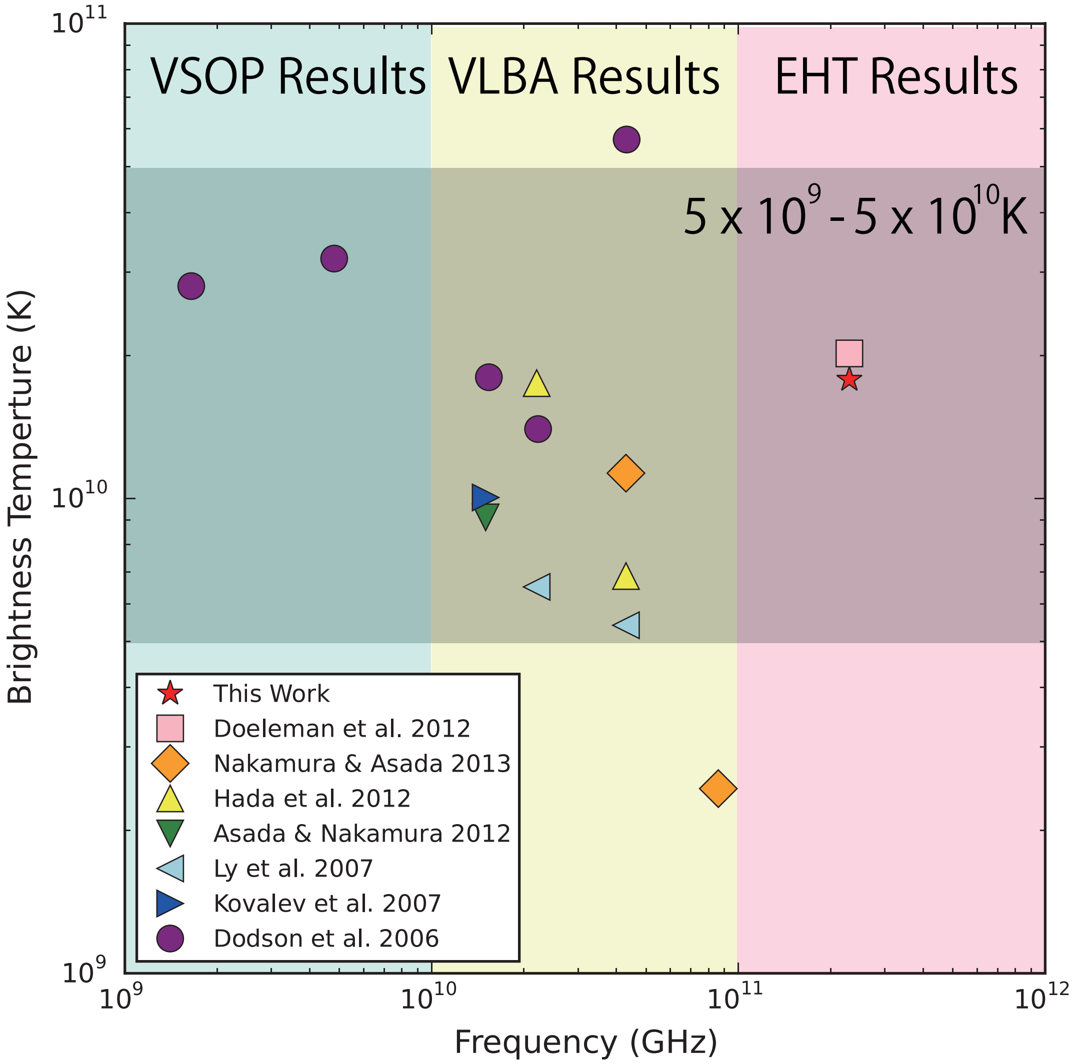

Figure 3.21: The brightness temperature of the radio core as a function of the frequency. The brightness temperature at 230 GHz are derived from the best Gaussian models in Doeleman et al. (2012) and this work. The brightness temperature at lower frequencies are derived from the peak brightness of the images observed with VLBI Space Observatory Programme (VSOP; Dodson et al., 2006) and Very Long Baseline Array (VLBA; Dodson et al., 2006; Ly et al., 2007; Kovalev et al., 2007; Asada & Nakamura, 2012; Hada et al., 2012; Nakamura & Asada, 2013a).

toroidal or poloidal magnetic fields starts to become a major issue on the jet formation in the inner $\sim 10^2\ R_{\rm s}$. Future EHT observations with additional stations and space VLBI observations (e.g. Radio Astron; Kardashev et al., 2013) will provide more detailed structure of the radio core including the profile of the stream line, enabling more precise analysis on the magnetic field structure of the relativistic jet in M87.

The measurements of the brightness temperature also give some implications for the energetics of the jet base. The equipartition brightness temperature (Readhead, 1994) of the non-thermal plasma with the flux density of 1 Jy at 230 GHz is $T_{\rm eq} \leq 10^{12}$ K, where the equality is given if 230 GHz emission is fully optically thick. This gives the ratio between the internal energy of non-thermal leptons and the magnetic-field energy density $U_B/U_e = T_{\rm eq}/T_b \leq 10^2$ (Readhead, 1994). This implies that, if the 230 GHz emission is dominated by optically-thick non-thermal synchrotron emission, the magnetic-field energy dominates the internal energy of the non-thermal particles at the jet base. Recently, Kino et al. (2014b) performed more careful analysis on the energetics at the jet base at 230 GHz, reporting $U_B \gg U_e$ even for partially optically-thick case unless protons are relativistic.

The brightness temperature is broadly consistent with the electron temperature of $\sim 10^{9-10}$ K as expected for RIAF-type accretion disks (e.g. Manmoto et al., 1997; Narayan et al., 1998; Manmoto, 2000; Yuan et al., 2003). The brightness temperature is a factor of $\sim 2-3$ smaller than that of Sgr A* with similar size and higher flux density (Doeleman et al., 2008; Fish et al., 2011). If 230 GHz emission is dominated by thermal synchrotron emission from the accretion disk in both Sgr A* and M87, it seems broadly consistent with a theoretical prediction that a disk with higher accretion rate has a lower electron temperature due to enhanced electron cooling (see Fig.2 in Mahadevan, 1997).

3.6.3 *Implications for the VHE Enhancement in March 2012*

Our observations were performed in the middle of the VHE enhancement reported in Beilicke & VERITAS Collaboration (2012) and Hada et al. (2014). There are several observational pieces of evidence for the existence of a radio counterpart to the VHE enhancement around our observations. First, the onset of the radio brightening at 22 and 43 GHz occurs simultaneously with the VHE enhancement, indicating that the radio and VHE emission regions are not spatially separated. Since the radio brightening starts $\sim 20-30$ days before our observations, 230 GHz emission is also expected to be enhanced at the epoch of our observations. The radio flux measured with the SMA in Hada et al. (2014) indeed shows a local maximum in its light curve during our observations, which is consistent with our results showing a radio flux greater than in April 2009 on arcsecond scales when M87 was in a quiescent state (Abramowski et al., 2012). Second, the radio counterpart was not resolved in the radio core in VERA observations, suggesting that the radio counterpart of the 2012 event should exist near the radio core at 43 GHz located at a few tens of Schwarzschild radii downstream from the central black hole and/or the jet base visible at 230 GHz.

The geometrical model (described in §3.5.2) suggests that there are no obvious structural changes on event-horizon scales between 2009 and 2012, despite the increase in the core flux on arcsecond scales. One plausible scenario for explaining the different behavior between event-horizon scales and arcsecond scales is that the structure of the flare component at 230 GHz has extended structure that is resolved out with the current array. The shortest VLBI baseline in our observations, SMT-CARMA, has a length of 600 Mλ. If we consider the Gaussian-like structure for the flaring region with a radio flux of few $\times$ 100 mJy corresponding to the flux increment at the local peak in the 230 GHz light curve of Hada et al. (2014), the flaring region should be extended enough to have a correlated flux smaller than the standard deviation on SMT-CARMA baselines of ~ 90 mJy so that the increment in the radio flux is not significantly detected on those baselines. The minimum FWHM size can be estimated to be ~ 140 μas ~ 20 $R_{\rm s}$, which has a HWHM size of ~ 600 Mλ in the visibility plane. This limitation is consistent with at least two aspects of VHE flares.

First, the 2-month duration of the 2012 VHE event implies that the size of the emission region is $< 60\delta$ light days $\sim 0.6\delta$ mas, from causality considerations. Similar constraints of < 0.44 mas $\sim 60 R_{\rm s}$ are provided with VERA at 43 GHz in Hada et al. (2014), since the flare component was not spatially resolved during their observations. Combining our measurement with these size limits, the VHE emission region size during our observations is constrained to be in the tight range of $\sim 0.14 - 0.44$ mas, corresponding to $\sim$20 - 60 $R_{\rm s}$.

Second, when the emission region size is larger than ~ 20 $R_{\rm s}$, the emitted VHE photons will not be affected by absorption due to the process of photon-photon pair creation ($\gamma\gamma$-absorption). In principle, γ-ray photons with energy E interact most effectively with target photons in the infrared (IR) and optical photon field of energy (e.g. Rieger, 2011)

$$\varepsilon(E) \sim \left(\frac{E}{1\,\mathrm{TeV}}\right)^{-1}\ \mathrm{eV}. \tag{3.5}$$

Since the 2012 enhancement was detected at $\sim 0.3-5$ TeV in VHE regime (see Beilicke & VERITAS Collaboration, 2012), the target photon wavelength is $\sim 0.4-6\ \mu$m in the near-infrared (NIR) and optical regimes. The optical depth of γ-rays of energy E for the center of an infrared source with a size R and luminosity $L(\varepsilon)$ can be written by (e.g. Neronov & Aharonian, 2007)

$$\begin{aligned} \tau_{\gamma\gamma}(E,R) &\approx \frac{\sigma_T}{5}\frac{L(\varepsilon(E))}{4\pi R^2 c\varepsilon}R \qquad (3.6)\\ &\approx 0.25\left(\frac{L\{[E/(1\,\mathrm{TeV})]\,\mathrm{eV}\}}{10^{40}\,\mathrm{erg\,s^{-1}}}\right)\\ &\quad\times\left(\frac{R}{20\,R_s}\right)^{-1}\left(\frac{E}{5\,\mathrm{TeV}}\right). \qquad (3.7)\end{aligned}$$

The NIR and optical luminosity is $L \sim 10^{40}$ erg s^{-1} within a few tens of parsecs at the nucleus (e.g. Biretta et al., 1991; Boksenberg et al., 1992). Even in the extreme case that the flaring region accounts for all nucleus emission in the NIR and optical regime, the optical depth is smaller than unity at $E <$ a few TeV, where the enhancement was detected in Beilicke & VERITAS Collaboration (2012), for the size of $\sim 20\ R_\mathrm{s}$. This allows γ-ray photons up to a few TeV to escape from the vicinity of the black hole, explaining why the 2012 event was detectable without introducing a special geometry of emission regions. Note that more careful calculation increases $\tau_{\gamma\gamma}$ by a factor of several (Brodatzki et al., 2011; Broderick & Tchekhovskoy et al., 2014), but even in this case the optical depth is smaller than unity for the upper half of the size range ($\sim 40-60\ R_\mathrm{s}$).

The scenario limiting the size to a range of $\sim$20-60 R_s during our observations in the middle of the 2012 event can naturally explain our results and other observational results. It is instructive to compare this scenario to various physical models proposed for the VHE emission in M87 (see Hada et al., 2014; Abramowski et al., 2012, for a review). Here, we briefly discuss general implications for the existing VHE models of M87 based on our scenario.

The size of $\sim$20-60 R_s is presumably incompatible with many existing models assuming extremely compact regions of $\lesssim$ 1-10 R_s, ascribing the VHE emission to particle acceleration in the BH magnetosphere (e.g. Neronov & Aharonian, 2007; Rieger & Aharonian, 2008; Levinson & Rieger, 2011; Vincent, 2014), multiple leptonic blobs in the jet launch/formation region (e.g. Lenain et al., 2008), leptonic models involving a stratified velocity field in the transverse direction (Tavecchio & Ghisellini, 2008), mini-jets within the main jet (e.g. Giannios et al., 2010; Cui et al., 2012), and interactions between a red giant star/gas cloud and the jet base (e.g. Barkov et al., 2010, 2012). These models can reasonably explain the very short variable time scale of $\lesssim$ 1 d in the past three flares in 2005, 2008 and 2010, but are not favored for this particular event in 2012.

Consistency with the size limitation is less clear for models assuming different emission regions or different kinds of emitting particles for radio and VHE emissions, such as hadronic models (e.g. Reimer et al., 2004; Barkov et al., 2010; Reynoso et al., 2011; Barkov et al., 2012; Cui et al., 2012; Sahu & Palacios, 2013). In these models, hadronic particles generally account for VHE emission, while radio emission originates in electrons that are not responsible for the VHE emission. Since the relation between radio and VHE emission has not been well formulated for these models, more detailed consideration including behavior at the low-energy bands is necessary for further discussions.

Consistency with the size limitation is also less clear for some multi-zone leptonic models with a stratified velocity field in radial or transverse directions of the jet by involving the deceleration flow (Georganopoulos et al., 2005) or the spine-layer structure (Tavecchio & Ghisellini, 2008), respectively. Georganopoulos et al. (2005) consider substantial deceleration of the jet on sub-parsec distances from the jet base (see, also Georganopoulos & Kazanas, 2003). VHE emission is produced upstream, while the lower (radio-to-HE) energy emission originates in the decelerating region downstream. The VHE emission can be reproduced when the jet decelerates from $\Gamma \sim 20$ to $\Gamma \sim 5$ at a region within $\Gamma \sim 0.1$ parsec from the jet base. This seems inconsistent with the sub-relativistic speed of $\lesssim 0.2c$ for the flare component derived in Hada et al. (2014). In addition, it also seems incompatible with the recent trend of theoretical MHD jet models (e.g. McKinney, 2006; Komissarov et al., 2007; Nakamura & Asada, 2013a) and recent VLBI observations (Asada et al., 2014) showing that the jet acceleration takes place on the same or larger scales over $10^{2-6}\,R_{\mathrm{S}}$. Furthermore, the radio/VHE correlation is not obvious for this model.

Tavecchio & Ghisellini (2008), on the other hand, involves a relativistic jet spine surrounded by a slower sheath. The lower (radio-to-HE) energy emission in the fast spine dominates emission from the unresolved radio core, while the VHE emission is generated in the slower sheath. The VHE emission in the slower sheath is dominated by external inverse Compton (EC) emission for which the seed photons come from the spine in the case of FR I radio galaxies with relatively large viewing angles (see also the case of Centaurus A and NGC 1275, Ghisellini et al., 2005; Tavecchio & Ghisellini, 2014). The coincident radio/VHE correlation could be explained by the relation of the spine and sheath emission through this EC process, but it is not yet clear because the seed photons for the EC emission in VHE regime are mainly IR photons and the radio emission of the source is considerably lower than the flux density observed with VLBI. In addition, the source size in the fast spine is compact ($< 10\ R_{\rm S}$) and seems incompatible with our scenario. Such multi-zone leptonic approaches including compact multi-blob models (e.g. Lenain et al., 2008) could possibly explain all observed properties of the 2012 event with some modifications, but more extended theoretical consideration would be required to explain at least (i) the relatively extended source size and (ii) the clear radio/VHE correlation.

Interestingly, a homogeneous one-zone synchrotron self-Compton (SSC) model (i.e. the standard leptonic model) predicts a comparable source size ($\sim$ 0.1 mas) to our scenario for a broadband SED in a relatively moderate state (Abdo et al., 2009). It also can naturally explain the radio-VHE connection in Hada et al. (2014). The simple leptonic one-zone SSC model seems more plausible than other existing models to explain some properties such as the size constraint and the radio-VHE connection, but further dedicated modeling for the 2012 event would be required to test consistency with overall observational properties such as the broadband SED, which is not discussed here. Note that leptonic models might be problematic for explaining the hard VHE spectrum, which is common in the previous three VHE flares and the 2012 events, against the Klein-Nishina and γ-ray opacity effects softening the VHE spectrum (see, discussions in Tavecchio & Ghisellini, 2008).

Our new observations clearly show that short-mm VLBI is an useful tool to constrain the size of the radio counterpart, which is a new clue to understand the VHE activities in M87. In particular, new constraints can be obtained by combining simultaneous EHT observations with measurements of VHE spectra at $\gtrsim$ 10 TeV highly affected by $\gamma\gamma$-absorption (see, Eq.(3.7)) with the Cherenkov Telescope Array (CTA, Actis et al., 2011). In addition, the complementary dedicated monitoring with lower frequency monitoring on mas and arcsec scales is also important to study details on radio/VHE connections and also constrain on the important physical parameters.

3.7 SUMMARY

New VLBI observations of M87 at 230 GHz wavelength in 2012 confirm presence of the event-horizon-scale structure reported in Doeleman et al. (2012). We summarize our results as follows;

1. For the first time, we have acquired 230 GHz VLBI interferometric phase information on M87 through measurement of closure phase on the triangle of long baselines. Measured closure phases are consistent with 0°, as expected by physically-motivated models for 230 GHz structure such as jet models and accretion disk models. Although our observations cannot currently distinguish the models, we show that future closure phase/amplitude measurements with additional stations and greater sensitivity can effectively distinguish and put a tight constrain on physical models.
2. The brightness temperature of the event-horizon-scale structure is $\sim 2 \times 10^{10}$ K both for previous observations (Doeleman et al., 2012) and our new observations. This brightness temperature is broadly consistent with that of the radio core at lower frequencies from 1.6 to 86 GHz located in the inner $\sim 10^2\ R_{\rm S}$. We demonstrated a simple analysis assuming that the observed radio core is the photosphere of synchrotron self-absorption. It shows that the constant brightness temperature may give the magnetic-field profile of $B \propto r_{\rm core}^{\sim -1}$ in the inner $\sim 10^2\ R_{\rm S}$, consistent with a prediction of the conical jet with no velocity gradient dominated by the toroidal magnetic field. This indicates that more precise imaging of the radio core with future EHT and space VLBI can address the magnetic field profile in the inner $\sim 10^2\ R_{\rm S}$ crucial for understanding the jet formation.
3. Our observations were conducted in the middle of a VHE enhancement originating in the vicinity of the central black hole. The effective size derived from our data and results of lower-frequency observations favor the relatively extended size of VHE emission region of $\sim$20-60 $R_{\rm S}$. This would not favor VHE emission models that predict a compact emission region of $\lesssim$ 10 $R_{\rm S}$ for this event.

4

MICROARCSECOND-SCALE STRUCTURE OF THE RELATIVISTIC JET IN NRAO 530 AFTER A GEV γ-RAY FLARE

4.1 REVIEW: γ-RAY EMISSION FROM THE BLAZARS

Non-thermal emission in the relativistic jet launched from super-massive black holes (SMBHs) dominates at a wide range of electromagnetic spectrum from radio to γ-rays of many Active Galactic Nuclei (AGNs). In particular, the relativistic jet in AGNs is predominant in the extragalactic γ-ray sky, and has been identified as one of the most popular γ-ray sources in the Universe (Nolan et al., 2012).

The blazars are the most extreme class of AGNs, where the jet is viewed from the direction very close to our line of sight. The whole emission spectra of blazars is dominated by emission from the approaching side of the jet, which is highly amplified by the Doppler beaming effect (e.g. Urry & Padovani, 1995). This indicates that the source is dominated by the jet properties, and then suitable for probing the physical nature of the relativistic jet with multi-frequency observations. Blazars are the most dominant γ-ray source in the Universe occupying more than 97% of γ-ray AGNs detected so far (Nolan et al., 2012).

The broadband SEDs of blazars have an unusual shape dominated by two bumps of the non-thermal emission from the jet (Figure 4.1). The synchrotron emission dominates the lower energy side from radio to X-ray, while the inverse Compton emission dominates the higher energy side from X-ray to γ-ray up to MeV, GeV

---

[1] G. Ghisellini's talk in HEPRO III: `http://icc.ub.edu/congress/HEPROIII-2011/`

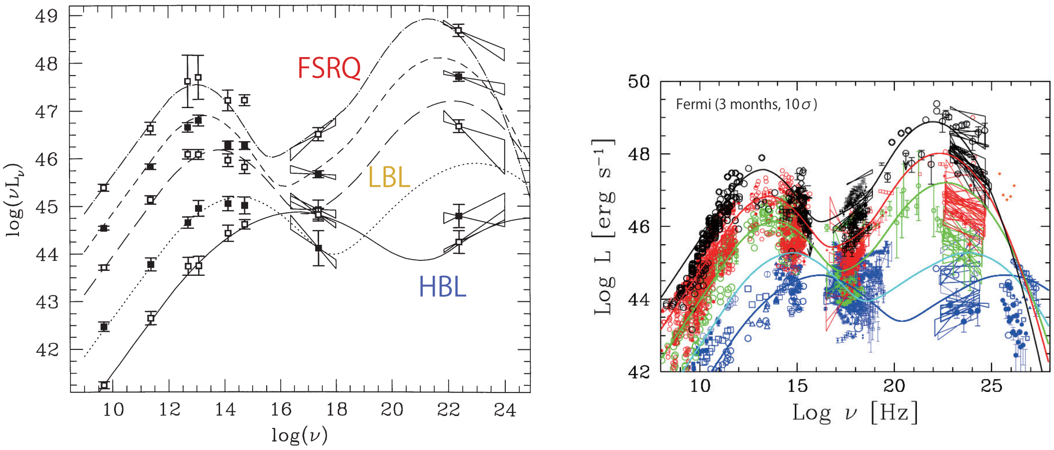

Figure 4.1: A composite of averaged SEDs of blazars and the blazar sequence. (Left panel) Original plot of the blazar sequence (Fossati et al., 1998). (Right panel) The blazar sequence in the *fermi* era (Ghisellini 2011[1])

and sometimes TeV energies. The SEDs of blazar are known to have an interesting systematic trend so-called the "*blazar sequence*" (Fossati et al., 1998; Donato et al., 2001); more luminous blazars tend to have lower peak frequencies of both synchrotron and inverse Compton (IC) emission (Figure 4.1). The lower side of blazars, i.e. BL Lac objects are categorized into subclasses based on the blazar sequence. BL Lac objects with the synchrotron peak in UV or X-ray regime is called *High-energy peaked BL Lac object* (HBL), while ones with the peak in IR or optical regime is called *Low-energy peaked BL Lac objects* (Fossati et al., 1998). In the Fermi era, more generalized subclasses for blazars started to be used: LSP (*Low-Synchrotron-Peaked*), ISP (*Intermediate-Synchrotron-Peaked*) and HSP (*High-Synchrotron-Peaked*) blazars (see Abdo et al., 2010c, for thier definitions) for avoiding confusions.

The multi-wavelength SED of blazars can be broadly explained by one-zone models assuming that the broadband emission originated a single, homogeneous emission region with uniform magnetic-field strength and electron energy distributions. For fainter blazars, i.e. HSP blazars (or IBL/HBL), the SEDs can be well explained by the synchrotron self-Compton model (SSC), in which the seed photons for the IC process are the synchrotron photons produced by the same population of relativistic electrons (e.g. Kino et al., 2002). On the other hand, for luminous blazars, i.e. ISP or LSP blazars (or FSRQ/LBL), the SEDs can be well explained by the external radiation Compton (ERC; or more simply external Compton; EC) model, in which the seed photons for the IC process are typically UV photons generated by the standard disk surrounding the SMBH, and reflected toward the jet by the BLR within a typical distance from the accretion disk of the order of 1 pc

(Sikora et al., 1994). If the emission occurs at larger distances, the external radiation is likely to be IR photons from a dusty torus (Sikora et al., 2002).

Many physical quantities are investigated for blazars in conventional framework of one-zone synchrotron-self Compton (SSC) and/or external Compton (EC) models. For example, γ-ray emission is ascribable to the region with a size of sub-parsecs or even smaller size (Kubo et al., 1998) possibly close to the jet base with a Doppler factor of ~ 10. However, the location and formation process of such luminous region have been long-standing issues, relative to production mechanisms of relativistic particles in the relativistic jet which are some of the most intriguing questions in astrophysics.

VLBI is an essential tool to identify the radio counterpart of γ-ray emission site in AGN jets. High spatial resolution of VLBI is useful to constrain the location of γ-ray emission relative to the jet structure. In addition, VLBI is an unique tool to measure the motion of the jet, allowing us to investigate whether the high-energy emission is beamed with the same Lorentz factor as indicated by kinematics measured with VLBI.

After the launch of the Fermi satellite, multi-wavelength observations have been intensively performed to investigate the nature of high energy emission regions. VLBI actually has played an important role to determine the site of GeV γ-ray emission, revealing variety of the locations of the emission region relative to the 7-mm core even in the same source; *upstream* of the 7-mm core: BL Lacertae: Marscher et al. 2008, PKS 1510-089: Marscher et al. 2010, etc; *dowstream* of the 7-mm core: OJ-287: (Agudo et al., 2011a), AO 0235+164 (Agudo et al., 2011b), PKS 1510-089 (Orienti et al., 2013), etc.

On the other hand, the trajectory of the flaring component has been one of the key issues to understand the observational properties of the γ-ray flares and high-activity state in blazars. Recent observational studies reported large rotations ($\gtrsim 180^\circ$) of the optical electric vector position angle (EVPA) in blazars in connection with γ-ray flares and high-activity states (e.g. BL Lacertae: Marscher et al. 2008; 3C 279: Abdo et al. 2010b, Hayashida et al. 2012, Aleksić et al. 2014; PKS 1510-089: Marscher et al. 2010; 3C 454.3: Sasada et al. 2012). These long, coherent rotations in EVPA have been interpreted as the signature of a global field topology (e.g. Marscher et al., 2008, 2010) or the curved trajectory of the jet (e.g. Abdo et al., 2010b; Hayashida et al., 2012; Aleksić et al., 2014), which are traced by a moving emission feature.

Short-millimeter ($\lambda \lesssim 1.3$ mm, $\nu \gtrsim$ 230 GHz) VLBI observations with EHT has been expected to provide important clues to understand the nature of γ-ray emission. First, its spatial resolution can reach at a few tens of microarcseconds corresponding to $\lesssim 0.1$ pc at $z \lesssim 2$, where most of *fermi*-detected AGNs exhibit (Ackermann et al., 2011a). This provides a potential to directly measure the size and detailed structure of high-energy emission region as well as the trajectory of the jet around it, which are key parameters in previous SED modeling (e.g. Abdo et al., 2010b; Hayashida et al., 2012; Aleksić et al., 2014). Second, observations at shorter wavelength are less affected by synchrotron self-absorption (SSA) effects, providing a deeper view of the relativistic jet (Lobanov, 1998). Previous studies revealed a delayed brightening of the radio flux density at lower frequencies that can be attributed to stronger SSA effect at the high γ-ray state (e.g. Orienti et al., 2013; Hada et al., 2014), suggesting that shorter-wavelength observations are desirable to investigate the jet structure in connection with γ-ray emission. In this chapter, we present the first EHT observations following up an active γ-ray state in the blazar NRAO 530.

4.2 SCOPE OF STUDIES IN THIS CHAPTER

NRAO 530 (also known as PKS 1730-130) is a well-known blazar at z=0.902 (Junkkarinen, 1984) classified as a flat spectrum radio quasar (FSRQ) and low-synchrotron-peaked (LSP) source (Ackermann et al., 2011a). NRAO 530 has a strong variability at various wavelength such as radio (e.g. Bower et al., 1997), optical (e.g. Webb et al., 1988), X-ray (e.g. Foschini et al., 2006) and γ-ray regime (e.g. Mukherjee et al., 1997; D'Ammando & Vandenbroucke, 2010). In γ-ray regime, NRAO 530 was identified with EGRET source 2EG 1735-1312(Thompson et al., 1995). After the launch of *fermi*, it did not appear as a bright source (Abdo et al., 2009) but as a relatively quiescent source (1FGL J1733.0-1308 and 2FGL J1733.1-1307; Abdo et al. 2010a and Ackermann et al. 2011a, respectively). However, its γ-ray activity increased at the latter half of 2010 at GeV band, and NRAO 530 flared in late-2010 (D'Ammando & Vandenbroucke, 2010) accompanied with flux enhancement in the radio core at 22 GHz (Nagai et al., 2013).

On parsec scales, NRAO 530 has a core-jet structure directed into the north from the core at radio band. Space VLBI observations with VLBI Space Observatory Programme (VSOP) revealed a brightness temperature of $\sim 2 - 3 \times 10^{12}$ K at 5 GHz, significantly in excess of the upper limit on inverse Compton catastrophe argu-

Table 4.1: Observatories of EHT observations in 2011

2011 observations (DOY 88, 90, 91, 92 and 94)				
Site	Observatory	Char.	DOY	Note
Arizona	ARO/SMT	S	88-94	Single 10 m dish
California	CARMA	C	88-94	Single 10.4 m dish, high band replaced by F on DOY 90-94
California	CARMA	D	88-94	Single 10.4 m dish
California	CARMA	F	91-94	Phased sum of three 10.4 m and four 6.1 m dishes
Hawaii	JCMT	J	88	Single 15 m dish
Hawaii	CSO	O	91-94	Single 10.4 m dish
Hawaii	SMA+CSO/JCMT	P	88-94	Phased sum of seven 6 m dishes and CSO (day 88)/JCMT (DOY 90-94)

ments (Bower & Backer, 1998b; Horiuchi et al., 2004). Superluminal motions of several jet components have been detected with apparent velocities in the range of 2-40 c (Bower et al., 1997; Jorstad et al., 2001; Feng et al., 2006; Hong et al., 2008; Lu et al., 2011). Previous studies indicated that the jet of NRAO 530 has an oscillating trajectory on a scale of $\sim$ 30 mas (e.g. Hong et al., 1999; Feng et al., 2006) and the non-ballistic motion and change of the jet orientation in the inner jet within a few mas from the southern core (Lu et al., 2011).

In this chapter, we report on 1.3 mm VLBI observations of NRAO 530 with EHT in April 2011, roughly 6 months after the above-mentioned GeV γ-ray flare. Observations impose new constraints on γ-ray emission models through the first measurements of the innermost structure of the relativistic jet at 1.3 mm just after the active state in GeV γ-ray regime. Throughout this chapter, we adopt the following cosmological parameters; $H_0 = 71$ km s^{-1} Mpc^{-1}, $\Omega_M = 0.27$ and $\Omega_\Lambda = 0.73$ (Komatsu et al., 2009), leading 1 mas = 7.818 pc = 2.412×10^{19} cm for NRAO 530.

4.3 OBSERVATIONS

NRAO 530 and other sources (3C 273, 3C 279, 3C 345, 3C454.3, 1633+382, 1749+096, 1921-293, M 87, BL Lac, Sgr A*) were observed with the seven telescopes at three sites in 2011 on the nights of March 29, 31 and April 1, 2 and 4 (DOY 88, 90, 91, 92 and 94) as summarized in Table 4.1: the Arizona Radio Observatory's Submillimeter Telescope (ARO/SMT) on Mt. Graham in Arizona, both two single antennas and a phased array of Combined Array for Research in Millimeter-Wave Astronomy (CARMA) on Cedar Flat in California, and Caltech Submillimeter Observatory(CSO), James Clerk Maxwell Telescope (JCMT) and a phased array of Submillimeter Array (SMA; Ho et al. 2004) with CSO/JCMT on Mauna Kea in Hawaii. Here we focus on NRAO 530; the results on 3C 279 were reported in Lu et al. (2013), and others will be presented elsewhere.

Observations were performed at two bands centered at 229.089 and 229.601 GHz (low and high band) with 480 MHz bandwidths. All telescopes observed left-hand circular polarization (LHCP). Reconfigurable Open Architecture Computing Hardware (ROACH)[2] digital backends (RDBE) designed at MIT Haystack Observatory and National Radio Astronomy Observatory were used for all single-antenna stations. Data were recorded onto modules of hard drives using the Mark 5B+ for RDBE systems. SMA and CARMA sites were equipped with 1 GHz bandwidth adaptive beamformers, built using an older generation of Collaboration for Astronomy Signal Processing and Electronics Research (CASPER)[3] technology. The beamformers compensate group delay and phase at each antenna in the array in real time, thereby recording a single data stream representing the coherent phased array sum of all antennas. The real time corrections are derived from simultaneous cross-correlations, and the data are formatted for Mark5B+ recorders at 4 Gb/s rate. Hydrogen masers were used as timing and frequency references at all sites, with an exception that the 10 MHz reference signal for the 1024 MHz sampler clock in the digital back ends at CARMA was erroneously derived from a local rubidium oscillator instead of the hydrogen maser on DOY 88-92. Data were correlated with the Haystack Mark 4 VLBI correlator.

4.4 DATA REDUCTION

4.4.1 *EHT Data at 1.3 mm*

Correlated data were analyzed using the Haystack Observatory Post-processing System (HOPS)[4]. Initial coherent baseline fringe fitting was done using the HOPS task `fourfit`. Detections with high S/N were used to determine several important quantities for further processing. First, we derived the phase offsets between the 32 MHz channels within each band. Second, approximate atmospheric coherence times maximizing the S/N of detection were calculated to guide further incoherent fringe searching in the HOPS task `cofit`. Third, the residual single-band delay, multi-band delay, and delay rate were used to set up narrow search windows for each source to assist in fringe finding. Detected fringes were segmented at a cadence of 1 s and averaged to produce noise-debiased estimates of the correlation coefficients. In addition, segmented bispectra were also formed at a 10 s cadence and averaged to construct scan-averaged estimates of the closure phase.

---

[2] https://casper.berkeley.edu/wiki/ROACH

[3] https://casper.berkeley.edu

[4] http://www.haystack.mit.edu/tech/vlbi/hops.html

We used a modified version of `fourfit` in initial fringe fitting to correct small delay and frequency drifts in 2011 data including exactly one CARMA station on DOY 88-92, due to the erroneous use of the rubidium standard to drive the sampler clocks at CARMA on these days (see Lu et al., 2013, for details on this issue). We found that these effects could be compensated by introducing an additional multi-band delay drift term along with an orthogonal local oscillator frequency offset. An analysis of high S/N scans indicated that the delay drift could be approximated as a linear variation within each scan lasting several minutes. The rates of the delay drift were determined on a scan-by-scan basis by maximizing the S/N of the SMT-CARMA baselines (SC, SD and SF) generally with the highest S/N baselines to CARMA thanks to their relatively short baseline length not resolving out as much source emission as the Hawaii-CARMA baselines. The modified version of `fourfit` removed the delay drift values determined in these ways before fringe fitting. The residual delay drift values are typically 0.2 ns during a 4 minute scan, resulting in a phase change of about 35° across the 480 MHz band. This causes a coherence loss of $\sim$ 2 % in the visibility amplitude, which is less than uncertainties imposed by calibration.

The visibilities were calibrated as in Lu et al. (2013) (see also Fish et al., 2011; Lu et al., 2012; Akiyama et al., 2014b). Visibilities were a-priori calibrated by multiplying the VLBI correlation coefficient by the geometric mean of the System Equivalent Flux Density (SEFD) of the pair of antennas. Additional amplitude loss effects on baselines with phased-SMA (P) were corrected (see Lu et al., 2013, for details). Finally, visibilities were amplitude self-calibrated assuming that the intra-site VLBI baseline at CARMA (FD) measures the same total flux density as the CARMA interferometer. Indeed, NRAO 530 appears as a point source in its CARMA interferometric image, requiring that the VLBI amplitudes measured on the intra-site CD/FD baseline is consistent with the arc-second-scale flux density measured with CARMA as a connected array. For each scan, band and site, gains were calculated for each station to maximize self-consistency of the visibilities, including consistency of the calibrated FD flux density with the total flux density measured by CARMA. Calibration errors of 5% have been added in quadrature to the random errors associated with the fringe search and estimation of the correlation coefficient on each baseline.

4.4.2 *Multi-wavelength Data-sets*

In addition to EHT data at 1.3 mm, we reduced multi-wavelength VLBI data at lower frequencies and SMA interferometric data at 1.3 mm for checking consistency to our EHT data and scientific interpretation. We briefly summarize multi-wavelength data-sets in the following subsections.

4.4.2.1 *VLBA Data at 7 mm*

NRAO 530 has been monthly monitored at 7 mm with the Very Long Baseline Array (VLBA) by the Boston University group. These data have been reduced in the same manner as described in Jorstad et al. (2005). Calibrated visibilities are available in the website of the Boston University group[5]. We fitted a sequence of circular Gaussians to calibrated visibilities using the DIFMAP software package (Shepherd et al., 1994).

4.4.2.2 *SMA Data at 1.3 mm*

The 230 GHz (1.3 mm) light curve was obtained at SMA near the summit of Mauna Kea (Hawaii). NRAO 530 is included in an ongoing monitoring program at SMA to determine the flux densities of compact extragalactic radio sources that can be used as calibrators at mm wavelengths (Gurwell et al., 2007). Observations of available potential calibrators are conducted for 3 to 5 minutes, and the measured source signal strength is calibrated against known standards, typically solar system objects (Titan, Uranus, Neptune, or Callisto). Data from this program are updated regularly and are available at SMA website[6]. Most of SMA measurements were obtained in its compact array configuration and the typical angular resolution is about $\sim$3 arcseconds.

4.5 RESULTS AND DISCUSSIONS

4.5.1 *Source Structure at 1.3 mm in 2011 Observations*

Figure 4.2 shows the calibrated visibility amplitudes, closure phases, and uv-coverage of EHT observations. We detected on all baselines and then robust closure phases on the VLBI triangles, which involve all three sites. The closure phase is consistent with zero on trivial triangles involving intra-site baselines (CD, FD in California and

---

[5] `https://www.bu.edu/blazars/research.html`

[6] `https://www.bu.edu/blazars/research.html`

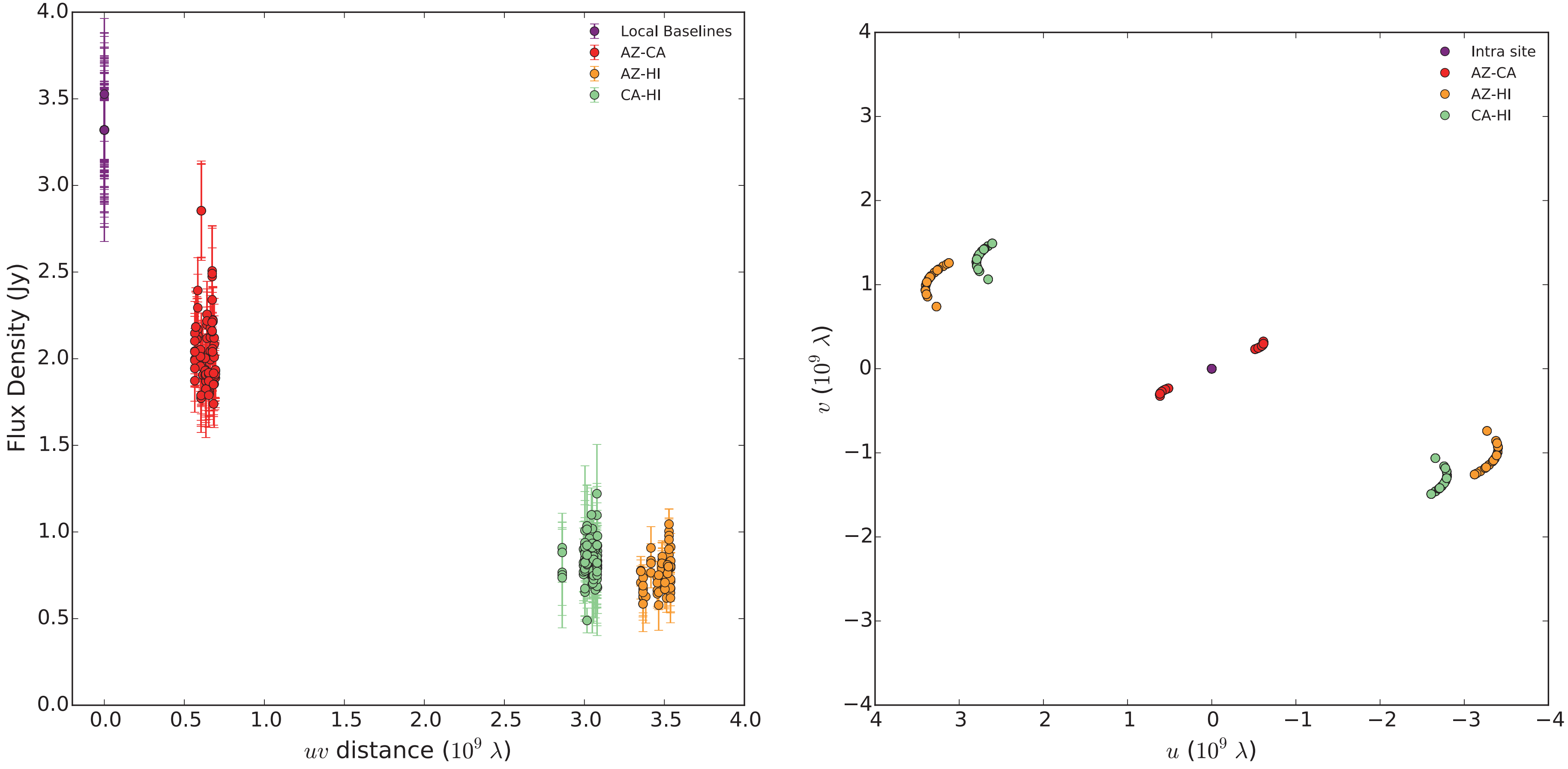

(a)

(b)

Figure 4.2: The calibrated data of 2011 observations. (a) The visibility amplitude as a function of uv-distance. (b) The uv-coverage of calibrated data. (c) The visibility amplitude as a function of the Greenwich sidereal time (GST). The black solid lines indicate the best fit model shown in Table4.2, while the gray area indicates 3σ uncertainties in the model. (d) The closure phase as a function of the Greenwich sidereal time (GST). The black solid lines indicate the best fit model, while the gray area indicates 3σ uncertainties in the model. The black solid lines indicate the best fit model, while the gray area indicates 3σ uncertainties in the model.

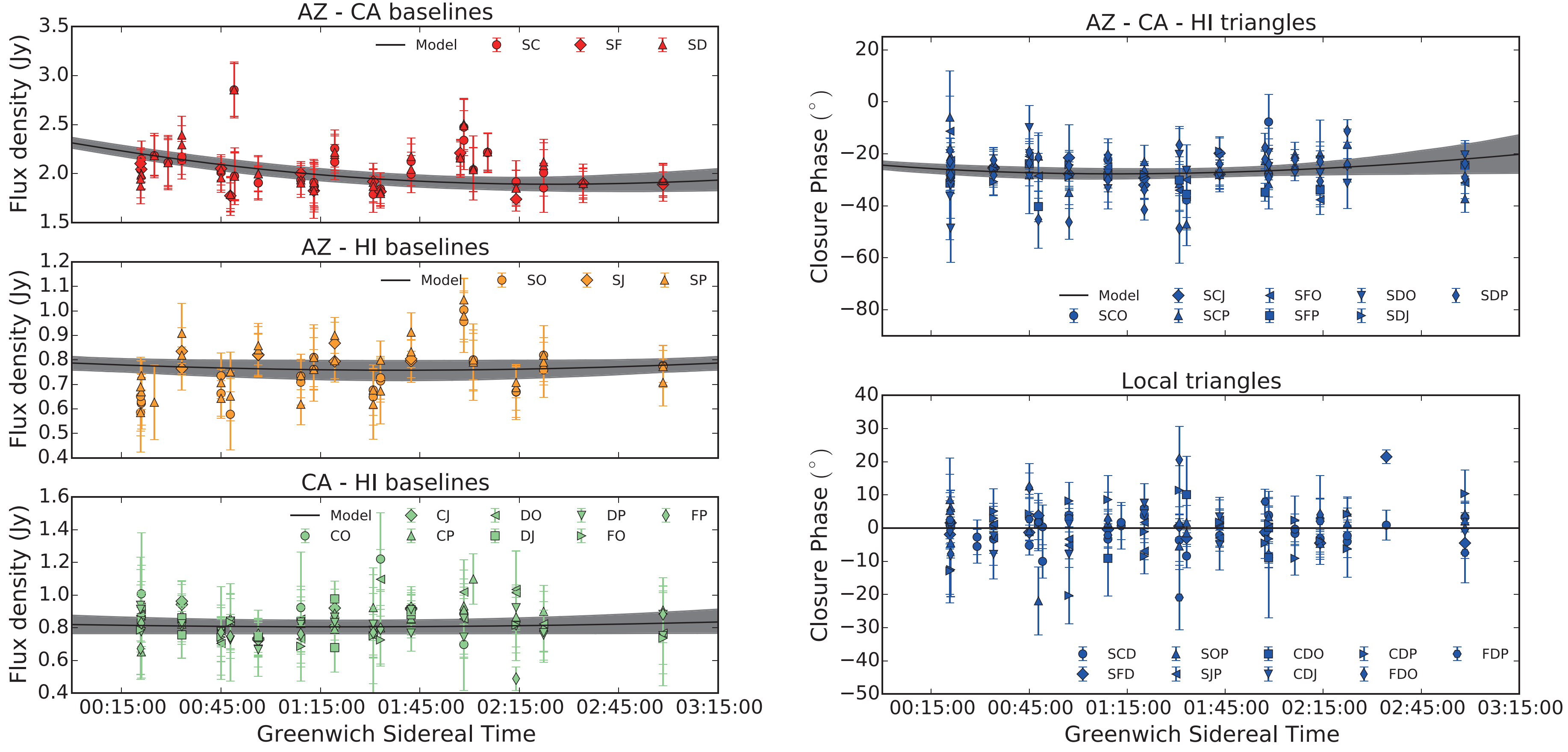

(c)

(d)

Figure 4.1: —Continued. (c) The visibility amplitude as a function of the Greenwich sidereal time (GST). The black solid lines indicate the best fit model shown in Table4.2, while the gray area indicates 3σ uncertainties in the model. (d) The closure phase as a function of the Greenwich sidereal time (GST). The black solid lines indicate the best fit model, while the gray area indicates 3σ uncertainties in the model. The black solid lines indicate the best fit model, while the gray area indicates 3σ uncertainties in the model.

Table 4.2: Geometrical models for NRAO 530

ID	Flux Density	Relative Position				The FWHM Size	Brightness Temperature
	(Jy)	RA (μas)	Dec (μas)	Radius (μas)	PA (°)	(μas)	(10^9 K)
2011 model[a]: $\chi^2_\nu = 1.13$, d.o.f$= 631$							
S0	$0.98^{+0.27}_{-0.20}$	—	—	—	—	$15.6^{+7.0}_{-14.9}$	$134\ (> 80)^{\rm b}$
S1	$2.33^{+0.22}_{-0.29}$	-107^{+55}_{-64}	-129^{+118}_{-132}	167^{+137}_{-118}	-129^{+7}_{-38}	$139.5^{+6.0}_{-6.6}$	$4.07^{+0.64}_{-0.65}$

[a] Errors are 3σ determined by 99.7% Bayesian confidence intervals.

[b] 3σ lower limit

OP, JP in Hawaii), as would be expected if the source is point-like on arcsecond scales. On the other hand, the closure phase on the VLBI triangles is clearly offset from zero, indicating that source structure of NRAO 530 is resolved into an asymmetric structure as in previous EHT observations on 1921-293 (Lu et al., 2012) and 3C 279 (Lu et al., 2013).

The structure of 1.3 mm emission was modeled with geometrical models consisting of circular Gaussians using the visibility amplitudes and closure phases jointly, following previous EHT observations (Lu et al., 2012, 2013), since we can not apply standard imaging techniques such as CLEAN to our dataset owing to the lack of visibility phases. We employed the Bayesian framework using the Exchange Monte Carlo (EMC) described in Appendix B, for determining the best-fit parameters and their uncertainties robustly. We adopted a parameter set with the maximum posterior probability (MAP) in the whole parameter sets sampled in EMC as the best-fit parameter. The 3σ uncertainty on each parameter is determined by the 99.7 % Baysian confidence interval which contains all sampled parameter sets except 0.15 % edges in its posterior probability density function (PDF). Note that the best-fit (i.e. MAP) parameter and uncertainties in our modeling principally correspond to those derived from the maximum-likelihood estimation in the traditional Frequentist inference, since the posterior probability coincides with the likelihood due to the uniform prior distribution for each parameter (see Eq.(B.1)). All data-sets through all 5 nights were used to model the source structure, since we could not find any systematic changes in visibility amplitudes and closure phases.

We modeled observational data with a model with two circular Gaussians, since a single circular Gaussian model is clearly rejected by the non-zero closure phase on the VLBI triangles. We show the best-fit parameters and their 3σ uncertainties in Table 4.2, marginal posterior PDF of parameters in Figure 4.2 and visibility amplitudes and closure phases of the best-fit model and their uncertainties in Figure 4.2. The calibrated data are well-explained by the two component model with a

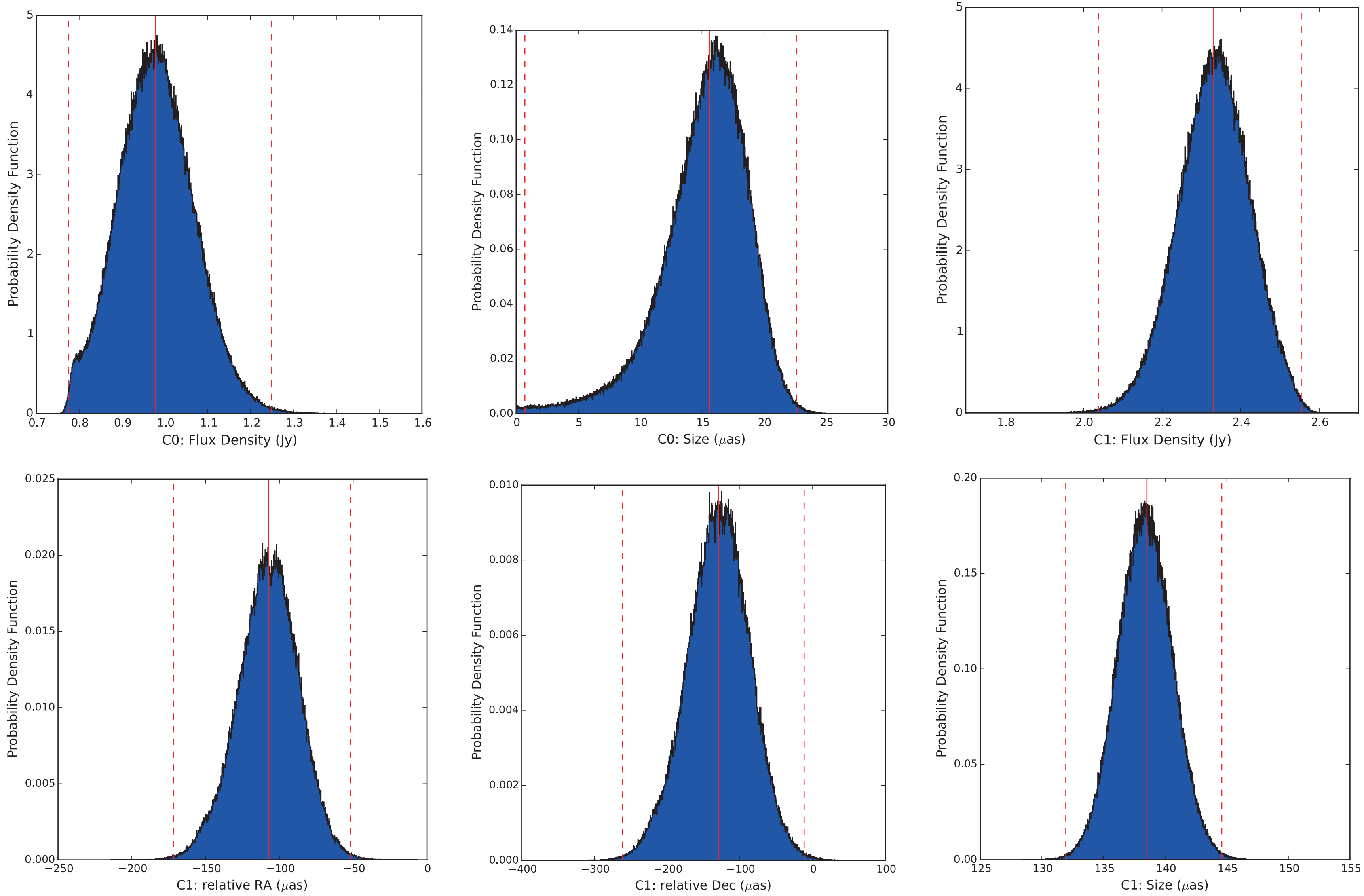

Figure 4.2: The probability density function on each parameter of the 2 circular Gaussian model for 2011 data. The red solid line indicates the best-fit value, while the red dashed lines indicate the range of 99.7 % Bayesian confidence interval.

reasonable goodness-of-fit ($\chi_\nu = 1.13$) as shown in Figure 4.2, indicating that they represent the most basic structure of the emission.

We show the image of the best-fit model in Figure 4.3. The structure is characterized by a compact weak component (S0) and a relatively extended bright component (S1). The position angle of S1 is well-constrained to $-129^{+7}_{-38}{}^\circ$ by the closure phase, while the separation of the two components has a relatively large uncertainty of 167^{+137}_{-118} μas as shown in Figure 4.4, where errors are 3σ.

Interestingly, the 1.3 mm source structure considerably resembles the results of the past 3 mm observations around a large millimeter flare in 1994-1995 (Bower & Backer, 1998b). The source was well-modeled with the compact radio core with a size of 55 ± 33 μas and relatively extended structure with a size of $\sim 100 - 200$ μas at the position angle of $\sim -100 - 150^\circ$ (Bower & Backer, 1998b). Our observations confirm the results of Bower & Backer (1998b) that the inner jet in NRAO 530 has a position angle to the South-West direction on scales of a few 100 μas, which is quite different from the position angle on milliarcsecond scales to the North direction. Other two past 3 mm observations on NRAO 530 did not resolve a structure with a size of ~ 100 μas, which is roughly consistent with the total extent of 1.3 mm structure (Rogers et al., 1994; Doeleman, 1995; Lu et al., 2011).

We show VLBA images at 7 mm observed within one month after the EHT observations in Figure 4.3. We can not robustly detect a counterpart of S1 at 7 mm, since both RA and Dec offsets of two components are rather smaller than the spatial resolution of VLBA at 7 mm. However, we detected ejection of a new component in later observations, which is the most probable counterpart of this component (see §4.5.3).

The flux density of S0 of ~ 1 Jy is consistent with typical flux density on arcsecond scales at the quiescent state between different flares[7], for instance, in 2007 when the core is a dominant component on milliarcsecond scales at 7 mm and also the core flux density at 7 mm is consistent with 2011 observations (see §4.5.3 and Lu et al. 2011). The core flux density of ~ 1 Jy is also expected at 1.3 mm by previous spectrum fitting to the core flux at the quiescent state in 2007 assuming the spectrum turn-over due to synchrotron self-absorption (SSA) (Lu et al., 2011). These facts and similarity in the source structure to the previous 3 mm observations strongly suggest that the compact component S0 is most probably the core at 1.3 mm and the extended S1 is a jet component at downward of the core.

---

[7] see `http://sma1.sma.hawaii.edu/callist/callist.html?plot=1733-130`

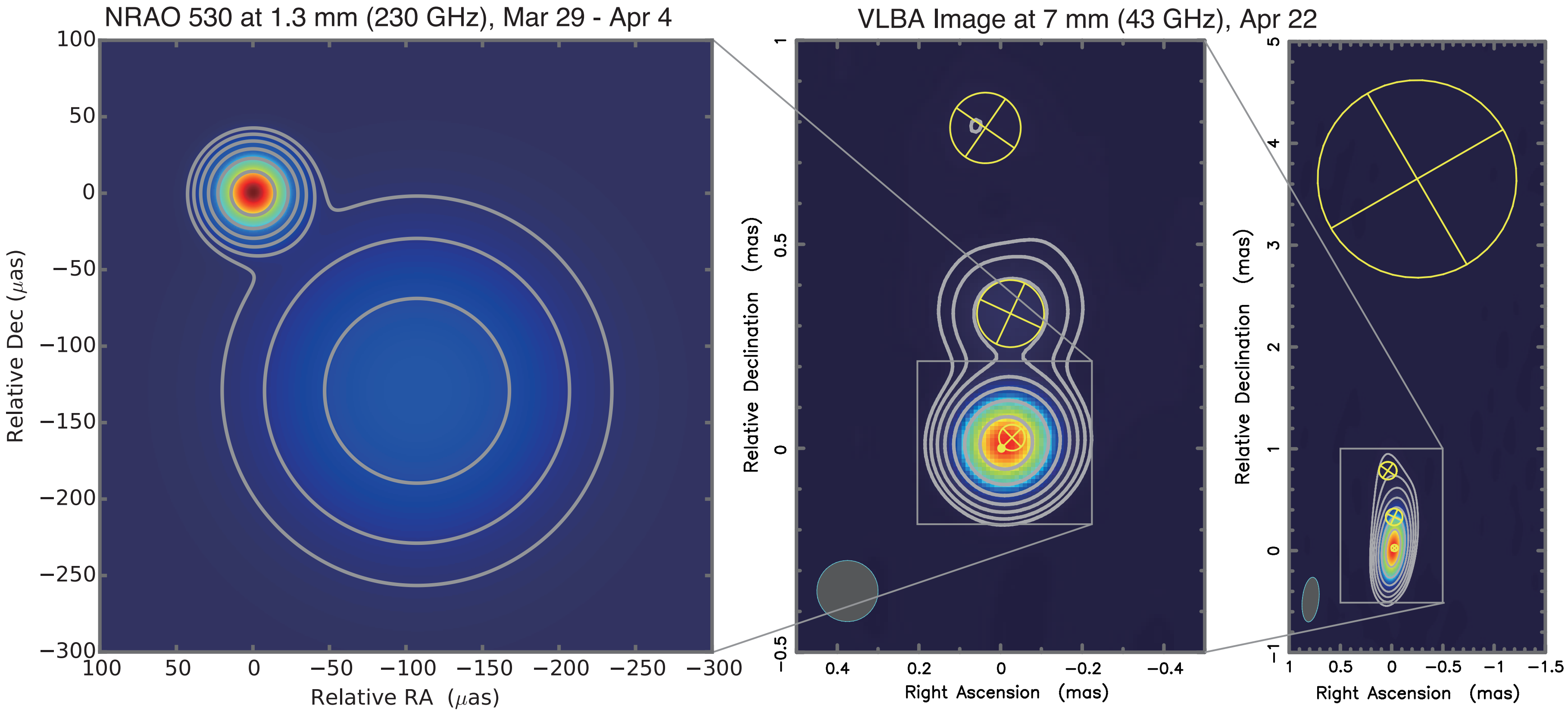

Figure 4.3: Left image: The best-fit model image of NRAO 530 at 1.3 mm for 2011 observations. The image is restored with a circular Gaussian beam with an FWHM size of 20 μas. The peak intensity is 1.34 Jy/beam. Contour levels are set to 1%, 2%, 4%, 8%, 16% and 32% of the peak intensity. Right two images: total intensity images at 7 mm obtained on 2011 April 22 with model-fit components superimposed. The right image is an uniform-weighted image of the whole mas-scale structure, while the left one is a super-resolution image near the radio core on sub-mas scales restored by a circular Gaussian beam with an FWHM size of 0.15 mas. The contours indicate 1%, 2%, 4%, 8%, 16%, 32% and 64% of the peak intensities that are mJy/beam and mJy/beam for the left and right images, respectively.

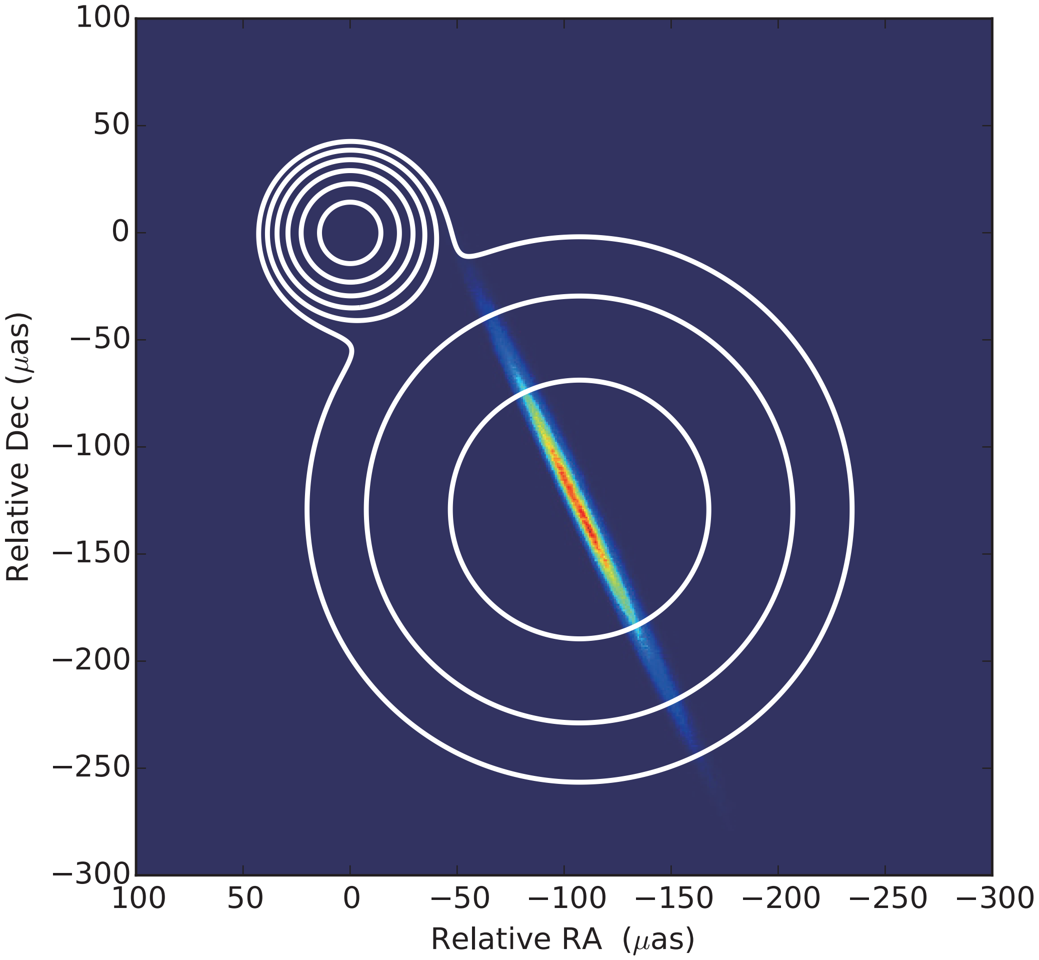

Figure 4.4: The two dimensional probability distribution for the position of S1. The color contour indicates the posterior probability distribution for the position of S1, while white contour lines indicate the brightness distribution of the best-fit model shown in Figure 4.3.

We estimate the effective brightness temperature of each component, which is given by (e.g. Akiyama et al., 2013)

$$T_b = \frac{c^2}{2k_B\nu^2}\frac{F}{\pi(\phi/2)^2} \tag{4.1}$$

$$= 2.1\times 10^{10}\,\mathrm{K}\times\left(\frac{\nu}{230\,\mathrm{GHz}}\right)^{-2}\left(\frac{F}{1\,\mathrm{Jy}}\right)\left(\frac{\phi}{40\,{}^{-}\mathrm{as}}\right)^{-2}, \tag{4.2}$$

where F, ν and ϕ are the total flux density, observation frequency, and the FWHM size of the circular Gaussian. The brightness temperature of S1 is $\sim 4.0\times 10^9$ K, which is smaller than the jet features including the core and jet components in other sources detected with 1.3 mm VLBI observations (1921-293, 3C279 Lu et al., 2012, 2013). On the other hand, only the best-fit parameter and the 3σ lower limit on the brightness temperature of $\sim 1.3\times 10^{11}$ K and $\sim 8.0\times 10^{10}$ K are obtained for C0, respectively, since the lower tail of its PDF on the size extends to zero indicating that possibly C0 is not resolved (see Figure 4.2).

It is noteworthy to mention that all the 1.3 mm VLBI observations on blazars NRAO 530 (this work), 3C 279 (Lu et al., 2013) and 1921-293 (Lu et al., 2012) revealed the curved geometry of the inner sub-parsec-scale jet with position angles more than $\sim 90^\circ$ offset from those of the larger-scale jet and its motion. The curved geometry in the inner sub-parsec region has been also indicated by recent mm-VLBI observations on some other blazars (e.g. NRAO 150 Agudo et al. 2007; OJ 287 Agudo et al. 2012) showing non-radial and non-ballistic motions on sub-parsec scales.

These results seem rather different from general properties of the parsec-scale jet in blazars recently reported in the MOJAVE program (e.g. Lister & Homan, 2005), that apparent speed changes are distinctly larger than changes in the direction (MOJAVE XII: Homan et al., 2014). In addition, Homan et al. (2014) reported the broad tendency of the kinematics on parsec scales that the jet feature changes the position angle of its motion into a direction getting the better alignment with the mean inner-jet position angle. Homan et al. (2014) discussed this tendency in connection with the jet collimation based on the recent measurements of collimation profiles at radio galaxies (M87: Asada & Nakamura 2012, Nakamura & Asada 2013a, Hada et al. 2013; 3C 84: Nagai et al. 2014). However, our observations indicate that the inner-jet position angle on sub-parsec scales is consistent between two epochs with an interval of ~10 years, largely offset from position angles of the larger scale jet and its motion. This indicates a stable offset between the position angles of the inner jet and larger-scale jet, favoring a scenario that the jet is following pre-established channels and jet features move around the bend, which is suggested in earlier works (Kellermann et al. 2004 and MOJAVE VII: Homan et al. 2009). This result imposes a possibility that the major mechanism of the non-radial and non-ballistic motion in the inner jet on sub-parsec scales in blazars could be different from that on-parsec scales. It is essential to measure the stability of the inner-jet structure, in particular, the position angle of the structure in blazars with multi-year EHT or other short-mm VLBI observations in future.

Finally, we note that we tried two more complicated models consisting of 1) two circular Gaussians with another extended component resolved out in VLBI baselines and 2) three compact circular Gaussians. The former model predicts a large missing flux (~1.2 Jy). However, it does not have a bright counterpart in mas-scale structure at 7 mm observed with VLBA, where the inner sub-milliarcsecond-scale structure at the core dominates the total radio flux. It seems also incompatible with previous observations reporting that the core flux on arcsecond scales and mas scales is consistent within ~ 5 % at 2 cm (e.g. Hong et al., 2008). The latter three circular Gaussians model predicts the structure with the extent of ~0.5 mas in RA direction which can be surely resolved with VLBA at 7 mm, but there is no such a structure in the vicinity of the core at 7-mm. In addition, these models do not improve a reduced chi-square significantly ($\Delta\chi_{\nu} \lesssim 0.1$). For above reasons, we stick to the two circular Gaussians model.

4.5.2 *Multi-wavelength Light Curves*

Figure 4.5.2 shows a multi-wavelength light curve during 2010 to 2012. The light curve includes (i) the γ-ray flux at $0.1 - 200$ GeV observed with *fermi* Large Area Telescope with time bins of a week (LAT; Jorstad et al. in prep.), (ii) the 1.3 mm flux density on arcsecond scales observed with SMA, (iii) the total flux density at 7 mm on milliarcsecond scales observed with VLBA (see §4.5.3).

The γ-ray activity in NRAO 530 has been quiescent after the launch of *fermi* with an average flux of $\sim 3 \times 10^{-9}$ photon cm^{-2} s^{-1} (Ackermann et al., 2011a). The γ-ray flux was mostly under the detection limit of few 10^{-7} photon cm^{-2} s^{-1} in the weekly light curve until 2010[8]. However, the source was enhanced in mid-2010, and detected at most of weekly time bins from mid-2010 to mid-2011. The γ-ray flux was a few 10^{-7} photon cm^{-2} s^{-1} near the detection limit in most of epochs

---

[8] see `http://fermi.gsfc.nasa.gov/ssc/data/access/lat/msl_lc/source/1730-130`

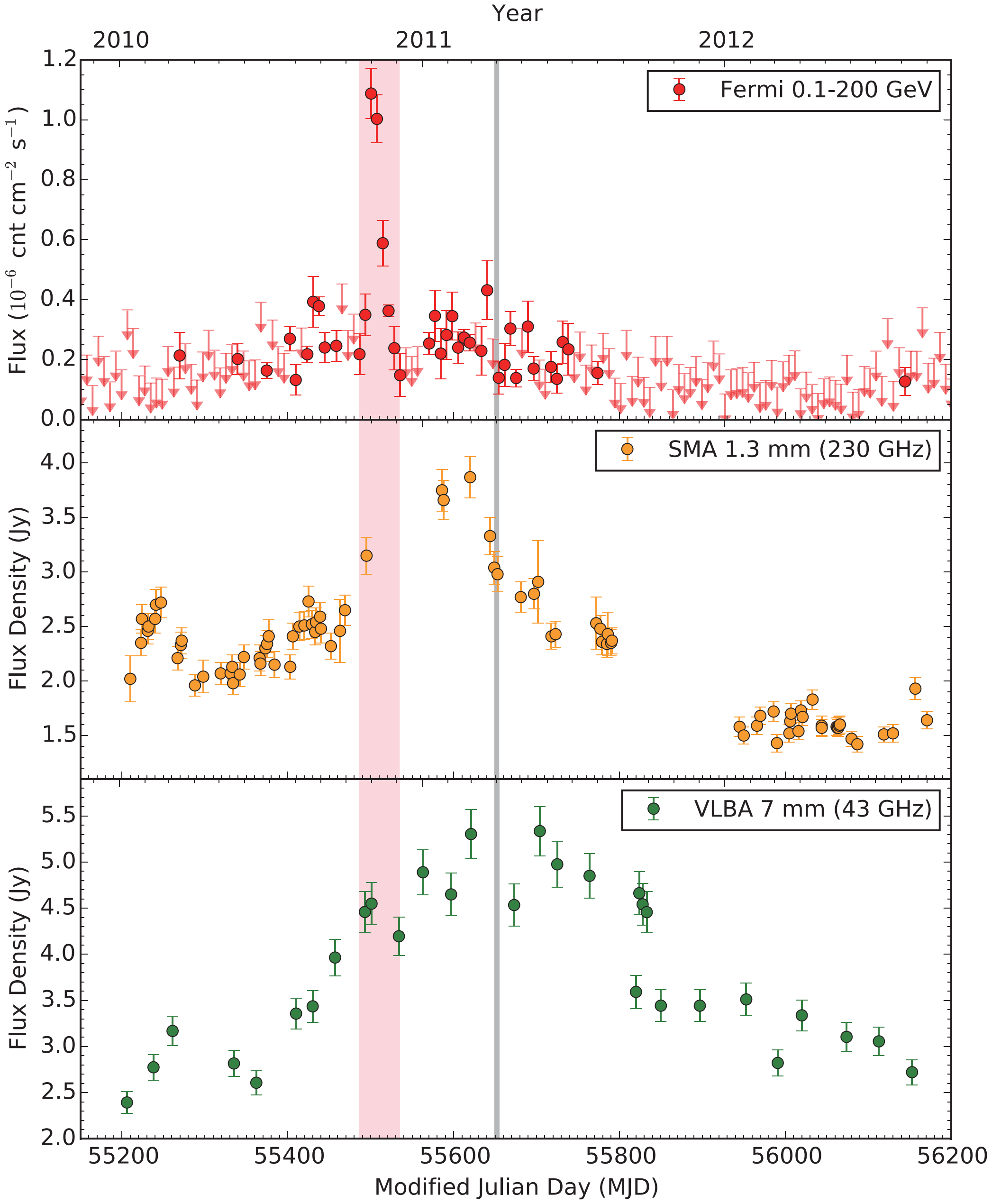

Figure 4.5: Multi-wavelength light curves of NRAO 530 between January 2010 and September 2012. The vertical shaded area colored in pink indicates the duration of the GeV γ-ray flare in 2010, while the other shaded area colored in gray indicates the period of 1.3 mm VLBI observations with EHT.

during this enhancement. On the other hand, in late 2010, the source was flared with a peak flux at least several times higher than other epochs. The duration of flares is $\Delta t = 49$ d between MJD 55486 and 55535, giving the maximum size of $R_{\mathrm{max}} = ct\delta/(1+z) = 6.67 \times 10^{16}\delta$ cm for the flaring region from the causality argument, where δ is the Doppler factor of the jet.

A strong brightening occurred at mm-wavelengths around the active state in GeV γ-ray after mid-2010 (Figure 4.5) as well as cm-wavelength (Nagai et al., 2013). The radio brightening started in April 2010 at both 1.3 mm and 7 mm. At 1.3 mm, NRAO 530 was not observed for 3 months during October 26 2010 and January 25 2011 including the period of the GeV γ-ray flare. Since the light curve shows rise and decay before and after this period, respectively, the 1.3 mm light curve reached at the peak in this period. At 7 mm, the light curve seems to reach at the peak around January 2011 similarly to 1.3 mm. The time variation in the total flux density at 7 mm is mainly attributed to ejections of two jet components from the core (see §4.5.3), strongly suggesting that increase in 1.3 mm flux is also due to new components ejected from the core.

4.5.3 *Source Structure at 7 mm*

Figure 4.6 shows 7-mm VLBA images of NRAO 530 with an interval of ~ 1 month from January 2011 to August 2012. The parsec-scale structure in NRAO 530 at 7-mm is a core-jet structure directed into the north, which is broadly consistent with previous observations (e.g. Lu et al., 2011). We identified components by checking parameters of circular Gaussian components during the epochs, assuming that the same component has similar total flux density and size in adjacent epochs.

Milliarcsecond structure is well-characterized with (i) the almost point-like core component (C0) in the south, (ii) the farthest faint component (C1) at outer $>$2.5 mas moving to the north, (iii) the stationary component (C2) with a flux density of ~ 0.5 Jy at a distance of ~ 0.3 mas from the core, (iv) several components (C3-C6) in the inner ~ 1 mas moving to the north. We show the flux density and angular distance of each component from the core in Figure 4.7 and Figure 4.8, respectively. All downward components except C2 show super-luminal motions beyond the light speed of ~ 0.02 mas yr^{-1} inferred for NRAO 530.

The time variation in the total flux density is mainly attributed to activities in the inner 1 mas from the core (see Figure 4.7 and Figure 4.8). The core flux increases at least from the beginning of 2010. In the middle of enhancement in the core flux,

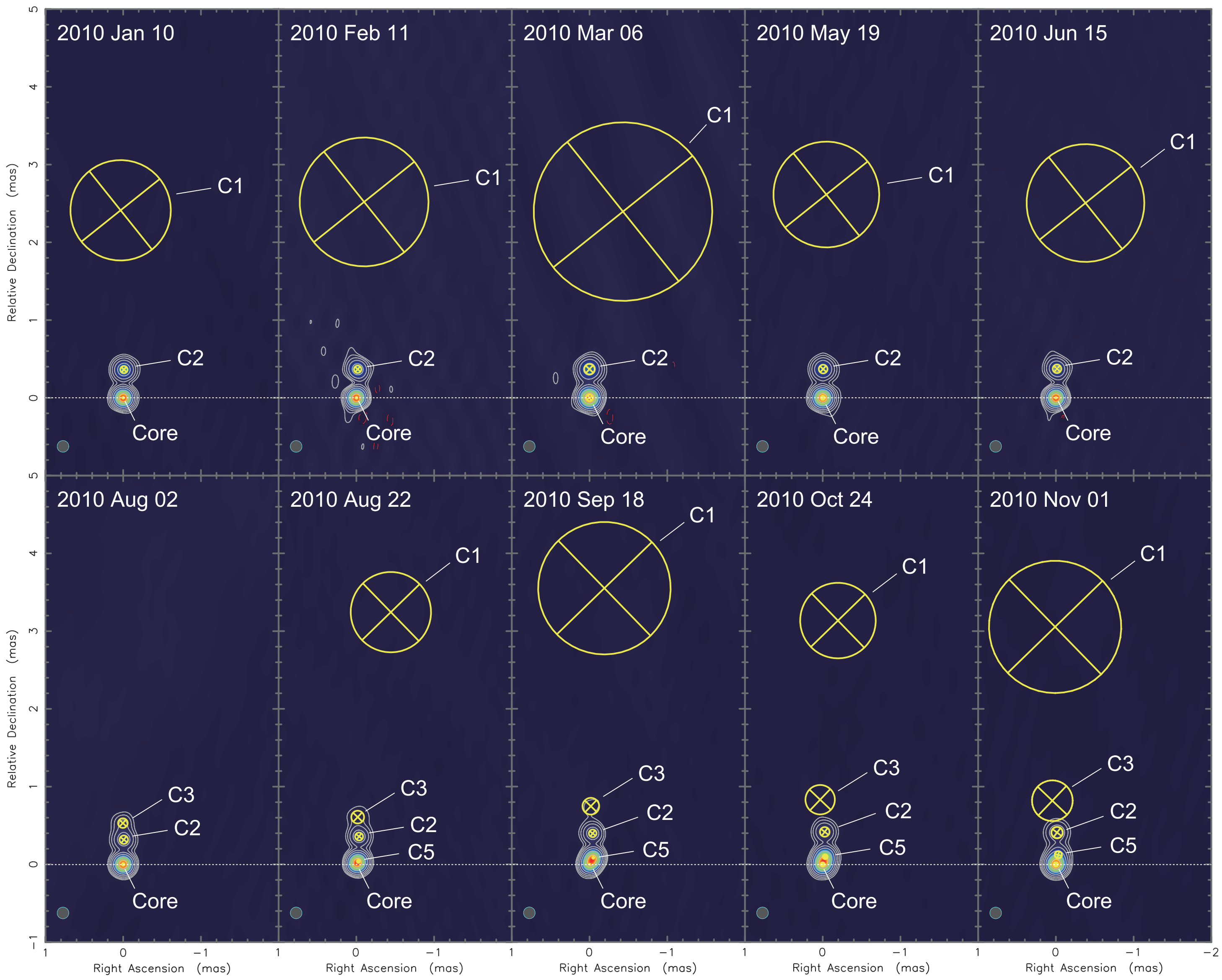

Figure 4.6: 7-mm images of NRAO 530 observed with VLBA from January 2011 to August 2012 with circular Gaussian components imposed. The images are restored with a circular Gaussian beam with an FWHM size of 0.15 mas, which is a typical minor-axis size of the synthesized beam. The contours indicate 1%, 2%, 4%, 8%, 16%, 32% and 64% of the peak intensity.

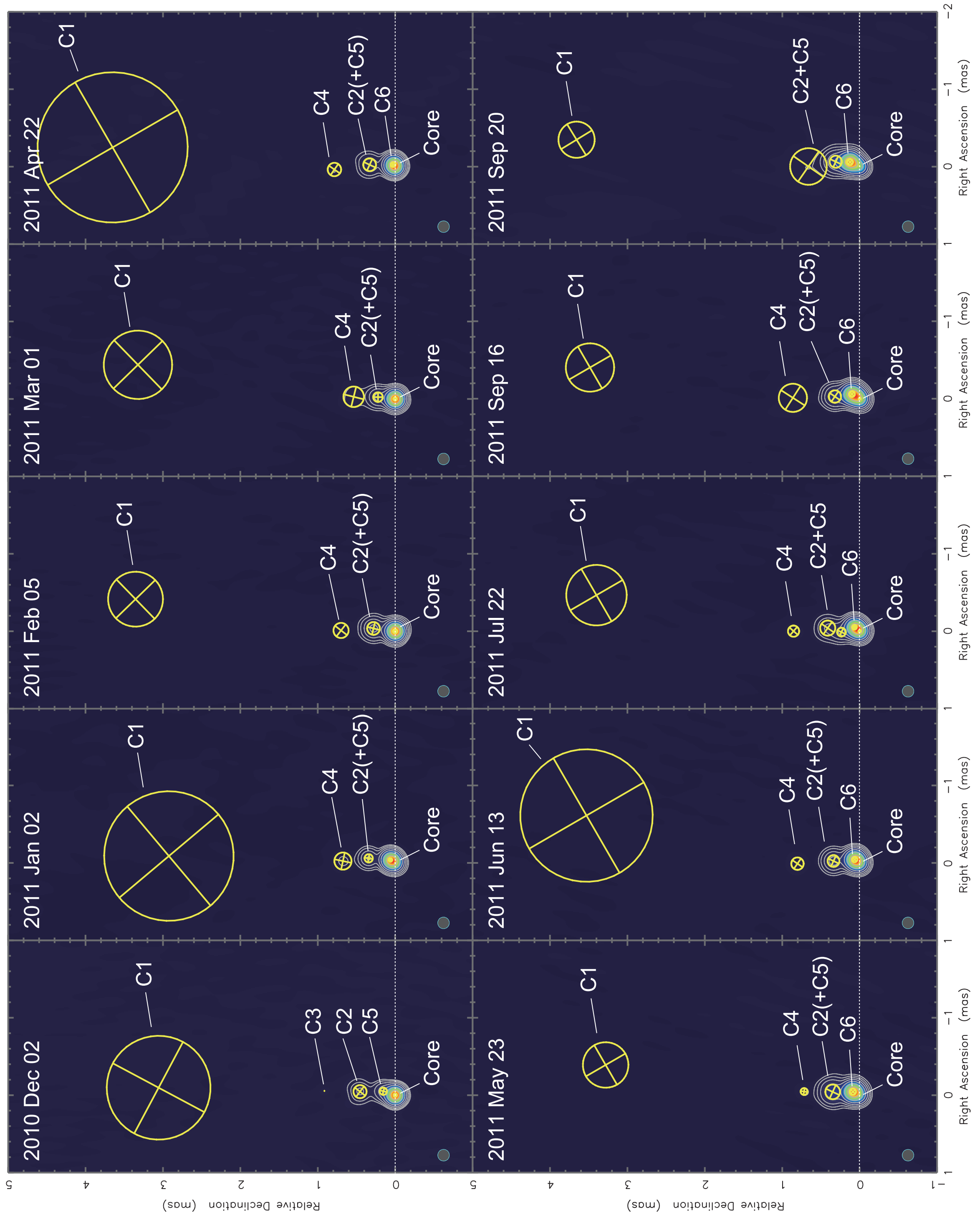

Figure 4.6: —Continued.

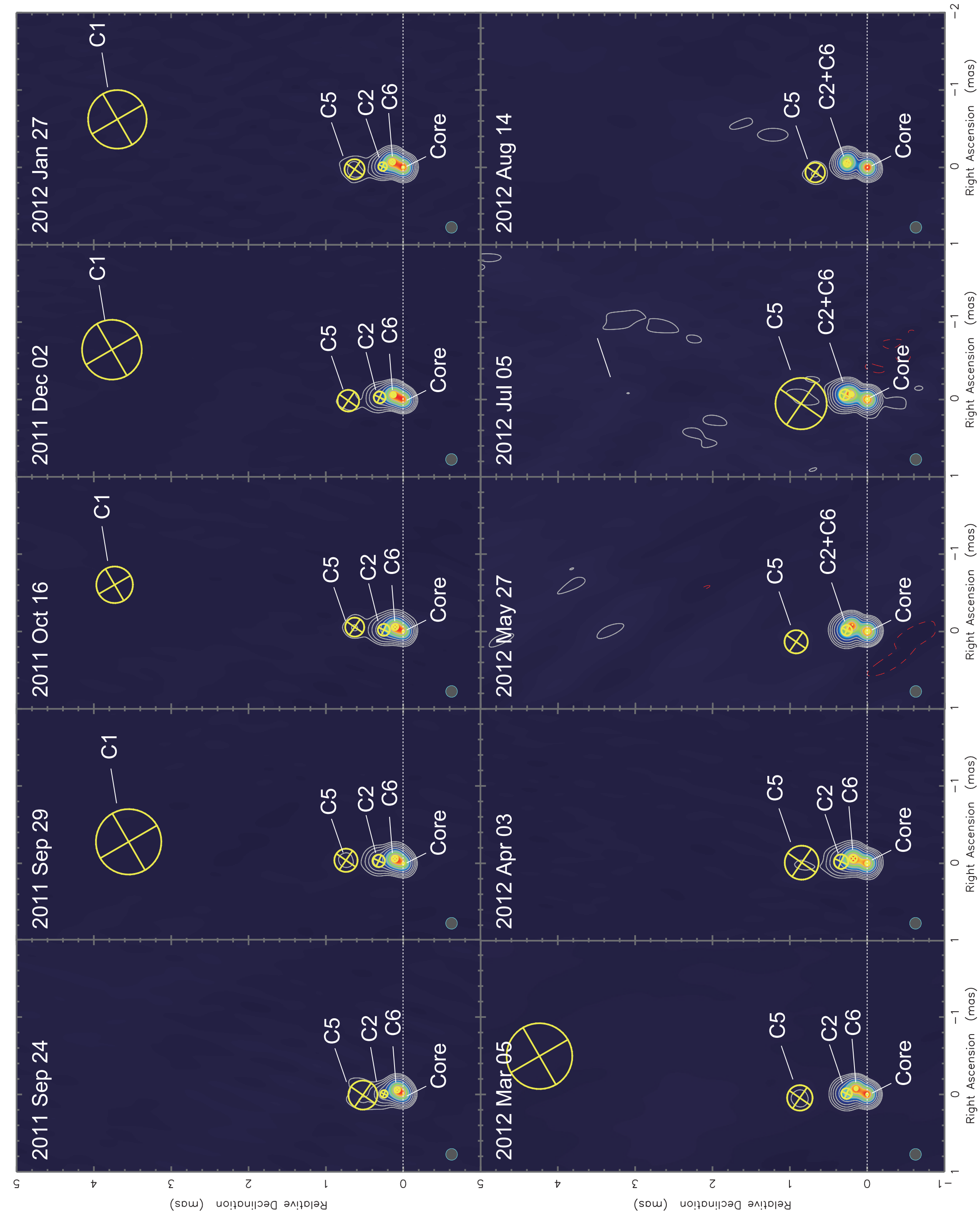

Figure 4.6: —Continued.

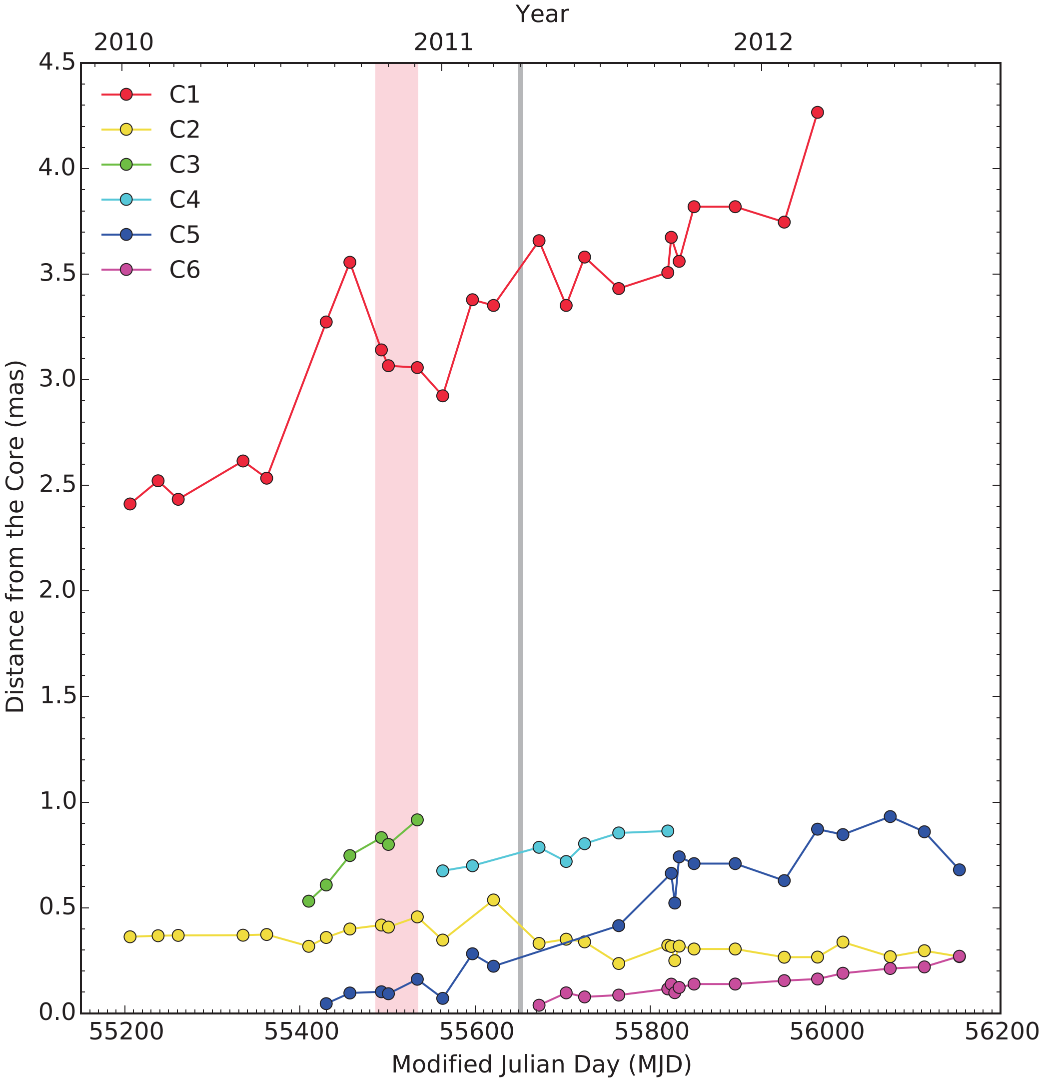

Figure 4.7: The angular separation between the core and each circular Gaussian component as a function of the Modified Julian Day (MJD) and year. The vertical shaded area colored in pink indicates the duration of the GeV γ-ray flare in 2010, while the other shaded area colored in gray indicates the period of 1.3 mm VLBI observations with EHT.

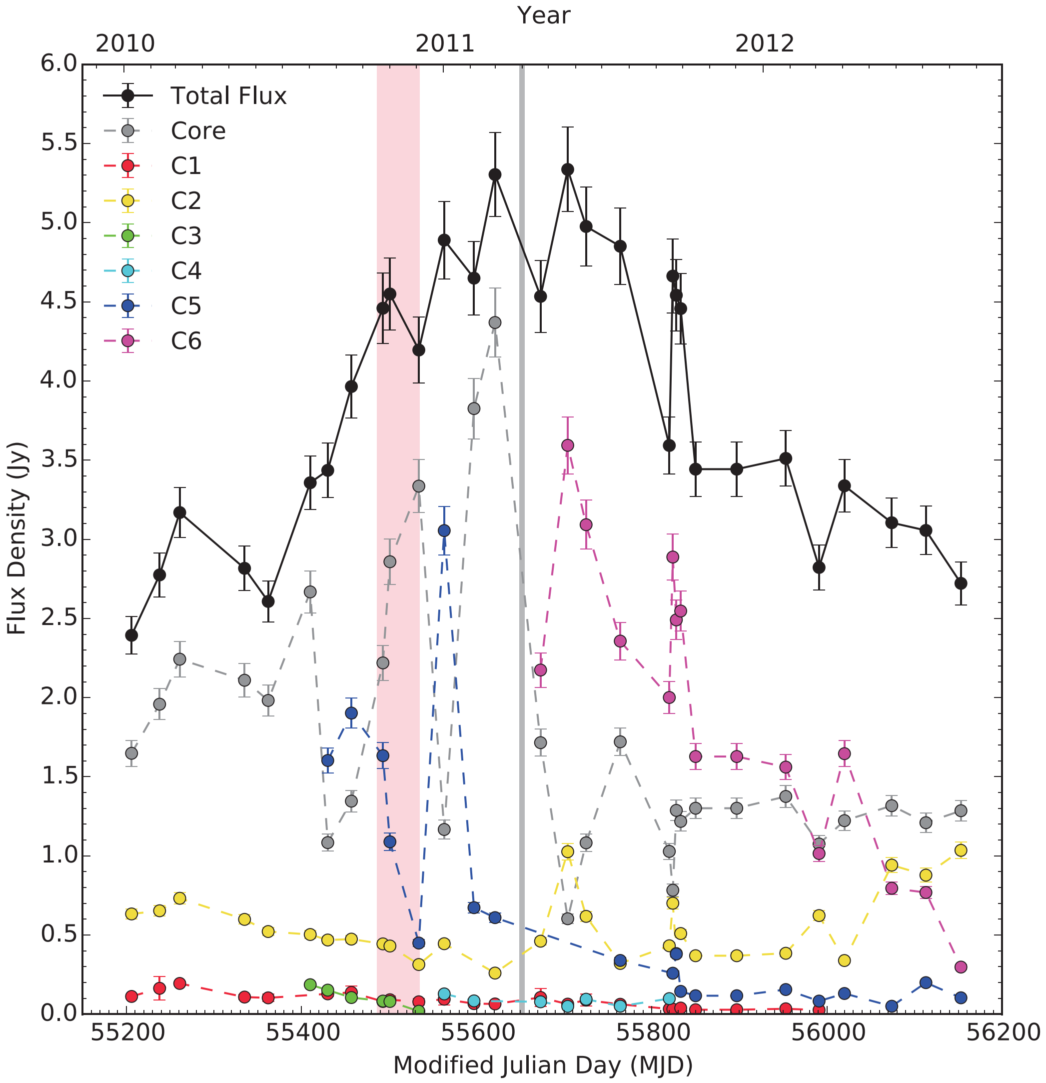

Figure 4.8: The flux density of 7 mm images and circular Gaussian components as a function of the Modified Julian Day (MJD) and year. We adopt 1σ errors of 5% for the total flux density, while 1σ errors are estimated to be the quadrature of 5% and the reciprocal of the dynamic range of each component. The vertical shaded area colored in pink indicates the duration of the GeV γ-ray flare in 2010, while the other shaded area colored in gray indicates the period of 1.3 mm VLBI observations with EHT.

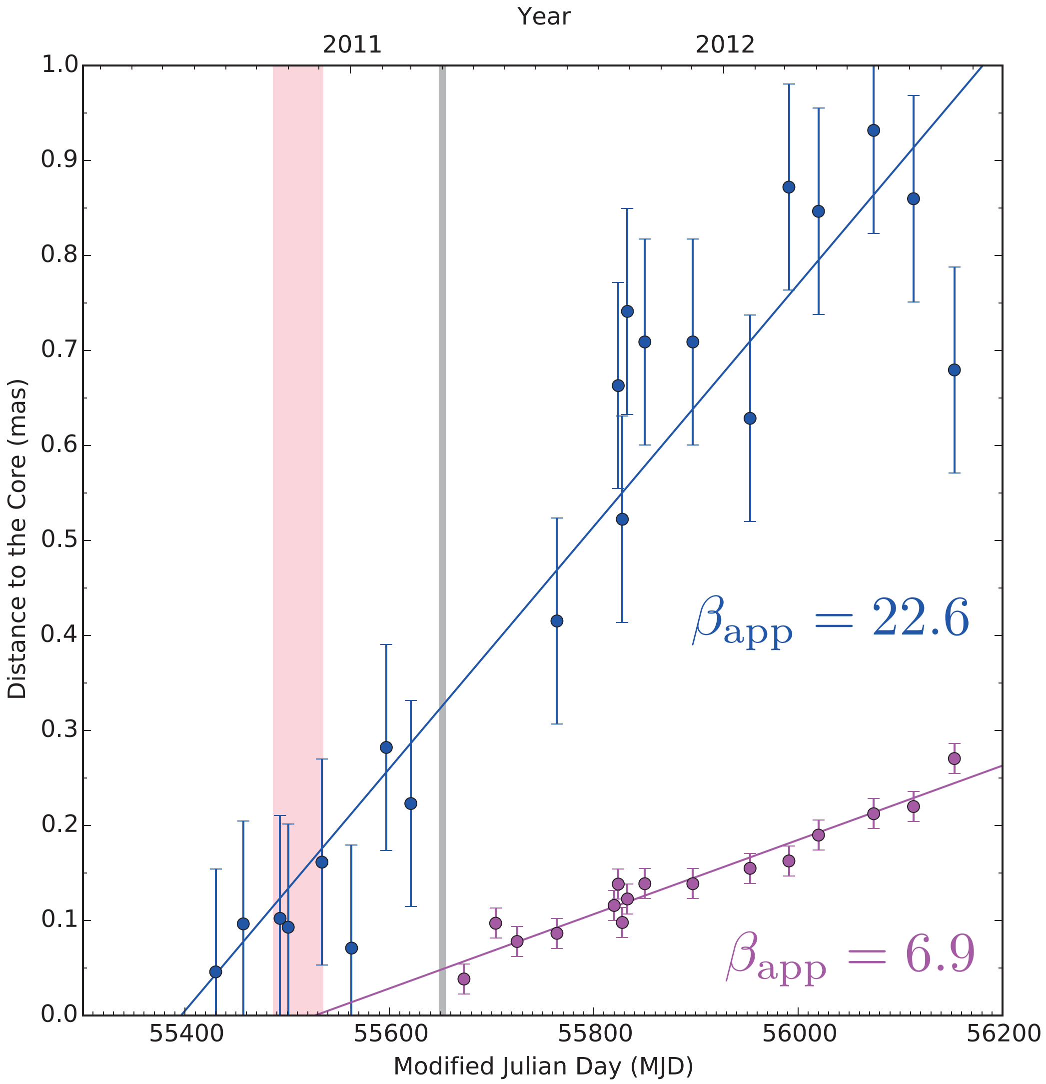

Figure 4.9: The angular separation between the core and two circular Gaussian components C5 and C6 as a function of the Modified Julian Day (MJD) and year. The errors are 1σ estimated by a method described in §4.5.3. The vertical shaded area colored in pink indicates the duration of the GeV γ-ray flare in 2010, while the other shaded area colored in gray indicates the period of 1.3 mm VLBI observations with EHT.

a new super-luminal component C5 starts to be spatially resolved and ejected in mid-2010. The core flux still continues to increase even after ejection of C5, and becomes stable after ejection of another new bright component C6 in mid-2011. The core flux density after ejection of two components is ~ 1.26 Jy, which is consistent with previous 7-mm observations in 2007 (Lu et al., 2011), when the source is in a quiescent state in radio regime.

We show time evolution of angular separation between the core and C5/C6 in Figure 4.9. Data of each component are linearly fitted to derive typical apparent speeds and dates of their ejections from the core under an assumption that the components have constant velocities. We employed a fitting method similar to a method described in Homan et al. (2001), since it is difficult to measure errors on positions quantitatively in each epoch independently. First, we performed a linear fit to data with equal errors of unity. We adopted fitted parameters as the best-fit parameter. Then, we uniformly rescaled errors on data, such that reduced-χ^2 of the best-fit parameter to be unity. The 3σ errors were determined by the confidence interval. The apparent speeds of C5 and C6 are estimated to be $\beta_{\rm app} = 22.6 \pm 6.4$ and $\beta_{\rm app} = 6.9^{+1.7}_{-1.6}$, while the ejection dates of C5 and C6 are 55396^{+34}_{-170} and 55528^{+78}_{-122} in Modified Julian Day (MJD), respectively, where errors are 3σ.

In relation to the source structure at 1.3 mm (§4.5.1), C6 is the most probable counterpart of the jet component S1 at 1.3 mm, since there is no other plausible candidates for the counterpart. Around the period of the EHT observations, C2 and C5 are already resolved from the core and located within 0.5 mas from the core, but their position angles directed into the north is significantly different from that of S1 tightly constrained by the 1.3 mm closure phase. On the other hand, the position of C6 was very close to the core around the period of the EHT observations and then broadly consistent with that of S1. We also note that the separation angle between the core and C6 around the EHT observations are expected to be 49^{+26}_{-27} μas by the best-fit model in Figure 4.9, where errors are 3σ, being consistent with the separation between S0 and S1. Since C6 moves to the north as other components, it requires a non-radial and non-ballistic motion on sub-parsec scales.

During the active state in GeV γ-ray regime from mid-2010 to mid-2011, two components were ejected from the core at 7 mm. Similar ejection of multiple jet components with different apparent velocities at a single active state in GeV γ-ray regime was reported in 3C 273 in 2009-2010 (Jorstad et al., 2012). Our results are the second discovery of such phenomena. Since the GeV γ-ray light curves at the active state in 3C 273 (Jorstad et al., 2012) and NRAO 530 (Figure 4.5.2) seem to have substructures ascribable to weaker flares in addition to the brightest flare, these components are probably attributed to multiple flares. In relation to the brightest GeV flare in late 2010, either C5 or C6 can be the radio counterpart of the flaring component in terms of the kinematics of these components, since the expected ejection dates are consistent with the duration of the flare. However, if these components are ascribable to different flares, the brightest component C6 is most likely the radio counterpart of the brightest GeV flare, while the weaker C5 is probably associated with weaker substructure in the GeV γ-ray light curve before the flare, since the radio flux density generally has a correlation with the γ-ray flux in AGNs (Garland et al., 2011; Nieppola et al., 2011; Ackermann et al., 2011b; León-Tavares et al., 2012) naturally explained in the conventional framework of one-zone synchrotron-self Compton (SSC) and/or external Compton (EC) models (e.g. Inoue & Takahara, 1996; Kubo et al., 1998; Kino et al., 2002).

4.5.4 *Implications for the GeV γ-ray Flare in Late-2010*

We performed 1.3 mm VLBI observations with EHT $\sim$6 months after the bright GeV γ-ray flare in late-2010 during the active state in GeV γ-ray regime from mid-2010 to mid-2011 (§4.5.2). The EHT observations revealed that the inner jet structure on sub-parsec scales resolved into the core component S0 and the extended jet component S1 (§4.5.1). The multi-epoch VLBA observations at 7 mm detected ejection of a bright super-luminal component C6 after the EHT observations, which is most probably the 7-mm counterpart of S1 (§4.5.3). The motion of C6 (=S1) is directed into the north, which is significantly different from the position angle of the inner jet detected with EHT. This requires that the inner jet in NRAO 530 has a curved trajectory on sub-parsec scales. In relation to the bright GeV γ-ray flare, the radio counterpart could be either of two components C5 and C6 ejected during the active state, but C6 (=S1) is the most probable counterpart of the bright GeV γ-ray flare considering the correlation between the radio flux density and the γ-ray flux expected from previous statistical studies and theoretical studies. In this section, we discuss general implications for the GeV γ-ray flare in late-2010 inferred from observational properties of S1.

The trajectory of the flaring component is one of the key issues to understand the observational properties of the γ-ray flares and high-activity state in blazars. Recent observational studies reported large rotations ($\gtrsim 180^\circ$) of the optical electric vector position angle (EVPA) in blazars in connection with γ-ray flares and high-activity states (e.g. BL Lacertae: Marscher et al. 2008; 3C 279: Abdo et al. 2010b, Hayashida et al. 2012, Aleksić et al. 2014; PKS 1510-089: Marscher et al. 2010; 3C 454.3: Sasada et al. 2012). These long, coherent rotations in EVPA have been interpreted as the signature of a global field topology (e.g. Marscher et al., 2008, 2010) or the curved trajectory of the jet (e.g. Abdo et al., 2010b; Hayashida et al., 2012; Aleksić et al., 2014), which are traced by a moving emission feature.

Current EHT observations on γ-ray blazars show presence of curved trajectories in the inner jets. In particular, this work shows that the component S1, which is a radio counterpart of the active state and most likely the counterpart of the bright GeV γ-ray flare, propagates along a highly curved trajectory on sub-parsec scales. Although the curved trajectory of the jet is common in blazars (e.g. Homan et al., 2014), the present work provides the first example that a jet component related with γ-ray activities actually moves with a curved trajectory, as suggested in previous studies to explain rotations in EVPA in other blazars (Abdo et al., 2010b; Hayashida et al., 2012; Aleksić et al., 2014).

Size of the radio counterpart provides some important physical implications for the flaring region. In the period of the GeV γ-ray flare, the size of the flaring region is constrained into $\lesssim$ 49 ld at the observer's frame by the flare duration using the causality argument. On the other hand, the radio counterpart of the flare S0 has a size of $140\ \mu$as $\sim$ 1304 ld in the period of EHT observations held on ~ 170 d after the GeV γ-ray flare.

In general, the spectrum energy distributions (SEDs) of blazars have been well explained by scenarios assuming co-spaciality of the broadband emission such as widely accepted one-zone synchrotron-self Compton (SSC) and/or external Compton (EC) models (e.g. Inoue & Takahara, 1996; Kubo et al., 1998; Kino et al., 2002). In such scenarios, the radio and γ-ray emissions originate in the same region, requiring that the radio emission region also has a size of $\lesssim$ 49 ld, being same to the γ-ray emission region in the period of the GeV γ-ray flare. Thus, the results of the EHT observations suggest a rapid expansion of the flaring region from $\lesssim$ 49 ld to $\sim$ 1304 ld during ~ 170 d between the GeV γ-ray flare and our observations on the observer's frame apparently. The apparent expansion speed $\beta_{\rm exp,app}$ is estimated to be $\beta_{\rm exp,app} \gtrsim (1+z)(1304-49)/170 = 7.4$, which is clearly super-luminal.

Such a super-luminal expansion can be seen in the jet of blazars with a high bulk Lorentz factor and a low viewing angle. If the jet component is expanding inside the jet on the co-moving frame of the jet, the velocity of a fluid particle in the jet component particularly on the approaching side becomes highly relativistic due to the relativistic velocity addition with the bulk velocity of the jet itself on the observer's frame. This can occur even if the expansion velocity is not relativistic on the co-moving frame. Depending on the speed and viewing angle of the velocity of the fluid particle on the observer's frame, the apparent speed of the fluid particle may exceed the light speed due to the time dilation effect similarly to the apparent super-luminal motion of the jet component itself. When the apparent speed of the fluid particle is at least $1c$ or larger than that of the center of the jet component (i.e. the apparent speed of the jet component), the apparent expansion speed is beyond the light speed in observed images.

The apparent expansion speed of the fluid particle depends on (i) the jet speed β, (ii) the viewing angle of the jet θ, (iii) the expansion speed on the co-moving frame $\beta'_{\rm exp}$, and (iv) direction of the expansion velocity on the co-moving frame (see Appendix B). One can constrain these physical quantities by investigating the range giving the estimated apparent expansion speed.

Here, we consider that the flaring region is spherical and expanding isotropically on the co-moving frame. The position of a fluid particle at the surface of the blob in observed image can be calculated by Eq (C.12). We can obtain the shape of the surface of the blob in the observed image by calculating the distribution of various fluid particles widely distributed in the surface of the blob in the observed image. Then, we can estimate the observed size from the total extent of the blob $R_{\rm ext}(R_0, t, z;\ \beta, \theta, \beta'_{\rm exp})$, where R_0, t, z are the initial extent of the blob in observed image, the elapsed time on observer's frame and the redshift of the source, respectively. The expansion speed on the co-moving frame must be smaller than the sound speed of the relativistic plasma $c/\sqrt{3}$. In addition, the initial extent of the blob is limited by the flare duration into $R_0 \lesssim 49$ ld. Thus, the maximum extent of the blob is given when $\beta'_{\rm exp} = 1/\sqrt{3}$ and $R_0 = 49$ ld. Since $R_{\rm ext}(R_0, t, z;\ \beta, \theta, \beta'_{\rm exp})$ is the size of "boundary" of the blob, the actual emission size should be smaller than the estimated extent of the blob considering the optical depth of the flaring region. Thus, one can expect $R_{\rm EHT} < R_{\rm ext}(R_0 = 49\,{\rm ld},\ t,\ z = 0.902;\ \beta,\ \Theta,\ \beta'_{\rm exp} = 1/\sqrt{3})$. The jet speed and viewing angle of the jet can be constrained by this inequality.

In Figure 4.10, we show the range of the jet speed and viewing angle in shaded area colored in orange satisfying the above inequality. Note that we adopt the 3σ

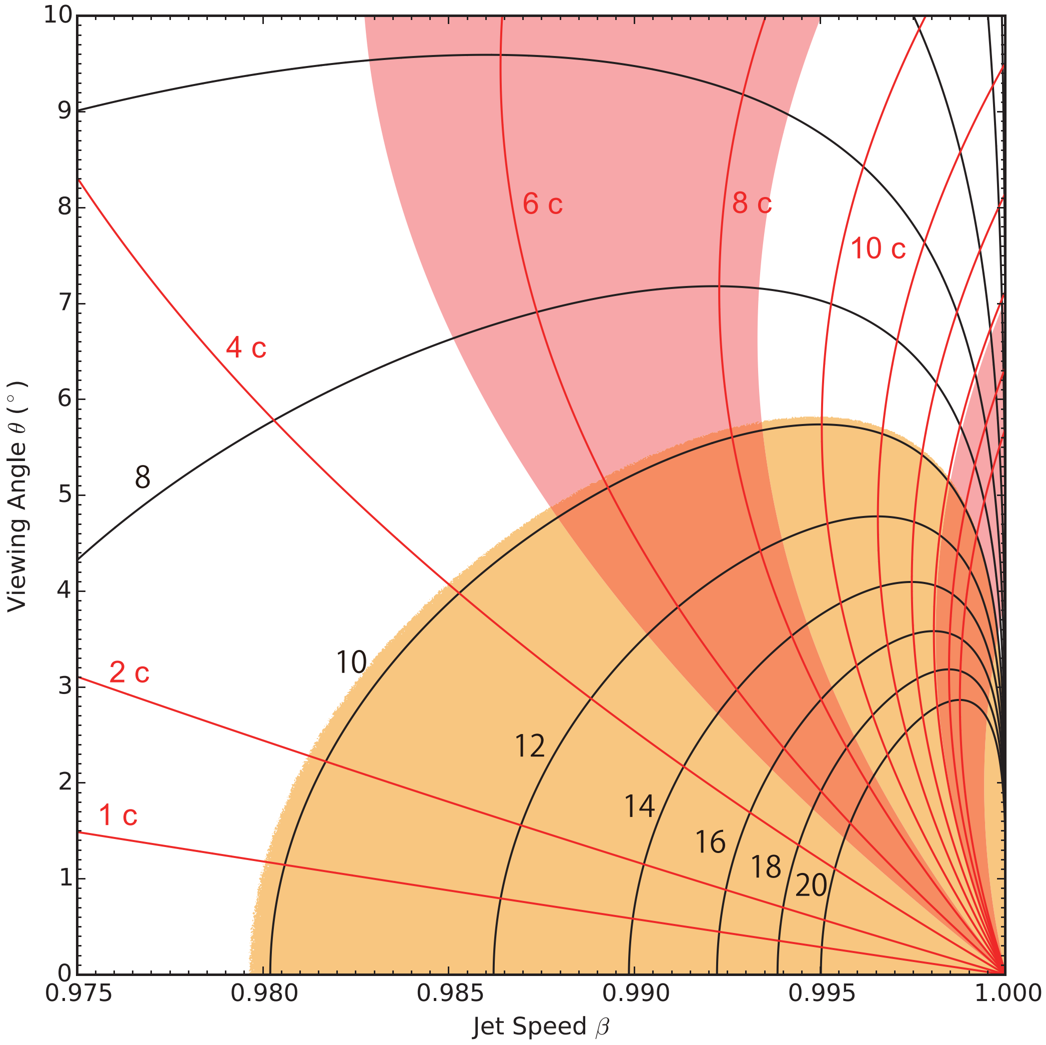

Figure 4.10: Constraint on the jet speed β and viewing angle θ from the 1.3 mm emission size (see §4.5.4 for details). The shaded area colored in orange satisfies a condition that the total extent of the flaring region is not smaller than the 1.3 mm emission size in April 2011 when the expansion speed on the co-moving frame is corresponding to the sound velocity of the relativistic plasma of $c/\sqrt{3}$. Black lines indicate contours of the Doppler factor, while red lines indicate contours of the apparent velocity of the jet component. The shared areas colored in red indicate apparent velocities of C5 and C6 measured with VLBA at 7 mm (see §4.5.3).

lower limit size of $132.9\ \mu$as for $R_{\rm EHT}$, and $t = 169$ d between the start day of the GeV γ-ray flare and the last day of EHT observations, providing the largest permitted range of the jet speed and viewing angle. The jet speed and viewing angle are constrained into $\beta > 0.979$ corresponding to the Lorentz factor of $\Gamma > 4.98$ and $\theta < 5.83^\circ$, respectively. The size also limits the Doppler factor of the jet to $\delta > 9.85$ (see black contour lines in Figure 4.10), which can not be constrained by the measurements of the apparent velocity. We show areas for the apparent speed of C5 and C6 measured with VLBA (§4.5.3). The constraint on the viewing angle from the size is much smaller than the constraint of $\theta < 21^\circ$ from the apparent velocity of C6. Combined with the apparent velocity of C6, one can obtain tighter constraints of $\beta > 0.988$ ($\Gamma > 6.41$), $\theta < 5.77^\circ$ and $\delta > 9.85$. Since these constraints are mainly based on an assumption of the co-spatiality of radio and GeV γ-ray emission, they can be used to test the theoretical models (e.g. one-zone SSC and/or EC models) based on this assumption through future SED modeling using multi-wavelength data at this GeV γ-ray flare.

In the discussions above, we derived constraints from the size observed with EHT assuming the co-spatiality of radio and GeV γ-ray emission, since we have only 1 epoch data with EHT. However, if one measures the size of components at multi epochs, one can directly make a constrain on physical quantities using variations in the size without any assumptions. We show that the size can provide constraints on the Doppler factor that cannot be constrained by velocity measurements, and also constraints on the viewing angle tighter than velocity measurements particularly in case of slower apparent speeds (e.g. $\beta_{\rm app}$ of few). It clearly shows that future multi-epoch observations with EHT are quite useful to constrain on the physical quantities of the relativistic jet.

4.6 SUMMARY

We present 1.3 mm VLBI observations of NRAO 530 with the Event Horizon Telescope in April 2011 which is $\sim$6 months after the bright GeV γ-ray flare in late-2010. We also present the multi-wavelength observations with the Fermi Gamma-ray Space Telescope (*fermi*) at GeV γ-ray, the Very Long Baseline Array (VLBA) at 7mm and the Submillimeter Array at 1.3 mm.We summarize our results as follows.

1. The 1.3 mm closure phase on VLBI triangles involving all 3 sites is clearly offset from zero, meaning that source structure of NRAO 530 is resolved into an asymmetric structure. The observed visibilities are well-explained

by the two component model consisting of a weak core component (S0) and a relatively extended bright jet component (S1). The position angle of the inner-jet structure is $-129^{+7}_{-38}{}^{\circ}$ consistent with past 3 mm observations around a large millimeter flare in 1994-1995. The position angle is considerably different from that of the milliarcsecond-scales and larger-scales jet to the north direction, requiring the highly curved trajectory in the inner jet on sub-parsec scales.

2. Current EHT observations revealed the curved trajectory of the inner-jet structure on sub-parsec scales in all three blazars NRAO 530, 1921-293 and 3C 279. In particular, in the case of NRAO 530, the inner-jet position angle on sub-parsec scales is consistent between two epochs with an interval of $\sim$10 years, largely offset from position angles of the larger scale jet and its motion. These results seem different from two broad trends of the parsec-scale jets in blazars that (1) the apparent speed changes are distinctly larger than changes in direction, and (2) the jet feature changes the position angle of its motion into a direction getting the better alignment with the mean inner-jet position angle. Current EHT results might favor a scenario that the jet is following pre-established channels and jet features move around the bend, as the major mechanism of the non-radial and non-ballistic motion on sub-parsec scales.
3. The GeV γ-ray light curve observed with *fermi* Large Area Telescope shows that NRAO 530 was in enhanced active state from mid-2010 to mid-2011. The bright γ-ray flare occurred in late-2010 with a duration of $\Delta t = 49$ d, giving the emission region size of $< ct\delta/(1+z) = 6.67 \times 10^{16}\delta$ cm, where δ is the Doppler factor of the jet. We found also a synchronized radio brightening from April 2010 at both 1.3 mm and 7 mm, and confirmed that our observations are performed in the middle of the radio flare associated with the active state in γ-ray regime.
4. VLBA observations at 7 mm reveals that two components were ejected from the core at 7 mm during the active state in GeV γ-ray regime from mid-2010 to mid-2011. The later component C6 is most probably the 7-mm counterpart of S1 detected with EHT. The motion of C6 (=S1) is directed into the north, which is significantly different from the position angle of the inner jet detected with EHT. This requires that the inner jet in NRAO 530 has a curved trajectory on sub-parsec scales. In relation to the bright GeV γ-ray flare, C6

(=S1) is the most probable counterpart component of the bright GeV γ-ray flare. This provides the first example that a jet component related with γ-ray activities actually moves along a curved trajectory, as suggested in previous studies to explain rotations in EVPA in other blazars.

5. EHT observations revealed that the radio counterpart of the γ-ray flare S0 has a size of $\sim 140\ \mu$as $\sim$ 1304 ld in the period of EHT observations held on ~ 170 d after the GeV γ-ray flare. The results of EHT observations suggest a rapid expansion of the flaring region from $\lesssim$ 49 ld to $\sim$ 1304 ld during ~ 170 d assuming the co-spaciality of the broadband emission as widely accepted one-zone synchrotron-self Compton (SSC) and/or external Compton (EC) models. It requires super-luminal expansion of the component with an expansion speed of $\beta_{\rm exp,app} \gtrsim 7.4$.
6. We explained that such a super-luminal expansion can be seen in the jet of blazars. The apparent expansion speed of the components depends on (i) the jet speed β, (ii) the viewing angle of the jet θ, (iii) the expansion velocity on the co-moving frame. We put constraints on the jet speed and the viewing angle from a condition that the total extent of the flaring region is not smaller than the 1.3 mm emission size in April 2011 with the maximum expansion speed corresponding to the sound velocity of the relativistic plasma of $c/\sqrt{3}$ on the co-moving frame. The jet speed, Lorentz factor, viewing angle and Doppler factor are limited into $\beta > 0.988$, $\Gamma > 6.41$, $\theta < 5.77^\circ$ and $\delta > 9.85$, respectively. They can be used to test the theoretical models (e.g. one-zone SSC and/or EC models) based on this assumption through future SED modeling using multi-wavelength data at this GeV γ-ray flare.
7. Through above new analysis on the observed size, we show that the accurate size measurement of the jet component can provide (i) constraints on the Doppler factor that cannot be constrained by velocity measurements, and also (ii) constraints on the viewing angle tighter than velocity measurements. This clearly shows that the high spatial resolution of EHT can provide unique constraints on the physical properties of the relativistic jet.

These observational results demonstrate that the future EHT observations can provide unique constraints on the physical nature of the relativistic jet in blazars.

5

CONCLUSION AND FUTURE PROSPECTS

5.1 CONCLUSIONS

In this thesis, we present mm-VLBI observations of (1) the galactic center Sgr A* with VLBI Exploration of Radio Astrometry (VERA), (2) the nearby radio galaxy M87 with the Event Horizon Telescope (EHT), and (3) the blazar NRAO 530 with EHT, all of which are the main targets of the Event Horizon Telescope in the next decade. All of three works in this thesis demonstrate the importance of the future mm-VLBI observations particularly with the Event Horizon Telescope to understand the fundamental nature of the high energy phenomena in the vicinity of the SMBHs. We conclude our new findings and new questions obtained in each work as follows.

5.1.1 *Works on Sgr A* (Chapter 2)*

New Findings

- Long-term monitoring observations with VERA revealed that Sgr A* underwent a flaring event in 2007 May. The duration of flare is at least 10 days, which is much longer than flaring events reported in the previous studies. The flaring event is most likely associated with changes in the intrinsic properties of Sgr A*, combining with our results and the spectrum index measurements at the flaring state.
- The stable structure on mas scales observed with VERA and VLBA around this new kind of the active state disfavors origins associated with an ejection of relativistic component or a temporal one-shot plasma heating such as an expanding plasma blob (e.g. Yusef-Zadeh et al., 2006b) or a hot spot orbiting around the central black hole (Broderick & Loeb, 2006). Thus, the flaring event is likely to be associated with a brightness increase at the photosphere of the accretion disk and/or the jet.

- The synchrotron cooling time-scale at millimeter wavelength is much shorter than the duration of the flare. This requires a mechanism that heats electrons continuously on timescales much longer than the orbital timescales of the accretion disk. We found that mas-scales properties around the flare can not be explained by increase in the mass accretion rate in the thermal radiatively inefficient accretion flow inferred for Sgr A*. It might be explained by other kinds of phenomena such as a standing shock in an accretion flow.

New Questions

- Both a flaring state in 2007 found in our observations and a flare detected in Event Horizon Telescope (EHT) observations in 2009 (Fish et al., 2011) show increase in the brightness temperature. How is the relation between event-horizon scale structure traced with EHT and larger-scale structure of few or several tens of R_s traced with cm/long-mm VLBI?
- How often such a kind of very long flares occurs in Sgr A*? What a typical frequency of the flare reflects?

It is important to investigate multi-frequency structure with quasi-simultaneous observations with EHT and cm/long-mm VLBI for tracing variations on many layers of the plasma photosphere for understanding the variability in Sgr A*. On the other hand, the dedicated monitoring is useful to study properties of variations on its time-domain properties.

5.1.2 *Works on M87 (Chapter 3)*

New Findings

- For the first time, we have acquired 1.3 mm VLBI interferometric phase information on M87 through measurement of closure phase on the triangle of long baselines. Measured closure phases are consistent with 0°, as expected by physically-motivated models for 1.3 mm structure such as jet models and accretion disk models. Although our observations can not currently distinguish models, we show that the future closure phase/amplitude measurements with additional stations and greater sensitivity can effectively distinguish and put a tight constrain on physical models.
- The brightness temperature of the event-horizon-scale structure is $\sim 2 \times 10^{10}$ K both for previous observations (Doeleman et al., 2012) and our new

observations. This brightness temperature is broadly consistent with that of the radio core at lower frequencies from 1.6 to 86 GHz located in the inner $\sim 10^2\ R_\mathrm{S}$. We demonstrated a simple analysis assuming that the observed radio core is the photosphere of synchrotron self-absorption. It shows that the constant brightness temperature may give the magnetic-field profile of $B \propto r_\mathrm{core}^{\sim -1}$ in inner $\sim 10^2\ R_\mathrm{S}$, consistent with a prediction of the conical jet with no velocity gradient dominated by the toroidal magnetic field.

- Our observations were conducted in the middle of a VHE enhancement originating in the vicinity of the central black hole. The effective size derived from our data and results of lower-frequency observations favor the relatively extended size of VHE emission region of $\sim$20-60 R_S. This would not favor VHE emission models that predict a compact emission region of $\lesssim$ 10 R_S for this particular event.

New Questions

- Our results revealed that the event-horizon-scale structure had almost same flux density and size in March 2009 and March 2012. Is it just eventual coincidence? or Is the event-horizon-scale structure highly stable in contrary to predictions from theoretical works on GRMHD models?
- In the middle of this long VHE events, the event-horizon-scale structure did not significantly change, favoring the extended size of VHE emission region. However, it is not clear that this implication can be applied to other flares with much shorter time-scale.

It is clear that future EHT observations are crucial not only to constrain on the event-horizon-scale structure but also to accumulate data sets to answer these newly raised questions on the time-domain properties of the phenomena on event-horizon scales.

5.1.3 *Works on NRAO 530 (Chapter 4)*

New Findings (particularly on sub-parsec-scale properties of blazars)

- Current EHT observations revealed the curved trajectory of the inner-jet structure on sub-parsec scales in all three blazars NRAO 530, 1921-293 and 3C 279. In particular, in the case of NRAO 530, the inner-jet position angle on sub-parsec scales is consistent between two epochs with an interval of

$\sim$10 years, largely offset from position angles of the larger scale jet and its motion. These results seem different from two broad trends of the parsec-scale jets in blazars that (1) the apparent speed changes are distinctly larger than changes in direction, and (2) the jet feature changes the position angle of its motion into a direction getting the better alignment with the mean inner-jet position angle. Current EHT results might favor a scenario that the jet is following pre-established channels and jet features move around the bend, as the major mechanism of the non-radial and non-ballistic motion on sub-parsec scales.

- EHT and VLBA observations strongly suggest that the inner jet in NRAO 530 has a curved trajectory on sub-parsec scales, and the counter part of γ-ray activities actually moves along a curved trajectory, as suggested in previous studies to explain rotations in EVPA in other blazars. This is the first example that γ-ray emission region is located in the bending jet.
- Using the size of the jet component observed with EHT, we performed new analysis to constrain on physical parameters of the jet. The accurate size measurement of the jet component can provide (i) constraints on the Doppler factor that cannot be constrained by velocity measurements, and also (ii) constraints on the viewing angle tighter than velocity measurements.

New Questions

- Our results and previous EHT results on other blazars show that all three blazars observed with EHT have curving structures on sub-parsec scales. How the bending structure is common in blazars on sub-parsec scales? Do sub-parsec-scales structures have statistical trends different to parsec-scales structure?
- Our results show that the γ-ray emission region most probably propagate down the bending jet on sub-parsec scales. How is it common for radio counterparts of γ-ray activities to propagate down the bending jet? How the propagation of the jet component affects polarization angles in radio and optical regimes?

It is important to increase samples in terms of the number of sources and also in terms of following-up observations of γ-ray activities with EHT for understanding these questions. Lower-frequency VLBI observations are also useful for deter-

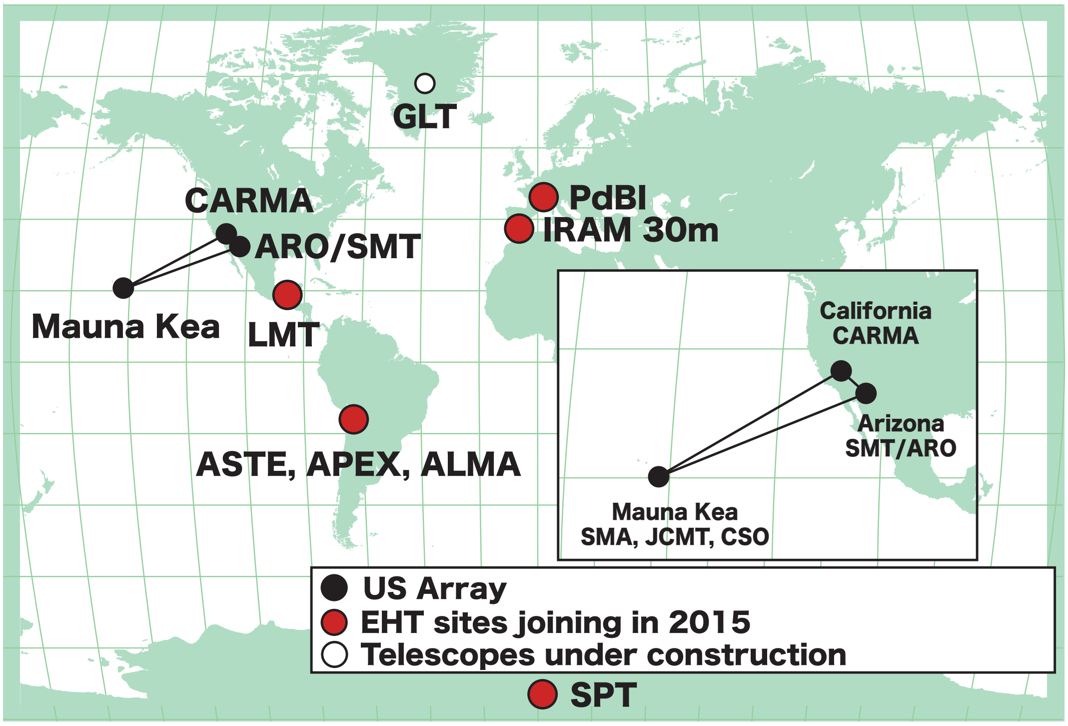

Figure 5.1: The array configuration of the Event Horizon Telescope after 2015.

mining the trajectory of the jet components from measurements of their proper motions.

5.2 FUTURE PROSPECTS

Early EHT results (Chapter 1, Chapter 3 and Chapter 4 and Doeleman et al. 2008, 2012; Fish et al. 2011; Lu et al. 2012, 2013; Akiyama et al. 2014b) were based on observations with telescopes at only three sites in the United States: CARMA in California, ARO/SMT in Arizona, SMA, JCMT and CSO in Mauna Kea in Hawaii (see Chapter 1). uv-coverage of three-site VLBI is not enough to image VLBI structures. In addition, the sensitivity might not be enough to detect fringes on longer baselines as in the results of M87 (Chapter 3).

These kinds of problems will be resolved in near future. uv-coverage and sensitivity of the array have been improved by participations of new telescopes and also upgrades in instruments at each observatory. For instance, we recently detected 1.3 mm VLBI fringes between Atacama Pathfinder Experiment telescope (APEX) in Chile, SMA and SMT in May 2012[1], providing longer baselines of several Gλ. In 2015, EHT will start test observations at new telescopes and/or interferom-

---

[1] http://www.eso.org/public/news/eso1229/

eters such as the phased-up ALMA (Atacama Large Millimeter/submillimeter Array) in Chile, the Large Millimeter Telescope (LMT) in Mexico, the IRAM 30m Telescope in Spain and the Plateau de Bure Interferometer (PdBI) in France (see Figure 5.1) as well as with new digital backend systems with a recoding rate of 16 Gbps much broader then early EHT observations. This will provide not only significant improvements on not only uv-coverage of the EHT, but also sensitivity of the EHT.

It is clear that the next decade will be the "EHT" era, when a great deal of progresses will be achieved in studies of astrophysical phenomena in the vicinity of the supermassive black holes (SMBHs) with EHT. As the closing section of this thesis, I briefly summarize my (our) prospects of the EHT era particularly on topics related with this thesis.

5.2.1 *Direct Imaging of the Event Horizon of Super-massive Black Holes*

Imaging Techniques

The most attractive issue for everyone must be direct imaging of the event horizon of SMBHs in our galactic center Sgr A* and M87. In Chapter 3, we have shown that the current uv-coverage of EHT is not long enough to catch up the signature of the strong gravity in the vicinity of the SMBH in M87. However, the complex behavior in the visibility distribution due to the signature of the event horizon can be expected to appear on large spatial frequencies over $\sim$4 Gλ, which can be surely observed in future EHT observations (Figure 3.18). We can expect the exactly same thing for Sgr A*, because the expected size of the SMBH is similar to that of M87. That means crucial information to clarify R_s-scale structure in Sgr A* and M87 will be obtained with EHT after 2015.

Indeed, recent works on imaging techniques for EHT have shown that the event-horizon scale structure can be properly imaged with EHT after 2015. First, we developed a new imaging technique for the radio interferometry "the sparse modeling" (Honma et al., 2014), which has been a standard imaging technique for the magnetic resonance imaging (MRI) in the medical field (e.g. Lustig et al., 2008). This technique avoids the image degradation by finite beam size as well as numerous side-lobes due to the dirty synthesized beam of interferometer, which is a technical problem of the standard imaging technique CLEAN (Högbom, 1974) solving the image using the synthesized beam. The sparse modeling is less affected by the effect of the synthesized beam, leading to super-resolution images in which structure finer than the standard beam size (diffraction limit) can be reproduced.

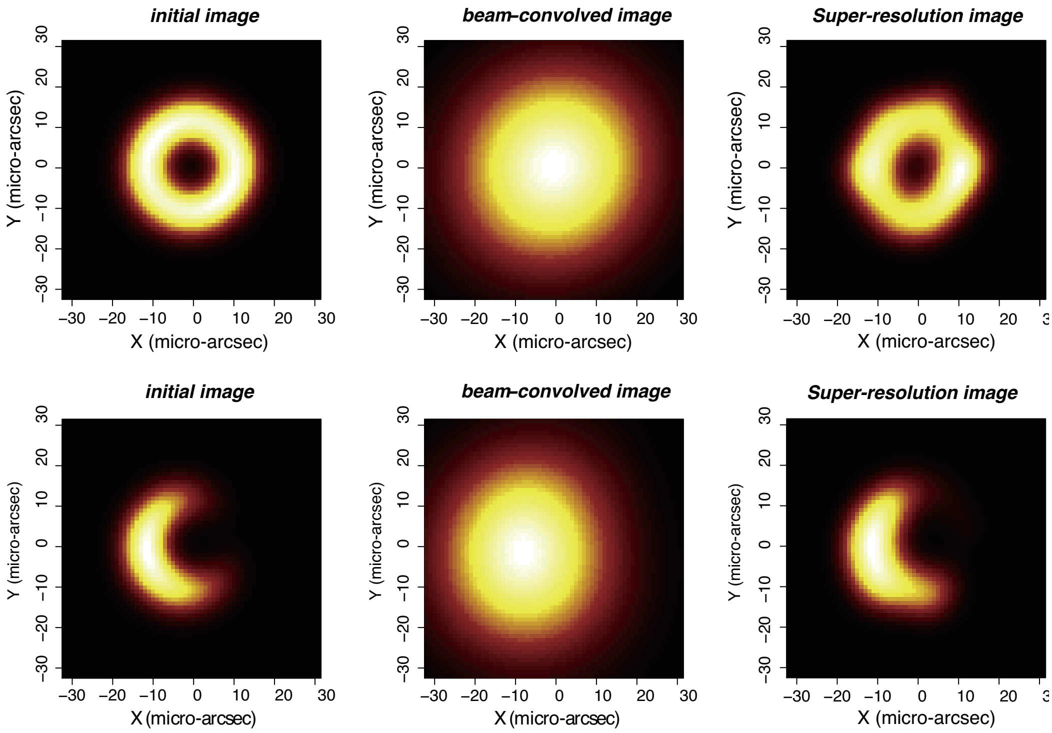

Figure 5.2: Examples of the reconstructed images with the sparse modeling (Honma et al., 2014). Left panels are model images with a black hole shadow for M87 in the case of the smaller black hole mass of 3×10^9 $M_\odot$. In that case, even with EHT after 2015, the synthesized beam is larger than the size of the black hole shadow and completely wash out the detailed structure on event-horizon scales (middle panels). Our new technique, the sparse modeling can reconstruct event-horizon scale structures properly even with realistic (or probably worth than real) thermal noises.

We found that this technique can reconstruct the signature of the gravitational lensing robustly for M87 with observational noises (Figure 5.2), even if they have black hole shadows with a size of $\sim 10\,\mu$as due to lower black-hole masses and/or the high spin. It indicates that with this new technique we can properly detect the signature of the event horizon even in the worst case that its size is much smaller than the synthesized beam of the EHT after 2015.

On the other hand, recent studies of other groups show that the event-horizon scale structure can be imaged for both M87 and Sgr A* using the another traditional imaging technique "Maximum Entropy Method" (Lu et al., 2014; Fish et al., 2014). Lu et al. (2014) reports that the event-horizon scale structure in M87 can be properly reproduced for the larger mass case with the Bi-Spectrum Maximum Entropy Method (BSMEM) developed for the optical/infra-red interferometry (Figure 5.3 (a)). Very recently, Fish et al. (2014) shows that Sgr A* can be also properly imaged with BSMEM by removing the effect of the interstellar scattering using well-determined elliptical-Gaussian scattering kernel (see §2.1.5.2) before the image reconstruction in advance (Figure 5.3 (b)).

The Exchange Monte Carlo (EMC) technique, which I developed for reconstructing an image of NRAO 530 in Chapter 4, can be also used for deriving information of the event-horizon scale structure. Since EMC can derive the best-fit parameter and also its probability distribution function robustly even for models with a large number of parameters and high complexity, the Baysian modeling with EMC would be one of useful tools for the EHT science in the next few years. I and Dr. Benkevich in MIT Haystack observatory have been working on the software reconstructing the signature of the gravitational lensing from Sgr A* data using geometrical models. We confirm that the Baysian modeling with EMC using geometrical models works well for reconstructing images from simulated data based on some physical models (Figure 5.4).

In summary, many powerful techniques have been developed for reconstructing images from the observed visibility. It is promising that we can discuss detailed structure on event-horizon scales with the upgraded EHT and such new imaging techniques.

5.2.1.1 *Scientific Prospects*

Here, I briefly describe some of what one can discuss based on the event-horizon scale structure observed with future EHT observations.

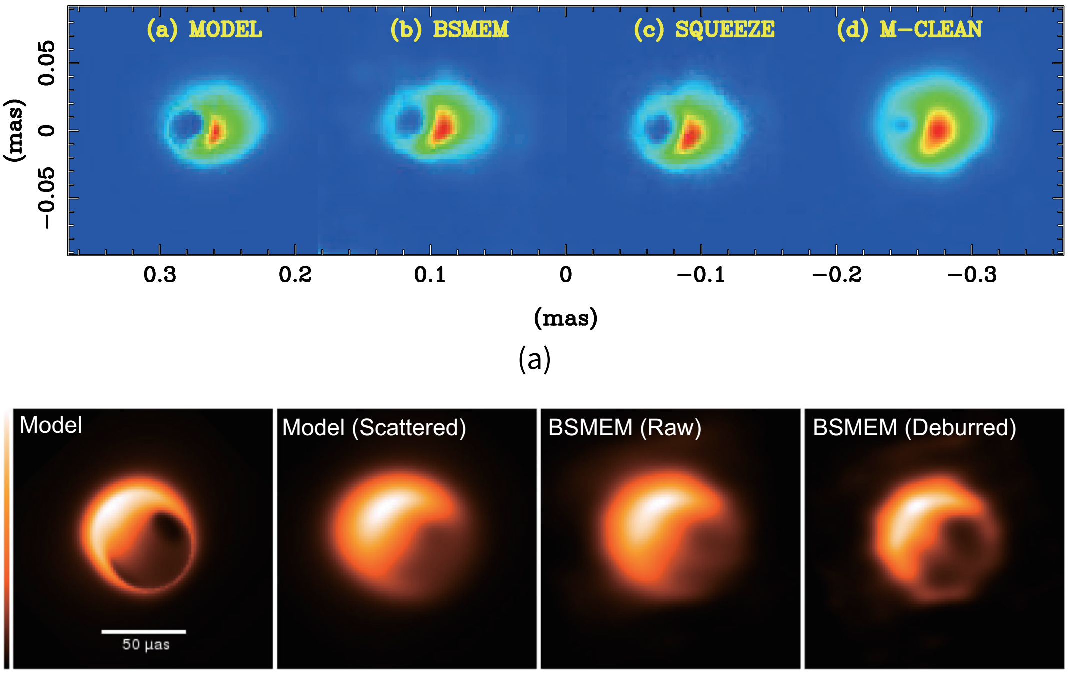

(a)

(b)

Figure 5.3: Examples of the reconstructed images with the Bi-Spectrum Maximum Entropy Method (BSMEM). (a) The results of imaging simulations using a M87 jet model in Broderick et al. (2009) on uv-coverages of EHT after 2015 (Lu et al., 2014). The left panel shows a model image, while right three panels show reconstructed images with BSMEM, SQEEZE (an imaging software using MCMC and BSMEM) and Multi-resolution CLEAN implemented in CASA. The reconstructed image using BSMEM regularizations (with BSMEM, SQEEZE) have higher fidelities than Multi-resolution CLEAN method. (b) The results of imaging simulations using semi-analytic RIAF model for Sgr A* in Broderick et al. (2011) on uv-coverages of EHT after 2015 (edited images in Fish et al., 2014). The left two panel show a model image and a model image convolved with the scattering kernel inferred for 1.3 mm, while the right two panels are a reconstructed image with BSMEM using a “raw” simulated data and a reconstructed image with BSMEM using a “de-burred” simulated data where the scattering effect on the visibility amplitude is corrected in advance. The reconstructed image on the de-burred data clearly has the highest fidelity and reconstruct a signature of the strong gravity of super-massive black holes.

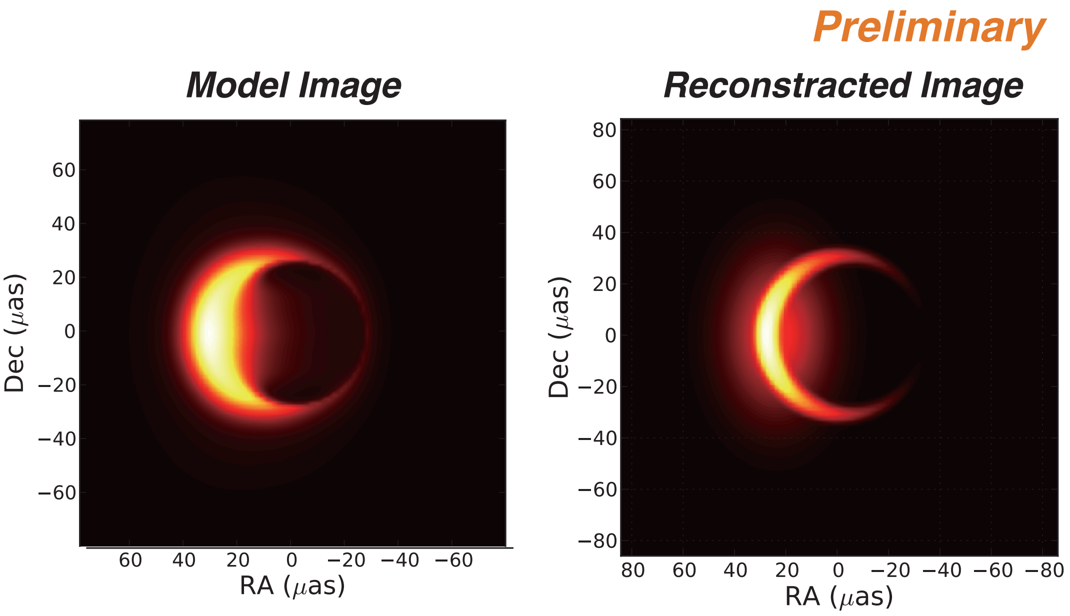

Figure 5.4: Examples of the reconstructed images with the Baysian modeling using the Exchange Monte Carlo method (Benkevich & Akiyama et al. in prep.). The left panel shows a model image of (Broderick et al., 2011), while the right panel shows a reconstructed image with the Exchange Monte Carlo method (Chapter 4) using a geometrical model with nine parameters.

First of all, it is trivial that the direct imaging of the event horizon is of great importance, since it would be an ultimate proof for existence of the black hole and also the first confirmation that Einstein's general relativity works well in the strong gravity regime. Since the mass of SMBHs in Sgr A* and M87 is well-determined, the measurement of the shadow feature provides strong constraints on the black-hole spin for these sources, which is very important to understand the physical properties of the accretion disk and/or the jet and also the evolutional history of the SMBH itself.

For M87, as explained in Chapter 3, the emission structure contains information crucial to understand mysteries of the relativistic jet. For instance, 1.3 mm emission structure can be significantly different depending on (i) the loading radius of non-thermal particles and (ii) the profiles of non-thermal particles and magnetic fields. Since the crescent-like feature appears more clearly at smaller particle loading radii, the emission structure around the last-photon orbit is quite useful to clarify one of the biggest mysteries on the relativistic jet "where leptons are accelerated and the jet starts to be luminous". In addition, the non-thermal particles and magnetic fields would affect how the jet is luminous at the downstream of the black hole, which would provide very important hints such as how large the particle-acceleration region is. The radio luminosity and the emission size also provide the magnetic field strength as well as the particle energy density (Kino et al., 2014b), which is quite important information to understand the energetics of the relativistic jet.

For Sgr A*, recent theoretical studies seem to have a consensus that 1.3 mm emission is dominated by emission from a hot accretion flow in radiatively inefficient regime (radiatively inefficient accretion flow; RIAF; see §2). RIAF and/or thermal jet have been proposed for the origin of the radio emission (see §2). However, recent theoretical works on the GRMHD jet model for Sgr A* (Mościbrodzka et al., 2014) reported that 1.3 mm emission would be dominated by RIAF to reproduce 1.3 mm visibility and broadband SED of Sgr A* observed with previous EHT and multi-wavelength observations, respectively, even if emission at lower frequency is dominated by the jet emission (see Figure 2.16 and Mościbrodzka et al., 2014). It means that EHT would provide an unique opportunity to image the accretion disk around the black hole on scales of R_S. Future EHT observations would be quite useful to investigate various variabilities in the accretion disk suggested by previous theoretical and/or observational studies, and also the nature of RIAF which is quite common in the most of nearby galaxies.

5.2.2 *Multi-scale Structure of Accretion Disk and/or Jet in Inner* 10^2 R_S

*Sgr A**

For works on Sgr A* with VERA, we conclude that it is important (i) to investigate multi-frequency structure with quasi-simultaneous observations with EHT and cm/long-mm VLBI for tracing variations on many layers of the plasma photosphere, and (ii) to monitor with the dedicated interval, for understanding more detailed properties of the time variability.

After works in Chapter 2, we have been working on monitoring with VERA (e.g. Akiyama et al., 2014a) and newly developed KVN and VERA Array (KaVA; Figure 5.5) for investigating topics mentioned above. KaVA consists of 7 stations in Korean VLBI Network (KVN; Lee et al., 2011) and VERA, and started regular observations at 13/7 mm (i.e. 22/43 GHz) in March 2014. KaVA is expected to achieve a good performance for Sgr A* observations, since it has shorter baselines than other VLBI arrays. One of reasons making it difficult to calibrate VLBI data of Sgr A* is its low correlated flux density in long baselines owing to the effect of the interstellar scat-

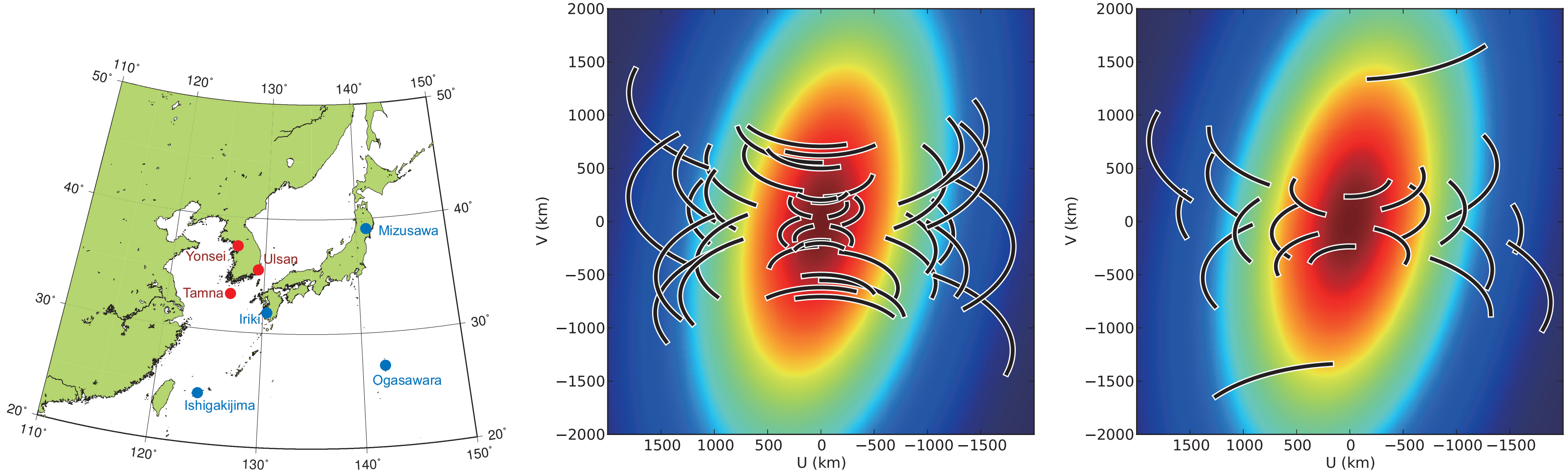

(a) (b) (c)

Figure 5.5: Left panel: Array configuration of KaVA. KaVA is a combination of Korean VLBI Network (KVN; colored in red) and VLBI Exploration of Radio Astrometry (VERA; colored in blue). Middle and right panels: The uv-coverage of KaVA (the middle panel) and VLBA (the right panel) for Sgr A*. Lines are the uv-coverage of each array. The colored contour is the visibility amplitude distribution of the best-fit elliptical Gaussian model in Bower et al. (2004).

tering. Short (2000 km) baselines in KaVA provide more effective sampling of the visibilities of Sgr A* than VLBA (Figure 5.5), enabling accurate determination of its size and good-quality images similar to or better than VLBA.

We successfully performed simultaneous observations with EHT and KaVA in 2013, and also multi-epoch observations with VERA and KaVA with intervals shorter than 1 month from 2012 to 2014. Through these observations, we expect to obtain new observational properties of time variation in Sgr A* and Sgr A* itself.

M87

Multi-frequency structure is quite useful to understand the observational properties of the relativistic jet as well as Sgr A*. Indeed, in Chapter 3, we have discussed implications for the profile of the magnetic-field strength and also for the nature of very-high-energy γ-ray activities combined with lower-frequency observations with VERA.

For instance, to understand acceleration and collimation mechanisms of the relativistic jet, it is quite important to measure (i) the acceleration profile (e.g. Asada et al., 2014), (ii) the collimation profile (Asada & Nakamura, 2012; Nakamura & Asada, 2013a; Hada et al., 2013) and (iii) the profile of the total magnetic-field strength (e.g. Kino et al., 2014a,b). We can estimate toroidal and poloidal magnetic-field profiles of $B_{\mathrm{toroidal}} \propto \Gamma(r)^{-1}R(r)^{-1}v(r)^{-1}$ and $B_{\mathrm{poloidal}} \propto R(r)^{-2}$ (e.g. Baum et al., 1997) for the case of the ideal-MHD jet, where $\Gamma(r)$, $v(r)$ and $R(r)$ are the Lorentz factor, the velocity of the jet and the width of the jet as a function of the distance from the central black hole. We can investigate, for instance, dominance of toroidal or poloidal magnetic field from comparison to the profile of total magnetic-field strength. We are now working on massive monitoring observations with VERA/KaVA of M87 to determine the acceleration profile in the inner 10^2 R_{S}, which has not been well-determined so far. In addition, future high-resolution observations with EHT and space VLBI (e.g. Radio Astron Kardashev et al., 2013) will provide the collimation profile more precisely. In the next several years, probably, we will be able to discuss acceleration and collimation mechanisms of the relativistic jet using the observational properties of the relativistic jet in the inner 10^2 R_{S}.

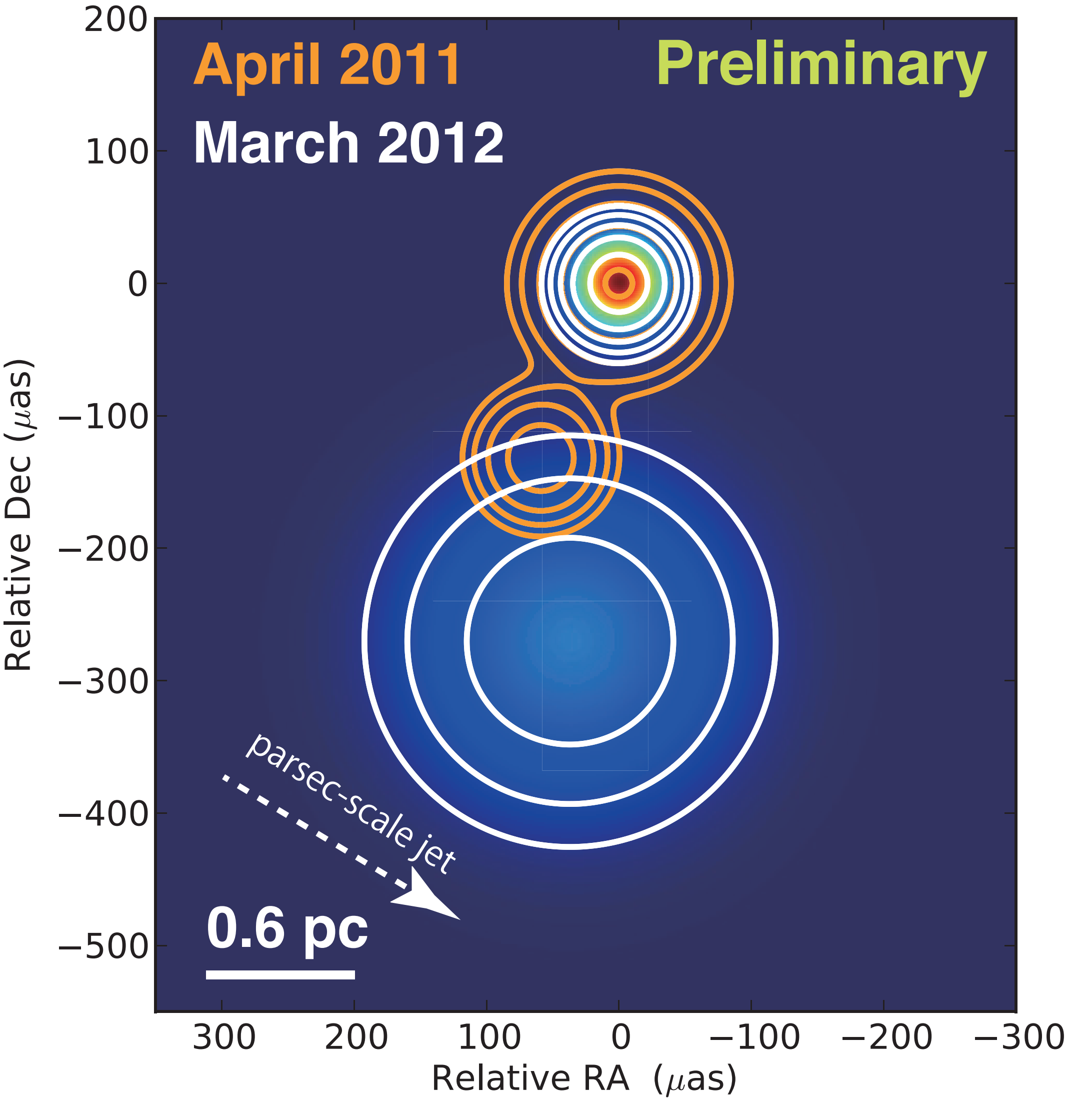

Figure 5.6: Preliminary results of EHT observations on 3C 279 (Akiyama, Lu, Fish et al. in prep.). 2 year's observations with EHT revealed super-luminal non-radial motion and super-luminal expansion of the component on sub-parsec scales which we found in NRAO 530 (Chapter 4).

5.2.3 *Blazars: Direct Imaging of the High-energy Emission Zone*

In Chapter 4, we have shown that sub-parsec-scale structure and accurately measured sizes of the jet components are useful to investigate the nature of the flaring activities in the jet and also the properties of the jet itself. The super-luminal expansion and non-radial motion along the curved geometry suggested the radio counterpart of the γ-ray activities in NRAO 530 have been actually observed in the jet components of other blazars in recent EHT observations (e.g. 3C 279, Akiyama et al. in prep., Figure 5.6), indicating that we can apply our new analysis in this thesis to many other blazar sources. By accumulating multi-year data on many sources with EHT, we will be able to discuss statistical properties of the blazar jets on sub-parsec scales.

In addition, future EHT observations with improved imaging techniques (§5.2.1) can provide more detailed structure of the jet component. This would be quite useful to understand the nature and formation process of the jet component itself, which are closely related with activities at high-energy bands in general. Combined with spectrum and proper motion measurements with lower-frequency VLBI observations, we will discuss more detailed physical nature of the high-energy emission zone in connection with particle acceleration mechanisms in the relativistic jet.

SELF-SIMILAR SOLUTION AND EQUIBRIUM TEMPERTURE OF ADIABATIC INFLOW-OUTFLOW SOLUTION

In this chapter, we derive a self-similar solution of Adiabatic Inflow-Outflow Solution (ADIOS; Blandford & Begelman, 1999). We also estimate the equibrium temperture of electorons in the inner $10^2\,R_s$ discussed in §2.5.2, following an approach of Mahadevan (1997) on Adovection Dominated Accretion Flow (ADAF; Ichimaru, 1977; Narayan & Yi, 1994, 1995; Manmoto et al., 1997).

A.1 EQUATIONS OF ADIOS

We consider an optically thin, axisymmetric and steady accretion flow around a black hole. Assuming the existence of randomly oriented magnetic fields that possibly originate from the turbulence in the gas flow, we take total pressure p to be

$$p \;=\; p_{\mathrm{gas}} + p_{\mathrm{mag}}, \tag{A.1}$$

where p_{gas} is the gas pressure and p_{mag} is the magnetic pressure. Since here we consider optically-thin and gas-pressure-dominated accretion flow, we neglect radiation pressure. We assume the ratio of gas pressure to the total pressure β is globally constant in the flow. Following Mahadevan (1997), the magnetic pressure p_{mag} is given by

$$p_{\mathrm{mag}} = (1-\beta)p = \frac{B^2}{24\pi}, \tag{A.2}$$

where B is the magnetic field strength. We define the isothermal sound speed c_s by

$$p = \rho c_s^2, \tag{A.3}$$

where ρ is the density and we assume that the gas has a fixed ratio of specific heat capacity at constant pressure c_p to specific heat capacity at constant c_v, $\gamma \equiv c_p/c_v$. For convenience, we define

$$\epsilon = \frac{5/3 - \gamma}{\gamma - 1}. \tag{A.4}$$

We vertically average the flow equations and consider a two-dimensional flow in the equatorial R-ϕ plane. We assume a steady antisymmetric flow so that $\partial/\partial t = \partial/\partial\phi = 0$ and all flow variables are functions only of R. We denote the Keplerian angular velocity by

$$\Omega_K(R) = \left(\frac{GM}{R^3}\right)^{1/2} \tag{A.5}$$

and the Keplerian velocity

$$v_K(R) = \left(\frac{GM}{R}\right)^{1/2}, \tag{A.6}$$

where M is the mass of central black hole. The surface density of the gas is $\Sigma = 2\rho H$, where H $\sim Rc_s/v_K$ is the vertical scale hight.

Following Shakura & Sunyaev (1973), we employ the usual α-prescription for the viscosity, and the kinematic coefficient of shear viscosity is written as

$$\nu(R) = \alpha c_s H = \frac{\alpha c_s^2}{\Omega_K}, \tag{A.7}$$

where α is a constant.

Before showing the equations of the ADIOS model, we introduce the equations of ADAF. In the ADAF model, the density of the gas ρ, its radical velocity v, angular velocity Ω, and isothermal sound speed c_s, introduced above, satisfy the following four equations (Kato et al., 2008; Abramowicz et al., 1988; Narayan & Popham, 1993; Narayan & Yi, 1994):

the conservation law of mass (the continuity equation):

$$\dot{M} = -4\pi R H v \rho. \tag{A.8}$$

the conservation law of the radial component of the momentum:

$$v\frac{dv}{dr} - \Omega^2 R = -\Omega_K^2 R - \frac{1}{\rho}\frac{d(\rho c_s^2)}{dr} \tag{A.9}$$

the conservation law of the angular momentum:

$$\rho R H v \frac{d(\Omega R^2)}{dR} = \frac{dG}{dR} \tag{A.10}$$

where

$$G \equiv \frac{\alpha \rho c_s^2 R^3 H}{\Omega_K}\frac{d\Omega}{dR}. \tag{A.11}$$

the conservation law of the energy:

$$\Sigma v T_i \frac{dS}{dR} = 3(1+\epsilon)\rho H v \frac{dc_s^2}{dR} - 2c_s^2 H v \frac{d\rho}{dR} = Q^+ - Q^-. \tag{A.12}$$

where T_i is the ion temperature and S is entropy. By integrating (A.10) with R, we obtain

$$-\frac{\dot{M}}{4\pi}\Omega R^2 - G = F_l, \tag{A.13}$$

where F_l is the constant. The physical meaning of F_l is the inwardly directed angular momentum flux. The left-hand side of (A.12) is the advected entropy, while the right-hand side gives the difference between the energy input per unit area due to viscous heating Q^+ and the energy loss due to radiative cooling Q^-. The viscous heating Q^+ is given as

$$Q^+ = \frac{2\alpha \rho c_s^2 R^2 H}{\Omega_K}\left(\frac{d\Omega}{dR}\right). \tag{A.14}$$

Following Narayan & Yi (1994), we define the degree to which the flow is advection-dominated as

$$f \equiv 1 - \frac{Q^-}{Q^+}. \tag{A.15}$$

In the extremely limit of no radiative cooling, f becomes unity, while in the opposite limit of very efficient radiative cooling, f becomes zero. We assume f is constant. Following Narayan & Yi (1994), we define

$$\epsilon' = \epsilon / f. \tag{A.16}$$

Putting (A.14) and (A.15), the right-hand side of the equation of energy conservation (A.12) is represented as

$$Q^+ - Q^- = f \frac{2\alpha \rho c_s^2 R^2 H}{\Omega_K} \left(\frac{d\Omega}{dR} \right) = 2f \frac{G}{R} \frac{d\Omega}{dR}. \tag{A.17}$$

Putting (A.8) and (A.17), (A.22) becomes

$$-\frac{\dot{M}}{4\pi} c_s^2 \left[\frac{3}{2} (1+\epsilon) \frac{d \ln c_s^2}{d \ln R} - \frac{d \ln \rho}{d \ln R} \right] = f \Omega G \frac{d \ln \Omega}{d \ln R} \tag{A.18}$$

Here, we consider the advection dominated accretion flow including the effect of a powerful wind that partially carries away mass, angular momentum and energy from the accreting gas (Blandford & Begelman, 1999; Yuan et al., 2003). Following Blandford & Begelman (1999), the equations of the ADAF model (A.8), (A.9), (A.12) and (A.13) are modified as below:

the conservation law of mass (the continuity equation):

$$\dot{M} = -4\pi R H v \rho = \dot{M}_{\rm out} \left(\frac{R}{R_{\rm out}} \right)^s \tag{A.19}$$

the conservation law of the radial component of the momentum:

$$v \frac{dv}{dr} - \Omega^2 R = -\Omega_K^2 R - \frac{1}{\rho} \frac{d(\rho c_s^2)}{dr} \tag{A.20}$$

the conservation law of the angular momentum:

$$-\frac{\dot{M}}{4\pi} \Omega R^2 - G = \lambda \frac{\dot{M}}{4\pi} R^{-1/2}. \tag{A.21}$$

the conservation law of the energy:

$$-\frac{\dot{M}}{4\pi}c_s^2\left[\frac{3}{2}(1+\epsilon)\frac{d\ln c_s^2}{d\ln R}-\frac{d\ln\rho}{d\ln R}\right]=f\Omega G\frac{d\ln\Omega}{d\ln R}-\varepsilon\frac{\dot{M}}{4\pi}R^{-1}. \tag{A.22}$$

As shown in (A.19), we define the mass loss index s and make the mass inflow rate satisfy $\dot{M}\propto R^s$. The value of s is restricted as $0\leq s<1$. This mass loss by wind allows the accreting mass to reduce with decreasing radius, while the energy release can still increase. The additional terms $\lambda\dot{M}R/4\pi$ in (A.21) and $-\varepsilon\dot{M}R^{-1}/4\pi$ in (A.22) indicate angular momentum and energy carried away due to the wind. Equivalently, for the specific angular momentum and energy carried off by the wind, we have

$$\frac{d}{d\dot{M}}\left(\lambda\frac{\dot{M}}{4\pi}R^{-1/2}\right)=\frac{\lambda(s+1/2)R^{1/2}}{4\pi s} \tag{A.23}$$

$$\frac{d}{d\dot{M}}\left(\varepsilon\frac{\dot{M}}{4\pi}R^{-1}\right)=\frac{\epsilon(s-1)}{4\pi sR}. \tag{A.24}$$

A.2 SOLUTION OF SELF-SIMILAR ADIOS

The equations of the ADAF model (A.8), (A.10), (A.9) and (A.12) permit a self-similar solution of the form (Kato et al., 2008, cf.)

$$v\propto R^{-1/2},\ \rho\propto R^{-3/2},\ c_s^2\propto R^{-1},\ \Omega\propto R^{-3/2}. \tag{A.25}$$

Here, we assume that the self-similar solution is modified from (A.25) by introducing the effect of the wind as

$$v=v_0R^{-1/2+\delta_1},\ \rho=\rho_0R^{-3/2+\delta_2},\ c_s^2=c_{s0}^2R^{-1+\delta_3},\ \Omega=\Omega_0R^{-3/2+\delta_4}, \tag{A.26}$$

where ρ_0, v_0, Ω_0 and c_{s0} are constants. Substituting the relations (A.26), the equations of the ADIOS model (A.19), (A.21), (A.20) and (A.22) become

$$s = \delta_2 + \frac{\delta_3}{2} \tag{A.27}$$

$$(\Omega^2 - \Omega_K^2)R^2 + v^2(\frac{1}{2} - \delta_1) + c_s^2\left(\frac{5}{2} - \delta_2 - \delta_3\right) = 0 \tag{A.28}$$

$$-\frac{\dot{M}}{4\pi}\left(\Omega R^2 + \lambda R^{1/2}\right) = G = -\frac{\dot{M}}{4\pi}\left[\alpha\frac{\Omega}{\Omega_K}\frac{c_s^2 R}{v}\left(-\frac{3}{2} + \delta_4\right)\right] \tag{A.29}$$

$$-\frac{\dot{M}}{4\pi}\left\{\left[\epsilon - (1+\epsilon)\delta_3 + \frac{2}{3}\delta_2\right]c_s^2 + \frac{2\varepsilon}{3R}\right\} = f\Omega G\left(1 - \frac{3}{2}\delta_4\right). \tag{A.30}$$

For deriving (A.27), we assume $H \propto Rc_s/v$. If we assume $H \propto Rc_s/v_K$ or $H \propto R$, the equation of the mass conservation (A.27) becomes $s = \delta_1 + \delta_2 + \delta_3/2$ or $s = \delta_1 + \delta_2$, but the solution of the ADIOS model does not change from in the case of $H \propto Rc_s/v$ (i.e. $\delta_1 = \delta_3 = 0$ in both cases as shown later). Substituting $\Omega = \Omega_0 R^{-3/2+\delta_4}$ for (A.29), the left-side hand of (A.29) becomes

$$-\frac{\dot{M}}{4\pi}\Omega R^2\left(1 + \frac{\lambda}{\Omega_0 R^{\delta_4}}\right) = G. \tag{A.31}$$

For convenience, we define

$$\lambda' \equiv \frac{\lambda}{\Omega_0 R^{\delta_4}}. \tag{A.32}$$

Thus, (A.29) is rearranged as

$$-\frac{\dot{M}}{4\pi}\Omega R^2(1+\lambda') = G = -\frac{\dot{M}}{4\pi}\left[\alpha\frac{\Omega}{\Omega_K}\frac{c_s^2 R}{v}\left(-\frac{3}{2} + \delta_4\right)\right]. \tag{A.33}$$

Substituting $c_s^2 = c_{s0}^2 R^{-1+\delta_3}$, (A.30) becomes

$$-\frac{\dot{M}}{4\pi}c_s^2\left[\epsilon - (1+\epsilon)\delta_3 + \frac{2}{3}\delta_2 + \frac{2\varepsilon}{3c_{s0}^2 R^{\delta_3}}\right] = f\Omega G\left(1 - \frac{3}{2}\delta_4\right). \tag{A.34}$$

Similarly, we define

$$\varepsilon' \equiv \frac{\epsilon}{c_{s0}^2 R^{\delta_3}}. \tag{A.35}$$

and (A.30) is rearranged as

$$-\frac{\dot{M}}{4\pi}c_s^2\left[\epsilon-(1+\epsilon)\delta_3+\frac{2}{3}\delta_2+\frac{2}{3}\varepsilon'\right]=f\Omega G\left(1-\frac{3}{2}\delta_4\right). \tag{A.36}$$

First, we rearrange equations of the conservation of the angular momentum (A.33) and the energy (A.36). Putting the right-hand side of (A.33) for G, (A.36) becomes

$$c_s^2\left[\epsilon-(1+\epsilon)\delta_3+\frac{2}{3}\delta_2+\frac{2}{3}\varepsilon'\right]=fR^2\Omega^2(1+\lambda')\left(1-\frac{3}{2}\delta_4\right). \tag{A.37}$$

When we define

$$\tilde{\epsilon}'\equiv\frac{\epsilon-(1+\epsilon)\delta_3+\frac{2}{3}(\delta_2+\varepsilon')}{f\left(1-\frac{3}{2}\delta_4\right)(1+\lambda')}, \tag{A.38}$$

(A.37) becomes

$$\tilde{\epsilon}'c_s^2=\Omega^2R^2. \tag{A.39}$$

Rearranging (A.33) for v,

$$v=-\frac{3}{2}\alpha\frac{c_s^2}{R\Omega_K}\frac{1-\frac{2}{3}\delta_4}{1+\lambda'}. \tag{A.40}$$

Putting (A.39) for c_s^2, (A.40) becomes

$$\begin{aligned}\tilde{\epsilon}'v &= -\frac{3}{2}\alpha R\Omega_K\left(\frac{\Omega}{\Omega_K}\right)^2\frac{1-\frac{2}{3}\delta_4}{1+\lambda'} && \text{(A.41)}\\ &\equiv -\frac{3}{2}\alpha R\Omega_K\left(\frac{\Omega}{\Omega_K}\right)^2(1+\delta_5), && \text{(A.42)}\end{aligned}$$

where $\delta_5=(1-2\delta_4/3)/(1+\lambda')-1$.

We rearrange the equation of the conservation of the radial momentum (A.28). Multiplying both members of (A.28) by $\tilde{\epsilon}'^2$, we get

$$\tilde{\epsilon}'^2(\Omega^2-\Omega_K^2)R^2+(\tilde{\epsilon}'v)^2\left(\frac{1}{2}-\delta_1\right)+(\tilde{\epsilon}'c_s^2)\tilde{\epsilon}'\left(\frac{5}{2}-\delta_2-\delta_3\right)=0. \tag{A.43}$$

Substituting (A.42) for $\tilde{\epsilon}' v$ and (A.39) for $\tilde{\epsilon}' c_s^2$, we obtain

$$\tilde{\epsilon}'^2(\Omega^2 - \Omega_K^2)R^2 + \frac{9}{4}\alpha^2 R^2 \Omega K^2 \left(\frac{\Omega}{\Omega_K}\right)^4 (1+\delta_5)^2 \left(\frac{1}{2} - \delta_1\right) + \tilde{\epsilon}' \Omega^2 R^2 \left(\frac{5}{2} - \delta_2 - \delta_3\right) = 0. \tag{A.44}$$

For convenience, we define $x \equiv (\Omega/\Omega_K)^2$. Multiplying by $1/\Omega x^2 R^2$ and substituting x, we obtain

$$\tilde{\epsilon}'^2(x-1) + \frac{9}{4}\alpha^2 x^2 (1+\delta_5)^2 \left(\frac{1}{2} - \delta_1\right) + \tilde{\epsilon}' x \left(\frac{5}{2} - \delta_2 - \delta_3\right) = 0. \tag{A.45}$$

Rearranging for x, we obtain

$$9\alpha^2\,(1-2\delta_1)\,(1+\delta_5)^2 x^2 + 4\tilde{\epsilon}'(2\tilde{\epsilon}' + 5 - 2\delta_2 - 2\delta_3)x - 8\tilde{\epsilon}'^2 = 0. \tag{A.46}$$

(A.46) is a quadratic equation for x. The discriminant of this quadratic equation is given as

$$\begin{aligned}
D/4 &= 4\tilde{\epsilon}'^2(2\tilde{\epsilon}' + 5 - 2\delta_2 - 2\delta_3)^2 - 72\tilde{\epsilon}'^2\alpha^2(1-2\delta_1)(1+\delta_5)^2 && \text{(A.47)}\\
&= 4\tilde{\epsilon}'^2\left[(2\tilde{\epsilon}' + 5 - 2\delta_2 - 2\delta_3)^2 + 18\alpha^2(1-2\delta_1)(1+\delta_5)^2\right] && \text{(A.48)}\\
&= 4\tilde{\epsilon}'^2(2\tilde{\epsilon}'^2 + 5)^2\left[\left\{1 - \frac{2(\delta_2+\delta_3)}{2\tilde{\epsilon}'+5}\right\}^2 + \frac{18\alpha^2(1-2\delta_1)(1+\delta_5)^2}{(2\tilde{\epsilon}'+5)^2}\right] && \text{(A.49)}\\
&= \left\{2\tilde{\epsilon}'(2\tilde{\epsilon}'+5)(\tilde{g}+1)\right\}^2, && \text{(A.50)}
\end{aligned}$$

where $\tilde{g}$ is defined as

$$\tilde{g} \equiv \sqrt{\left\{1 - \frac{2(\delta_2+\delta_3)}{2\tilde{\epsilon}'+5}\right\}^2 + \frac{18\alpha^2(1-2\delta_1)(1+\delta_5)^2}{(2\tilde{\epsilon}'+5)^2}} - 1. \tag{A.51}$$

Solving (A.46), x becomes

$$\begin{aligned}
x &= \frac{1}{9\alpha^2(1-2\delta_1)(1+\delta_5)^2}\left[-2\tilde{\epsilon}'(2\tilde{\epsilon}' + 5 - 2\delta_2 - 2\delta_3) + 2\tilde{\epsilon}'(2\tilde{\epsilon}'+5)(\tilde{g}+1)\right] && \text{(A.52)}\\
&= \frac{2\tilde{\epsilon}'(2\tilde{\epsilon}'+5)}{9\alpha^2(1-2\delta_1)(1+\delta_5)^2}\left[\tilde{g} + \frac{2(\delta_2+\delta_3)}{2\tilde{\epsilon}'+5}\right] && \text{(A.53)}\\
&= \frac{2\tilde{\epsilon}'(2\tilde{\epsilon}'+5)}{9\alpha^2}\hat{g}, && \text{(A.54)}
\end{aligned}$$

where $\hat{g}$ is defined as

$$\hat{g} \equiv \frac{1}{(1-2\delta_1)(1+\delta_5)^2}\left[\tilde{g} + \frac{2(\delta_2+\delta_3)}{2\tilde{\epsilon}'+5}\right]. \tag{A.55}$$

Here, we summarize the results of previous paragraphs. Substituting x in (A.54) for (A.39) and (A.42), the basic equations of ADIOS become

$$s = \delta_2 + \frac{\delta_3}{2} \tag{A.56}$$

$$\Omega = \Omega_K \sqrt{\frac{2\tilde{\epsilon}'(2\tilde{\epsilon}'+5)}{9\alpha^2}\hat{g}} \tag{A.57}$$

$$v = -\frac{\hat{g}}{3\alpha}(2\tilde{\epsilon}'+5)v_K\left(1-\frac{2}{3}\delta_4\right) \tag{A.58}$$

$$c_s^2 = \frac{2\tilde{\epsilon}'(2\tilde{\epsilon}'+5)}{9\alpha^2}\hat{g}v_K^2, \tag{A.59}$$

where $\tilde{\epsilon}'$ and $\hat{g}$ are defined as

$$\tilde{\epsilon}' = \frac{\epsilon-(1+\epsilon)\delta_3+\frac{2}{3}(\delta_2+\varepsilon')}{f\left(1-\frac{3}{2}\delta_4\right)(1+\lambda')} \tag{A.60}$$

$$\hat{g} = \frac{1}{(1-2\delta_1)(1+\delta_5)^2}\left[\tilde{g}+\frac{2(\delta_2+\delta_3)}{2\tilde{\epsilon}'+5}\right] \tag{A.61}$$

$$\tilde{g} = \sqrt{\left\{1-\frac{-2(\delta_2+\delta_3)}{2\tilde{\epsilon}'+5}\right\}^2+\frac{18\alpha^2(1-2\delta_1)(1+\delta_5)^2}{(2\tilde{\epsilon}'+5)^2}}-1 \tag{A.62}$$

$$\delta_5 = \frac{1-\frac{2}{3}\delta_4}{1+\lambda'}-1. \tag{A.63}$$

By using the R-dependence of (A.26) and by equating the index of R of both members in (A.57) - (A.59), we get

$$\delta_1 = \delta_3 = \delta_4 = 0. \tag{A.64}$$

Substituting (A.64) for (A.56), we obtain

$$\delta_2 = s. \tag{A.65}$$

Substituting (A.64) and (A.65) for (A.56) - (A.59), we get the self-similar solution of ADIOS:

$$\dot{M} = \dot{M}_{\text{out}} \left(\frac{R}{R_{\text{out}}} \right)^s \tag{A.66}$$

$$\Omega = \Omega_K \sqrt{\frac{2\tilde{\epsilon}'(2\tilde{\epsilon}'+5)(1+\lambda')^2}{9\alpha^2} \left(\tilde{g} + \frac{2s}{2\tilde{\epsilon}'+5} \right)} \tag{A.67}$$

$$v = -v_K \frac{(2\tilde{\epsilon}'+5)(1+\lambda')}{3\alpha} \left(\tilde{g} + \frac{2s}{2\tilde{\epsilon}'+5} \right) \tag{A.68}$$

$$c_s^2 = v_K^2 \frac{2\tilde{\epsilon}'(2\tilde{\epsilon}'+5)(1+\lambda')^2}{9\alpha^2} \left(\tilde{g} + \frac{2s}{2\tilde{\epsilon}'+5} \right), \tag{A.69}$$

where $\tilde{\epsilon}'$ and $\tilde{g}$ are defined as,

$$\tilde{\epsilon}' = \frac{\epsilon + \frac{2}{3}(s+\varepsilon')}{f(1+\lambda')} \tag{A.70}$$

$$\tilde{g} = \sqrt{\left\{ 1 + \frac{-2s}{2\tilde{\epsilon}'+5} \right\}^2 + \frac{18\alpha^2}{(2\tilde{\epsilon}'+5)^2(1+\lambda')^2}} - 1. \tag{A.71}$$

We note that in the case of ADAF (s = $\varepsilon' = \lambda' = 0$) this self-similar solution coincides with the self-similar solution of ADAF derived in Narayan & Yi (1994).

A.3 THE EQUILIBRIUM ELECTRON TEMPERATURE IN THE INNER REGION

We calculate the equilibrium electron temperature in the inner region ($R \leq\sim 10^2$ R_s) following Mahadevan (1997). Following Narayan & Yi (1995), we define

$$c_1 \equiv -\frac{1}{\alpha}\frac{v}{v_K} = \frac{(2\tilde{\epsilon}'+5)(1+\lambda')}{3\alpha^2} \left(\tilde{g} + \frac{2s}{2\tilde{\epsilon}'+5} \right) \tag{A.72}$$

$$c_2 \equiv \frac{\Omega}{\Omega_K} = \sqrt{\frac{2\tilde{\epsilon}'(2\tilde{\epsilon}'+5)(1+\lambda')^2}{9\alpha^2} \left(\tilde{g} + \frac{2s}{2\tilde{\epsilon}'+5} \right)} \tag{A.73}$$

$$c_3 \equiv \frac{c_s^2}{v_K^2} = \frac{2\tilde{\epsilon}'(2\tilde{\epsilon}'+5)(1+\lambda')^2}{9\alpha^2} \left(\tilde{g} + \frac{2}{2\tilde{\epsilon}'+5} \right). \tag{A.74}$$

Following Mahadevan (1997), we rearrange the solution of ADIOS in terms of scaled quantities the mass is scaled in solar mass units

$$M = mM_{\odot}, \tag{A.75}$$

the radius in Schwarzschild radii

$$R = rR_s, \; Rs = \frac{2GM}{c^2} = 2.95 \times 10^5 \,\mathrm{cm} \; \times m \tag{A.76}$$

and the accretion rate in Eddington units

$$\dot{M} = \dot{m}\dot{M}_{\rm Edd}, \; \dot{M}_{\rm Edd} = \frac{L_{\rm Edd}}{\eta_{\rm eff}c^2} = 1.39 \times 10^{18} \,\mathrm{g\,s^{-1}} \; \times m \equiv Cm, \tag{A.77}$$

where $\eta_{\rm eff} = 0.1$ is the standard efficiency in converting matter to energy (Frank et al., 1992). From previous subsection, we define

$$\dot{m} = \dot{m}_{\rm out}\left(\frac{r}{r_{\rm out}}\right)^s. \tag{A.78}$$

Using scaled quantities, v_K, Ω_K, v, Ω and c_s^2 are written as

$$v_K = \sqrt{\frac{GM}{R}} = \sqrt{\frac{GM_\odot mc^2}{2GM_\odot mr}} = \frac{1}{\sqrt{2}}cr^{-1/2} \tag{A.79}$$

$$\Omega_K = \sqrt{\frac{GM}{R^3}} = \sqrt{\frac{GM_\odot mc^6}{2^3G^3M_\odot^3m^3r^3}} = \frac{1}{2\sqrt{2}}\frac{c^3}{GM_\odot}r^{-3/2} \tag{A.80}$$

$$\|v\| = \alpha c_1 v_K = \frac{1}{\sqrt{2}}c\alpha c_1 r^{-1/2} \tag{A.81}$$

$$\Omega = c_2\Omega_K = \frac{1}{2\sqrt{2}}\frac{c^3}{GM_\odot}c_2 r^{-3/2} \tag{A.82}$$

$$c_s^2 = c_3 v_K^2 = \frac{1}{2}c^2 c_3 r^{-1}. \tag{A.83}$$

Following Mahadevan (1997), we assume that the vertical scale hight of the disk H is set equal to the radius R in the equations that follow, since flow is essentially spherical in geometry (Narayan & Yi, 1995). The density ρ is given as

$$\rho = \frac{\dot{M}}{4\pi RH\|v\|} = \frac{\dot{M}}{4\pi R^2\|v\|} \tag{A.84}$$

$$= \frac{\sqrt{2}}{16\pi}\frac{Cc^3}{G^2M_\odot^2}\alpha^{-1}c_1^{-1}m^{-1}\dot{m}_{\rm out}r_{\rm out}^{-s}r^{-3/2+s} \tag{A.85}$$

$$= 6.00 \times 10^{-5} \,\mathrm{g\,cm^{-3}} \; \times \alpha^{-1}c_1^{-1}m^{-1}\dot{m}_{\rm out}r_{\rm out}^{-s}r^{-3/2+s}. \tag{A.86}$$

The gas pressure $p = \rho c_s^2$ is given as

$$p = \frac{\sqrt{2}}{32\pi} \frac{Cc^5}{G^2 M_\odot^2} \alpha^{-1} c_1^{-1} c_3 m^{-1} \dot{m}_{\rm out} r_{\rm out}^{-s} r^{-5/2+s}. \tag{A.87}$$

Since magnetic field strength B is given as $B = \sqrt{24\pi(1-\beta)p}$, B becomes

$$\begin{aligned} B &= \sqrt{\frac{3\sqrt{2}}{4} \frac{C^{1/2} c^{5/2}}{GM_\odot}} \alpha^{-1/2} (1-\beta)^{1/2} c_1^{-1/2} c_3^{1/2} m^{-1/2} \dot{m}_{\rm out}^{1/2} r_{\rm out}^{-s/2} r^{-5/4+s/2} && \text{(A.88)} \\ &= 1.43 \times 10^9\,{\rm G} \ \times \alpha^{-1/2} (1-\beta)^{1/2} c_1^{-1/2} c_3^{1/2} m^{-1/2} \dot{m}_{\rm out}^{1/2} r_{\rm out}^{-s/2} r^{-5/4+s/2}. && \text{(A.89)} \end{aligned}$$

Electron number densities n_e becomes,

$$\begin{aligned} n_e &= \frac{\rho}{\mu_e m_u} = \frac{\rho(1+X)}{2m_u} && \text{(A.90)} \\ &= \frac{\sqrt{2}(1+X)}{32\pi m_u} \frac{Cc^3}{G^2 M_\odot^2} \alpha^{-1} c_1^{-1} m^{-1} \dot{m}_{\rm out} r_{\rm out}^{-s} r^{-3/2+s} && \text{(A.91)} \\ &= 3.16 \times 10^{19}\,{\rm cm}^{-3} \ \times \alpha^{-1} c_1^{-1} m^{-1} \dot{m}_{\rm out} r_{\rm out} r^{-3/2+s}, && \text{(A.92)} \end{aligned}$$

where μ_e is effective molecular weight, X is the hydrogen mass fraction and m_u is the atomic mass unit. Equations (A.86), (A.89) and (A.92) are almost same as equations (5) in Mahadevan (1997), but slightly differ because of the mass loss effect, and they are consistent with the equations of the self-similar ADAF model of Mahadevan (1997) in the limit of $s = 0$.

The equilibrium electron temperature T_e in inner region ($R \lesssim 10^2\ R_s$) is obtained samely as Mahadevan (1997). Equations corresponding to equation (9) and equation (24) in Mahadevan (1997) are

$$\begin{aligned} Q^+ &= 9.39 \times 10^{38} (1-s)^{-1} (1-\beta) f^{-1} c_3 m \dot{m}_{\rm out} r_{\rm out}^{-s} r_{\rm min}^{-(1-s)}\ {\rm erg\,s^{-1}} && \text{(A.93)} \\ \nu_p L_p &= s_1^3 s_2^3 s_3 r_{\rm min}^{-7/4+3s/2} m^{1/2} \dot{m}_{\rm out}^{3/2} r_{\rm out}^{-3s/2} T_e^7\ {\rm ergs\,s^{-1}\,Hz^{-1}}. && \text{(A.94)} \end{aligned}$$

Then, an analytic expression of the equilibrium electron temperature corresponding to equation (40) in Mahadevan (1997) is given by

$$\begin{aligned} T_e &= \frac{4.4 \times 10^{10}\,{\rm K}}{A_c^{1/7}} \delta^{1/7} \chi_M^{-3/7} \alpha^{3/14} (1-\beta)^{-1/14} c_1^{3/14} c_3^{-1/14} \\ &\quad \times (1-s)^{-1/7} r_{\rm min}^{3/28-s/14} m^{1/14} \dot{m}_{\rm out}^{-1/14} r_{\rm out}^{s/14}. && \text{(A.95)} \end{aligned}$$

Here δ is the fraction of viscous energy transferred to electrons. The difference from equation (40) in Mahadevan (1997) is that the equilibrium electron temperature have a dependence on the mass loss index s and varies with s by the factor of $(1-s)^{-1/7} r_{\mathrm{min}}^{-s/14} r_{\mathrm{out}}^{s/14}$.

B

THE BAYSIAN INFERENCE WITH THE EXCHANGE MONTE CARLO

We successfully obtained both the visibility amplitudes and the closure phases on NRAO 530 (see §4.5). We modeled the source structure from them using geometrical models consisting of circular Gaussians following previous EHT observations (Lu et al., 2012, 2013). In this work, we employed the Bayesian framework using the Exchange Monte Carlo (EMC), which is a subclass of Markov Chain Monte Carlo (MCMC), to model observed visibilities. We briefly introduce the advantages of this method in §B.1, the parameter estimation in the Bayesian framework in §B.2, the Metropolis method implemented in our EMC modeling in §B.3, an overview of our EMC modeling in §B.4 and other settings for modeling visibilities in §B.5.

B.1 THE STRENGTHS OF THE EXCHANGE MONTE CARLO

Here, we briefly summarize the strengths of EMC compared to the traditional least-square methods and other MCMC techniques.

Advantages of MCMC techniques compared to the least square methods

The traditional least-square methods have been adopted to model images from observed visibilities in the past EHT observations (Lu et al., 2012, 2013). However, it has several technical difficulties as follows.

1. In general, the geometrical models are described as a non-linear function of parameters, requiring an initial guesses of the parameter values to perform the traditional least-square fitting. However, we cannot estimate initial conditions for EHT data from Fourier transformed images owing to the lack of

visibility phases. In addition, it is often very difficult to guess the image for the EHT-detected structure from other wavelength data-sets, because no other instruments have provided images at comparable spatial resolutions.

2. Traditionally, the grid search has been used to derive the confidence intervals of parameters. However, the computational cost of the grid search becomes too expensive for models with a large number of parameters, because the total grid size is proportional to $\propto N_g^{N_p}$ where N_p and N_g are the number of parameters and search grids for each parameter, respectively.

MCMC techniques have a potential to overcome these difficulties. First, MCMC does not require good initial guesses of the parameter values. It can efficiently explore all regions of prior parameter space with a significant probability. This would be a big advantage so far, because we cannot estimate initial conditions for EHT data from Fourier transformed images owing to the lack of visibility phases. In addition, MCMC gives the full marginal posterior distributions for each model parameter, not just the maximum a posteriori (MAP) values and a Gaussian approximation of their uncertainties.

Advantages of the EMC method compared to other MCMC techniques

Although MCMC techniques have great advantages in deriving the confidence interval of each parameter efficiently, sometimes it has a difficulty to explore a target probability distribution, if the distribution has several local maximums with separations much larger than the step size (Figure B.1). In such cases, a chain can easily get trapped around a local maximum and miss other regions of parameter space with a significant probability.

Such a situation often occurs when models have a large number of parameters. We actually encountered this problem when we model visibility data sets with relatively complicated models such as models with three or four circular Gaussian components. This problem is similar to that of non-linear least square methods where can be easily trapped at a local minimum of the chi-square surface if the initial condition is not good.

EMC has a great advantage to handle this problem. It introduces the temperature of the probability distribution (see, B.4 for details), and execute MCMC simulations with several chains at different temperatures. The target distribution is at the lowest temperature, while the probability distribution at higher temperatures has flatter shapes as the probability distributions of the particles become flatter at

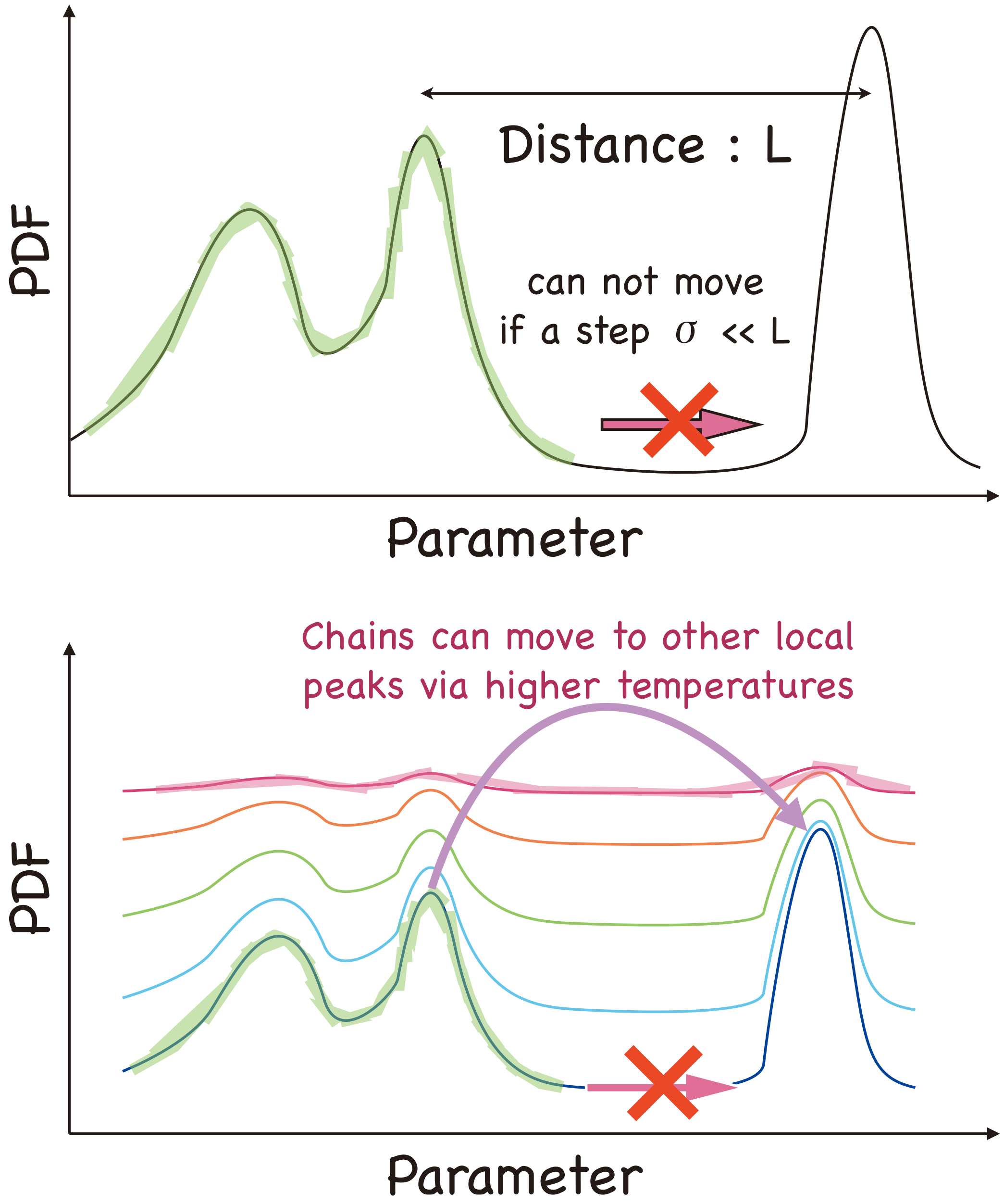

Figure B.1: A schematic view explaining the advantages of the Exchange Monte Carlo (EMC) compared to the other MCMC techniques. (Top panel) the weakness of the standard Metropolis method. If the target probability distribution has local peaks with intervals much longer than the step size of the Markov chain, the chain can not move to other peaks. (Bottom panel) the strength of the EMC. EMC can overcome such a difficulty by introducing the temperature of the probability distribution. The chain can move to other local peaks via higher temperatures where the probability distribution is much flatter and the chain can move around much broader region than lower temperatures.

higher temperatures in the statistical physics (Figure B.1). In the EMC simulation, the chain can move to other local peaks by going through the region at higher temperatures where the chain can move around much broader region than lower temperatures. This enable the Marco chain to explore the whole region of the parameter space efficiently.

B.2 PARAMETER ESTIMATION IN THE BAYESIAN FRAMEWORK

In the Bayesian Framework, parameters $X = (x_1, x_2, ..., x_{N_p})$ of model M are estimated by calculating the posterior distribution $p(X|M, D, I)$, which is the conditional probability distribution of parameters X under model M, observational data D and prior information I. The posterior distribution can be calculated using the Bayes theorem given by

$$p(X|M, D, I) = \frac{p(D|X, M, I)p(X|M, I)}{p(D|M, I)}, \tag{B.1}$$

where $p(D|M, I)$ is the marginal likelihood (or the global likelihood) defined by

$$p(D|M, I) = \int dX\, p(D|X, M, I)p(X|M, I). \tag{B.2}$$

The term $p(D|X, M, I)$ is the likelihood representing the conditional probability that observational data D are obtained from observations under model M, its parameters X and prior information I. The term $p(X|M, I)$ is the “prior distribution” reflected the background information on model M and its parameters X. The posterior distribution of a parameter x_i, $p(x_i|M, D, I)$ is obtained by

$$p(x_i|M, D, I) = \int p(X|M, D, I)\, dx_0 ... dx_{i-1} dx_{i+1} ... dx_{N_p}. \tag{B.3}$$

B.3 THE METROPOLIS METHOD

The MCMC technique using the Metropolis method offers an efficient method of sampling pseudorandom numbers from the posterior distribution in Eq. (B.1). This method has the following advantages: 1. one can obtain a sequence of random samples from a probability distribution for which direct sampling is difficult; 2.

one does not need to calculate the integration in Eq. (B.2,B.3). One can obtain the posterior distribution of each parameter in Eq. (B.2) from the histogram of sampled pseudorandom numbers.

Here, we briefly summarize a method to generate a chain of sets of model parameters X based on the Metropolis method. An initial set of parameter values X_0 is randomly generated from a prior distribution $P(X|M, I)$. At each iteration, a new set of model parameters $X_t = (x_{t,1}, x_{t,2}, \dots, x_{t,N_p})$ is generated as follows. The new proposal set of model parameters P_{t+1} is generated from the proposal distribution $q(X_t|X_{t+1})$. The new proposal set is then randomly accepted or rejected with a probability α written as

$$\alpha = \min\left(\frac{p(D|P_{t+1}, M, I)p(P_{t+1}|M, I)q(X_t|P_{t+1})}{p(D|X_t, M, I)p(X_t|M, I)q(P_{t+1}|X_t)}, 1\right). \tag{B.4}$$

We adopted a Gaussian proposal distribution for $q(X_t|X_{t+1})$, written as

$$q(X_t|X_{t+1}) = \prod_{j}^{N_p} \frac{1}{\sqrt{2\pi\sigma_j^2}} \exp\left(\frac{(x_{t+1,j} - x_{t,j})^2}{2\sigma_j^2}\right). \tag{B.5}$$

Then, the probability α becomes

$$\alpha = \min\left(\frac{p(D|P_{t+1}, M, I)p(P_{t+1}|M, I)}{p(D|X_t, M, I)p(X_t|M, I)}, 1\right). \tag{B.6}$$

We assumed a Gaussian uncertainty in observational data and uniform prior distribution for each parameter. Then, the probability α is written in

$$\begin{aligned} \alpha &= \min\left(\frac{p(D|P_{t+1}, M, I)}{p(D|X_t, M, I)}, 1\right) && \text{(B.7)} \\ &= \min\left(\exp\left(-\frac{1}{2}\left[\chi^2(D|P_{t+1}, M, I) - \chi^2(D|P_t, M, I)\right]\right), 1\right), && \text{(B.8)} \end{aligned}$$

where $\chi^2(D|X_t, M, I)$ is χ^2 of the parameter set X_t.

A proposal set of parameters P_{t+1} is always accepted as X_{t+1}, if the probability of parameters leads to an improvement in the χ^2-fit and a higher prior probability compared to the previous parameters X_t. On the other hand, a proposal state leading to a worse fit or a lower prior probability is accepted according to the probability based on the ratio of the posterior probabilities. If the proposal set is rejected, the previous state will be repeated in the chain.

When the model has several parameters, α tends to become small if several parameters are stepped simultaneously. That would cause a low accept-rate and a low efficiency of this method. In our calculations, following Muller (1991), we stepped only one parameter at a time with other parameters fixed as follows.

1. Choose $x_{t,j}$ from X_t randomly with the uniform probability.
2. Generate a candidate of $x_{t+1,j}$ from proposal distribution.
3. Calculate α and accept or reject it with the probability α.
4. Repeat 1-3 for N_p times and after that, memorize the newly generated state as X_{t+1}.

In early iterations, generated sets of parameters in the chain are affected by the initial set, and then the chain converges into the area with a significant probability independently on the initial set. Such early iterations are called as "burn-in", and generally discarded. In our calculations, we checked the auto-correlation function of each parameter and each parameter chain to check the convergence of each chain. After all chains seem to converge, we discarded the early chains as "burn-in", and move to the “main” simulation with iterations 10 times greater than “burn-in”. We tried several MCMC simulations with different initial conditions which are randomly generated from the prior distribution, and confirmed that all chains converge into consistent probability distributions.

The efficiency of this method is also sensitive to the step-size of proposal distributions. In the case of the Gaussian proposal distribution, the step-size is characterized by its variance. If it is too small, most of the trial points are accepted, and the MCMC is slow to sample the full parameter space. If it is too large, most of the trial points are rejected and though the MCMC may make large jumps in parameter space, it could get stuck at a certain point for long. We adjusted the step-size of each parameter by the following methods to achieve an accept rate of $\sim 50\%$, which is an efficient accept rate in previous empirical studies on the Metropolis method (Roberts et al., 1997). In the burn-in period, after updating the j-th parameter $x^i_{t,j}$, if the accept rate of the newest 100 trials is more than 55 %, then the variance σ_j is multiplied by 1.1. Else if the accept rate of the newest 100 trials is less than 45 %, the variance σ_j is divided by 1.1. Finally, we confirmed that the accept rate converged into ~ 50 %.

B.4 THE EXCHANGE MONTE CARLO (EMC) METHOD

In our cases, a simple Metropolis method failed to fully explore a target probability distribution, since the distribution has several local maximums with the separations being much larger than the step size. In such case, a chain gets trapped around a local maximum and miss other regions of parameter space with a significant probability. The Exchange Monte Carlo (EMC; also known as Parallel Tempering and Replica Exchange MCMC) is one of the improved class of MCMC techniques, called an extended ensemble method, designed to handle this problem. EMC was developed at first in the physics community to improve sampling in glassy systems (Hukushima & Nemoto, 1996) and recently has been applied to some astronomical problems (e.g. Gregory, 2005, 2007; Varghese et al., 2011; Benneke & Seager, 2012). This method involves generating the sample sequence from a distribution that consists of many distributions with different temperatures. This method is based on two MCMC simulation steps. One step is the conventional update of the MCMC simulation for each distribution. The other is a probabilistic exchange process between two neighboring sequences. We employ the Metropolis method for the former step, and the exchange probability of the Metropolis-type for the latter step.

In this method, the posterior distribution is extended using the temperature β_k as follows:

$$\begin{aligned} \pi(X_k|M,D,I,\beta_k) &= \frac{p(D|X_k,M,I)^{\beta_k} p(X_k|M,I)}{Z(\beta_k)} && \text{(B.9)} \\ &\propto \exp\left(\beta L(D|X_k,M,I)\right) p(X_k|M,I) && \text{(B.10)} \end{aligned}$$

where $L(D|X_k,M,I)$ is a log-likelihood and $Z(\beta_k)$ is the normalization factor given by

$$Z(\beta_k) = \int dX_k\, p(D|X_k,M,I)^{\beta_k} p(X_k|M,I). \tag{B.11}$$

One can understand the origin of the name of “temperature” considering $-L(D|X_k,M,I)$ as an energy E_k of a certain state in the thermodynamical system. In that case, $\pi(X_k|M,D,I,\beta_k)$ is proportional to $\exp(\beta_k E_k)$ and then represents a canonical distribution. The normalization factor $Z(\beta_k)$ can be related with the partition func-

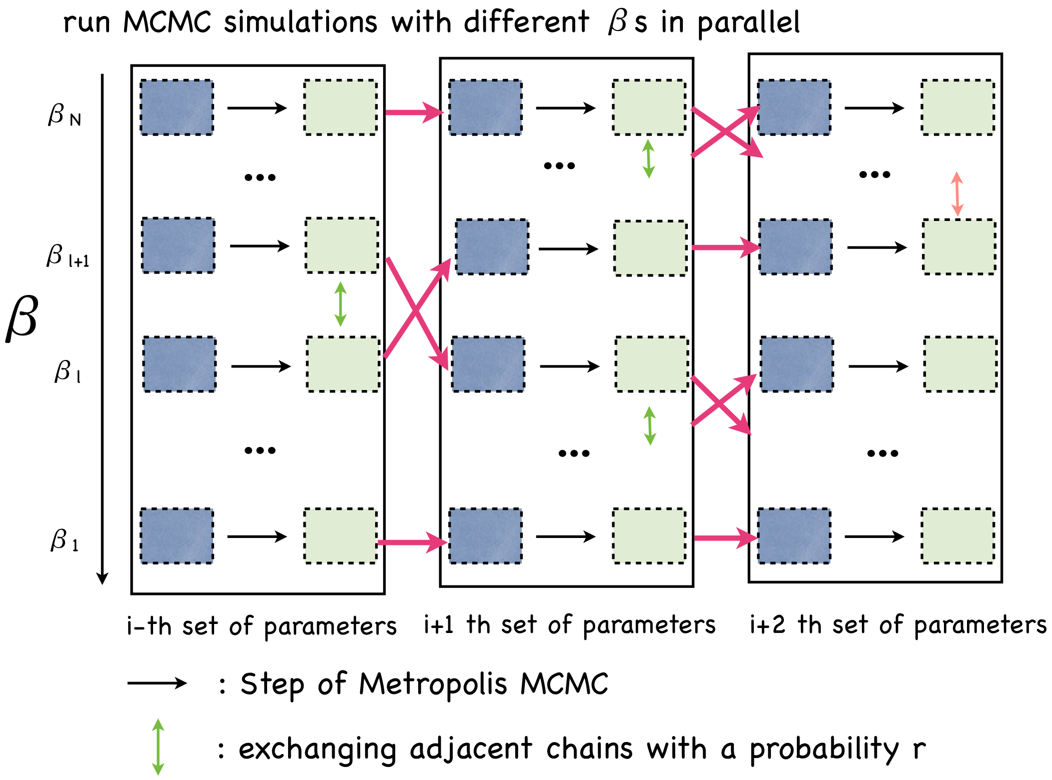

Figure B.2: A schematic view of the Exchange Monte Carlo (EMC) method

tion. A high temperature (low β) makes a likelihood function flatter and also makes the probability of acceptance in the Metropolis method (Eq.B.8) higher as

$$\alpha = \min\left(\exp\left(-\frac{1}{2}\beta\left[\chi^2(D|P_{t+1},M,I)-\chi^2(D|P_t,M,I)\right]\right),1\right) \quad \text{(B.12)}$$

Thus, the Metropolis algorithm at high temperature enables exploration of a wide range of parameter space.

Figure B.2 shows a schematic view of the EMC method. In the EMC method, multiple chains with different initial conditions and different temperatures $(\beta_1, \beta_2, \ldots, \beta_{N_\beta})$ are generated in parallel. After generating t-th parameter sets $X^i_{k,t}$ at all temperatures, adjacent chains β_k and β_{k+1} are selected randomly with an uniform probability, and then exchanged with a probability $\alpha = \min(1, r)$. The probability r is a Metropolis ratio defined by

$$\begin{aligned} r &= \frac{\pi(X_{k+1,t}|M,D,I,\beta_k)\,\pi(X_{k,t}|M,D,I,\beta_{k+1})}{\pi(X_{k,t}|M,D,I,\beta_k)\,\pi(X_{k+1,t}|M,D,I,\beta_{k+1})} \qquad (B.13)\\ &= \left[\frac{p(D|X_{k+1,t},M,I)}{p(D|X_k,M,I)}\right]^{-(\beta_{k+1}-\beta_k)} \qquad (B.14)\\ &= \exp\left(\frac{1}{2}(\beta_{k+1}-\beta_k)\left[\chi^2(D|X_{k+1,t},M,I)-\chi^2(D|X_{k,t},M,I)\right]\right) \qquad (B.15)\end{aligned}$$

In our calculation, we set temperatures as follows, since a previous study on EMC method indicates that a geometric series of βs would give a constant averaged exchange rate (Nagata & Watanabe, 2008).

$$\beta_k = \begin{cases} \beta_{\mathrm{min}}^{(N_\beta-k)/(N_\beta-2)} & (k = 2,3,\ldots,N_\beta) \\ 0 & (k=1) \end{cases} \qquad (B.16)$$

β_{min} is set to be $\sim 1/\left\langle \chi^2(D|X^i_{N_\beta},M^i,I)\right\rangle$. After every generation of t-th parameters sets, $100N_\beta$ trials of the exchange are performed to mix chains.

B.5 SETTINGS FOR MODELING VISIBILITIES

Following Lu et al. (2012, 2013), we defined chi-squares of these models as follows;

$$\chi^2 = \sum_i \left(\frac{V^{\mathrm{model}}_{\mathrm{amp},i} - V^{\mathrm{data}}_{\mathrm{amp},i}}{\sigma_i^{\mathrm{amp}}}\right)^2 + \sum_j \left(\frac{\phi_j^{\mathrm{model}} - \phi_j^{\mathrm{data}}}{\sigma_j^{\mathrm{cphase}}}\right)^2 \qquad (B.17)$$

where $V_{\mathrm{amp},i}$ and ϕ_j are visibility amplitudes and closure phases with errors σ_i^{amp} and $\sigma_j^{\mathrm{cphase}}$, respectively. We adopted uniform distribution for the prior distribution of each parameter. We set the number of temperatures as $N_\beta = 16$. We performed 10^5 iterations for the burn-in simulation, and 10^6 iterations for the main simulation.

C

APPARENT EXPANSION VELOCITY OF THE PLASMA BLOB IN THE RELATIVISTIC JET

We consider a spherical blob in a jet expanding isotropically with an expansion speed of β'_{exp} on the co-moving frame (with ’). The jet propagates along the x-axis with a velocity of $\tilde{\mathbf{fi}} = (\beta, 0, 0)$ from the line of sight of $\vec{n} = (\cos\Theta, -\sin\Theta, 0)$ on the observer’s frame (without ’), respectively. The center of the blob seems to move with an apparent speed β_{app} in the image, given by

$$\beta_{\mathrm{app}} = \frac{\beta\sin\Theta}{1-\beta\cos\Theta}. \tag{C.1}$$

Let the expansion velocity on the co-moving frame be

$$\vec{\beta'}_{\mathrm{exp}} = \beta'_{\mathrm{exp}}\left(\cos\phi'\sin\theta',\, \sin\phi' sin\theta',\, \cos\theta'\right) \quad , \tag{C.2}$$

where ϕ' and θ' are the azimuthal and elevation angles, respectively. The expansion velocity on the rest frame is given by

$$\begin{aligned}\vec{\beta}_{\rm exp} &= \vec{\beta} \oplus \vec{\beta}'_{\rm exp} \quad &\text{(C.3)}\\ &= \frac{1}{1+\beta\beta'_{\rm exp}\cos\phi'\sin\theta'} \\ &\quad\times\left(\beta+\beta'_{\rm exp}\cos\phi'\sin\theta',\ \sqrt{1-\beta^2}\beta'_{\rm exp}\sin\phi'\sin\theta',\ \sqrt{1-\beta^2}\beta'_{\rm exp}\cos\theta'\right). &\text{(C.4)}\end{aligned}$$

using the velocity-addition formula of the special relativity. In the observed image, the expansion speed $\beta_{\rm exp} = \left|\vec{\beta}_{\rm exp}\right|$ is also affected by the time-dilation effect as well as the jet velocity β. The apparent expansion speed $\beta_{\rm exp,app}$ is given by

$$\beta_{\rm exp,app} = \frac{\beta_{\rm exp}\sin\Theta_{\rm exp}}{1-\beta_{\rm exp}\cos\Theta_{\rm exp}}, \qquad \text{(C.5)}$$

where $\Theta_{\rm exp}$ is an angle between the expansion velocity $\vec{\beta}_{\rm exp}$ and the line of sight $\vec{n}$ obtained from

$$\Theta_{\rm exp} = \arccos\frac{\vec{\beta}_{\rm exp}\cdot\vec{n}}{\beta_{\rm exp}}. \qquad \text{(C.6)}$$

On the other hand, the time dilation effect does not change the direction of the expansion velocity in the observed image. Thus, the direction of the apparent expansion velocity is parallel to a projected vector of $\vec{\beta}_{\rm exp}$ to a plane parallel to the observed image (i.e. a plane perpendicular to the line of sight $\vec{n}$). It is given by

$$\vec{\beta}_{\rm exp,proj} = \vec{\beta}_{\rm exp} - \beta_{\rm exp}\cos\Theta_{\rm exp}\,\vec{n}. \qquad \text{(C.7)}$$

The plane of the observed image can be characterized by two orthogonal vectors $\vec{n}_{||} = (\sin\Theta,\ \cos\Theta,\ 0)$ and $\vec{n}_{\perp} = (0,\ 0,\ 1)$, where $||$ and $\perp$ mean parallel and perpendicular to the apparent (i.e. projected) jet axis in the observed image. On the observed image, the direction of the apparent expansion velocity is parallel to a vector $\vec{d} = (d_{||}, d_{\perp})$ given by

$$\begin{aligned} d_{||} &= \vec{\beta}_{\rm exp,proj}\cdot\vec{n}_{||} \qquad &\text{(C.8)}\\ d_{\perp} &= \vec{\beta}_{\rm exp,proj}\cdot\vec{n}_{\perp}. &\text{(C.9)}\end{aligned}$$

The apparent expansion velocity in the observed image is a vector along $\vec{d}$ with a speed of $\beta_{\rm exp}$ obtained by

$$\beta_{\|} = \beta_{\rm exp,app}\frac{d_{\|}}{\left|\vec{d}\right|} - \beta_{\rm app} \tag{C.10}$$

$$\beta_{\perp} = \beta_{\rm exp,app}\frac{d_{\perp}}{\left|\vec{d}\right|}. \tag{C.11}$$

Thus, a fluid element at the boundary of the spherical blob in the direction of (ϕ', θ') on the co-moving frame has a position in the observed image of

$$\vec{r}(\vec{r}_0, t, z; \phi', \theta', \beta, \Theta, \beta'_{\rm exp}) = \frac{1}{1+z}\left(\beta_{||}(\phi', \theta', \beta, \Theta, \beta'_{\rm exp}),\ \beta_{\perp}(\phi', \theta', \beta, \Theta, \beta'_{\rm exp})\right) t + \vec{r}_0. \tag{C.12}$$

where $\vec{r}_0$, t, z are an initial position of the fluid element on observer's frame, the elapsed time on observer's frame and the redshift of the source, respectively.

BIBLIOGRAPHY

Abdo, A. A., Ackermann, M., Ajello, M., et al. 2009, ApJ, 707, 55

Abdo, A. A., Ackermann, M., Ajello, M., et al. 2010, ApJS, 188, 405

Abdo, A. A., Ackermann, M., Ajello, M., et al. 2010, Nature, 463, 919

Abdo, A. A., Ackermann, M., Agudo, I., et al. 2010, ApJ, 716, 30

Abramowicz, M. A., Czerny, B., Lasota, J. P., & Szuszkiewicz, E. 1988, ApJ, 332, 646

Abramowicz, M. A., Chen, X., Kato, S., Lasota, J.-P., & Regev, O. 1995, ApJ, 438, L37

Abramowski, A., Gillessen, S., Horns, D., & Zechlin, H.-S. 2010, MNRAS, 402, 1342

Abramowski, A., Acero, F., Aharonian, F., et al. 2012, ApJ, 746, 151

Acciari, V. A., Beilicke, M., Blaylock, G., et al. 2008, ApJ, 679, 397

Acciari, V. A., Aliu, E., Arlen, T., et al. 2009, Science, 325, 444

Ackermann, M., Ajello, M., Allafort, A., et al. 2011, ApJ, 741, 30

Ackermann, M., Ajello, M., Allafort, A., et al. 2011, ApJ, 743, 171

Actis, M., Agnetta, G., Aharonian, F., et al. 2011, Experimental Astronomy, 32, 193

Agudo, I., Bach, U., Krichbaum, T. P., et al. 2007, A&A, 476, L17

Agudo, I., Jorstad, S. G., Marscher, A. P., et al. 2011, ApJ, 726, LL13

Agudo, I., Marscher, A. P., Jorstad, S. G., et al. 2011, ApJ, 735, LL10

Agudo, I., Marscher, A. P., Jorstad, S. G., et al. 2012, ApJ, 747, 63

Aharonian, F., Akhperjanian, A., Beilicke, M., et al. 2003, A&A, 403, L1

Aharonian, F., Akhperjanian, A. G., Bazer-Bachi, A. R., et al. 2006, Nature, 439, 695

Aharonian, F., Akhperjanian, A. G., Bazer-Bachi, A. R., et al. 2006, ApJ, 636, 777

Aharonian, F., Akhperjanian, A. G., Bazer-Bachi, A. R., et al. 2006, Science, 314, 1424

Aharonian, F., Akhperjanian, A. G., Barres de Almeida, U., et al. 2008, A&A, 492, L25

Aharonian, F., Akhperjanian, A. G., Anton, G., et al. 2009, A&A, 503, 817

Akiyama, K., Takahashi, R., Honma, M., Oyama, T., & Kobayashi, H. 2013, PASJ, 65, 91

Akiyama, K., Kino, M., Sohn, B., et al. 2014, IAU Symposium, 303, 288

Akiyama, K., Lu, R.-S, Fish, V. L., et al. 2014, submitted to ApJ

Aleksić, J., Ansoldi, S., Antonelli, L. A., et al. 2014, A&A, 567, AA41

Angel, J. R. P., & Stockman, H. S. 1980, ARA&A, 18, 321

Antonucci, R. R. J. 1984, ApJ, 278, 499

Antonucci, R. R. J., & Miller, J. S. 1985, ApJ, 297, 621

Antonucci, R. 1993, ARA&A, 31, 473

Albert, J., Aliu, E., Anderhub, H., et al. 2008, ApJ, 685, L23

Armstrong, J. W., Rickett, B. J., & Spangler, S. R. 1995, ApJ, 443, 209

Armus, L., Bernard-Salas, J., Spoon, H. W. W., et al. 2006, ApJ, 640, 204

Asada, K., & Nakamura, M. 2012, ApJ, 745, L28

Asada, K., Nakamura, M., Doi, A., Nagai, H., & Inoue, M. 2014, ApJ, 781, L2

Baade, W., & Minkowski, R. 1954, ApJ, 119, 215

Baade, W. 1956, ApJ, 123, 550

Baum, S. A., O’Dea, C. P., Giovannini, G., et al. 1997, ApJ, 483, 178

Baganoff, F. K., Bautz, M. W., Brandt, W. N., et al. 2001, Nature, 413, 45

Baganoff, F. K., Maeda, Y., Morris, M., et al. 2003, ApJ, 591, 891

Balick, B., & Brown, R. L. 1974, ApJ, 194, 265

Bare, C., Clark, B. G., Kellermann, K. I., Cohen, M. H., & Jauncey, D. L. 1967, Science, 157, 189

Bartel, N., Herring, T. A., Ratner, M. I., Shapiro, I. I., & Corey, B. E. 1986, Nature, 319, 733

Barkov, M. V., Aharonian, F. A., & Bosch-Ramon, V. 2010, ApJ, 724, 1517

Barkov, M. V., Bosch-Ramon, V., & Aharonian, F. A. 2012, ApJ, 755, 170

Beilicke, M., & VERITAS Collaboration 2012, American Institute of Physics Conference Series, 1505, 586

Bender, R., Kormendy, J., Bower, G., et al. 2005, ApJ, 631, 280

Benneke, B., & Seager, S. 2012, ApJ, 753, 100

Broten, N. W., Legg, T. H., Locke, J. L., et al. 1967, Science, 156, 1592

Broten, N. W., Clarke, R. W., Legg, T. H., et al. 1967, Nature, 216, 44

Bicknell, G. V., & Begelman, M. C. 1996, ApJ, 467, 597

Biretta, J. A., Owen, F. N., & Hardee, P. E. 1983, ApJ, 274, L27

Biretta, J. A., Stern, C. P., & Harris, D. E. 1991, AJ, 101, 1632

Biretta, J. A., & Meisenheimer, K. 1993, Jets in Extragalactic Radio Sources, 421, 159

Biretta, J. A., Sparks, W. B., Macchetto, F., & Capetti, A. 1995, BAAS, 27, 1360

Biretta, J. A., Sparks, W. B., & Macchetto, F. 1999, ApJ, 520, 621

Biretta, J. A., Junor, W., & Livio, M. 2002, New Astronomy Reviews, 46, 239

Begelman, M. C., McKee, C. F., & Shields, G. A. 1983, ApJ, 271, 70

Begelman, M. C., Blandford, R. D., & Rees, M. J. 1984, Reviews of Modern Physics, 56, 255

Blakeslee, J. P.,Jordán, A., Mei, S., et al. 2009, ApJ, 694, 556

Blandford, R. D., & Rees, M. J. 1974, MNRAS, 169, 395

Blandford, R. D. 1976, MNRAS, 176, 465

Blandford, R. D., & Znajek, R. L. 1977, MNRAS, 179, 433

Blandford, R. D., Königl, A. 1979, ApJ, 232, 34

Blandford, R. D., & Payne, D. G. 1982, MNRAS, 199, 883

Blandford, R. D., & Begelman, M. C. 1999, MNRAS, 303, L1

Boksenberg, A., Macchetto, F., Albrecht, R., et al. 1992, A&A, 261, 393

Bolton, J. G., Stanley, G. J., & Slee, O. B. 1949, Nature, 164, 101

Bower, G. C., Backer, D. C., Wright, M., et al. 1997, ApJ, 484, 118

Bower, G. C., & Backer, D. C. 1998, ApJ, 496, L97

Bower, G. C., & Backer, D. C. 1998, ApJ, 507, L117

Bower, G. C., Wright, M. C. H., Falcke, H., & Backer, D. C. 2003, ApJ, 588, 331

Bower, G. C., Falcke, H., Herrnstein, R. M., Zhao, J.-H., Goss, W. M., & Backer, D. C. 2004, Science, 304, 704

Bower, G. C., Goss, W. M., Falcke, H., Backer, D. C., & Lithwick, Y. 2006, ApJ, 648, L127

Bradt, H., Mayer, W., Naranan, S., Rappaport, S., & Spada, G. 1967, ApJ, 150, L199

Brodatzki, K. A., Pardy, D. J. S., Becker, J. K., & Schlickeiser, R. 2011, ApJ, 736, 98

Broderick, A. E., & Loeb, A. 2006, MNRAS, 367, 905

Broderick, A. E., Fish, V. L., Doeleman, S. S., & Loeb, A. 2009, ApJ, 697, 45

Broderick, A. E., & Loeb, A. 2009, ApJ, 697, 1164

Broderick, A. E.,Fish, V. L., Doeleman, S. S., & Loeb, A. 2010, arXiv:1011.2770

Broderick, A. E., Fish, V. L., Doeleman, S. S., & Loeb, A. 2011, ApJ, 735, 110

Broderick, A. E., & Tchekhovskoy, A. 2014, submitted to ApJ

Bromberg, O., & Levinson, A. 2009, ApJ, 699, 1274

Chernyakova, M., Malyshev, D., Aharonian, F. A., Crocker, R. M., & Jones, D. I. 2011, ApJ, 726, 60

Cheung, C. C., Harris, D. E., & Stawarz, Ł. 2007, ApJ, 663, L65

Chikada, Y., Kawaguchi, N., Inoue, M., Morimoto, M., Kobayashi, H., & Mattori, S. 1991, Frontiers of VLBI, 79

Chiueh, T., Li, Z.-Y., & Begelman, M. C. 1991, Relativistic Hadrons in Cosmic Compact Objects, 391, 135

Cui, Y.-D., Yuan, Y.-F., Li, Y.-R., & Wang, J.-M. 2012, ApJ, 746, 177

Curtis, H. D. 1918, Publications of Lick Observatory, 13, 9

D'Ammando, F., & Vandenbroucke, J. 2010, The Astronomer'sTelegram, #3002, 3002, 1

Dexter, J., Agol, E., & Fragile, P. C. 2009, ApJ, 703, L142

Dexter, J., Agol, E., Fragile, P. C., & McKinney, J. C. 2010, ApJ, 717, 1092

Dexter, J., & Fragile, P. C. 2011, ApJ, 730, 36

Dexter, J., McKinney, J. C., & Agol, E. 2012, MNRAS, 421, 1517

Di Matteo, T., Allen, S. W., Fabian, A. C., Wilson, A. S., & Young, A. J. 2003, ApJ, 582, 133

Dodds-Eden, K., Porquet, D., Trap, G., et al. 2009, ApJ, 698, 676

Dodds-Eden, K., Sharma, P., Quataert, E., et al. 2010, ApJ, 725, 450

Dodds-Eden, K., Gillessen, S., Fritz, T. K., et al. 2011, ApJ, 728, 37

Dodson, R., Edwards, P. G., & Hirabayashi, H. 2006, PASJ, 58, 243

Doeleman, S. S. 1995, Ph.D. Thesis,

Doeleman, S. S., Shen, Z.-Q., Rogers, A. E. E., et al. 2001, AJ, 121, 2610

Doeleman, S. S., Weintroub, J., Rogers, A. E. E., et al. 2008, Nature, 455, 78

Doeleman, S. S., Fish, V. L., Broderick, A. E., Loeb, A., & Rogers, A. E. E. 2009, ApJ, 695, 59

Doeleman, S. S., Fish, V. L., Schenck, D. E., et al. 2012, Science, 338, 355

Doi, A., Hada, K., Nagai, H., et al. 2013, European Physical Journal Web of Conferences, 61, 8008

Donato, D., Ghisellini, G., Tagliaferri, G., & Fossati, G. 2001, A&A, 375, 739

Eckart, A., Genzel, R., Krabbe, A., et al. 1992, Nature, 355, 526

Eckart, A., & Genzel, R. 1996, Nature, 383, 415

Eckart, A., & Genzel, R. 1997, MNRAS, 284, 576

Eckart, A., Genzel, R., Ott, T., & Schödel, R. 2002, MNRAS, 331, 917

Eckart, A., et al. 2004, A&A, 427, 1

Eckart, A., et al. 2006, A&A, 455, 1

Eckart, A., et al. 2008, A&A, 479, 625

Eisenhauer, F., Schödel, R., Genzel, R., et al. 2003, ApJ, 597, L121

Eisenhauer, F., Genzel, R., Alexander, T., et al. 2005, ApJ, 628, 246

Falcke, H. 1996, ApJ, 464, L67

Falcke, H., Goss, W. M., Matsuo, H., et al. 1998, ApJ, 499, 731

Falcke, H., Kern, S., & Cotera, A. 1999, The Central Parsecs of the Galaxy, 186, 536

Falcke, H., & Markoff, S. 2000, A&A, 362, 113

Falcke, H., Melia, F., & Agol, E. 2000, ApJ, 528, L13

Falcke, H., Körding, E., & Markoff, S. 2004, A&A, 414, 895

Falcke, H., Markoff, S., & Bower, G. C. 2009, A&A, 496, 77

Fanaroff, B. L., & Riley, J. M. 1974, MNRAS, 167, 31P

Fender, R., Koerding, E., Belloni, T., et al. 2007, arXiv:0706.3838

Feng, S.-W., Shen, Z.-Q., Cai, H.-B., et al. 2006, A&A, 456, 97

Ferrarese, L., & Ford, H. 2005, Space Sci. Rev., 116, 523

Fish, V. L., Broderick, A. E., Doeleman, S. S., & Loeb, A. 2009, ApJ, 692, L14

Fish, V. L., Doeleman, S. S., Beaudoin, C., et al. 2011, ApJ, 727, L36

Fish, V. L., Alef, W., Anderson, J., et al. 2013, arXiv:1309.3519

Fish, V. L., Johnson, M. D., Lu, R.-S., et al. 2014, ApJ, 795, 134

Ford, H. C., Harms, R. J., Tsvetanov, Z. I., et al. 1994, ApJ, 435, L27

Foschini, L., Pian, E., Maraschi, L., et al. 2006, A&A, 450, 77

Fossati, G., Maraschi, L., Celotti, A., Comastri, A., & Ghisellini, G. 1998, MNRAS, 299, 433

Frank, J., King, A., & Raine, D. 1992, Camb. Astrophys. Ser., Vol. 21„

Gammie, C. F. 2009, Bulletin of the American Astronomical Society, 41, #210.02

Garland, G., Ghisellini, G., Tavecchio, F., Foschini, L., Bonnoli, G. 2011 MNRAS, 413, 852

Gebhardt, K., & Thomas, J. 2009, ApJ, 700, 1690

Gebhardt, K., Adams, J., Richstone, D., et al. 2011, ApJ, 729, 119

Genzel, R., & Townes, C. H. 1987, ARA&A, 25, 377

Genzel, R., Schödel, R., Ott, T., et al. 2003, Nature, 425, 934

Georganopoulos, M., & Kazanas, D. 2003, ApJ, 594, L27

Georganopoulos, M., Perlman, E. S., & Kazanas, D. 2005, ApJ, 634, L33

Ghez, A. M., Klein, B. L., Morris, M., & Becklin, E. E. 1998, ApJ, 509, 678

Ghez, A. M., Morris, M., Becklin, E. E., Tanner, A., & Kremenek, T. 2000, Nature, 407, 349

Ghez, A. M., Duchêne, G., Matthews, K., et al. 2003, ApJ, 586, L127

Ghez, A. M., Salim, S., Hornstein, S. D., et al. 2005, ApJ, 620, 744

Ghez, A. M., et al. 2008, ApJ, 689, 1044

Ghisellini, G., Tavecchio, F., & Chiaberge, M. 2005, A&A, 432, 401

Goldreich, P., & Sridhar, S. 1995, ApJ, 438, 763

Goldwurm, A. 2007, Progress of Theoretical Physics Supplement, 169, 113

Goodman, J., & Narayan, R. 1989, MNRAS, 238, 963

Giannios, D., Uzdensky, D. A., & Begelman, M. C. 2010, MNRAS, 402, 1649

Gillessen, S., Eisenhauer, F., Trippe, S., et al. 2009, ApJ, 692, 1075

Giroletti, M., Hada, K., Giovannini, G., et al. 2012, A&A, 538, L10

Gracia, J., Vlahakis, N., Agudo, I., Tsinganos, K., & Bogovalov, S. V. 2009, ApJ, 695, 503

Greenstein, J. L., & Schmidt, M. 1964, ApJ, 140, 1

Gregory, P. C. 2005, ApJ, 631, 1198

Gregory, P. C. 2007, MNRAS, 381, 1607

Gurwell, M. A., Peck, A. B., Hostler, S. R., Darrah, M. R., & Katz, C. A. 2007, From Z-Machines to ALMA: (Sub)Millimeter Spectroscopy of Galaxies, 375, 234

Gwinn, C. R., Kovalev, Y. Y., Johnson, M. D., & Soglasnov, V. A. 2014, ApJ, 794, LL14

Hada, K., Doi, A., Kino, M., et al. 2011, Nature, 477, 185

Hada, K., Kino, M., Nagai, H., et al. 2012, ApJ, 760, 52

Hada, K., Kino, M., Doi, A., et al. 2013, ApJ, 775, 70

Hada, K., Giroletti, M., Kino, M., et al. 2014, ApJ, 788, 165

Harris, D. E., Cheung, C. C., Biretta, J. A., et al. 2006, ApJ, 640, 211

Harris, D. E., Cheung, C. C., Stawarz, L., et al. 2008, Extragalactic Jets: Theory and Observation from Radio to Gamma Ray, 386, 80

Harris, D. E., Cheung, C. C., Stawarz, Ł., Biretta, J. A., & Perlman, E. S. 2009, ApJ, 699, 305

Harris, D. E., Massaro, F., Cheung, C. C., et al. 2011, ApJ, 743, 177

Harms, R. J., Ford, H. C., Tsvetanov, Z. I., et al. 1994, ApJ, 435, L35

Hartman, R. C., Bertsch, D. L., Bloom, S. D., et al. 1999, ApJS, 123, 79

Hayashida, M., Madejski, G. M., Nalewajko, K., et al. 2012, ApJ, 754, 114

Heckman, T. M. 1980, A&A, 87, 152

Herrnstein, R. M., Zhao, J.-H., Bower, G. C., & Goss, W. M. 2004, AJ, 127, 3399

Heyvaerts, J., & Norman, C. 1989, ApJ, 347, 1055

Hirotani, K. 2005, ApJ, 619, 73

Ho, L. C., Filippenko, A. V., & Sargent, W. L. W. 1993, ApJ, 417, 63

Ho, L. C., Filippenko, A. V., & Sargent, W. L. W. 1997, ApJS, 112, 315

Ho, L. C., Filippenko, A. V., & Sargent, W. L. W. 1997, ApJ, 487, 568

Ho, L. C., Feigelson, E. D., Townsley, L. K., et al. 2001, ApJ, 549, L51

Ho, P. T. P., Moran, J. M., & Lo, K. Y. 2004, ApJ, 616, L1

Ho, L. C. 2008, ARA&A, 46, 475

Högbom, J. A. 1974, A&AS, 15, 417

Homan, D. C., Ojha, R., Wardle, J. F. C., et al. 2001, ApJ, 549, 840

Homan, D. C., Kadler, M., Kellermann, K. I., et al. 2009, ApJ, 706, 1253

Homan, D. C., Lister, M. L., Kovalev, Y. Y., et al. 2014, arXiv:1410.8502

Hong, X. Y., Venturi, T., Wan, T. S., et al. 1999, A&AS, 134, 201

Hong, X.-Y., Sun, C.-H., Zhao, J.-H., et al. 2008, ChJAA., 8, 179

Honma, M., Kawaguchi, N., & Sasao, T. 2000, Proc. SPIE, 4015, 624

Honma, M., Fujii, T., Hirota, T., et al. 2003, PASJ, 55, L57

Honma, M., Nagayama, T., Ando, K., et al. 2012, PASJ, 64, 136

Honma, M., Akiyama, K., Uemura, M., & Ikeda, S. 2014, PASJ, 82

Horiuchi, S., Fomalont, E. B., Taylor, W. K., et al. 2004, ApJ, 616, 110

Hornstein, S. D., Ghez, A. M., Tanner, A., et al. 2002, ApJ, 577, L9

Hornstein, S. D., Matthews, K., Ghez, A. M., Lu, J. R., Morris, M., Becklin, E. E., Rafelski, M., & Baganoff, F. K. 2007, ApJ, 667, 900

Huang, L., Liu, S., Shen, Z.-Q., Yuan, Y.-F., Cai, M. J., Li, H.,& Fryer, C. L. 2009, ApJ, 703, 557

Hukushima, K., and K. Nemoto. 1996, J. Phys. Soc. Jpn., 65, 1604

Ichimaru, S. 1977, ApJ, 214, 840

Iguchi, S., Kurayama, T., Kawaguchi, N., & Kawakami, K. 2005, PASJ, 57, 259

Inoue, S., & Takahara, F. 1996, ApJ, 463, 555

Inoue, M., et al. 2014, arXiv:1407.2450

Jordán, A., Côté, P., Blakeslee, J. P., et al. 2005, ApJ, 634, 1002

Jorstad, S. G., Marscher, A. P., Mattox, J. R., et al. 2001, ApJS, 134, 181

Jorstad, S. G., Marscher, A. P., Lister, M. L., et al. 2005, AJ, 130, 1418

Jorstad, S., Marscher, A., Smith, P., et al. 2012, International Journal of Modern Physics Conference Series, 8, 356

Junkkarinen, V. 1984, PASP, 96, 539

Junor, W., Biretta, J. A., & Livio, M. 1999, Nature, 401, 891

Kato, S., Fukue, J., & Mineshige, S. 2008, Black-Hole Accretion Disks — Towards a New Paradigm —, 549 pages, including 12 Chapters, 9 Appendices, ISBN 978-4-87698-740-5, Kyoto University Press (Kyoto, Japan), 2008.,

Kato, Y., Umemura, M., & Ohsuga, K. 2009, MNRAS, 400, 1742

Kardashev, N. S., Khartov, V. V., Abramov, V. V., et al. 2013, Astronomy Reports, 57, 153

Kellermann, K. I., Sramek, R. A., Schmidt, M., Green, R. F., & Shaffer, D. B. 1994, AJ, 108, 1163

Kellermann, K. I., & Pauliny-Toth, I. I. K. 1969, ApJ, 155, L71

Kellermann, K. I., Lister, M. L., Homan, D. C., et al. 2004, ApJ, 609, 539

Khachikian, E. E., & Weedman, D. W. 1971, Astrofizika, 7, 389

Khachikian, E. Y., & Weedman, D. W. 1974, ApJ, 192, 581

Kino, M., Takahara, F., & Kusunose, M. 2002, ApJ, 564, 97

Kino, M., Takahara, F., Hada, K., & Doi, A. 2014, ApJ, 786, 5

Kino, M., Takahara, F., Hada, K., Akiyama, K., Nagai, H., Sohn, B. W., 2014, submitted to ApJ

Komatsu, E., Dunkley, J., Nolta, M. R., et al. 2009, ApJS, 180, 330

Komissarov, S. S., Barkov, M. V., Vlahakis, N., Knigl, A. 2007, MNRAS, 380, 51

Komissarov, S. S., Vlahakis, N., Königl, A., & Barkov, M. V. 2009, MNRAS, 394, 1182

Königl, A. 1981, ApJ, 243, 700

Kormendy, J., & Ho, L. C. 2013, ARA&A, 51, 511

Kovalev, Y. Y., Lister, M. L., Homan, D. C., & Kellermann, K. I. 2007, ApJ, 668, L27

Kraus, A., et al. 2003, A&A, 401, 161

Kubo, H., Takahashi, T., Madejski, G., et al. 1998, ApJ, 504, 693

Kuo, C. Y., Asada, K., Rao, R., et al. 2014, ApJ, 783, L33

Lambert, H. C., & Rickett, B. J. 1999, ApJ, 517, 299

Lovelace, R. V. E. 1976, Nature, 262, 649

Lee, S.-S., Lobanov, A. P., Krichbaum, T. P., et al. 2008, AJ, 136, 159

Lee, S.-S., Byun, D.-Y., Oh, C. S., et al. 2011, PASP, 123, 1398

Lenain, J.-P., Boisson, C., Sol, H., & Katarzyński, K. 2008, A&A, 478, 111

Levinson, A., & Rieger, F. 2011, ApJ, 730, 123

León-Tavares, J., Valtaoja, E., Giommi, P., et al. 2012, ApJ, 754, 23

Li, Z.-Y., Chiueh, T., & Begelman, M. C. 1992, ApJ, 394, 459

Li, J., Shen, Z.-Q., Miyazaki, A., Huang, L., Sault, R. J., Miyoshi, M., Tsuboi, M., & Tsutsumi, T. 2009, ApJ, 700, 417

Lister, M. L., & Homan, D. C. 2005, AJ, 130, 1389

Lister, M. L., Cohen, M. H., Homan, D. C., et al. 2009, AJ, 138, 1874

Lister, M. L., Aller, M. F., Aller, H. D., et al. 2013, AJ, 146, 120

Liu, S., Petrosian, V., & Melia, F. 2004, ApJ, 611, L101

Lo, K. Y., Shen, Z.-Q., Zhao, J.-H., & Ho, P. T. P. 1998, ApJ, 508, L61

Lobanov, A. P. 1998, A&A, 330, 79

Lobanov, A. 2007, Exploring the Cosmic Frontier: Astrophysical Instruments for the 21st Century, 39

Loeb, A., & Waxman, E. 2007, JCAP, 3, 11

Lu, R.-S., Krichbaum, T. P., Eckart, A., König, S., Kunneriath, D., Witzel, G., Witzel, A., & Zensus, J. A. 2011, A&A, 525, A76

Lu, R.-S., Krichbaum, T. P., & Zensus, J. A. 2011, MNRAS, 418, 2260

Lu, R.-S., Fish, V. L., Weintroub, J., et al. 2012, ApJ, 757, L14

Lu, R.-S., Fish, V. L., Akiyama, K., et al. 2013, ApJ, 772, 13

Lu, R.-S., Broderick, A. E., Baron, F., et al. 2014, ApJ, 788, 120

Lustig, M., Donoho, D. L., Santos, J. M., & Pauly, J. M. 2008, IEEE Signal Processing Magazine, 25, 72

Ly, C., Walker, R. C., & Wrobel, J. M. 2004, AJ, 127, 119

Ly, C., Walker, R. C., & Junor, W. 2007, ApJ, 660, 200

Macchetto, F., Marconi, A., Axon, D. J., et al. 1997 ApJ, 489, 579

Macquart, J.-P., & Bower, G. C. 2006, ApJ, 641, 302

Macquart, J.-P., Bower, G. C., Wright, M. C. H., Backer, D. C., & Falcke, H. 2006, ApJ, 646, L111

Mahadevan, R. 1997, ApJ, 477, 585

Maitra, D., Markoff, S., & Falcke, H. 2009, A&A, 508, L13

Marshall, H. L., Miller, B. P., Davis, D. S., et al. 2002, ApJ, 564, 683

Manmoto, T., Mineshige, S., & Kusunose, M. 1997, ApJ, 489, 791

Manmoto, T. 2000, ApJ, 534, 734

Markoff, S., Falcke, H., Yuan, F., & Biermann, P. L. 2001, A&A, 379, L13

Markoff, S., Nowak, M. A., & Wilms, J. 2005, ApJ, 635, 1203

Markoff, S., Bower, G. C., & Falcke, H. 2007, MNRAS, 379, 1519

Marrone, D. P. 2006, Ph.D. Thesis,

Marrone, D. P., Moran, J. M., Zhao, J.-H., & Rao, R. 2006, ApJ, 640, 308

Marrone, D. P., et al. 2008, ApJ, 682, 373

Marscher, A. P. 1983, ApJ, 264, 296

Marscher, A. P., & Gear, W. K. 1985, ApJ, 298, 114

Marscher, A. P., Jorstad, S. G., D'Arcangelo, F. D., et al. 2008, Nature, 452, 966

Marscher, A. P., Jorstad, S. G., Larionov, V. M., et al. 2010, ApJ, 710, L126

Marscher, A. P. 2014, ApJ, 780, 87

Maitra, D., Markoff, S., & Falcke, H. 2009, A&A, 508, L13

McKinney, J. C. 2006, MNRAS, 368, 1561

McKinney, J. C., Tchekhovskoy, A., & Blandford, R. D. 2013, Science, 339, 49

Melia, F., Bromley, B. C., Liu, S., & Walker, C. K. 2001, ApJ, 554, L37

Merloni, A., Heinz, S., & di Matteo, T. 2003, MNRAS, 345, 1057

Meyer, L., Schödel, R., Eckart, A., Karas, V., Dovčiak, M., & Duschl, W. J. 2006, A&A, 458, L25

Meyer, L., Eckart, A., Schödel, R., Duschl, W. J., Mužić, K., Dovčiak, M., & Karas, V. 2006, A&A, 460, 15

Meyer, E. T., Sparks, W. B., Biretta, J. A., et al. 2013, ApJ, 774, LL21

Miller, J. S., Goodrich, R. W., & Mathews, W. G. 1991, ApJ, 378, 47

Miyazaki, A., Tsutsumi, T., & Tsuboi, M. 2004, ApJ, 611, L97

Mościbrodzka, M., Gammie, C. F., Dolence, J. C., Shiokawa, H., & Leung, P. K. 2009, ApJ, 706, 497

Mościbrodzka, M., Shiokawa, H., Gammie, C. F., & Dolence, J. C. 2012, ApJ, 752, L1

Mościbrodzka, M., & Falcke, H. 2013, A&A, 559, LL3

Mościbrodzka, M., Falcke, H., Shiokawa, H., & Gammie, C. F. 2014, A&A, 570, AA7

Moran, J. M. 1998, IAU Colloq. 164: Radio Emission from Galactic and Extragalactic Compact Sources, 144, 1

Mukherjee, R., Bertsch, D. L., Bloom, S. D., et al. 1997, ApJ, 490, 116

Muller, P. 1991, Technical report, Institute of Statistics and Decision Sciences, Duke University, # 91-09,

Mundy, L. G., & Scott, S. L. 2000, Imaging at Radio through Submillimeter Wavelengths, 217, 235

Nakamura, M., Li, H., & Li, S. 2006, ApJ, 652, 1059

Nakamura, M., & Asada, K. 2013, ApJ, 775, 118

Nakamura, M., & Asada, K. 2013, European Physical Journal Web of Conferences, 61, 01004

Nagakura, H., & Takahashi, R. 2010, ApJ, 711, 222

Nagai, H., Kino, M., Niinuma, K., et al. 2013, PASJ, 65, 24

Nagai, H., Haga, T., Giovannini, G., et al. 2014, ApJ, 785, 53

Nagata, K. & Watanabe, S. 2008, Neural Networks, Vol.21, No.7, 980-988

Narayan, R. 1988, Radio Wave Scattering in the Interstellar Medium, 174, 17

Narayan, R., & Goodman, J. 1989, MNRAS, 238, 995

Narayan, R. 1992, Royal Society of London Philosophical Transactions Series A, 341, 151

Narayan, R., & Popham, R. 1993, Nature, 362, 820

Narayan, R., & Yi, I. 1994, ApJ, 428, L13

Narayan, R., & Yi, I. 1995, ApJ, 444, 231

Narayan, R., Mahadevan, R., Grindlay, J. E., Popham, R. G., & Gammie, C. 1998, ApJ, 492, 554

Narayan, R., Igumenshchev, I. V., & Abramowicz, M. A. 2000, ApJ, 539, 798

Narayan, R., & Fabian, A. C. 2011, MNRAS, 415, 3721

Neronov, A., & Aharonian, F. A. 2007, ApJ, 671, 85

Newport, R. W. 1986, Journal of the British Interplanetary Society, 39, 211

Nieppola, E., Tornikoski, M., Valtaoja, E., et al. 2011, A&A, 535, AA69

Niinuma, K., Lee, S.-S., Kino, M., et al. 2014, arXiv:1406.4356

Nolan, P. L., Abdo, A. A., Ackermann, M., et al. 2012, ApJS, 199, 31

O'Sullivan, S. P., & Gabuzda, D. C. 2009, MNRAS, 400, 26

Okamoto, I. 1975, MNRAS, 173, 357

Okamoto, I. 1999, MNRAS, 307, 253

Orienti, M., Koyama, S., D'Ammando, F., et al. 2013, MNRAS, 428, 2418

Osterbrock, D. E. 1977, ApJ, 215, 733

Osterbrock, D. E. 1981, ApJ, 249, 462

Osterbrock, D. E., & Pogge, R. W. 1985, ApJ, 297, 166

Owen, F. N., Hardee, P. E., & Cornwell, T. J. 1989, ApJ, 340, 698

Owen, F. N., Eilek, J. A., & Kassim, N. E. 2000, ApJ, 543, 611

Özel, F., Psaltis, D., & Narayan, R. 2000, ApJ, 541, 234

Perlman, E. S., Biretta, J. A., Sparks, W. B., Macchetto, F. D., & Leahy, J. P. 2001, ApJ, 551, 206

Perlman, E. S., Sparks, W. B., Radomski, J., et al. 2001, ApJ, 561, L51

Perlman, E. S. 2013, Planets, Stars and Stellar Systems. Volume 6: Extragalactic Astronomy and Cosmology, 305

Psaltis, D., Ozel, F., Chan, C.-K., & Marrone, D. P. 2014, arXiv:1411.1454

Quataert, E., & Gruzinov, A. 2000, ApJ, 539, 809

Readhead, A. C. S. 1994, ApJ, 426, 51

Rees, M. J. 1966, Nature, 211, 468

Reid, M. J., Biretta, J. A., Junor, W., Muxlow, T. W. B., & Spencer, R. E. 1989, ApJ, 336, 112

Reid, M. J., & Brunthaler, A. 2004, ApJ, 616, 872

Reid, M. J., Menten, K. M., Trippe, S., Ott, T., & Genzel, R. 2007, ApJ, 659, 378

Reid, M. J., Broderick, A. E., Loeb, A., Honma, M., & Brunthaler, A. 2008, ApJ, 682, 1041

Reid, M. J., Menten, K. M., Zheng, X. W., et al. 2009, ApJ, 700, 137

Reid, M. J., Menten, K. M., Brunthaler, A., et al. 2014, ApJ, 783, 130

Reimer, A., Protheroe, R. J., & Donea, A.-C. 2004, A&A, 419, 89

Reynolds, C. S., Di Matteo, T., Fabian, A. C., Hwang, U., & Canizares, C. R. 1996, MNRAS, 283, L111

Reynoso, M. M., Medina, M. C., & Romero, G. E. 2011, A&A, 531, A30

Rickett, B. J. 1990, ARA&A, 28, 561

Rieger, F. M., & Aharonian, F. A. 2008, International Journal of Modern Physics D, 17, 1569

Rieger, F. M. 2011, International Journal of Modern Physics D, 20, 1547

Rieger, F. M., & Aharonian, F. 2012, Modern Physics Letters A, 27, 1230030

Riquelme, M. A., Quataert, E., Sharma, P., & Spitkovsky, A. 2012, arXiv:1201.6407

Roberts, G. O., Gelman, A., & Gilks,W. R. 1997, Ann. Appl. Probability, 7, 110

Rogers, A. E. E., Hinteregger, H. F., Whitney, A. R., et al. 1974, ApJ, 193, 293

Rogers, A. E. E., Doeleman, S., Wright, M. C. H., et al. 1994, ApJ, 434, L59

Rogers, A. E. E., Doeleman, S. S., & Moran, J. M. 1995, AJ, 109, 1391

Rybicki, G. B., & Lightman, A. P. 1986, Radiative Processes in Astrophysics, by George B. Rybicki, Alan P. Lightman, pp. 400. ISBN 0-471-82759-2. Wiley-VCH , June 1986.,

Sahu, S., & Palacios, E. 2013, arXiv:1310.1381

Sakurai, T. 1985, A&A, 152, 121

Sakurai, T. 1987, PASJ, 39, 821

Sargent, W. L. W., Young, P. J., Lynds, C. R., et al. 1978, ApJ, 221, 731

Sasada, M., Uemura, M., Fukazawa, Y., et al. 2012, PASJ, 64, 58

Schödel, R., Ott, T., Genzel, R., et al. 2002, Nature, 419, 694

Schödel, R., Eckart, A., Mužić, K., et al. 2007, A&A, 462, L1

Schödel, R., Merritt, D., & Eckart, A. 2009, A&A, 502, 91

Schödel, R., Morris, M. R., Muzic, K., et al. 2011, A&A, 532, AA83

Serabyn, E., Carlstrom, J., Lay, O., et al. 1997, ApJ, 490, L77

Seyfert, C. K. 1943, ApJ, 97, 28

Shakura, N. I., & Sunyaev, R. A. 1973, A&A, 24, 337

Shcherbakov, R. V., Penna, R. F., & McKinney, J. C. 2010, arXiv:1007.4832

Shen, Z.-Q., Lo, K. Y., Liang, M.-C., Ho, P. T. P., & Zhao, J.-H. 2005, Nature, 438, 62

Shepherd, M. C., Pearson, T. J., & Taylor, G. B. 1994, BAAS, 26, 987

Sikora, M., Begelman, M. C., & Rees, M. J. 1994, ApJ, 421, 153

Sikora, M., Błażejowski, M., Moderski, R., & Madejski, G. M. 2002, ApJ, 577, 78

Stawarz, Ł., Aharonian, F., Kataoka, J., et al. 2006, MNRAS, 370, 98

Takahara, F., Rosner, R., & Kusunose, M. 1989, ApJ, 346, 122

Takahashi, R., & Mineshige, S. 2011, ApJ, 729, 86

Tatarskii, V. I. 1971, Jerusalem: Israel Program for Scientific Translations, 1971,

Tavecchio, F., & Ghisellini, G. 2008, MNRAS, 385, L98

Tavecchio, F., & Ghisellini, G. 2014, arXiv: 1

Terashima, Y., & Wilson, A. S. 2003, ApJ, 583, 145

Thompson, D. J., Bertsch, D. L., Dingus, B. L., et al. 1995, ApJS, 101, 259

Thompson, A. R., Moran, J. M., & Swenson, G. W., Jr. 2001, ”Interferometry and synthesis in radio astronomy by A. Richard Thompson, James M. Moran, and George W. Swenson, Jr. 2nd ed. New York : Wiley, c2001.xxiii, 692 p. : ill. ; 25 cm. ”A Wiley-Interscience publication.” Includes bibliographical references and indexes. ISBN : 0471254924”,

Toma, K., & Takahara, F. 2013, Progress of Theoretical and Experimental Physics, 2013, 083E02

Tomimatsu, A. 1994, PASJ, 46, 123

Tomimatsu, A., & Takahashi, M. 2003, ApJ, 592, 321

Tran, H. D. 2001, ApJ, 554, L19

Tran, H. D. 2003, ApJ, 583, 632

Trippe, S., Paumard, T., Ott, T., Gillessen, S., Eisenhauer, F., Martins, F., & Genzel, R. 2007, MNRAS, 375, 764 404.6894

Urry, C. M., & Padovani, P. 1995, PASP, 107, 803

van der Laan, H. 1966, Nature, 211, 1131

van Langevelde, H. J., Frail, D. A., Cordes, J. M., & Diamond, P. J. 1992, ApJ, 396, 686

Varghese, A., Ibata, R., & Lewis, G. F. 2011, MNRAS, 417, 198

Veilleux, S., & Osterbrock, D. E. 1987, ApJS, 63, 295

Vlahakis, N., Königl, A. 2003, ApJ, 596, 1080

Villarroel, B., & Korn, A. J. 2014, Nature Physics, 10, 417

Vincent, S. 2014, International Journal of Modern Physics Conference Series, 28, 60189

Wada, K. 2012, ApJ, 758, 66

Wall, J. V., & Jenkins, C. R. 2003, Cambridge University Press,

Walsh, J. L., Barth, A. J., Ho, L. C., & Sarzi, M. 2013, ApJ, 770, 86

Wang, Q. D., Nowak, M. A., Markoff, S. B., et al. 2013, Science, 341, 981

Webb, J. R., Smith, A. G., Leacock, R. J., et al. 1988, AJ, 95, 374

Winkler, H. 1992, MNRAS, 257, 677

Whitney, A. R., Shapiro, I. I., Rogers, A. E. E., et al. 1971, Science, 173, 225

Whysong, D., & Antonucci, R. 2004, ApJ, 602, 116

Young, P. J., Westphal, J. A., Kristian, J., Wilson, C. P., & Landauer, F. P. 1978, ApJ, 221, 721

Young, A. J., Wilson, A. S., & Mundell, C. G. 2002, ApJ, 579, 560

Yuan, F., Markoff, S., & Falcke, H. 2002, A&A, 383, 854

Yuan, F., Quataert, E., & Narayan, R. 2003, ApJ, 598, 301

Yuan, F., Shen, Z.-Q., & Huang, L. 2006, ApJ, 642, L45

Yuan, F. 2007, The Central Engine of Active Galactic Nuclei, 373, 95

Yuan, Y.-F., Cao, X., Huang, L., & Shen, Z.-Q. 2009, ApJ, 699, 722

Yuan, F., & Narayan, R. 2014, arXiv:1401.0586

Yusef-Zadeh, F., et al. 2006, ApJ, 644, 198

Yusef-Zadeh, F., Roberts, D., Wardle, M., Heinke, C. O., & Bower, G. C. 2006, ApJ, 650, 189

Yusef-Zadeh, F., Wardle, M., Heinke, C., Dowell, C. D., Roberts, D., Baganoff, F. K., & Cotton, W. 2008, ApJ, 682, 361

Yusef-Zadeh, F., et al. 2009, ApJ, 706, 348

Zhao, J.-H., Bower, G. C., & Goss, W. M. 2001, ApJ, 547, L29

Zhao, J.-H., Young, K. H., Herrnstein, R. M., et al. 2003, ApJ, 586, L29

Zhou, H.-Y., & Wang, T.-G. 2002, CJAA, 2, 501

Zakamska, N. L., Begelman, M. C., & Blandford, R. D. 2008, ApJ, 679, 990

CORRESPONDENCE

Kazunori AKIYAMA

Mizusawa VLBI Observatory, National Astronomical Observatory of Japan

Adress: 2-21-1 Osawa, Mitaka, Tokyo 181-8588, Japan

e-mail: kazunori.akiyama@nao.ac.jp, kazunori.akiyama.kazu@gmail.com

(As of April 2015)